



**HAL**  
open science

# Development of an innovative instrument for the measurement of peroxy radicals and ozone production in the atmosphere

Goufrane Abichou

► **To cite this version:**

Goufrane Abichou. Development of an innovative instrument for the measurement of peroxy radicals and ozone production in the atmosphere. Atmospheric and Oceanic Physics [physics.ao-ph]. Université du Littoral Côte d'Opale, 2023. English. NNT : 2023DUNK0694 . tel-04575716

**HAL Id: tel-04575716**

**<https://theses.hal.science/tel-04575716>**

Submitted on 15 May 2024

**HAL** is a multi-disciplinary open access archive for the deposit and dissemination of scientific research documents, whether they are published or not. The documents may come from teaching and research institutions in France or abroad, or from public or private research centers.

L'archive ouverte pluridisciplinaire **HAL**, est destinée au dépôt et à la diffusion de documents scientifiques de niveau recherche, publiés ou non, émanant des établissements d'enseignement et de recherche français ou étrangers, des laboratoires publics ou privés.



# Thèse de Doctorat

*Mention : Physique*  
*Spécialité : Physique Milieux dilués et optique fondamentale*

présentée à l'Ecole Doctorale en Sciences Technologie et Santé (ED 585)

de l'Université du Littoral Côte d'Opale

par

**Goufrane ABICHOU**

pour obtenir le grade de Docteur de l'Université du Littoral Côte d'Opale

*Développement d'un instrument innovant dédié à la  
mesure des radicaux peroxy et la production d'ozone  
dans l'atmosphère*

Soutenue le 28 novembre 2023, après avis des rapporteurs, devant le jury d'examen :

M<sup>me</sup> K. Deboudt, Professeure, Université du Littoral Côte d'Opale  
M. S. Le Calvé, Directeur de recherche CNRS, Université de Strasbourg  
M<sup>me</sup> L. Whalley, Senior scientist, NCAS, Leeds University  
M<sup>me</sup> C. Schoemaeker, Chargée de recherche, Université de Lille  
M. W. Chen, Professeur, Université du Littoral Côte d'Opale  
M. S. Dusanter, Maître Assistant, IMT Nord Europe  
M. A. Tomas, Professeur, IMT Nord Europe

Présidente  
Rapporteur  
Rapportrice  
Examinatrice  
Directeur de thèse  
Co-directeur  
Encadrant





# **THESIS**

for the degree of

**Doctor of Philosophy**

in

Physics

by

**Goufrane ABICHOU**

Title of thesis:

**Development of an innovative instrument for the  
measurement of peroxy radicals and ozone production  
in the atmosphere**

Defended on 28 November 2023

Hosting laboratories:

LPCA (Laboratoire de Physico-Chimie de l'Atmosphère), ULCO, Dunkerque, France  
CERI EE (Research unit of the Energy and Environment Centre), IMT Nord Europe,  
Douai, France

Doctoral School of Sciences Technology and Health  
Discipline: Physics Diluted media and fundamental optics



# Acknowledgments

First of all, I want to thank ULCO and IMT Nord Europe, as well as the Region Hauts-de-France for funding my project and providing me the opportunity to conduct this research work.

I would also like to thank the jury members, Karine Deboudt, Stéphane Le Calvé, Lisa Whalley and Coralie Schoemaeker for accepting to evaluate my work and for their insightful suggestions and advices to improve my work before and during the defense. Thank you for dedicating your time and expertise to assess my project and for offering invaluable feedback.

I take this opportunity to express my heartfelt gratitude to my directors and supervisor. First, I extend my sincere thanks to my director, Weidong Chen, for his enthusiastic encouragement and guidance in my development as a scientist. Despite my initial lack of technical skills, he always believed in me, which I think was a key factor in the success of this project. I am truly grateful for all the opportunities he has provided me over these years. Moreover, I wish to show my greatest appreciation to my co-director Sebastien Dusanter, for his support and supervision throughout the entirety of this project. I cannot say thank you enough for his invaluable help with the experimental work and manuscript writing. Each meeting with him left me feeling motivated and inspired. Of course, I must also express my deepest recognition to my supervisor, Alexandre Tomas, for his assistance, for the patient direction and mentorship he provided during this PhD journey. I consider myself incredibly fortunate to have the opportunity to work with him, as it has not only facilitated my academic growth but also enriched me intellectually.

I also want to address my gratitude to Tong Nguyen Ba and Ngo Minh Nhut for accompanying me during the initial stages of my PhD. Their help and willingness to dedicate their time, particularly when working with the PAS technology, were precious.

I couldn't miss thanking Ahmad Lahib, who offered me the essential assistance and guidance in the lab when I first arrived at IMT Nord Europe. Additionally, I would like to thank Marina Jamar for her help in the lab along the second half of my PhD.

I am also very grateful for all the support of Eric Fertein, who collaborated with me during challenging times with my experiments and patiently answered so many of my questions. I extend my special thanks to Karine deboudt, Pascal Flament and Soulemane Halif Ngagine for their help along my PhD, especially for our collaboration on Black Carbon measurements.

I also want to thank Joel Brito for his assistance with Matlab and for the interesting conversions we shared. Furthermore, I want to thank all members at IMT Nord Europe and ULCO who indirectly contributed to the success of this project.

Furthermore, I would like to extend my gratitude to my office mates at both IMT Nord Europe and ULCO for the time we shared in the same working environment. Alongside the great scientific support, I want to emphasize the significance of a positive work atmosphere. Therefore, I express my sincere appreciation to Nhut, Jonas, Fatima and Khaoula in Dunkerque, as well as Pablo, Antonia and Clara in Douai.

There are many more people I want to mention who brought joy to my life during my PhD. I would like to thank all of you: Raafa, Tamara, Sahar, Hasna, Vinay, Yamina. A special thank is addressed to Nesrine Shamas, whom I consider was one of the best discoveries I made during the ROxComp campaign.

Last but certainly not least, I want to express my deepest gratitude to my family, particularly my mom and dad, for their never-ending encouragement and belief in me. All of this would not have been possible without your tremendous support and love. Words cannot adequately convey how thankful I am to have you in my life!

لِقَلْبِ أُمِّي وَ سَاعِدِي أَبِي ...





# Table of Contents

<b>Introduction .....</b>	<b>19</b>
<b>Chapter 1. Tropospheric ozone: Impacts, chemistry and regulations .....</b>	<b>22</b>
<b>1. Tropospheric ozone .....</b>	<b>23</b>
<b>1.1. Environmental impacts .....</b>	<b>24</b>
<b>1.2. Ozone formation chemistry .....</b>	<b>28</b>
<b>1.3. Control strategies.....</b>	<b>35</b>
<b>2. Analytical techniques for measuring peroxy radicals, nitrogen oxides and ozone production rates .....</b>	<b>37</b>
<b>2.1. Peroxy radicals – HO<sub>2</sub> + RO<sub>2</sub> .....</b>	<b>38</b>
<b>2.2. Nitrogen Oxide Measurements.....</b>	<b>46</b>
<b>2.3. Ozone production rate – P(O<sub>3</sub>).....</b>	<b>50</b>
<b>3. Field measurements.....</b>	<b>56</b>
<b>3.1. Quantification of P(O<sub>3</sub>) from RO<sub>x</sub> radicals.....</b>	<b>56</b>
<b>3.2. Direct measurements of P(O<sub>3</sub>) .....</b>	<b>59</b>
<b>3.3. Conclusions .....</b>	<b>62</b>
<b>4. Outline of dissertation.....</b>	<b>64</b>
<b>Chapter 2. Development and characterization of photo-acoustic spectrometers.....</b>	<b>67</b>
<b>1. Introduction .....</b>	<b>68</b>
<b>2. Photoacoustic spectroscopy .....</b>	<b>68</b>
<b>2.1. Principle of photoacoustic spectroscopy.....</b>	<b>68</b>
<b>2.2. Light sources .....</b>	<b>70</b>
<b>2.3. Photo-acoustic cells.....</b>	<b>71</b>
<b>2.4. Signal processing unit.....</b>	<b>73</b>
<b>3. Characterization and optimization of a photoacoustic spectrometer for measuring black carbon .....</b>	<b>74</b>
<b>3.1. Experimental setup.....</b>	<b>74</b>
<b>3.2. Optimization of operating conditions .....</b>	<b>76</b>
<b>3.3. Calibration and figures of merit .....</b>	<b>82</b>
<b>3.4. Conclusions .....</b>	<b>87</b>
<b>4. Development of a 2-channel PAS for measuring NO<sub>2</sub> .....</b>	<b>89</b>

4.1. Experimental setup.....	90
4.2. Characterization and optimization of operating conditions.....	91
4.3. Calibration and figures of merit .....	97
4.4. Intercomparison of PAS and CAPS measurements in ambient air .....	100
4.5. Conclusions .....	107
<b>Chapter 3. Comparison of the IMT Chemical Amplifier to a Laser-Induced Fluorescence instrument during ROxComp .....</b>	<b>110</b>
1. Introduction .....	111
2. Description of the ROxComp campaign .....	111
2.1. Characteristics of the SAPHIR chamber .....	112
2.2. Peroxy radical instruments coupled to SAPHIR.....	113
2.3. Ancillary measurements performed in SAPHIR.....	117
2.4. Conducted experiments.....	118
3. Setup and calibration of the IMT-CA instrument .....	121
3.1. Setup of the Chemical Amplifier.....	121
3.2. Calibration of the Chemical Amplifier .....	122
3.3. Assessment of measurement biases from ozone.....	128
4. Comparison: IMT-CA vs FZJ-FAGE .....	131
4.1. Assessment of humidity effects.....	131
4.2. Assessment of O <sub>3</sub> effects .....	135
4.3. Assessment of NO effects .....	139
4.4. Detection efficiency for various types of peroxy radicals .....	148
5. Conclusions .....	165
<b>Chapter 4. Evaluation of a methodology to quantify ozone production rates using a Chemical Amplifier .....</b>	<b>169</b>
1. Introduction .....	170
2. Description of P(O <sub>3</sub> ) quantification methodologies.....	170
2.1. P(O <sub>x</sub> ) inferred from ambient measurements of HO <sub>2</sub> +RO <sub>2</sub> and NO .....	171
2.2. P(O <sub>x</sub> ) inferred from temporal variations of O <sub>x</sub> .....	172
3. Description of selected chamber experiments .....	173
3.1. SAPHIR chamber .....	173
3.2. Experimental conditions .....	174
4. Evaluation of the CA-based P(O <sub>x</sub> ) quantification approach.....	175

4.1. Rational of low vs high NO conditions .....	176
4.2. P(O <sub>x</sub> ) quantification under low NO conditions.....	178
4.3. P(O <sub>x</sub> ) quantification under high NO .....	186
4.4. Contrasting chamber results to ambient observations .....	199
4.5. Discussion on potential raisons leading to the P(O <sub>x</sub> ) <sup>HO<sub>2</sub>+RO<sub>2</sub></sup> / P(O <sub>x</sub> ) <sup>O<sub>x</sub></sup> disagreement at high NO .....	201
5. Conclusions .....	206
References .....	209
General conclusions and perspectives .....	222
Appendix: Publications and presentations on conferences .....	228
Abstract .....	229
Résumé .....	232

## List of Figures

<b>Figure 1. 1:</b> Ozone chemical structures.....	23
<b>Figure 1. 2:</b> Change in the earth Effective Radiative forcing between 1750 and 2019, and aggregated uncertainties for the main drivers of climate change.....	26
<b>Figure 1. 3:</b> Radical chain cycling leading to the oxidation of ambient trace gases and the formation of O <sub>3</sub> .....	30
<b>Figure 1. 4:</b> Ozone formation regimes .....	33
<b>Figure 1. 5:</b> Modeling of ozone formation sensitivity.....	37
<b>Figure 1. 6:</b> Schematic representation of PERCA.....	38
<b>Figure 1. 7:</b> Schematic representation of the chemistry occurring in a PERCA.....	39
<b>Figure 1. 8:</b> Dependence of the PERCA CL on both NO and CO .....	41
<b>Figure 1. 9:</b> Dependence of the PERCA CL on relative humidity.....	41
<b>Figure 1. 10:</b> Schematic representation of PerCIMS .....	43
<b>Figure 1. 11:</b> Schematic representation of RO <sub>x</sub> -LIF .....	45
<b>Figure 1. 12:</b> Schematic representation of MOPS.....	52
<b>Figure 1. 13:</b> Schematic of OPR.....	54
<b>Figure 1. 14:</b> Time series of ozone and P(O <sub>3</sub> ) for the SHARP 2009 field campaign.....	60
<b>Figure 1. 15:</b> Trend of P(O <sub>3</sub> ) on NO for the SHARP 2009 field campaign .....	61
<b>Figure 2. 1:</b> Schematic presentation of a PAS.....	69
<b>Figure 2.2:</b> Schematic presentation of the laser-induced photoacoustic effect .....	70
<b>Figure 2.3:</b> Schematics of PAS cells .....	72
<b>Figure 2.4:</b> Schematic representation of the PA spectrophone for BC measurements .....	75
<b>Figure 2.5:</b> Linear dependence of the net and background signals with laser power measured at the output of the PA cell.....	78
<b>Figure 2.6:</b> Dependence of the PA signal on the modulation frequency.....	79
<b>Figure 2.7:</b> Dependence of the PA noise and signal-to-noise ratio on the sampling flow rate .....	80
<b>Figure 2.8:</b> Time series of PAS measurements from filtered ambient air, dry compressed air, and dried and filtered ambient air .....	82

<b>Figure 2.9:</b> Schematic of the experimental setup for the measurement of incense-generated BC with the PAS instrument and a reference aethalometer .....	83
<b>Figure 2.10:</b> Schematic representation of the 2-channel measurement approach .....	84
<b>Figure 2. 11:</b> Time series of PAS and AE51 measurements of incense-generated BC.....	84
<b>Figure 2.12:</b> PA signals versus BC mass concentrations measured by the AE51 during three calibration experiments. ....	85
<b>Figure 2.13:</b> Annual-averaged surface BC concentrations for the year 2005 .....	86
<b>Figure 2.14:</b> Schematic representation of the PAS for NO <sub>2</sub> measurements.....	90
<b>Figure 2.15:</b> Emission spectra of the two diode lasers and NO <sub>2</sub> absorption cross sections between 446 and 460 nm.....	91
<b>Figure 2.16:</b> Dependence of the PA signal on the modulation frequency for channels 1 and 2.....	92
<b>Figure 2.17:</b> Dependence of the laser power on the current intensity.....	93
<b>Figure 2.18:</b> Dependence of the effective PA signal on laser power for channels 1 (a) and 2 (b) at constant NO <sub>2</sub> concentrations in zero air .....	94
<b>Figure 2.19:</b> Dependences of the net PA signal, PA noise and signal-to-noise ratio on the sampling flow rate .....	95
<b>Figure 2.20:</b> Dependence of the Eff PAS signal on H <sub>2</sub> O concentration for channel 1.....	96
<b>Figure 2.21:</b> Setup for the generation of NO <sub>2</sub> /water/air mixtures .....	97
<b>Figure 2.22:</b> Calibration - Time series of NO <sub>2</sub> measurements by PAS for channels 1 (a) and 2 (b) and by CAPS .....	98
<b>Figure 2.23:</b> Calibration - Effective PAS signal versus NO <sub>2</sub> for channels 1 (a) and 2 (b) 98	
<b>Figure 2.24:</b> Annual ground-level NO <sub>2</sub> concentrations in the world for 2019 .....	99
<b>Figure 2.25:</b> Schematic presentation of the NO <sub>2</sub> -PAS & CAPS setup for sequential measurements in ambient and background modes. ....	101
<b>Figure 2.26:</b> Time series of indoor and outdoor measurements of NO <sub>2</sub> using the two PAS channels and the CAPS monitor.....	102
<b>Figure 2.27:</b> Correlation between NO <sub>2</sub> concentrations measured by the two PAS channels and the CAPS instrument .....	103
<b>Figure 2.28:</b> Time series of 1-s raw PA signals for channels 1 (a) and 2 (b).....	104
<b>Figure 2.29:</b> Time series of the background PA signal of channel 2, NO <sub>2</sub> concentrations, relative humidity, temperature and absolute humidity.....	105

<b>Figure 2.30:</b> Correlation of the background PA signal of channel 2 with absolute humidity .....	106
<b>Figure 2.31:</b> Time series of the residual NO <sub>2</sub> concentrations measured by channel 2 relative to the reference CAPS analyzer.....	106
<b>Figure 3. 1:</b> Picture of the SAPHIR chamber, FZJ, Germany.....	112
<b>Figure 3.2:</b> Schematic presentation of the IMT Nord Europe CA .....	115
<b>Figure 3.3:</b> Schematics of the home-made 3D printed nylon coupler.....	116
<b>Figure 3. 4:</b> IMT-CA coupling to SAPHIR.....	121
<b>Figure 3.5:</b> IMT-CA inlets, <b>A-</b> direct inlet, <b>B-</b> high flow inlet .....	122
<b>Figure 3.6:</b> Cross-section of the IMT-CA calibrator.....	123
<b>Figure 3.7:</b> Calibration of the chain length for IMT–CA during ROxComp and Across and determination of radical losses in the high flow rate inlet .....	125
<b>Figure 3.8:</b> Cross calibration of IMT-CA with: A) FZJ calibrator and B) Leeds calibrator. ....	127
<b>Figure 3.9:</b> Peroxy radical measurement bias at (A) variable O <sub>3</sub> concentrations and dry conditions, and (B) constant O <sub>3</sub> concentrations and varying humidity conditions .....	129
<b>Figure 3.10:</b> Measured vs predicted O <sub>3</sub> biases in IMT-CA measurements using the empirical model.....	130
<b>Figure 3.11:</b> Results from selected RH-relevant experiments - (A) 19 Aug .22 and (B) 20 Aug. 22.....	132
<b>Figure 3.12:</b> Correlation between IMT-CA and FZJ-FAGE measurements for the RH-relevant experiments.....	134
<b>Figure 3.13:</b> Results from selected O <sub>3</sub> -relevant experiments - (A) 19 Aug. 22 and (B) 26 Aug .22.....	136
<b>Figure 3.14:</b> Correlation between IMT-CA and FZJ-FAGE measurements for the experiments of 19 Aug. 22 and 26 Aug. 22.....	138
<b>Figure 3.15:</b> Results from 24 Aug. experiment.....	139
<b>Figure 3.16:</b> Results from selected NO-relevant experiments - (A) 11 Aug. 22, (B) 12 Aug. 22, (C) 14 Aug. 22 and (D) 20 Aug. 22.....	141
<b>Figure 3.17:</b> Results from selected Low NO <sub>x</sub> -relevant experiments - (A) 13 Aug. 22 and (B) 16 Aug. 22.....	145
<b>Figure 3.18:</b> Correlations between (a) IMT-CA and FZJ-FAGE measurements and (b) the IMT-CA/FZJ-FAGE ratio and NO for the NO-relevant experiments of 11 Aug. 22, 12 Aug. 22, 14 Aug. 22 and 20 Aug. 22. ....	147

<b>Figure 3.19:</b> Results from selected NO <sub>3</sub> -relevant experiments - (A) 17 Aug. 22 and (B) 22 Aug. 22 .....	152
<b>Figure 3.20:</b> Correlation between IMT-CA and FZJ-FAGE measurements for the NO <sub>3</sub> -relevant experiments of 17 Aug. 22 and 22 Aug. 22 .....	154
<b>Figure 3.21:</b> Results from selected ozonolysis-experiments - (A) 13 Aug. 22, (B) 19 Aug. 22 and 26 Aug. 22 .....	157
<b>Figure 3.22:</b> Correlation between IMT-CA and FZJ-FAGE measurements for the ozonolysis-experiments of 13 Aug. 22, 19 Aug. 22 and 26 Aug. 22 .....	160
<b>Figure 3.23:</b> Results from the 23 Aug. 22 experiment for the measurement of ambient air under irradiated conditions.....	162
<b>Figure 3.24:</b> Correlation between (a) IMT-CA and FZJ-FAGE measurements and (b) the ratio IMT-CA/FZJ-FAGE and NO for the experiment of 23 Aug. 22.....	163
<b>Figure 4. 1:</b> Two-dimensional space defining "low" and "high" NO VOC oxidation regimes .....	177
<b>Figure 4.2:</b> Experimental chamber observations for the (1) β-pinene, (2) methane and (3) MVK experiments. ....	180
<b>Figure 4.3:</b> Ozone production rates for the (A) β-pinene, (B) methane and (C) MVK experiments. ....	183
<b>Figure 4.4:</b> A - Stacked O <sub>x</sub> loss rates in ppb h <sup>-1</sup> for the (1) β-pinene, (2) methane and (3) MVK experiments, B - Contribution of each O <sub>x</sub> loss process to the total loss .....	184
<b>Figure 4.5:</b> Comparison between $P(O_x)^{HO_2+RO_2}$ and $P(O_x)^{O_x}$ for the (A) β-pinene, (B) methane and (C) MVK experiments. ....	186
<b>Figure 4.6:</b> Experimental chamber observations for the (1) isoprene, (2) i-pentane+n-hexane, (3) α-pinene and (4) mesitylene experiments.....	188
<b>Figure 4.7:</b> Ozone production rates for the (A) isoprene, (B) i-pentane+n-hexane, (C) α-pinene and (D) mesitylene experiments .....	193
<b>Figure 4.8:</b> A -Stacked O <sub>x</sub> loss rates in ppb h <sup>-1</sup> for the (1) isoprene, (2) i-pentane+n-hexane, (3) α-pinene and (4) mesitylene experiments, B - Contribution of each O <sub>x</sub> loss process to the total loss.....	194
<b>Figure 4.9:</b> Comparison between $P(O_x)^{HO_2+RO_2}$ and $P(O_x)^{O_x}$ for the (A) isoprene, (B) i-pentane+n-hexane (C) α-pinene and (D) mesitylene experiments .....	196
<b>Figure 4.10:</b> Dependence of $P(O_x)^{HO_2+RO_2}$ and $P(O_x)^{O_x}$ on NO for the (A) isoprene, (B) i-pentane+n-hexane (C) α-pinene and (D) mesitylene experiments. ....	197
<b>Figure 4.11:</b> Dependence of $P(O_x)^{HO_2+RO_2} - P(O_x)^{O_x}$ on NO for all experiments from Table 4.1 .....	198



<b>Figure 4.12:</b> Trend of the ratio $\mathbf{P(O_x)^{HO_2+RO_2}/P(O_x)^{O_x}}$ with NO for all experiments reported in Table 4.1.....	199
<b>Figure 4.13:</b> Trends in ozone production rate ratios with NO for the 2009 SHARP campaign .....	200
<b>Figure 4.14:</b> Scatter plot of $\mathbf{P(O_x)^{HO_2+RO_2} - P(O_x)^{O_x}}$ vs. $k_{NO+peroxy}[NO]$ for A) high NO experiments and B) low NO experiments. ....	203
<b>Figure 4.15:</b> Scatter plot of $\mathbf{P(O_x)^{HO_2+RO_2} - P(O_x)^{O_x}}$ vs. $k_{NO+peroxy} \times [HO_2+RO_2]$ for all experiments. ....	204

# List of Tables

<b>Table 1. 1:</b> Comparison between peroxy radical techniques .....	46
<b>Table 1. 2:</b> Comparison between NO <sub>2</sub> techniques .....	49
<b>Table 1. 3:</b> Required performance of the PAS instrument .....	89
<b>Table 2. 1:</b> Summary of ambient NO <sub>2</sub> measurements by PAS and CAPS .....	103
<b>Table 3. 1:</b> Peroxy radical instruments coupled to SAPHIR during ROxComp .....	114
<b>Table 3. 2:</b> Ancillary measurements during ROxComp .....	118
<b>Table 3. 3:</b> Experimental conditions for ROxComp experiments .....	119
<b>Table 3. 4:</b> Radicals produced from isoprene and β-pinene oxidation by NO <sub>3</sub> and O <sub>3</sub> (dark conditions).....	150
<b>Table 3. 5:</b> Peroxy radicals produced from the oxidation of α-pinene, trans-2-hexene, TME and isoprene by O <sub>3</sub> and OH.....	156
<b>Table 3. 6:</b> Tentative list of peroxy radicals produced during the 23 Aug. 22 experiment from reactions of VOCs with OH.....	164
<b>Table 4. 1:</b> Selected ROxComp experiments for P(O <sub>x</sub> ) quantification .....	175



# Introduction

Tropospheric ozone is a major air pollutant, both in terms of health (irritation of the upper airways) and climate (greenhouse effect). This pollutant is not directly emitted in the atmosphere, but is photochemically produced by solar radiation in the presence of primary chemical precursors: volatile organic compounds (VOCs) and nitrogen oxides ( $\text{NO}_x = \text{NO} + \text{NO}_2$ ). Given the secondary nature of this pollutant and the complexity of its formation chemistry, predictive atmospheric chemistry models are usually used to assess reduction strategies. However, multiple sources of errors are associated to emission inventories, chemistry and air mass transport, which limits the reliability of these predictive models. It is therefore essential to develop alternative approaches allowing to assess the most efficient reduction strategies.

The main objective of this PhD consisted in assessing the reliability of quantifying ozone production rates on the basis of simultaneous measurements of peroxy radicals ( $\text{HO}_2 + \text{RO}_2$ ) and nitrogen monoxide ( $\text{NO}$ ) in ambient air. The ozone production rate,  $P(\text{O}_3)$ , is inferred from the oxidation rate of  $\text{NO}$  into  $\text{NO}_2$  due to its reaction with peroxy radicals. The  $P(\text{O}_3)$  metric would be useful for public authorities in the management of pollution peaks since real-time measurements of  $P(\text{O}_3)$  would help assessing the ozone formation regime at a particular location ( $\text{NO}_x$ -limited or  $\text{NO}_x$ -saturated), identifying periods of intense photochemical activities leading to pollution episodes, and testing predictions from atmospheric models.

The work performed during this PhD consisted in (i) testing and improving a Chemical Amplifier (CA) developed at IMT Nord Europe for measuring peroxy radicals in ambient air and (ii) assessing the reliability of the methodology to quantify ozone production rates from concomitant measurements of peroxy radicals and  $\text{NO}$ .

- For (i), it required to develop a two-channel Photoacoustic Absorption Spectrometer (PAS) for  $\text{NO}_2$  measurements, simultaneously at the outlet of the background and amplification reactors of the CA. It was intended to replace two commercial  $\text{NO}_2$  analyzers, previously used on the CA, with the purpose of significantly reducing the construction cost of CA instruments.

It also required to test the reliability of the CA for measuring peroxy radicals by participating to an intercomparison study at the SAPHIR simulation chamber in Forschungszentrum Jülich, Germany. The CA was compared to other instruments relying on different analytical techniques.

- For (ii), results from the chamber experiments mentioned above were used to investigate whether the methodology of  $P(O_3)$  quantification is reliable.

The first chapter is a bibliographical study providing some context and motivations. A first section focuses on the impacts of tropospheric ozone on both air quality and climate change, its complex formation chemistry, and ozone control strategies implemented in various regions of the world. This chapter also provides a description of analytical techniques used for peroxy radical and ozone production rate measurements. Selected field measurements are also presented to highlight the importance of identifying the formation regimes of ozone to apply the right strategy for its reduction.

The second chapter presents experimental results focusing on the development and characterization of two photoacoustic spectrometers (PAS). First, we present characterization and calibration results for a PAS dedicated to black carbon measurements (prototype already present in the laboratory). The purpose of this work was to be trained on the PAS technology before designing a 2-channel instrument for  $NO_2$ . Then, we present results for the development of the  $NO_2$ -PAS instrument, including the optimization of operating conditions, calibrations of the instrumental response, and a comparison to a reference instrument.

The third chapter reports on the deployment of the CA during the intercomparison experiment performed at the SAPHIR chamber (ROxComp). During this campaign, several chamber experiments were conducted to challenge the radical instruments, producing different types of peroxy radicals under various conditions of temperature, humidity,  $NO_x$  and solar radiation.

The fourth and last chapter reports on the evaluation of the ozone production rate quantification methodology, taking advantage of photochemical experiments performed during ROxComp.  $P(O_3)$  values inferred from peroxy radical measurements were compared to ozone production rates inferred from the temporal change in  $O_x$  ( $O_3+NO_2$ ) species inside the chamber.



# **Chapter 1.**

## **Tropospheric ozone:**

### **Impacts, chemistry and regulations**

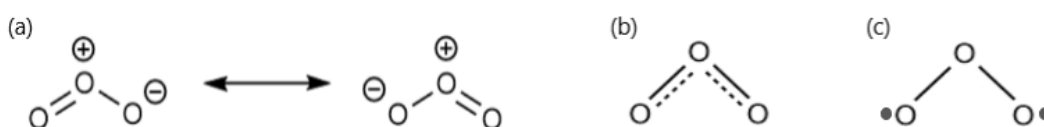
This chapter provides a description of the formation chemistry of ozone in the troposphere, highlighting the role of peroxy radicals and nitrogen oxides, and addressing its impacts on climate, vegetation, and human health. In addition, different approaches proposed for measuring peroxy radicals and ozone production rates are presented in this chapter, as well as a brief overview of peroxy radicals and ozone production rates measurements in the field. The motivations and main objectives of the PhD are presented in the last section.

# 1. Tropospheric ozone

Ozone ( $O_3$ ) is a highly active allotropic form of oxygen; it is a polar molecule made up of three oxygen atoms. This molecule has a 82% resonant character, as shown in Figure 1. 1 (a), with two contributing structures, each with a single bond on one side and a double bond on the other, that can be fused to a single structure with one and a half bond to each O-O interaction (Figure 1. 1 (b))<sup>1</sup>. It also has a biradical character (18%) as displayed in Figure 1. 1 (c)<sup>1</sup>. The strong oxidant nature of ozone is defined by its resonant structure<sup>2</sup>.

At the Earth's surface, i.e. in the troposphere, ozone reacts with a variety of molecules of living systems, leading to their oxidation, hence detrimental effects<sup>3</sup>. High concentrations of ozone (i.e. higher than 70 ppb) are considered to be toxic to the different life-forms<sup>3</sup>. Harmful impacts are reported in the literature on crop production, forest growth, and human health<sup>4,5</sup>. Future increases of tropospheric ozone within cities in the world, in rural areas, as well as remote locations represent a main societal challenge<sup>6</sup>. It is interesting to note that adverse effects of tropospheric ozone are in contradiction with its benefits in filtering the biologically damaging ultraviolet sunlight (UV-B radiations) in the stratosphere<sup>3</sup>.

In this work, we are focusing on the tropospheric compartment and the chemistry leading to ozone formation, developing state-of-the-art instrumentation to probe  $O_3$  precursors (peroxy radicals) and instantaneous  $O_3$  production rates.



**Figure 1. 1:** Ozone chemical structures: (a) Closed-Shell Resonance Structures (b) Closed-Shell Structure (c) Biradical Structure<sup>1</sup>.

In this section, we present how  $O_3$  impacts human health, vegetation and the Earth's radiative balance. We also present basics on tropospheric chemistry that leads to the formation and accumulation of  $O_3$  in the troposphere. Finally, we discuss the implementation of  $O_3$  reduction strategies using chemical transport models, highlighting the need of alternative methods to optimize their design.



## **1.1. Environmental impacts**

In the troposphere, ozone is a secondary air pollutant formed through complex photochemical reactions involving primary precursors, such as NO<sub>x</sub> and VOCs. Increases in the amounts of ozone are generally observed in areas affected by anthropogenic pollution, mainly during warm and sunny days<sup>4</sup>. Currently, ozone is considered as a major climate pollutant with detrimental impacts on human health and vegetation<sup>4</sup>.

### **1.1.1. Health impacts**

Ozone pollution is a global health threat. On the basis of respiratory effects, it is estimated that this pollutant causes more than 0.7 million deaths per year worldwide<sup>7</sup>. In 2018, a study reported on the global burden of different pollutants on asthma incidence, indicating that ozone exposure worldwide resulted in 8-20% of the total asthma related emergency cases in 2015<sup>8</sup>. In many areas of the world, ozone concentrations are expected to rise in the near future, resulting in higher ozone-related mortality and morbidity<sup>9</sup>. For instance, ozone is projected to increase with future climate change scenarios in Southeast Asia (SEA) (IPCC AR6 Interactive atlas)<sup>10</sup>.

The effects of ozone on human health are dependent to its concentration, frequency and duration of exposures, age, gender, and other risk factors<sup>11</sup>. According to the 2020 US EPA (Environmental Protection Agency) Integrated Science Assessment (ISA) for Ozone<sup>12</sup>, the responses of human health to ozone include respiratory and cardiovascular diseases, as well as some reactions of the nervous system<sup>12</sup>. The oxidative capacity of ozone allows it to strongly react with different biological molecules, such as proteins, lipids, lining fluids of the airways, inducing many physiological reactions, such as immune-inflammatory responses in the lungs, that can promote asthma development for long-term ozone exposure<sup>9</sup>. It is also responsible to induce premature mortality due to cancer, respiratory and cardio-vascular diseases<sup>9</sup>. In addition, children are more likely to be at risk from the exposure to ozone, given that they have a higher dose per body weight and their lungs continue to develop<sup>9</sup>.

In 2010 in Europe, ozone accounted for 19,200 and 86,000 respiratory and cardiovascular hospitalizations, respectively, and more than 109 million days of limited minor activities<sup>9</sup>. By examining long-term exposure to ozone and life expectancy in the

United States between 2002 and 2008, Li et al. <sup>5</sup> found that an increase of about 5 ppb ( $10 \mu\text{g m}^{-3}$ ) in ozone exposure can lead to a reduction of life expectancy by 0.25 and 0.21 year in males and females, respectively <sup>9</sup>. These data were first reported in the 2013 Ozone ISA<sup>13</sup>, and are still valid for the 2019 ISA <sup>12</sup>.

Future increases in tropospheric ozone concentrations will be accompanied by increases in ozone associated mortalities. For instance, it is forecasted that during the 2040's compared to 2000, a rise of 0.43 ppb in the average ozone concentration will be associated to a 0.01% increase in the rate of mortality across 19 urban communities in the southeastern United States <sup>9</sup>. Which corresponds to an increase of 14% in global mortality linked to ozone. It is clear that one of the major challenges that our society is facing in the field of air quality is the identification of the best measures to regulate long-term exposure to ozone, as it exhibits different diurnal and seasonal changes <sup>9</sup>, in part due to its complex formation chemistry (see section 1.2).

### **1.1.2. Climate impacts**

Ozone is an important greenhouse gas <sup>14</sup>. Different models have reported the increase in tropospheric ozone since the pre-industrial era, which has significantly contributed to the earth global warming. This was mainly observed in the Northern Hemisphere and in particular in the Arctic during winter and mostly since the middle of the 20<sup>th</sup> century <sup>15</sup>.

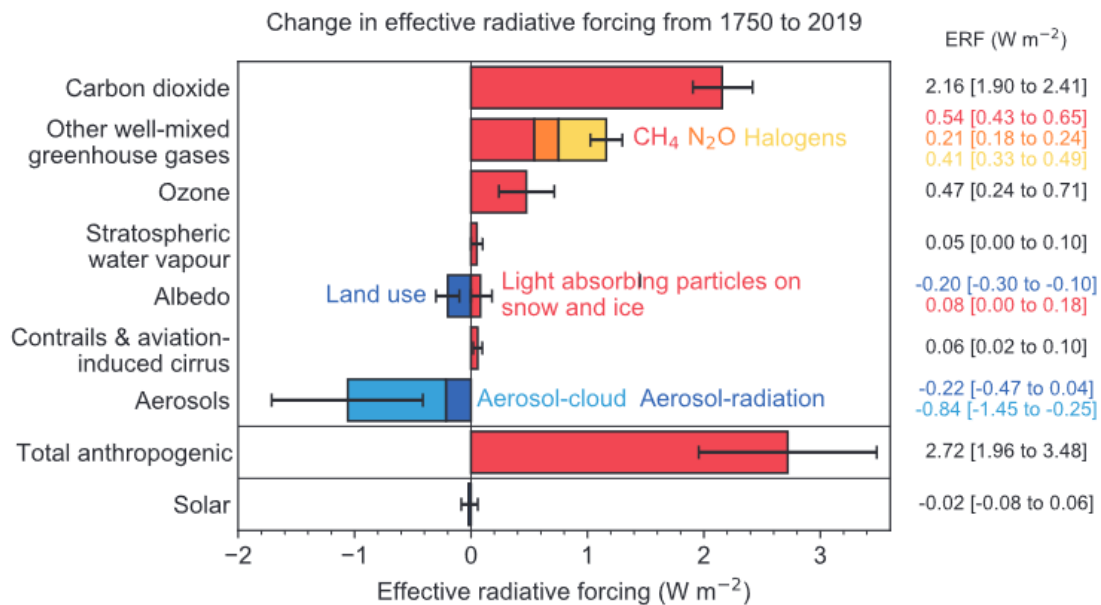
Figure 1.2 shows that atmospheric ozone has a significant positive Effective Radiative Forcing<sup>1</sup> since 1750. In the troposphere, the oxidation of methane, other volatile organic compounds, CO and the photolysis of NO<sub>2</sub> leads to ozone production (see section 1.2), which in turn absorbs a large amount of the terrestrial infrared radiation, leading to a positive effective radiative forcing <sup>15</sup>.

While the naturally emitted greenhouse gases (H<sub>2</sub>O, CO<sub>2</sub>, CH<sub>4</sub> and N<sub>2</sub>O) and the photochemically produced O<sub>3</sub> regulate the temperature and enable the development of life on Earth, large increases in the concentrations of these gases in the lower atmosphere result in an increase of the ground level temperature. Since the pre-industrial period, tropospheric

---

<sup>1</sup> Effective Radiative forcing (ERF) is a measure of the net change in the energy balance of the Earth system in response to some external perturbations, with positive ERF leading to a warming of the atmosphere and negative ERF to a cooling.

ozone highly increased, resulting in a rise of the global average ERF by  $0.47 \pm 0.23 \text{ W m}^{-2}$ . This makes it the third most impacting greenhouse gas after  $\text{CO}_2$  and  $\text{CH}_4$  <sup>15</sup>.



**Figure 1. 2:** Change in the earth Effective Radiative forcing between 1750 and 2019, and aggregated uncertainties for the main drivers of climate change <sup>15</sup>

Ozone also indirectly impacts the concentrations of other greenhouse gases through (1) the formation of the hydroxyl radical (OH), one of the most important oxidants in the atmosphere (see section 1.2), (2) the reduction of photolysis rates (UV absorption in the stratosphere), and (3) carbon sequestration, thereby increasing  $\text{CO}_2$  concentrations <sup>16</sup>.

Due to both direct and indirect effects, the increase of tropospheric ozone concentrations will continue to be an influential factor in global warming <sup>16</sup>, making assessments of its impact on the climate more challenging <sup>17</sup>.

### 1.1.3. Impacts on vegetation

Severe damages to plants from ground-level ozone were observed for the first time in the 1940's during the Los Angeles smog episodes <sup>18</sup>, and a quantification of crop loss in North America was settled during the 1970's <sup>19</sup>. These research programs found that 40% reductions in ozone exposure could lower the annual costs of its damage by \$3 billion <sup>20</sup>.

The effect of ozone on vegetation depends on its concentration as well as the plant phenotype <sup>18</sup>. The major impact is due to its intake through plant stomata during normal gas exchange, followed by its reaction with the inner tissues of the plant producing strongly

reactive oxidants that damages plant metabolism <sup>20</sup>. This mechanism also leads to a reduction in the plant CO<sub>2</sub> uptake, which in turns results in a decrease of photosynthesis, thereby lowering crop yield and growth <sup>18</sup>.

The sensitivity to ozone was shown for different species of plants and agricultural crops, such as (1) wheat, tomato, and rice, (2) salad crops like lettuce, spinach and onion and (3) some variety of trees, for instance beech, birch and Holm oak <sup>20</sup>. All of these impacts on plants affect the efficiency of their role in the ecosystem, namely the protection of soil against erosion, avalanches and flooding, the uptake of carbon, as well as the production of timber and the safety of food <sup>20</sup>.

Several global modelling studies have pointed out that nowadays, China, India and the United States are among the most concerned countries, with more than half of the worldwide losses and areas at risk from the exposure of crops to ozone <sup>20</sup>. For instance, in the years 2013-2014, the crop production losses of wheat and rice in the Indian states of Punjab and Haryana were estimated to 10.3 million tons (~27%) and 3.2 million tons (~21%), respectively <sup>18</sup>. This would be sufficient to provide more than 50% and 10% of the wheat and rice needs, respectively, for people living below the poverty line <sup>18</sup>. In Europe, wheat yield losses due to ozone exposure were about € 2 billion in 2020, which is equivalent to 9% of the economic value <sup>21</sup>.

The overall trends in exposure of vegetation to ozone are evolving. NO<sub>x</sub> and VOC emission control measures implemented in North America and Western Europe (see section 1.3), in which ozone has a well-defined effect on agricultural production and forest vitality, are likely to result in a decrease in the upper limit ozone concentrations.

However, the global background concentration of tropospheric ozone might rise simultaneously due to man-made activities, and mainly to the increase in worldwide NO<sub>x</sub> emissions <sup>4</sup>. This trend was previously observed in long-term monitoring of ozone concentrations in the UK. In fact, a decrease of 30% in the peak O<sub>3</sub> concentrations was observed over the past decade, which is likely due to a reduction in the emission of regional precursors. However, the annual mean concentrations were found to increase with a rate of 0.1 ppb per year <sup>4</sup>.

## 1.2. Ozone formation chemistry

### 1.2.1. Fundamentals

Although ozone is a crucial photochemically active gas in the troposphere, reducing its ambient concentration is challenging due to its secondary nature, i.e. ozone is formed in the atmosphere instead of being directly emitted. In this context, it is interesting to note that despite being of interest to many studies over the last decades<sup>22 23</sup>, its formation chemistry implicating several compounds present in the parts per billion range or even less, has not yet been fully understood.

Up until approximately half a century ago, the prevalent belief was that all tropospheric ozone was primarily generated in the stratosphere, and any downward transport to the troposphere was balanced by losses occurring at the surface of the Earth<sup>24</sup>. Nowadays, it is clear that NO<sub>2</sub> photolysis and the subsequent reaction of the photoproduct O(<sup>3</sup>P) with O<sub>2</sub> (R 1.1 and R 1.2) are the major sources of ozone during daylight hours. If we consider that the troposphere only contains O<sub>2</sub>, N<sub>2</sub> and trace amounts of NO<sub>2</sub>, NO and O<sub>3</sub>, an equilibrium between the latter species, known as the ozone photostationary state (PSS), should be observed during daytime<sup>23</sup>:



M is a third body (molecular oxygen or nitrogen) that carries off the excess energy of the reaction. O(<sup>3</sup>P) is an oxygen atom at the ground-state of energy, which is highly reactive and, under tropospheric conditions of pressure (200-1000 mbar) and temperature (220-300 K), combines with molecular oxygen to generate ozone. If O(<sup>3</sup>P) is presumed to be in a steady state in R 1.1-R 1.2 (since it is very reactive), the resulting steady-state concentration of ozone can be given by<sup>23</sup>:

$$[\text{O}_3]_{\text{ss}} = \frac{j_{\text{NO}_2}[\text{NO}_2]}{k_{\text{NO}+\text{O}_3}[\text{NO}]} \quad \text{Eq 1. 1}$$

where the enclosed brackets denote the concentrations of the different species,  $j_{\text{NO}_2}$  the photolysis rate of NO<sub>2</sub>, and  $k_{\text{NO}+\text{O}_3}$  the bimolecular rate coefficient for reaction R 1.3.

However, the PSS shown in Eq 1. 1 usually breaks down due to the presence of additional trace species in the troposphere such as carbon monoxide, VOCs and water-vapor. The PSS deviates from Eq 1. 1 due to the chemistry discussed below.

Solar ultraviolet radiation with wavelengths under 340 nm can break down O<sub>3</sub> into O<sub>2</sub> and an electronically excited oxygen atom O(<sup>1</sup>D) <sup>24</sup>:



Most of the excited O(<sup>1</sup>D) atoms are collisionally deactivated to their ground state O(<sup>3</sup>P) atoms, which leads to the reformation of O<sub>3</sub> via reaction R 1.2:



However, a small fraction of O(<sup>1</sup>D) atoms reacts with water-vapor to produce the hydroxyl radical (OH) <sup>24</sup>:



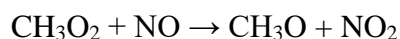
Reactions R 1.4 and R 1.6 are considered to be the main contributors to the formation of OH in the global troposphere <sup>25</sup>.

OH can react with CO, leading to the formation of the hydroperoxyl radical (HO<sub>2</sub>) as shown in reactions R 1.7-R 1.8. Accumulation of ozone, i.e. a shift of O<sub>3</sub> PSS towards higher concentrations, can then occur when NO is oxidized into NO<sub>2</sub> by reaction with HO<sub>2</sub> (reaction R 1.9) <sup>25</sup>:



The reaction between OH and CH<sub>4</sub> will also lead to the formation of peroxy radicals, which in turn will convert NO into NO<sub>2</sub>, as shown below. The latter will result in an accumulation of O<sub>3</sub> as well (R 1.1-R 1.3) <sup>25</sup>:

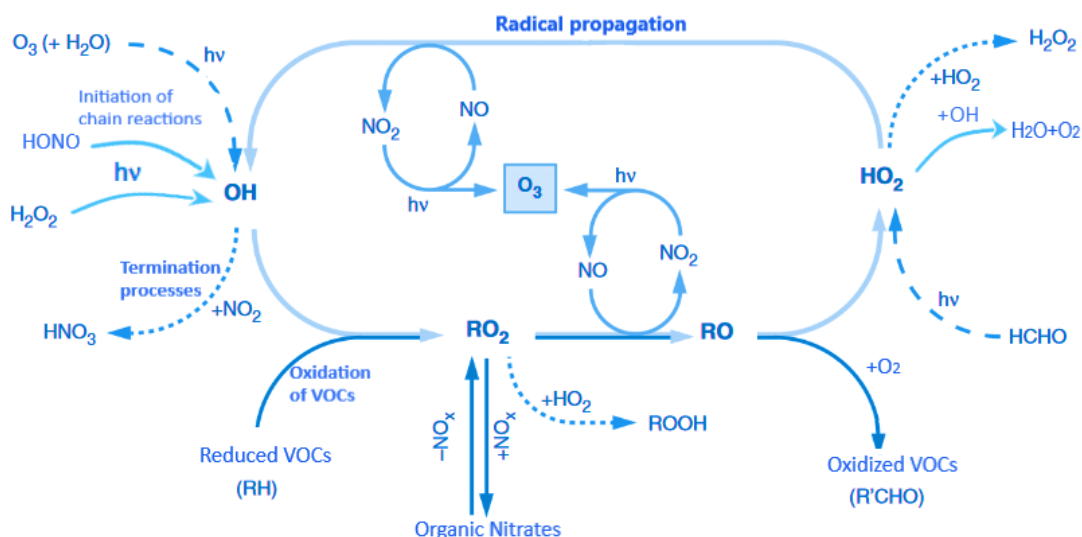




R 1.12

The two examples shown above, of particular importance for remote locations, indicate that the oxidation of trace gases such as CO and CH<sub>4</sub> leads to the conversion of NO into NO<sub>2</sub> (reactions R 1.9 and R 1.12), thus resulting in an accumulation of O<sub>3</sub> (R 1.1 and R 1.2) without its consumption (reaction R 1.3).

In rural and urban areas, the chemistry of the hydroxyl radical involves a large number of VOCs, with mainly high molecular weight, that can be emitted from both anthropogenic and natural sources. This chemistry cannot be studied independently because it is a closely interconnected system including RO<sub>x</sub> (OH, HO<sub>2</sub> and RO<sub>2</sub>), NO<sub>x</sub>, VOCs and O<sub>3</sub><sup>25</sup>. Figure 1. 3 shows a simplified schematic of tropospheric photochemistry, where it is clear that the RO<sub>x</sub> radical cycling leads to an efficient ozone formation.



**Figure 1. 3:** Radical chain cycling leading to the oxidation of ambient trace gases and the formation of O<sub>3</sub><sup>26</sup>

It is interesting to see from Figure 1. 3 that the RO<sub>x</sub> chemistry is very sensitive to the amount of NO<sub>x</sub>, since NO drives the lifetime of peroxy radicals. For instance, the hydroperoxyl radical HO<sub>2</sub> typically has a lifetime of approximately 1 min in unpolluted air (low NO<sub>x</sub> conditions), however in air masses containing considerable amount of NO<sub>x</sub>, its lifetime is significantly shorter, reaching values of 5 s<sup>27</sup>.

In low NO<sub>x</sub> regions, such as forested areas and the marine boundary layer, HO<sub>2</sub> exhibits a long lifetime, allowing it to react with ozone, and initiate a chain sequence that continuously produces hydroxyl radicals while contributing to some ozone destruction<sup>25</sup>.



In addition, HO<sub>2</sub> can react with itself to generate hydrogen peroxide (H<sub>2</sub>O<sub>2</sub>) (R 1.15) and can also react with organic peroxy radicals like CH<sub>3</sub>O<sub>2</sub>, resulting in the formation of organic hydroperoxides (R 1.16). Peroxides formation represents a chain termination process since, in most cases, these species may serve as effective sinks for HO<sub>x</sub> (HO<sub>2</sub> and OH) <sup>25</sup>.



Larger organic peroxy radicals can also react together to form more peroxides (R 1.17) <sup>28</sup>. These termination reactions limit the oxidation capacity of an air mass, and hence O<sub>3</sub> formation.



Under more polluted conditions where NO<sub>x</sub> are significant, the cross- and self-reactions of peroxy radicals (R 1.15, R 1.16 and R 1.17) are less significant due to their competition with propagation reactions involving NO:



As a result of reactions R 1.9, R 1.12 and R 1.18, OH radicals can continue reacting with VOCs, leading to further formation of peroxy radicals and O<sub>3</sub> (through NO<sub>2</sub> photolysis).

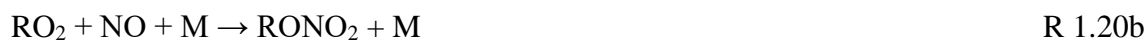
Under high NO<sub>x</sub> conditions, this radical chain cycling can be terminated in different ways. For instance, OH may react with NO<sub>2</sub> to produce nitric acid (HNO<sub>3</sub>), which is then lost via wet deposition <sup>28</sup>:



Another possible terminating channel is the formation of organic nitrates (RONO<sub>2</sub>) from the reaction of RO<sub>2</sub> and NO <sup>28</sup>:







Reaction R 1.20b has an important effect on ozone formation as it consumes both  $\text{RO}_2$  and  $\text{NO}$  (without conversion of  $\text{NO}$  into  $\text{NO}_2$ ) to form  $\text{RONO}_2$ , leading to less ozone production. The reaction between  $\text{RO}$  and  $\text{NO}$  resulting in the production of organic nitrites ( $\text{RONO}$ ) (R 1.21) is not significant in the atmosphere but can be of importance during laboratory measurements where high  $\text{NO}$  concentrations are usually used to perform kinetic experiments. This termination reaction also leads to less ozone formation similar to reaction R 1.20b.



The set of chemical processes discussed above consider only gas phase processes. However, in recent literature heterogeneous phase processes, mainly  $\text{HO}_2$  uptake on organic aerosols, was found to influence the ozone formation chemistry as shown in Ivatt et al. (2022)<sup>29</sup> and Dyson et al. (2023)<sup>30</sup>.

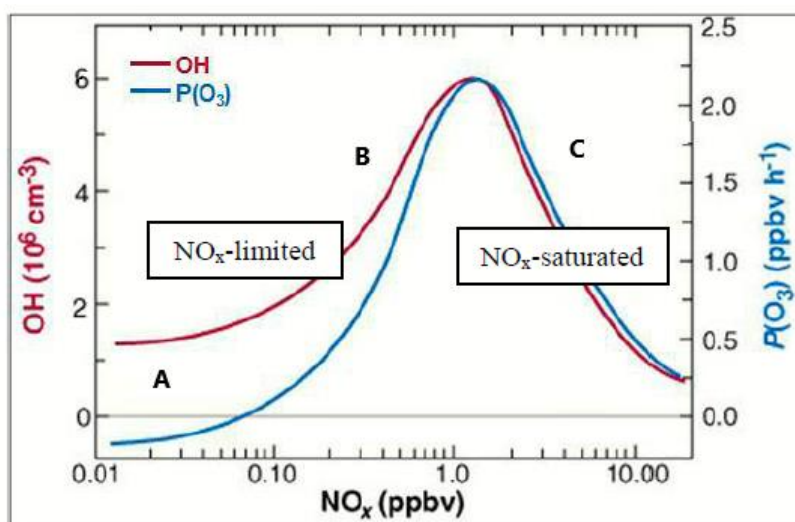
Ivatt et al. (2022) highlight how the  $\text{HO}_2$  uptake onto aerosol particles significantly influences regional ozone concentrations using a chemistry transport model. This aerosol-inhibited chemistry, which may be highly significant in regions like China and India, represents a challenge for air quality policies. Reductions in particulate matter could unintentionally increase surface ozone concentrations. Despite the aerosol inhibition from a radical perspective, aerosols also play other roles in ozone production through various processes (additional heterogeneous reactions, alterations in photolysis rates, and modifications to the boundary layer), complicating air quality management strategies. This highlights the necessity of comprehensive policies addressing together particulate matter and ozone precursor emissions to mitigate adverse health, ecosystem, and climate impacts<sup>29</sup>.

By examining  $\text{HO}_2$  loss pathways during a summer campaign in Beijing, Dyson et al. (2023) have found that the  $\text{HO}_2 + \text{NO}$  reaction drives the total loss rate of  $\text{HO}_2$  across varying  $\text{NO}$  concentrations, with  $\text{HO}_2$  uptake onto aerosol surfaces contributing to less than 0.3% on average. However, when  $\text{NO}$  is low ( $< 0.1$  ppb), aerosol uptake could represent up to 29% of the  $\text{HO}_2$  loss rate, particularly in cleaner environments with high aerosol surface areas. While incorporating aerosol uptake into models didn't significantly alter the overall ozone production regime, which remained VOC-limited, especially in  $\text{NO}_x$ -rich

environments like Beijing, regions with lower  $\text{NO}_x$  and substantial aerosol surface areas must consider concurrent PM reduction strategies alongside  $\text{NO}_x$  reduction policies due to potential impacts on  $\text{HO}_2$  uptake and subsequent ozone production rates<sup>30</sup>.

### 1.2.2. Ozone production regimes

As shown in the above section, the presence of  $\text{NO}_x$  affects not only the cycling of  $\text{RO}_x$  between OH,  $\text{HO}_2$  and  $\text{RO}_2$ , but it also governs the production of  $\text{O}_3$ . Figure 1. 4 shows a nonlinear relationship between  $\text{NO}_x$  and OH as well as  $\text{NO}_x$  and the net production rate of  $\text{O}_3$  ( $P(\text{O}_3)$ ). For this figure,  $P(\text{O}_3)$  was calculated from measurements of OH and  $\text{NO}_x$  at a clean rural site of eastern Germany during summertime of 1994<sup>31</sup>.



**Figure 1. 4:** Ozone formation regimes.  $[\text{OH}]$  and net  $P(\text{O}_3)$  as a function of  $[\text{NO}_x]$ , calculated for a clean rural site in eastern Germany<sup>31</sup>

Figure 1. 4 shows that two regimes of  $\text{O}_3$  production can be observed in the troposphere:  $\text{NO}_x$ -limited when  $\text{NO}_x$  concentrations are lower than a certain threshold (approximately 1 ppb for the chemical conditions of Figure 1. 4) and  $\text{NO}_x$ -saturated above this threshold.

In the  $\text{NO}_x$ -limited regime and at very low  $\text{NO}$  concentrations (region A in Figure 1. 4,  $[\text{NO}_x] < 60$  ppt), the oxidation of trace gases induced by OH results in a net destruction of  $\text{O}_3$ <sup>25</sup>. This phenomenon is typically observed solely in clean background air<sup>31</sup> where reactions R 1.13 and R 1.14 are the significant contributors to the  $\text{RO}_x$  cycling chemistry. When  $P(\text{O}_3)$  changes its sign at approximately  $[\text{NO}_x] = 60$  ppt, a transition from a state of chemical  $\text{O}_3$  destruction to a state of chemical  $\text{O}_3$  production is observed<sup>26</sup>.

In the next part of the NO<sub>x</sub>-limited regime (region B in Figure 1. 4), the increase of NO<sub>x</sub> causes an increase of radical propagation rates (R 1.9 and R 1.20a). As these radical propagation rates compete with self- and cross-reactions of peroxy radicals (R 1.15 and R 1.16), this leads to an increase of both OH and net O<sub>3</sub> production.

Assuming that enough OH and HO<sub>2</sub> recycling occurs to lead to ozone production and that the majority of radical losses are associated with the formation of H<sub>2</sub>O<sub>2</sub>, Eq. 1.2 can be demonstrated <sup>26</sup>:

$$P(O_3) \approx 2k_9 \left( \frac{P_{HO_x}}{k_{15}} \right)^{0.5} [NO] \quad \text{Eq 1. 2}$$

where k<sub>9</sub> and k<sub>15</sub> are the rate coefficients for reactions R 1.9 and R 1.15, respectively, and P<sub>HO<sub>x</sub></sub> is the production rate of HO<sub>x</sub>. P(O<sub>3</sub>) increases linearly with NO (hence NO<sub>x</sub>), and it also depends on P<sub>HO<sub>x</sub></sub>.

In the NO<sub>x</sub>-saturated regime (region C in Figure 1. 4), also known as VOC-limited, a further increase of NO<sub>x</sub> concentration leads to a faster increase of radical termination rates (R 1.19 and R 1.20b) compared to propagation rates (reactions R 1.9, R 1.12 and R 1.20), causing a decrease of both [OH] and net O<sub>3</sub> production. In this regime, the chemical system mainly responds to the rates of reactions R 1.22 (VOC+OH) and R 1.19 (NO<sub>2</sub>+OH). Assuming a steady-state for HO<sub>x</sub> species <sup>26</sup> Eq. 1.3 can be demonstrated



$$P(O_3) \approx \frac{2P_{HO_x} \sum_i k_{22} [VOC_i]}{k_{19} [NO_2]} = 2rP_{HO_x} \quad \text{Eq 1. 3}$$

where k<sub>22</sub> and k<sub>19</sub> represent the rate coefficients of reactions R 1.22 and R 1.19, respectively.

It is therefore important to note that a reduction of NO<sub>x</sub> will lead to antagonist effects, whether O<sub>3</sub> production occurs under NO<sub>x</sub>-saturated or NO<sub>x</sub>-limited conditions. The maximum in [OH] and net P(O<sub>3</sub>) indicates the transition between these two regimes <sup>31</sup>.

Depending on NO<sub>x</sub> concentrations, there is a balance between gross photochemical ozone production, p(O<sub>3</sub>), and loss, l(O<sub>3</sub>), presented in different regions of Figure 1. 4 in terms of net ozone production, P(O<sub>3</sub>). For instance, in region A, the loss rate of ozone

exceeds the gross production rate, leading to a negative net production for these specific conditions,  $P(O_3) < 0$  (Eq 1. 4) <sup>25</sup>.

$$P(O_3) = p(O_3) - l(O_3) \quad \text{Eq 1. 4}$$

A compensation point is defined as the moment at which the ozone production and loss rates are balanced ( $P(O_3) = 0$ ). This occurs at a critical level of  $NO_x$ , which in turn depends on VOCs emissions and solar radiation. Above this point (region B),  $p(O_3)$  is greater than  $l(O_3)$  ( $P(O_3) > 0$ ), which implies that the system is producing ozone <sup>25</sup>.

### 1.3. Control strategies

The lifetime of ozone typically ranges from several weeks in the free troposphere to few hours in polluted regions characterized by high concentrations of its precursors <sup>20</sup>, which requires considering both the local ozone formation chemistry and trace gas transport when modelling ozone concentrations at specific locations. Numerous simulations involving chemical transport models have been performed to obtain a comprehensive picture of ozone formation in the Earth's atmosphere, including the chemistry transport CHIMERE model <sup>32</sup>, the Comprehensive Air quality Model with Extensions (CAMx) <sup>33</sup>, or the Community Multiscale Air Quality (CMAQ) model deployed by the U.S. Environmental Protection Agency <sup>34</sup>.

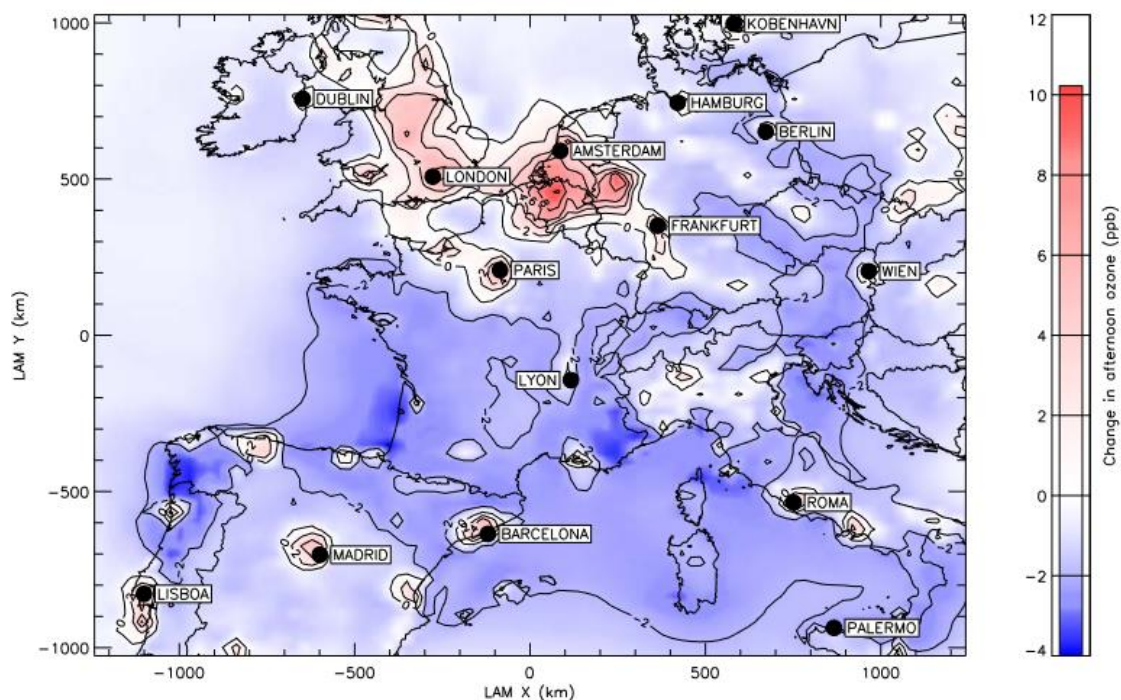
In the 1970s, ozone control strategies in the U.S. were based on a reduction of hydrocarbon (HC) emissions, relying on the results of most models that had shown the sensitivity of ozone formation to VOCs ( $NO_x$ -saturated) <sup>35</sup>. It was thought that nearly 50% of HC emissions were caused by mobile sources, with nearly all of them linked to the consumption of petroleum or natural gas. Despite implementing control strategies that led to a reduction of HC emissions by around 10% from 1977 to 1989 in the U.S, a decrease in ozone levels was not observed. It was later realized, in the 1990's, that the failure in achieving a significant decrease in ozone was due to the omission in models of the large burden of VOCs emitted by the vegetation. The best example to give is isoprene, a biogenic HC, which is now known as the most emitted HC in the atmosphere. Isoprene was disregarded for a long time due to its low concentrations in the urban atmosphere compared to anthropogenic hydrocarbons. Nonetheless, its reactivity with OH surpasses that of the majority of other hydrocarbons, which means that its actual influence on chemistry is considerably greater than what its low concentration may indicate. Starting from the 1990's,

the emphasis was put on NO<sub>x</sub> regulations and the 1990 Clean Air Act imposed NO<sub>x</sub> and hydrocarbons emission standards for the automobile industry and power plants<sup>35</sup>. This strategy was efficient to reduce significantly ozone concentrations, where a decrease of about 19% in the highest ozone concentrations was observed in the eastern US, for the period 2000-2018<sup>36</sup>.

Since the early 1990's, emissions of man-made ozone precursors (NO<sub>x</sub> and VOC) have been considerably reduced in Europe with the implementation of VOC and NO<sub>x</sub> control approaches. The strategies applied varied between regions based on sensitivity analysis of P(O<sub>3</sub>) from models<sup>37</sup>. While observations at polluted locations confirmed a reduction of these ozone precursors by up to a factor of two from 1990 to 2005, long-term measurements of ozone showed minimal or no decrease over the same timeframe<sup>37</sup>. These contrasting observations were explained by an increase in background ozone that compensated the reduction in local ozone formation.

A modeling exercise investigating the ozone formation sensitivity to a 30% reduction in either anthropogenic NO<sub>x</sub> or VOC emissions in Europe for June 2006 showed that NO<sub>x</sub> reductions were efficient to decrease afternoon ozone levels in rural areas of Europe (NO<sub>x</sub>-limited) while resulting in a rise of a few ppb in ozone in urban areas (NO<sub>x</sub>-saturated)<sup>37</sup>. Conversely, a decrease in VOC emissions induced an ozone reduction primarily in industrial and urban regions. These model results are presented in Figure 1. 5, where blue areas indicate a NO<sub>x</sub>-limited regime, while red areas are representative of a NO<sub>x</sub>-saturated regime. Hence, implementing NO<sub>x</sub> regulations to reduce ozone would be effective in most of Europe, whereas VOC regulations are necessary in major cities and industrial zones.

Integrated assessment models as shown above are important predictive tools to help improving the integration of air quality policies and to assess emission reductions that are necessary to avoid future high O<sub>3</sub> pollution events. Although, there are instances where modeled ozone concentrations do not correspond with the observed levels and a validation step of the chemical mechanisms used in these models is a prerequisite for reliable model simulations<sup>38</sup>. Of particular interest, ozone production rates simulated by models could be compared to that observed in the troposphere as a critical test of our understanding of ozone chemistry.



**Figure 1. 5:** Modeling of ozone formation sensitivity. Difference in modelled ozone concentrations when a 30% reduction in NO<sub>x</sub> emissions is applied (June 2006) (blue: NO<sub>x</sub>-limited, red: NO<sub>x</sub>-saturated regimes) <sup>37</sup>

## 2. Analytical techniques for measuring peroxy radicals, nitrogen oxides and ozone production rates

Since the second half of the 19<sup>th</sup> century, scientists have developed instruments that allowed the identification and the quantification of various types of trace gases in the atmosphere <sup>39</sup>. Long-term and accurate measurements of these pollutants in the troposphere are necessary to examine upcoming patterns in air quality and climate change, to test atmospheric models, and ultimately provide guidance to policy makers <sup>40</sup>.

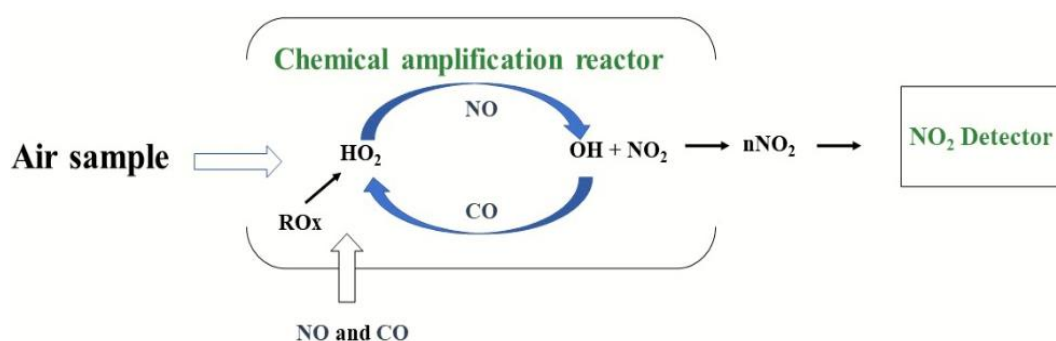
In this section, we present techniques that were developed for measuring peroxy radicals and ozone production rates. This information will be useful for the interpretation of results presented in chapters 3 (Comparison of the IMT Chemical Amplifier to a Laser-Induced Fluorescence instrument during ROxComp) and 4 (Evaluation of a methodology to quantify ozone production rates using a Chemical Amplifier).

## 2.1. Peroxy radicals – HO<sub>2</sub> + RO<sub>2</sub>

### 2.1.1. Chemical Amplification

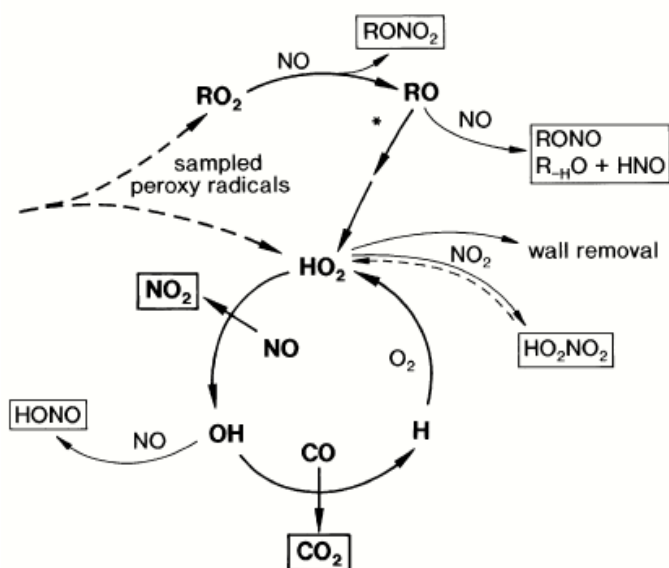
The Peroxy Radical Chemical Amplifier (PERCA) technique is an indirect method developed by Cantrell and Stedman<sup>41</sup> for measuring the sum of RO<sub>x</sub> radicals. RO<sub>x</sub> are converted into NO<sub>2</sub> via an amplification chemistry described in details below. Since HO<sub>2</sub>+RO<sub>2</sub> in ambient air are much more abundant than OH+RO, PERCA measurements are referred to as HO<sub>2</sub>+RO<sub>2</sub> measurements<sup>42</sup>.

The chemical amplifier is composed of three main parts as shown in Figure 1. 6<sup>41</sup>: (a) a coupler allowing the addition of reagent gases (CO or N<sub>2</sub> and NO) to the sample, (b) a flow reactor where RO<sub>x</sub> radicals are converted into NO<sub>2</sub>, and (c) a NO<sub>2</sub> detector.

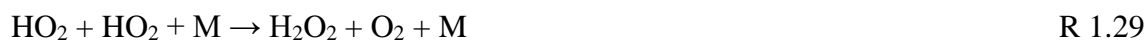
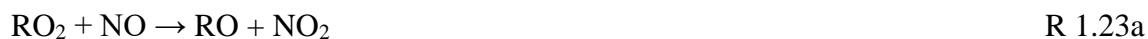


**Figure 1. 6:** Schematic representation of PERCA<sup>41</sup>

The conversion chemistry shown in Figure 1. 6 and Figure 1. 7 occurs in the sampling reactor at the proximity of the sampling point by rapidly mixing two reagent gases (NO and CO) with ambient air. In the flow reactor, NO reacts with ambient RO<sub>2</sub> radicals, converting them into HO<sub>2</sub> (reactions R 1.23a and R 1.24). The latter, in addition to ambient HO<sub>2</sub>, are converted into OH (reaction R 1.26a). As indicated in reactions R 1.27 and R 1.28, CO converts OH back to HO<sub>2</sub>, and therefore, the cycling between reactions R 1.27, R 1.28 and R 1.26a represents an amplification mechanism where multiple NO<sub>2</sub> molecules are generated for each radical that enters the cycle. This amplification chemistry is defined by a chain length (CL), which is the number of NO<sub>2</sub> molecules formed per sampled RO<sub>x</sub> radical. NO<sub>2</sub> exiting the sampling reactor is subsequently conveyed to an appropriate detector based on Luminol Chemiluminescence<sup>43</sup>, LIF<sup>44</sup>, Cavity Ring-Down Spectroscopy<sup>45</sup>, Cavity Attenuated Phase-shift Spectroscopy (CAPS)<sup>46</sup> or broadband cavity-enhanced spectroscopy (BBCEA)<sup>47</sup>.



**Figure 1. 7:** Schematic representation of the chemistry occurring in a PERCA <sup>42</sup>



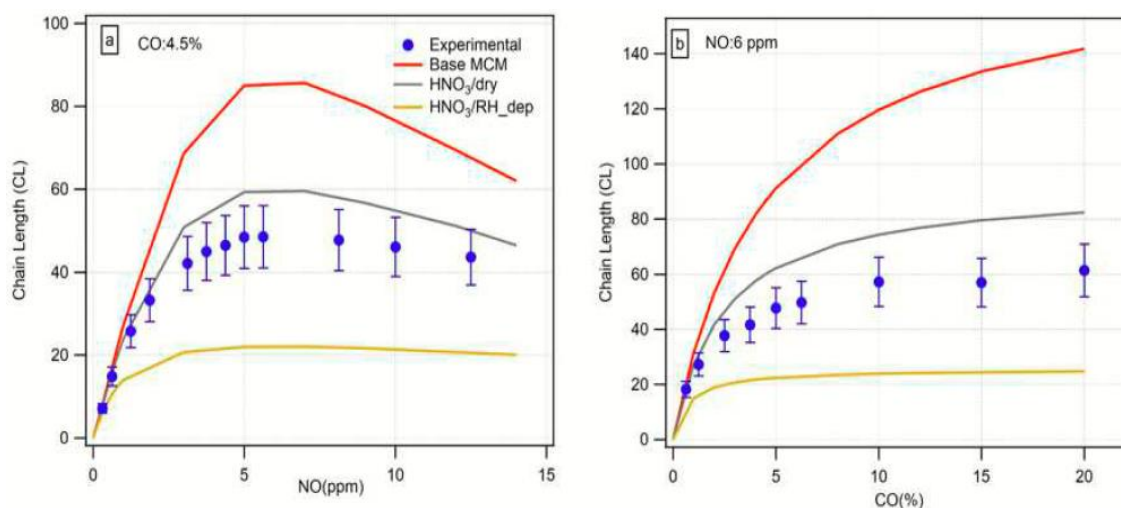




The CL is a finite number as OH (reactions R 1.31, R 1.32 and R 1.35) and HO<sub>2</sub> (reactions R 1.26b, R 1.33 and R 1.36) termination reactions will progressively deplete the pool of radicals inside the sampling reactor. Due to the high concentration of NO inside the inlet, termination reactions resulting from cross- and self-reactions of RO<sub>x</sub> radicals (reactions R 1.29 and R 1.30) are not significant and the major radical sinks are radical reactions with NO (reactions R 1.23b and R 1.26b). The CL is generally on the order of 100-200 under dry conditions <sup>48</sup>.

The CL can be influenced by several factors, including (1) the concentration of reagent gases (CO and NO), which affects the balance between radical propagation and termination, and (2) relative humidity (RH), that can promote heterogeneous losses of peroxy radicals on the reactor wall as well as the formation of H<sub>2</sub>O dimers and HO<sub>2</sub>-H<sub>2</sub>O adducts with potentially different reactivity compared to HO<sub>2</sub> <sup>48</sup>.

The dependence of the CL on reagent gases is illustrated in Figure 1. 9 for an instrument developed at IMT Nord Europe <sup>48</sup>. This PERCA is based on two sampling reactors that were operated alternatively in amplification and background modes, connected to two Cavity Attenuated Phase Shift (CAPS) instruments for measuring NO<sub>2</sub>. In the amplification mode, the measured NO<sub>2</sub> represents the converted and amplified RO<sub>x</sub> radicals, in addition to the ambient NO<sub>2</sub> and the titrated O<sub>3</sub> to NO<sub>2</sub> (via a reaction with NO). While in the background mode, the detected NO<sub>2</sub> constitutes only the ambient NO<sub>2</sub> and the titrated O<sub>3</sub>. A difference between the measured NO<sub>2</sub> in the two modes allow determining the amplified NO<sub>2</sub>, hence RO<sub>x</sub> concentrations. Figure 1. 8 (a) shows that the CL increases with NO up to 5-6 ppm at a constant CO mixing ratio of 4.5%, for both experimental observations and numerical simulations. Beyond 6 ppm of NO, the CL decreases due to a larger enhancement of the OH + NO termination rate (reaction R 1.32) compared to the HO<sub>2</sub> + NO propagation rate (reaction R 1.26a). Figure 1. 8 (b) shows that the CL also strongly depends on CO. For a constant NO mixing ratio of 6 ppm (optimum value found in Figure 1. 8 (a)), the CL increases with [CO] up to 10%, and then levels off at higher mixing ratios. Optimum reagent concentrations leading to the highest CL, i.e. the highest sensitivity, were derived from these tests.

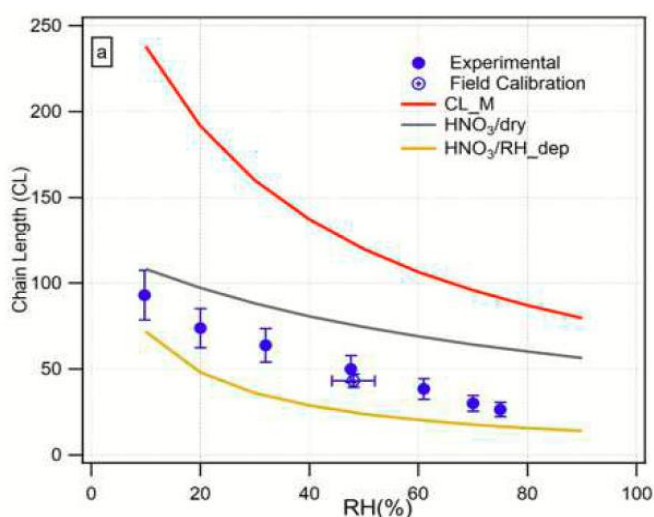


**Figure 1. 8:** Dependence of the PERCA CL on both NO (a) and CO (b). Experimental and modeled values are shown as markers and lines, respectively <sup>48</sup>. In the legend, "Base MCM", "HNO<sub>3</sub>/dry" and "HNO<sub>3</sub>/RH\_dep" refer to different modelling conditions (see <sup>48</sup>).

The authors also investigated how the CL changes with ambient humidity <sup>48</sup>. Figure 1. 9 shows that the CL decreases significantly with RH, with a reduction by a factor of approximately 3-4 between 10 and 70% RH. Several explanations were proposed for the water dependence. The main drivers were the enhanced radical losses on wet surfaces and the formation of HO<sub>2</sub>-H<sub>2</sub>O adducts that can terminate the radical cycling (R 1.37) <sup>49</sup>.



R 1.37



**Figure 1. 9:** Dependence of the PERCA CL on relative humidity (T=23°C). Experimental and modeled values are shown as markers and lines, respectively. The empty circle represents calibration experiments performed in the field <sup>48</sup>. In the legend, "CL\_M", "HNO<sub>3</sub>/dry" and "HNO<sub>3</sub>/RH\_dep" refer to different modelling conditions (see <sup>48</sup>).

In 2017, Wood et al.<sup>50</sup> reported a new amplification chemistry where CO is replaced by ethane (C<sub>2</sub>H<sub>6</sub>), i.e. replacing reactions R 1.27 and R 1.28 above by the set of following reactions (R 1.38 - R 1.42). This new methodology is referred to as Ethane Chemical AMPlifier (ECHAMP).



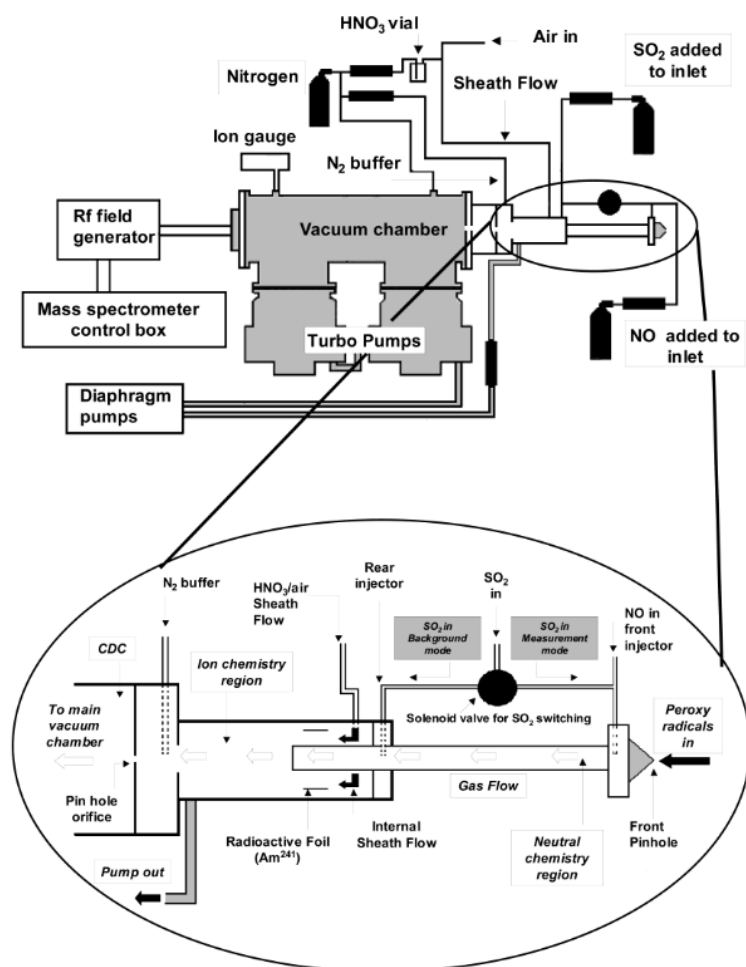
The initial step of propagating RO<sub>2</sub> radicals to HO<sub>2</sub> is similar to the PERCA method (reactions R 1.23a and R 1.24). The resultant HO<sub>2</sub> then propagates to OH (reaction R 1.26a), which then reacts with ethane (reaction R 1.38) to produce an ethyl peroxy radical (C<sub>2</sub>H<sub>5</sub>O<sub>2</sub>). This peroxy radical propagates to the ethoxy radical (C<sub>2</sub>H<sub>5</sub>O) (reaction R 1.40a), which then reacts with O<sub>2</sub> to reform HO<sub>2</sub>. The propagation cycle for this approach is more complex compared to CO and includes multiple additional steps where radicals may be lost (reactions R 1.40b and R 1.42). For example, when C<sub>2</sub>H<sub>5</sub>O<sub>2</sub> reacts with NO, part of the reaction flux is directed towards the formation of C<sub>2</sub>H<sub>5</sub>ONO<sub>2</sub>. Likewise, the reaction of C<sub>2</sub>H<sub>5</sub>O with NO results in the formation of C<sub>2</sub>H<sub>5</sub>ONO. These two reactions lead to further losses of radicals during the amplification process, which in turn leads to a lower CL<sup>50</sup>. Duncianu et al. reported a CL of 15 at about 50% RH for ECHAMP, which is 3-4 times lower than for PERCA<sup>48</sup>.

Over the past two decades, PERCA and to some extent ECHAMP were employed in various sites in the field thanks to their simplicity, their low cost, and their portability.

## 2.1.2. Other techniques

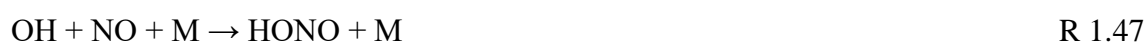
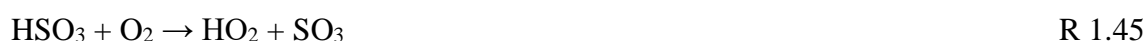
### 2.1.2.1. Peroxy radical Chemical Ionization Mass Spectrometry (PerCIMS)

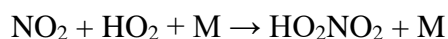
The PerCIMS technique is based on chemical conversion of ambient RO<sub>x</sub> into sulfuric acid (H<sub>2</sub>SO<sub>4</sub>), which is then ionized into HSO<sub>4</sub><sup>-</sup> and measured using mass spectrometry.



**Figure 1. 10:** Schematic representation of PerCIMS <sup>51</sup>

As shown in Figure 1. 10, the instrument operates by sampling ambient air through an orifice. Both SO<sub>2</sub> and NO are added to the ambient airflow within the inlet to convert OH and peroxy radicals into gas-phase H<sub>2</sub>SO<sub>4</sub> as shown in reactions R 1.43 - R 1.46. RO<sub>x</sub> are then quantified as a sum through the detection of HSO<sub>4</sub><sup>-</sup> by a quadrupole mass spectrometer. Similarly to PERCA measurements, since tropospheric concentrations of HO<sub>2</sub> and RO<sub>2</sub> are generally 100 times larger than OH, measuring RO<sub>x</sub> (OH, HO<sub>2</sub>, RO<sub>2</sub>) can be regarded as measurements of peroxy radicals exclusively.





R 1.48

The formation of  $\text{HSO}_3$  regenerates  $\text{HO}_2$  in reaction R 1.45, resulting in an amplification chemistry. Chain lengths reported for this chemistry are in the range of 10 cycles. This amplification chemistry occurs because the OH radicals formed in reaction R 1.43 can either undergo reaction R 1.44, leading to sulfuric acid formation through reaction R 1.46 and propagation of the chain reaction, or react via reaction R 1.47, terminating the radical chain mechanism. The amount of  $\text{H}_2\text{SO}_4$  measured in the PerCIMS instrument allows a determination of the peroxy radical concentration in the sampled air, taking into account the amplification factor and the ambient concentration of  $\text{H}_2\text{SO}_4$ .

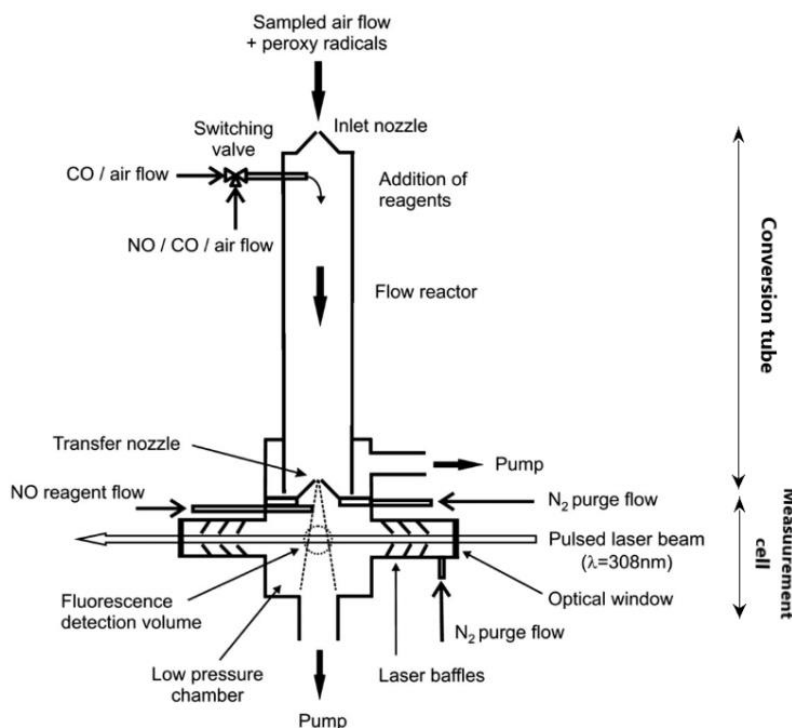
It is interesting to note that this technique allows measuring either the sum of  $\text{HO}_2 + \text{RO}_2$  ( $\text{HO}_x\text{RO}_x$  mode), or only  $\text{HO}_2$  radicals ( $\text{HO}_2$  mode), by controlling  $\text{SO}_2$  and NO concentrations added to the setup<sup>51</sup>. It has been shown that this instrument detects organic peroxy radicals efficiently in the  $\text{HO}_x\text{RO}_x$  mode (regardless of the R group) but with low efficiency in the  $\text{HO}_2$  mode. Radical concentrations can be determined with an accuracy of approximately 40%, a precision of 10% and a detection limit of  $10^7$  radicals  $\text{cm}^{-3}$  for an averaging time of 15s<sup>51</sup>.

#### 2.1.2.2. $\text{RO}_x$ Laser-Induced Fluorescence ( $\text{RO}_x\text{-LIF}$ )

The  $\text{RO}_x\text{-LIF}$  technique was proposed in 2008 by Fuchs et al.<sup>52</sup>. It is based on a two-step chemical conversion system to convert  $\text{RO}_x$  into OH, which is then detected by Laser-Induced Fluorescence (LIF). Figure 1. 11 provides a schematic representation of the  $\text{RO}_x\text{-LIF}$  instrument.

The sampling of ambient air occurs in a differentially pumped flow reactor, where atmospheric  $\text{RO}_x$  are chemically transformed into  $\text{HO}_2$  at a low pressure of 25 hPa by adding NO and CO ( $\text{RO}_x$  mode). Reagent concentrations are optimized to get a low OH/ $\text{HO}_2$  ratio and hence minimize the loss of OH on the reactor walls. By adding only CO as a reagent gas, the total amount of  $\text{HO}_2 + \text{OH}$  is converted into  $\text{HO}_2$  ( $\text{HO}_x$  mode). It is thus possible to measure either  $\text{RO}_x$  or  $\text{HO}_2$  depending on the measurement mode. Subsequently,  $\text{HO}_2$  is sampled into the OH detection cell at the bottom of the conversion flow tube. In this cell,  $\text{HO}_2$  is converted into OH by introducing NO at a lower-pressure (approx. 3.5 hPa). The generated OH is detected by the LIF technique at a wavelength of 308 nm using the Fluorescent Assay by Gas Expansion (FAGE) approach<sup>52</sup>. On a  $\text{RO}_x\text{-LIF}$  instrument

equipped with an additional detection cell for ambient OH, sequential measurements of RO<sub>x</sub> and HO<sub>x</sub>, together with concomitant measurements of OH, allow deriving speciated concentrations of OH, HO<sub>2</sub> and RO<sub>2</sub>.



**Figure 1. 11:** Schematic representation of RO<sub>x</sub>-LIF. RO<sub>2</sub>-to-HO<sub>2</sub> conversion flow reactor coupled to an OH LIF instrument <sup>52</sup>

The calibration has an estimated accuracy of approximately 40% at 2σ. It has been shown that the RO<sub>x</sub>-LIF instrument has a very high sensitivity, leading to a low detection limit of about 10<sup>6</sup> radicals cm<sup>-3</sup> at a measurement time resolution of 1 min <sup>52</sup>.

### 2.1.3. Comparison of the analytical techniques

Table 1. 1 summarizes the performances of the three techniques for peroxy radical measurement. Including the detected species, where PerCIMS and RO<sub>x</sub>-LIF techniques can provide speciated measurements of OH, HO<sub>2</sub> and RO<sub>2</sub>, while the CA allow only measuring the sum of HO<sub>2</sub>+RO<sub>2</sub>. The 3-σ detection limits are close for the three techniques, with higher sensitivity for PerCIMS. However, PerCIMS and RO<sub>x</sub>-LIF exhibit a faster time resolution than CA.

Given the simplicity and the low cost of the CA method compared to the PerCIMS and the RO<sub>x</sub>-LIF techniques, this technique was selected in this work for the detection of peroxy radicals with the aim of quantifying ozone production rate.

**Table 1. 1:** Comparison between peroxy radical techniques

<i>Technique</i>	<i>Principle</i>	<i>Detected species</i>	<i>3-<math>\sigma</math> LoD</i> ( $\times 10^7$ $cm^{-3}$ )	<i>1-<math>\sigma</math> Accuracy</i>	<i>Advantages</i>	<i>Limits</i>
CA	Chemical conversion/ amplification	HO <sub>2</sub> +RO <sub>2</sub>	0.8 - 7.9 (RH < 10 %) <sup>45,47,48</sup>	15-20%	- Low cost & Simple setup	- Indirect method
	NO <sub>2</sub> detection				- High sensitivity	- RH dependent sensitivity
PerCIMS	Chemical conversion	OH	< 0.15 <sup>50</sup>	25 - 30 %	- High sensitivity	- Non-selective (meas. sum HO <sub>2</sub> + RO <sub>2</sub> )
	Chemical Inization	HO <sub>2</sub> +RO <sub>2</sub>			- Selective meas. of HO <sub>2</sub> and RO <sub>2</sub> if oxygen modulation implemented <sup>53</sup>	- Time resolution of a few min
	Mass Spectrometry				- High sensitivity	- Indirect methods
RO <sub>x</sub> -LIF	Chemical conversion	HO <sub>2</sub>	0.4 - 8.6 <sup>52,54</sup>	13 - 18 %	- Selective meas. of OH, HO <sub>2</sub> and RO <sub>2</sub>	- Complex & expensive setup
	Laser-induced fluorescence	OH			- High sensitivity	- Indirect methods for HO <sub>2</sub> and RO <sub>2</sub>
					- Fast time resolution (<1 min)	- Relatively high sampling flow rate of ~ 10-20 L/min

## 2.2. Nitrogen Oxide Measurements

Currently, the chemiluminescence (CL) technique is widely employed for atmospheric monitoring of both NO and NO<sub>2</sub> with a time resolution of a few minutes. On the other hand, new optical methods based on absorption spectroscopy can also offer high sensitivity, high selectivity and fast response for ambient NO<sub>2</sub> measurements<sup>55</sup>. These techniques include TDLAS (infrared Tunable Diode Laser Absorption Spectroscopy)<sup>56</sup>, LIF (Laser Induced

Fluorescence)<sup>57</sup>, CAPS (Cavity Attenuated Phase-shift Spectroscopy)<sup>58</sup>, CRDS (Cavity Ring Down Spectroscopy)<sup>59</sup>, CEAS (Cavity Enhanced Absorption Spectroscopy)<sup>60</sup> and Photo-Acoustic Spectroscopy (PAS)<sup>61</sup>.

### 2.2.1. Nitrogen oxide (NO)

The most common technique for NO measurements is based on the chemiluminescent reaction between NO and O<sub>3</sub> at low pressure which produces measurable light emission. The intensity of this emission is directly proportional to the mass flow rate of NO that enters the instrument's measurement cell<sup>62</sup>. The reaction employed by the chemiluminescent detector is as follows:



Under low pressure, approximately 10% of NO<sub>2</sub> molecules become electronically excited, and their transition back to the ground state emits a measurable light. The light emission is detected with a photomultiplier tube. The chemiluminescent reaction with ozone is specific for NO measurements.

Detection of NO concentrations as low as 0.4 ppb is achievable with this technique, at 60 s integration time. However, the presence of ambient humidity, which increases chemiluminescence quenching, can lead to errors of several percent by lowering readings<sup>63</sup>.

In the present work, this technique was used for the detection of NO required for the quantification of the ozone production rate in Chapter 4.

### 2.2.2. Nitrogen dioxide (NO<sub>2</sub>)

In order to quantify NO<sub>2</sub> using the chemiluminescence technique, a catalytic or photolytic converter is employed to dissociate NO<sub>2</sub> to NO<sup>62</sup>, the chemiluminescence instrument measuring the total concentration of NO<sub>x</sub> (NO+NO<sub>2</sub>) as NO. NO<sub>2</sub> is then derived by subtraction between the measured NO<sub>x</sub> and NO. The bimolecular reaction of the catalytic converter is described below:





Continuous monitoring of NO and NO<sub>x</sub> across a wide range of concentrations is made possible with this method. However, the main issue of this technique is related to the indirect detection of NO<sub>2</sub>, and its subsequent conversion to NO, requiring NO<sub>2</sub> to be measured by subtracting the ambient NO background. While this approach is suitable for ambient measurements of NO<sub>2</sub> due to the low concentrations of NO in the atmosphere, it presents limitations when coupled to a chemical amplifier as the use of ppm of NO in the CA leads to a large NO background, and as a consequence to a detection limit that wouldn't be good enough for the chemical amplifier <sup>62</sup>. In addition, when a catalytic converter is used to convert NO<sub>2</sub> into NO, this technique is known to be prone to interferences from compounds like alkyl and peroxy nitrates.

For the direct detection of NO<sub>2</sub> in ambient air, it is mainly based on optical techniques. For instance, the CAPS, CRDS, CEAS and TDLAS are direct absorption techniques relying on the scanning of a light source across a spectrum of frequencies relevant to the analysis. These analyzers comprise a light source, a cavity with two highly reflective mirrors to produce a long optical path (up to 2 km), and a photodetector. It was found that these instruments can reach remarkable sensitivities, with detection limits in the ppt range and time resolutions of few seconds <sup>64</sup>. Contrary to the chemiluminescence method, these techniques are not based on the conversion of NO<sub>2</sub> to NO and are not sensitive to interferences from other nitrogenous components.

The LIF technique comprises an excitation laser, a detection cell and an adequate photodetector <sup>65</sup>. The laser emits typically in the UV or visible range (e.g. 585 nm <sup>65</sup>) in a pulsed mode and the beam is directed into a low pressure sampling cell containing ambient NO<sub>2</sub>. The excitation of NO<sub>2</sub> at the selected wavelength results in the release of the excess energy as fluorescence. This fluorescence emission occurs at longer wavelengths than the excitation wavelength and is characteristic of the fluorescing species. NO<sub>2</sub> concentrations are then determined by monitoring the fluorescence signal using a photodetector. This technique has the advantage of high sensitivity and selectivity, with limits of detection in the ppt range <sup>65</sup>.

Despite the high sensitivity and accuracy of these techniques, they can be complex to use in the field and require careful calibration and maintenance. In addition, the use of multi-pass cavities can lead to the increase of these instruments costs.

On the other hand, Photo-Acoustic Spectroscopy (PAS) is a low-cost optical technique for trace gas and particle monitoring (PM, CH<sub>4</sub>, NO<sub>2</sub> ...), which does not require highly skilled operators. It comprises three main components: a power modulated light source, a PA cell to amplify acoustic waves and an acoustic transducer to detect the PA signal <sup>66</sup>. It has the advantage of providing a high sensitivity that increases with the excitation light power, allowing PAS-based sensors to benefit from rapid advances in semiconductor technology <sup>67</sup>. Photoacoustic approaches are classified by the different types of PA cells and transducers. In 2015, Zheng et al. <sup>67</sup> proposed a quartz-enhanced photoacoustic spectroscopy (QEPAS) instrument for NO<sub>2</sub> measurements using a 1 W multimode LED emitting at 450 nm. The 1- $\sigma$  limit of detection was found to be 1.3 ppb at a time resolution of 1 s. Based on the HITRAN database, NO<sub>2</sub> exhibits a strong absorption spectrum in the visible range between 250–600 nm. The PAS technique is presented in more details in chapter 2. The characteristics of these NO<sub>2</sub> techniques are summarized in Table 1.2:

**Table 1. 2:** Comparison between NO<sub>2</sub> techniques

<i>Technique</i>	<i>Principle</i>	<i>3-<math>\sigma</math> LoD (ppb)</i>	<i>1-<math>\sigma</math> Accuracy</i>	<i>Advantages</i>	<i>Limits</i>
<b>CL</b>	Chemical conversion into NO	0.02 <sup>68</sup>	6 %	- High sensitivity - Also measures NO	- Indirect method - Time resolution of a few min - Prone to interferences from N-containing species (catalytic converter only)
<b>CAPS</b>	Direct light absorption	$\sim$ 0.04 <sup>69</sup>	4 %	- High sensitivity - Fast time resolution (<1 min)	- Expensive
<b>CRDS</b>		0.15 <sup>64</sup>	5 %		
<b>CEAS</b>		0.1 <sup>70</sup>	6 %		
<b>TDLAS</b>		0.2 <sup>56</sup>	-		
<b>LIF</b>	Laser-Induced Fluorescence	0.02 <sup>65</sup>	5 %	High sensitivity	- Complex & expensive
<b>PAS</b>	Light absorption	3.9 <sup>67</sup>	2 %	- Low cost & Simple setup - Fast time resolution (<1 min)	- Lower sensitivity than other techniques above

## 2.3. Ozone production rate – P(O<sub>3</sub>)

### 2.3.1. Measurement rational

Atmospheric measurements of ozone at ground level were first made in 1858 by Schönbein<sup>39</sup> and have been continued since then by monitoring networks. Eq 1. 5 shows that a change in ozone at a local area depends on the formation chemistry P(O<sub>3</sub>), surface deposition SD, and local meteorology A<sup>71</sup>.

$$\frac{\partial[\text{O}_3]}{\partial t} = \underbrace{p(\text{O}_3) - l(\text{O}_3)}_{\text{P}(\text{O}_3)} - \underbrace{\frac{v}{H}[\text{O}_3]}_{\text{SD}} + \underbrace{u_i \frac{\partial[\text{O}_3]}{\partial x_i}}_{\text{A}} \quad \text{Eq 1. 5}$$

As mentioned previously, P(O<sub>3</sub>) is the net chemical production of ozone which is derived from its gross production rate, p(O<sub>3</sub>), and its loss rate, l(O<sub>3</sub>) (see section 1.2). SD is a term accounting for surface deposition, which can be inferred from the O<sub>3</sub> deposition velocity, v, and the boundary layer height, H. The term A is the advection rate which depends on the air velocity in three directions, u<sub>i</sub>, and the ozone gradient in those three directions.

The net ozone production rate P(O<sub>3</sub>) is the term that leads to the accumulation of ozone in ambient air. However, Eq 1. 5 shows that local ozone budgets can also be significantly affected by meteorological conditions. The transport of air masses, including horizontal advection and vertical dilution, can significantly alter the accumulation of ozone at a specific location. Moreover, as can be seen in Eq 1. 5, surface deposition, which is proportional to the ambient ozone concentration [O<sub>3</sub>], can also significantly impact O<sub>3</sub> budget. In order to design efficient strategies for O<sub>3</sub> reduction, it is therefore important to assess the contribution of each term presented in Eq 1. 5 to the local ozone budget<sup>71</sup>.

So far, atmospheric monitoring networks have only measured ozone concentrations to track ozone trends and pollution incidents, which is not enough to distinguish the contribution of each term in Eq 1. 5. The measurement of ozone production rates together with ambient O<sub>3</sub> would allow assessing the role of both, transport and chemical production, by comparing the direct measurement of ozone production, P(O<sub>3</sub>), to the observed rate of ozone change ( $\frac{\partial[\text{O}_3]}{\partial t}$ ). Contrasting P(O<sub>3</sub>) values measured under different VOC/NO<sub>x</sub>

conditions would also help in identifying the ozone formation regime at the measurement site. These, in turn, would be useful in the development of ozone control strategies.

### 2.3.2. Direct approach

Currently, just four instruments were developed for P(O<sub>3</sub>) measurements in the world, including the Measurement of Ozone Production Sensor (MOPS) from Pennsylvania State University, USA <sup>71</sup>, the Ozone Production Rates (OPR) instrument from Birmingham University, UK (William Bloss' group, unpublished work), the OPR instrument developed at IMT Nord Europe during the PhD project of S. Sklaveniti <sup>72</sup>, and the MOPS instrument developed by Sadanaga et al. in collaboration between Osaka Prefecture University and Kyoto University in Japan <sup>73</sup>.

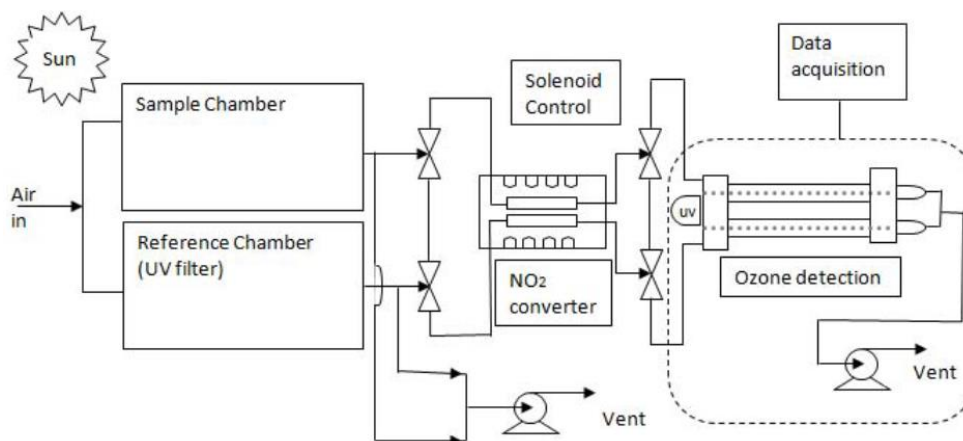
#### 2.3.2.1. Measurement of Ozone Production Sensor (MOPS)

The concept of direct P(O<sub>3</sub>) measurements was first proposed about fifty years ago <sup>74</sup>, but was never published in a scientific journal. The principle of MOPS consists in differential ozone measurements between two environmental chambers made of Teflon, continuously exposed to solar radiation. These chambers are referred to as "sample chamber" and "reference chamber" in the following. Ambient air is continuously sampled through these two chambers. The walls of the sample chamber allow solar ultraviolet light to pass through, exposing the air inside to the same photochemistry as in ambient air. Some of the ozone generated in this chamber reacts with ambient NO and is converted into NO<sub>2</sub> following the O<sub>3</sub>-NO<sub>x</sub> photostationary state (reactions R 1.1-R 1.3). The reference chamber is covered with a UV filter that blocks radiation of wavelengths lower than 400 nm, which in turn avoid ozone production via radical chemistry. Hence, the ozone present in the reference chamber solely originates from the O<sub>3</sub>-NO<sub>x</sub> photo-stationary state. Figure 1. 12 shows a schematic presentation of the first version of the MOPS instrument (MOPSV1). The production rate of ozone is given by the difference in O<sub>x</sub> (O<sub>3</sub>+NO<sub>2</sub>) between the two chambers, ΔO<sub>x</sub>, divided by the same residence time inside these chambers, τ, as shown below:

$$P(O_3) = \frac{\Delta O_x}{\tau} \quad \text{Eq 1. 6}$$

Here, the amount of ozone produced in the sample chamber compared to the reference chamber is derived from O<sub>x</sub> measurements instead of O<sub>3</sub> due to the rapid interconversion

between  $O_3$  and  $NO_2$  in these two chambers. The measurement of  $\Delta O_x$  is carried out via a two-step procedure, the first one being the conversion of  $NO_2$  into  $O_3$ , and the second one being the measurement of the resulting  $O_3$  (ambient  $O_3$  + ambient  $NO_2$ ) by a differential ozone monitor directly connected to the 2 chambers. A homemade converter unit, which consists of two photolytic conversion cells (395 nm), one for the air exiting the sample chamber and one for the air exiting the reference chamber, is used for the conversion of  $NO_2$  into  $O_3$  (R1.1-R1.2)<sup>71</sup>.



**Figure 1. 12:** Schematic representation of MOPS - MOPsv1 <sup>71</sup>

In September 2008, MOPsv1 was tested on the campus of Pennsylvania State University exhibiting a detection limit of  $0.7 \text{ ppb h}^{-1}$  at a time resolution of 10 min. The absolute uncertainty was found to be 30% for measurements performed at a relative humidity lower than 70% <sup>71</sup>. It was then deployed in Houston during the SHARP campaign (Study of Houston Atmospheric Radical Precursors) in April and May 2009, as a first attempt to evaluate model-derived  $P(O_3)$  <sup>75</sup>. Detailed results from this study are presented in section 3.2.

Main instrumental issues for this first version of MOPS included  $O_3$ ,  $NO_2$  and radical losses in the chambers,  $NO_x$  and VOC degassing from the chamber walls, as well as a non-unity conversion efficiency of  $NO_2$  into  $O_3$  <sup>71</sup>. The latter was found to be inversely proportional to ambient  $NO_2$ , ranging from 58 to 88% for  $NO_2$  concentrations between 17 and 125 ppb.

A second generation of the MOPS instrument (MOPsv2) was developed later, with optimizations of the shape, size, and airflow pattern within the chambers in order to reduce wall effects. In 2013, the new instrument was deployed during the NASA's DISCOVER-

AQ field campaign (Deriving Information on Surface Conditions from Column and Vertically-resolve observations Relevant to Air Quality), in Houston, Texas. This study is discussed in detail in section 3.2. The NO<sub>2</sub>-to-O<sub>3</sub> conversion efficiency was also improved in this version using a highly-efficient UV LED converter. A relative increase of the conversion efficiency by 5-10% was achieved for NO<sub>2</sub> concentrations lower than 35 ppb, and 10-30% for NO<sub>2</sub> concentrations ranging from 35-100 ppb. Nevertheless, the authors still reported a potential measurement bias from the heterogeneous formation of HONO in the sampling chambers, which can lead to higher production rates of OH and an overestimation of P(O<sub>3</sub>), in addition to some issues in the ozone analyzer mainly linked to variations in temperature and relative humidity<sup>38</sup>.

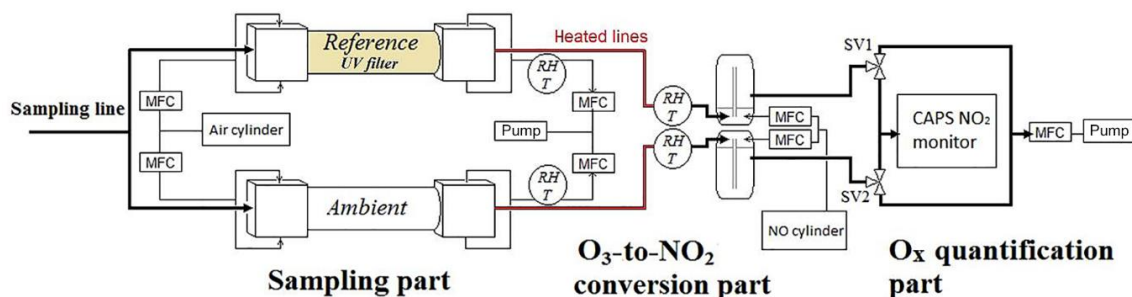
In 2017, another MOPS instrument was introduced by a group of researchers from Osaka Prefecture University and Kyoto University in Japan. This system is based on the measurement of O<sub>x</sub> concentrations by conversion of O<sub>3</sub> to NO<sub>2</sub> using an excess of NO and the subsequent detection of NO<sub>2</sub> with a Laser-Induced Fluorescence analyzer. Regardless of the O<sub>3</sub> concentration, the conversion efficiency of O<sub>3</sub> into NO<sub>2</sub> was nearly 100%. The authors reported negligible wall losses of NO<sub>2</sub> and O<sub>3</sub> within the chambers, allowing for minimal uncertainties in the measured production rates. This instrument was then deployed for field measurements at the Wakayama Forest Research Station (WFRS), Kyoto University, Wakayama Prefecture, Japan, in July-August 2014<sup>73</sup>. Ambient measurements ranged from the detection limit of 0.54 ppb h<sup>-1</sup> (at 60 s) up to 10.5 ppb h<sup>-1</sup><sup>73</sup>.

#### **2.3.2.2. Ozone Production Rates (OPR)**

As mentioned above, an OPR instrument was developed during the thesis of S. Sklaveniti at IMT Nord Europe, in collaboration with the School of Public and Environmental Affairs from Indiana University<sup>72</sup>. This instrument is based on the MOPS principle but using a different design.

Similarly to MOPS, the OPR operates on the basis of differential measurements of O<sub>x</sub> between two separate sampling units. Two flow tubes, one exposed to direct sunlight to reproduce ambient photochemistry, and the other covered with a UV filter that inhibits ozone production. A schematic of the OPR instrument is shown in Figure 1. 13. Just like the MOPS, the rapid interconversion between O<sub>3</sub> and NO<sub>2</sub> necessitates measuring O<sub>x</sub>

instead of  $O_3$ .  $P(O_3)$  is obtained from the difference in  $O_x$  ( $\Delta O_x$ ) between the two flow tubes, divided by the average residence time ( $\tau$ ) of air inside the tubes, as presented in Eq 1. 6<sup>72</sup>.



**Figure 1. 13:** Schematic of the OPR instrument<sup>72</sup>.

The main parts of the instrument consist of two flow tubes made of quartz, with identical geometries, an  $O_3$ -to- $NO_2$  conversion unit and a  $NO_2$  monitor (Aerodyne Cavity Attenuated Phase-shift Spectroscopy (CAPS)).

In order to solve issues of wall losses identified for the MOPS instrument, the geometries of the flow-tube inlet and outlet were optimized to reduce the occurrence of radial mixing and recirculation eddies, which can intensify wall impacts. Ambient air is drawn through a shared inlet at a total flow rate of  $4 \text{ L min}^{-1}$  and conveyed into the two flow tubes. At the output of each flow tube, the air is directed into a conversion unit where  $NO$  is added to convert more than 99.9% of  $O_3$  into  $NO_2$  in less than 23 s (determination based on the  $NO$  concentration injected in the conversion unit and the rate constant for the titration reaction)<sup>76</sup>.  $O_x$  is then sequentially measured at the output of the 2 conversion cells using the CAPS  $NO_2$  monitor, allowing the calculation of ozone production rate as shown in Eq 1. 6.

To characterize this instrument, several tests were performed<sup>72</sup>:

- Pulse experiments using toluene allowed characterizing the residence time ( $\tau$  in Eq 1. 6) under field operating conditions:  $271 \pm 13 \text{ s}$  ( $1\sigma$ ).
- Wall-loss experiments allowed assessing that  $O_3$  and  $NO_2$  losses within the flow tubes were lower than 5% and 3%, respectively, under dark conditions. In the ambient flow tube, a photo-enhanced loss of  $O_3$  was also noted, mainly at wavelengths around 312 nm, which can potentially reach up to 15-20% of the ambient  $O_3$ . This aspect was considered as one of the main limitations of this instrument.
- HONO-formation tests allowed to determine that  $NO_2$  can be transformed into HONO at the flow-tube surface. Similarly to MOPS, this can disturb the  $P(O_3)$  measurement by

increasing the amount of OH inside the ambient flow tube, leading to an overestimation of  $P(O_3)$ . It was found that the production rates of HONO in the ambient flow tube was around 10 to 20 ppb  $h^{-1}$  for dark and irradiated conditions, respectively. It was estimated that  $P(O_3)$  could be overestimated by approximately 27% on average <sup>72</sup>.

The limitations observed for the OPR system presented above are likely impacting other MOPS instruments and further characterizations and improvements are required for ozone production rate instruments. This instrument was deployed during the IRRONIC (Indiana Radical, Reactivity and Ozone Production Intercomparison) field campaign <sup>72</sup>. The field measurements are discussed in section 3.2.

### 2.3.3. Indirect approach

In addition to the MOPS/OPR techniques described above, ozone production rates can also be inferred from peroxy radical measurements. Based on the chemistry described in section 1.2,  $P(O_3)$  can be calculated using the following equations <sup>77</sup>:

$$p(O_3) = k_{NO+HO_2} [NO][HO_2] + \sum_i (\varphi_i k_{NO+RO_{2,i}} [NO][RO_{2,i}]) \quad \text{Eq 1. 7}$$

$$l(O_x) = j(O^1D) \cdot [O_3] \cdot f + k_{OH+NO_2} [OH][NO_2] + k_{HO_2+O_3} [HO_2][O_3] + \quad \text{Eq 1. 8}$$

$$k_{OH+O_3} [OH][O_3] + \sum_i (k_{O_3+alkene_i} [O_3][alkene_i])$$

$$P(O_3) = p(O_3) - l(O_x) \quad \text{Eq 1. 9}$$

where the gross production rate of ozone,  $p(O_3)$ , is derived from the oxidation rate of NO due to its reaction with peroxy radicals,  $k_{NO+HO_2}$  and  $k_{NO+RO_2}$  being the rate coefficients for the  $NO+HO_2$  and  $NO+RO_2$ , respectively. In this equation,  $\varphi_i$  is the branching ratio of the  $NO-RO_2$  reaction that only leads to the generation of RO and  $NO_2$ , and not  $RONO_2$ . The term  $l(O_x)$  is the  $O_x$  loss rate due to  $O_3$  photolysis and reactions of  $O_3$  with OH,  $HO_2$  and alkenes, and the loss of  $NO_2$  via its reaction with OH. The term  $f$  is the fraction of  $O(^1D)$  that reacts with  $H_2O$  to produce OH.

It is noteworthy that  $\varphi_i$  is usually assumed to be equal to 1. Nevertheless, it has been found that this factor decreases with higher carbon number, higher pressure, and lower temperature. Consequently, calculations considering a branching ratio of 1 for all  $NO-RO_2$  reactions would lead to a non-negligible overestimation of  $p(O_3)$ .



This indirect method for the calculation of  $P(O_3)$  requires measurements of OH,  $HO_2$ ,  $RO_2$ ,  $O_3$ , NO and  $NO_2$  concentrations, as well as j-values. It is interesting to note that if only peroxy radicals and NO measurements are available, it is still possible to compute the gross production rate of  $O_3$ ,  $p(O_3)$ .

### **3. Field measurements**

Besides laboratory studies and computer modelling, field measurements are important to fully understand complex processes occurring in the atmosphere. Across a broad spectrum of temporal and spatial scales, field measurements allow both monitoring long-term trends and checking the reliability of models in predicting the current atmospheric composition<sup>40</sup>. In fact, the development of sensitive and accurate field instrumentation allowed the discovery of relationships between ambient species and atmospheric issues, such as the role of specific trace gases/aerosols for global warming, the formation of the ozone hole in the stratosphere and the decline of air quality in urbanized areas<sup>40</sup>.

In the following, selected field measurements of  $P(O_3)$  are reviewed with the purpose to highlight how such measurements can help improving our understanding of tropospheric ozone formation. This section is not intended to be exhaustive and only few examples were selected.

#### **3.1. Quantification of $P(O_3)$ from $RO_x$ radicals**

As discussed in section 2.2.3, the quantification of  $P(O_3)$  requires first the knowledge of the abundance of  $RO_x$  radicals and NO present at a particular location. Concentrations of  $NO_x$ ,  $O_3$  and alkene (needed to calculate  $I(O_x)$ ) are usually measured during intensive field campaigns or over large spatial and temporal scales by air quality networks, while concentrations of  $RO_x$  radicals can be obtained either from the output of box models or by direct measurements (section 2.1).

##### **3.1.1. $P(O_3)$ values inferred from modeled $RO_x$ concentrations**

The calculation of  $P(O_3)$  in zero-dimensional (0-D) box models is performed by simulating radical concentrations required in Eq 1. 7-Eq 1. 9 for different types of environments (remote, marine, forested, urbanized), taking advantage that radicals'

lifetimes are too short to be influenced by transportation or deposition processes <sup>78</sup>. When observations of RO<sub>x</sub> radicals are available for the modelled area, chemical mechanisms embedded in these models can be tested by comparing observed and simulated RO<sub>x</sub> concentrations and P(O<sub>3</sub>) values.

Different types of chemical mechanisms exist in the literature: the most widely used in box models are the Regional Atmospheric Chemistry Mechanism version 1 and 2 (RACM <sup>79</sup> and RACM2 <sup>75</sup>), the Carbon Bond Mechanism version 2005 and version 6 (CB05 <sup>80</sup> and CB6 <sup>81</sup>), the Statewide Air Pollution Research Center mechanism version 2007 (SAPRC-07 <sup>82</sup>), the NASA Langley Research Center mechanism (LaRC <sup>83</sup>) and the Master Chemical Mechanism versions 3.1 and 3.2 (MCM v3.1 <sup>84</sup> and MCM v3.2 <sup>85</sup>).

During a campaign carried out in summer 2005 in the urban area of Santiago, Chile <sup>86</sup>, a photochemical box model implementing MCMv3.1 was used to analyze the O<sub>3</sub>-VOC-NO<sub>x</sub> sensitivity by simulating ozone formation under different VOC/NO<sub>x</sub> regimes. The measured ozone concentrations reached levels as high as 125 ppb, while usual peak concentrations fell within the range of 40 to 80 ppb during the majority of the campaign. The average P(O<sub>3</sub>) simulated by the model reached a maximum of 160 ppb h<sup>-1</sup>, which is among the largest production rates reported in the literature. This average ozone production rate is higher than the modelled values of 20 ppb h<sup>-1</sup> reported for New York City <sup>87</sup> and 89 ppb h<sup>-1</sup> reported for Mexico City <sup>88</sup>. The ozone sensitivity inferred from the model showed that ozone formation during summertime in Santiago was NO<sub>x</sub>-saturated. Reducing VOC concentrations by 50% in the model led to a decrease in the O<sub>3</sub> maximum by 36%, while reducing NO<sub>x</sub> by 50% resulted in an increase in the O<sub>3</sub> maximum by 66%. A 50% decrease in both VOCs and NO<sub>x</sub> caused a 10% rise in the peak O<sub>3</sub> concentration <sup>86</sup>.

Recently, an in situ O<sub>3</sub> production sensitivity study was carried out in an Indian Megacity (Delhi) during the Atmospheric Pollution and Human Health program (APHH-India) in October 2018 <sup>77</sup>. A box model incorporating MCM v3.1.1 was used for the analysis. The O<sub>3</sub> mean peak concentration was found to be approximately 78 ppb with modeled P(O<sub>3</sub>) values up to 220 ppb h<sup>-1</sup>. The model was also used to test the effect of VOCs and NO<sub>x</sub> on local P(O<sub>3</sub>), highlighting a NO<sub>x</sub>-saturated chemical regime. A significant increase in P(O<sub>3</sub>) was observed when only NO<sub>x</sub> concentrations were decreased, indicating that reducing, or even maintaining, O<sub>3</sub> levels in the future will require a reduction in VOC emissions. The sensitivity of morning P(O<sub>3</sub>) to VOC classes was also examined, aromatics being found as

the most crucial contributors, as reducing their ambient concentrations by 50% resulted in a 15.6% decrease in the modelled morning  $P(O_3)$ . Other important VOC classes were monoterpenes and alkenes, as sensitivity tests indicated a 13% reduction in  $P(O_3)$  from a 50% reduction in emissions for these compounds <sup>77</sup>.

### 3.1.2. $P(O_3)$ values inferred from $RO_x$ measurements

$P(O_3)$  values can also be calculated using measured radical concentrations. Some selected field campaigns are briefly discussed below to illustrate this aspect.

As part of the Second Texas Air Quality Study (TexAQS 2006), a field campaign was conducted during summer 2006 along the Gulf coast of the United States to measure total peroxy radical concentrations aboard the NOAA research vessel R/V Brown <sup>89</sup>. Measurements performed from a mobile platform such as a ship offers a distinctive view of radical chemistry under various chemical conditions. During these measurements, a PERCA instrument was deployed to measure total  $RO_x$  concentrations. NO and  $NO_2$  concentrations were measured by chemiluminescence and  $O_3$  by UV-absorbance. When sampling oceanic air mixed with anthropogenic emissions during day-time, maximum mixing ratios of  $RO_x$  varied between 25 and 110 ppt, and  $NO_x$  concentrations were approximately 2.4 ppb on average. Open ocean air masses, however, had lower mixing ratios of  $RO_x$  (30–35 ppt) and  $NO_x$  (0.7 ppb), likely related to the low reactivity of CO,  $CH_4$  and oxygenated VOCs (most abundant) with atmospheric oxidants (low rate coefficients). The median  $P(O_3)$  varied from 0.5 ppb  $h^{-1}$  in the open ocean up to 44 ppb  $h^{-1}$  in the industrial areas located along the entire Texas coastline. These measurements were compared to those collected during the previous TexAQS 2000 campaign <sup>90</sup>, where  $HO_2$  measurements were conducted at a nearby site (LaPorte airport, south of Houston). Both datasets exhibited similar ranges of values for  $P(O_3)$  and similar  $NO_x$  dependencies, suggesting that ozone production in the Houston area was  $NO_x$ -limited because of high emissions of reactive VOCs, notably alkenes, from urban and industrial sources <sup>89</sup>.

A field campaign performed in a megacity during March 2006 as part of the MILAGRO (Megacity Initiative: Local And Global Research Observations) project, MCMA (Mexico City Metropolitan Area) <sup>91</sup>, reported measurements of tropospheric OH and  $HO_2$  radicals. A FAGE instrument was deployed for the measurement of these radicals.  $O_3$  and  $NO_x$  were monitored using commercial monitors based on UV absorption and chemiluminescence,

respectively. Maximum median OH and HO<sub>2</sub> concentrations were found to be  $4.6 \times 10^6$  and  $1.9 \times 10^8 \text{ cm}^{-3}$ , respectively. P(O<sub>3</sub>) values calculated from the measured HO<sub>2</sub> were as high as 80 ppb h<sup>-1</sup> during the early morning and declined to 31 ppb h<sup>-1</sup> around noon. The counterintuitive high P(O<sub>3</sub>) values observed in the early morning were due to the presence of significant concentrations of HO<sub>2</sub> during high NO episodes. Later in the afternoon, they reached a minimum of 3–4 ppb h<sup>-1</sup>. P(O<sub>3</sub>) values determined by MCMA-2003<sup>92</sup> were approximately half of those calculated for 2006<sup>91</sup>.

Later on, the Clean air for London project (ClearfLo) conducted radical observations in central London during the summer of 2012 to evaluate factors governing the radical budget and, consequently, to assess local ozone production rates<sup>93</sup>. HO<sub>2</sub> and RO<sub>2</sub> radicals were measured using the FAGE and RO<sub>x</sub>-LIF techniques, respectively (see section 2.1.2). To compare with the observed concentrations, a 0-D box model incorporating MCM v3.2 was utilized to predict RO<sub>x</sub> radical concentrations. Under high NO<sub>x</sub> conditions (more than 3 ppb), the box model under-predicted total RO<sub>2</sub> concentrations, with a model-measurement agreement getting worse when NO<sub>x</sub> concentrations are increasing. However, modelled and observed HO<sub>2</sub> concentrations agreed, but with NO concentrations varying between 7 and 15 ppb. On the other hand, P(O<sub>3</sub>) values inferred from simulated peroxy radicals were significantly lower, up to one order of magnitude, than values assessed from observed peroxy radicals, the latter reaching up to 30 ppb h<sup>-1</sup> at the highest NO concentrations. Similar observations were recently reported by Tan et al. (2017) for the Wangdu (a rural site) study conducted in China<sup>94</sup>.

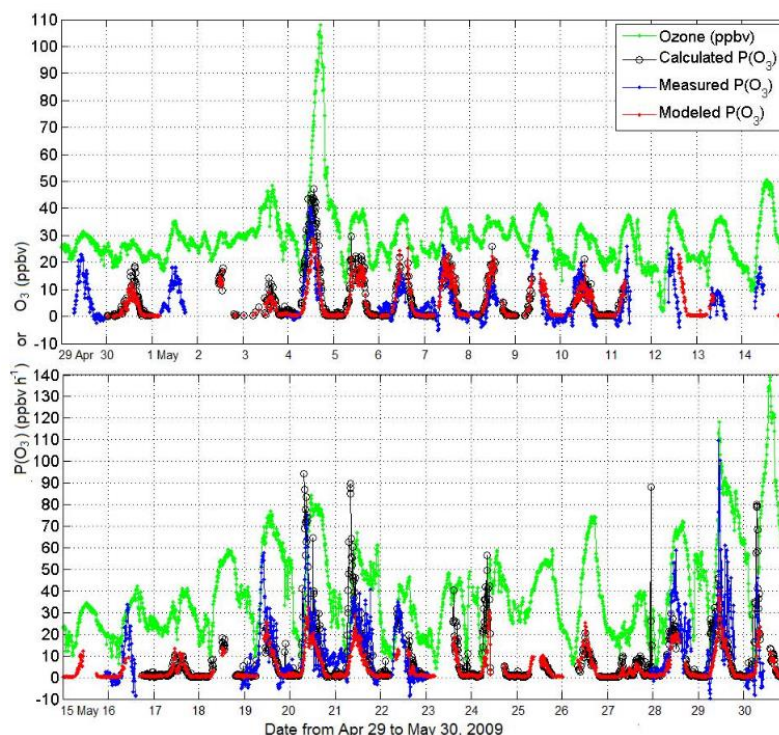
It is worth noting that the contribution of individual RO<sub>2</sub> radicals to P(O<sub>3</sub>) depends on their chemical structure and reactivity. Since current RO<sub>x</sub> instruments only measure the sum of RO<sub>2</sub> at best, speciated information on the contribution of different RO<sub>2</sub> radicals to ozone production rates can only be assessed from models<sup>77</sup>.

### **3.2. Direct measurements of P(O<sub>3</sub>)**

As mentioned previously, the first direct measurements of ambient ozone production rates was performed by Cazorla et al. (2012)<sup>75</sup> during the SHARP field campaign in Houston (April - May 2009). The deployment of the MOPSV1 instrument allowed to compare measured P(O<sub>3</sub>) values with calculations from measured concentrations of HO<sub>2</sub>

and NO (referred to as calculated  $P(O_3)$ ) in addition to modeled concentrations of radicals from a box model based on the RACM2 mechanism (referred to as modeled  $P(O_3)$ ).

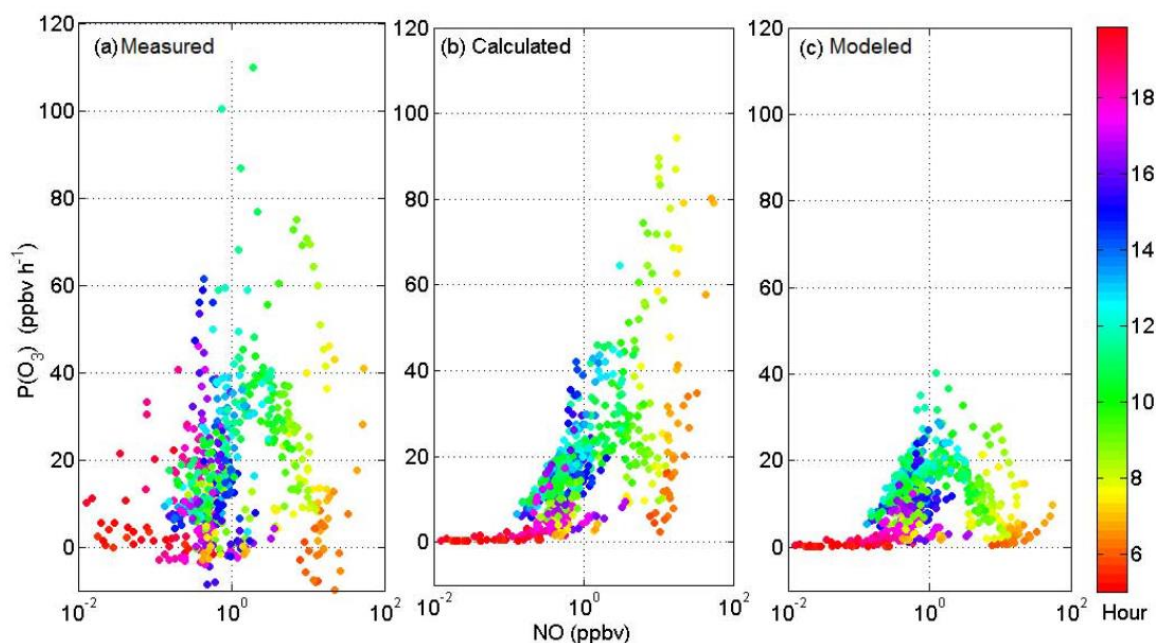
Figure 1. 14 displays the time series of  $P(O_3)$  values obtained by MOPS, as well as those calculated from measured and modeled radical concentrations. In the late morning, the measured  $P(O_3)$  values peaked with a range of 15-100  $\text{ppb h}^{-1}$ , with typical values of 40-80  $\text{ppb h}^{-1}$  observed on high ozone days.



**Figure 1. 14:** Time series of ozone and  $P(O_3)$  for the SHARP 2009 field campaign <sup>75</sup>. Ambient ozone (green dots). Calculated  $P(O_3)$  values from measured radicals (black circles) and MOPS measurements (blue dots). Simulated values from RACM2 (red dots).

A comparison between measured, modeled and calculated  $P(O_3)$  was then conducted as function of NO, as shown in Figure 1. 15 (the color scale represents the hour of the day). It was highlighted that modeled  $P(O_3)$  values were low compared to direct measurements or values calculated from radical measurements, for almost all NO concentrations. On the other hand, it has been found that the maximum of measured  $P(O_3)$  were observed for NO concentrations around 1  $\text{ppb}$ , reaching more than 100  $\text{ppb h}^{-1}$ . Under the same NO conditions, calculated  $P(O_3)$  exhibited lower values, in the range of 40  $\text{ppb h}^{-1}$ . For higher NO concentrations, an opposite behavior was observed, where measured  $P(O_3)$  decreased to reach approximately 40  $\text{ppb h}^{-1}$  in the morning, while calculated  $P(O_3)$  continued increasing, up to more than 90  $\text{ppb h}^{-1}$  for the same time period. A general agreement was

observed between the two quantities for NO concentrations lower than 1 ppb (a significant scatter is observed in measured  $P(O_3)$  values in this region likely due to measurement noise in the MOPS data).



**Figure 1. 15:** Trend of  $P(O_3)$  on NO for the SHARP 2009 field campaign - (a) measured by the MOPS, (b) calculated from measured radicals and (c) modeled <sup>75</sup>

These field measurements showed the potential of the MOPS instrument for contributing to the understanding of ozone photochemistry, but was limited by high measurement uncertainties due to  $NO_2$  wall losses in the sampling chambers under humid conditions ( $RH > 50\%$ ) <sup>75</sup>.

Later in 2013, a second version of the MOPS instrument (MOPsv2) was deployed for the NASA's DISCOVER-AQ field campaign (Deriving Information on Surface Conditions from Column and VERTically-resolve observations relevant to Air Quality), in Houston, Texas. Two MOPsv2s measured  $P(O_3)$  in separate locations (Moody Towers and Smith Point) from 1 to 28 September 2013 and were later compared while collocated at the same site. Field testing performed to assess the accuracy of  $P(O_3)$  measurements showed that HONO concentrations in the sampling chambers were two to five times larger than in ambient air (likely due to heterogeneous conversion of  $NO_2$  onto the chambers' wall), which may result in a bias in the order of 5 to 10 ppb h<sup>-1</sup> in the  $P(O_3)$  measurements. Despite this issue, the new MOPS design was found to be promising <sup>75</sup>. The comparison between measured, calculated, and modeled  $P(O_3)$  values showed a better agreement than during the

2009 SHARP campaign, but the model values were systematically underpredicting measured and calculated  $P(O_3)$ .

The first field measurements using the OPR instrument from IMT Nord Europe was performed during the Indiana Radical, Reactivity and Ozone Production Intercomparison campaign (IRRONIC) in Bloomington, Indiana, in July 2015<sup>72</sup>. Different parameters were measured within this campaign, such as OH concentrations, total  $RO_x$  concentrations, total OH reactivity,  $NO_x$ ,  $O_3$ , anthropogenic and biogenic VOCs, radiation and meteorological data. Measurements of NO were performed using chemiluminescence,  $NO_2$  using CAPS and ozone using a commercial sensor (2B Tech model 202 sensor). Days from this campaign were chosen to model ambient net  $P(O_x)$  and its sensitivity to  $NO_x$ . The simulations were made using a box model incorporating the RACM chemical mechanism.

Most of the days in the measurement site were dominated by biogenic emissions, with isoprene levels exceeding 5 ppb, while anthropogenic VOCs and  $NO_x$  were below 500 ppt and 3 ppb, respectively. The low  $NO_x$  levels at the measurement site resulted in ozone production rates that were below the OPR detection limit of  $6.2 \text{ ppb h}^{-1}$ . According to the  $P(O_x)$  calculations based on total peroxy radical measurements performed using the PERCA technique, the peak ozone production rates were around  $2 \text{ ppb h}^{-1}$ . The OPR instrument was therefore used to look at the sensitivity of  $P(O_3)$  by adding various amounts of  $NO_x$  in the sampled ambient air. Ozone production rates showed significant changes, increasing up to  $20 \text{ ppb h}^{-1}$  when 6 ppb of  $NO_x$  was added to the flow tube, indicating a  $NO_x$ -limited production regime. However, this field deployment uncovered another bias in  $P(O_x)$  measurements caused by the photo-enhanced loss of ozone at the inner surface of the ambient flow tube and the challenge of detecting changes in  $P(O_x)$  when the sampled air mass is altered by the addition of NO<sup>72</sup>.

### **3.3. Conclusions**

The  $P(O_3)$  field measurements discussed above were useful for the understanding of tropospheric ozone formation in different regions in the world along the last two decades. Modeled  $P(O_3)$  and calculated ones from modeled and measured  $RO_x$  were in agreement in the identification of the ozone chemistry in various megacities and industrial areas, that was found to be a  $NO_x$ -limited chemistry.

Despite the advantage of models in considering the contribution of individual  $RO_2$  to  $P(O_3)$  quantification, this method showed a consistent underestimation compared to the direct and indirect methods for  $P(O_3)$  measurement. On the other hand, the comparison between the measured  $P(O_3)$  and the calculated one from  $RO_x$  measurements, revealed a dependency of their agreement to the  $NO$  concentration.

While the presented techniques for  $P(O_3)$  measurement (MOPS & OPR) are in continuous improvement, significant uncertainties in their measurements are always observed, mainly related to HONO formation and  $NO_2$  wall losses.

Among these three methods, the calculation of  $P(O_3)$  based on  $RO_x$  measurements seems to be the most accurate one. Therefore, this approach was adopted in the present work to be investigated for the monitoring of ozone production rates during chamber experiments.



## 4. Outline of dissertation

As discussed above, peroxy radicals play a crucial role in maintaining the oxidative capacity of the atmosphere via propagation reactions to the hydroxyl radical (OH). Additionally, they have the ability to convert NO into NO<sub>2</sub> in the troposphere, whose subsequent photolysis leads to the formation of tropospheric ozone, a significant air pollutant with profound impacts on both human health and climate. Given the photochemical and secondary nature of ozone, efforts to control and reduce its concentration only rely on predictive atmospheric chemistry models. Given the substantial socio-economic implications associated with this issue, it becomes imperative to undertake research and develop alternative approaches for addressing ozone pollution.

The work proposed in this project involves testing a methodology, based on simultaneous measurements of peroxy radicals and NO, to assess the rate of ground-level ozone formation. The latter is expected to provide useful information on ozone formation regimes and the formation of other secondary species, which will ultimately help public authorities in the management of pollution peaks.

Briefly, this project consists of (1) testing and improving a chemical amplifier (CA) designed to measure peroxy radicals and (2) assessing the reliability of a methodology based on peroxy radical measurements in ambient air to quantify ozone production rates.

The CA device developed at the CERI EE, IMT Nord Europe, allows measuring ambient concentrations of peroxy radicals by chemical conversion and amplification to nitrogen dioxide. Specific objectives were to (i) develop a 2-channel photoacoustic spectrometer (PAS) for NO<sub>2</sub> measurements and couple it to the CA, (ii) reduce uncertainties associated to peroxy radical measurements using CA, and (ii) evaluate the methodology for quantifying ozone production rates by combining simultaneous measurements of peroxy radicals and NO.

The present PhD project was implemented as follows:

1. First 18 months at ULCO, LPCA, Dunkerque
  - Optimizations and characterization of an existing PAS instrument dedicated to black carbon measurements, with the aim of getting trained on this technology,

- Construction and characterization of the 2-channel PAS for NO<sub>2</sub> at LPCA, and assessment of its suitability for peroxy radical measurements using the PERCA technique at CERI EE.
2. Last 18 months at IMT Nord Europe, CERI EE, Douai
- Participation to the ROxComp intercomparison campaign performed at the Forschungszentrum Jülich GmbH (Germany) in August 2022, with the goal comparing the IMT chemical amplifier to other instruments capable of measuring peroxy radicals, and hence improving our understanding of uncertainties associated to this technique,
  - Evaluation of the methodology for ozone production rate quantification using data from experiments made in the SAPHIR simulation chamber during the ROxComp.



## **Chapter 2. Development and characterization of photo-acoustic spectrometers**

This chapter presents some Research & Development work performed on the photoacoustic spectroscopy technology. This work includes the optimization of an existing Photoacoustic spectrometer (PAS) for the detection of black carbon, and the development of a new 2-channel PAS for NO<sub>2</sub> measurements. The latter was aimed to be coupled to a chemical amplifier for the measurement of ambient peroxy radicals.

# 1. Introduction

This chapter reports the work performed for testing and improving an existing prototype of a PhotoAcoustic Spectrometer (PAS) operating at 880 nm for the detection and quantification of black carbon (BC). The aim of this work was to take over the use of a PAS (training) and optimize its performance, in order to later design an improved PAS setup for NO<sub>2</sub> measurements. A series of parameters was optimized, for instance, gas sampling flow rate, laser power and resonance frequency of the PA sampling cell. All of these optimizations led to a better signal-to-noise ratio (SNR) and therefore better figures of merit.

Once the instrument was optimized, particle matter (PM) emitted from incense smoke was used to calibrate the PAS. Side-by-side measurements of incense-generated particulate matters (PM) have been performed using the PAS and a reference instrument (Aethalometer AE51), the latter providing PM concentrations sampled by the PAS.

The second part of this chapter is devoted to present the development of the 2-channel NO<sub>2</sub>-PAS. Similarly to the BC-PAS, a series of parameters was improved in order to reach the optimal sensitivity and the best limit of detection. The PAS instrument was then calibrated using a standard mixture of NO<sub>2</sub>. This work was finalized by a series of ambient and indoor measurements in parallel to a reference NO<sub>x</sub> analyzer to validate the developed setup.

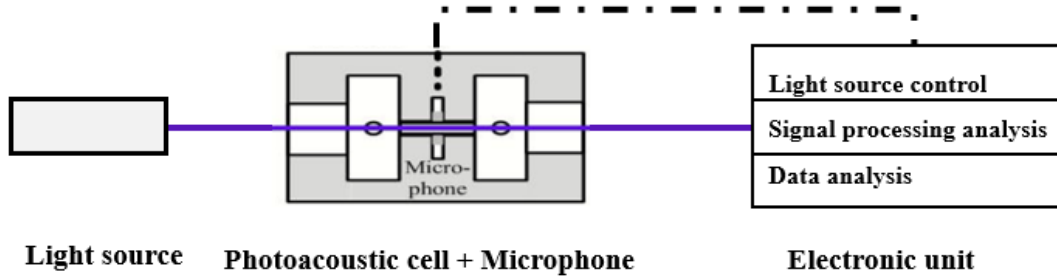
## 2. Photoacoustic spectroscopy

### 2.1. Principle of photoacoustic spectroscopy

Photoacoustic spectroscopy is an analytical technique exhibiting good performances for measuring trace gases and particles in ambient air<sup>95</sup>, with advantages related to its simple setup and relatively low cost. This technique is based on measuring an acoustic signal induced by the absorption of photons from a modulated laser beam by the targeted species. The demodulated signal is then used to provide an information on absorption properties of the detected species (absorption coefficients) and their concentrations<sup>95</sup>.

A photoacoustic (PA) spectrophone is composed of four main parts as shown in Figure 2. 1: a light source with appropriate modulation, a PA cell in which the targeted species

generates a PA signal, acoustic transducer devices (microphones) for detection of the PA signal, and an electronic unit for signal amplification and data processing <sup>66</sup>. A detailed description of these components will be given in the following sub-sections.



**Figure 2. 1:** Schematic presentation of a PAS <sup>66</sup>

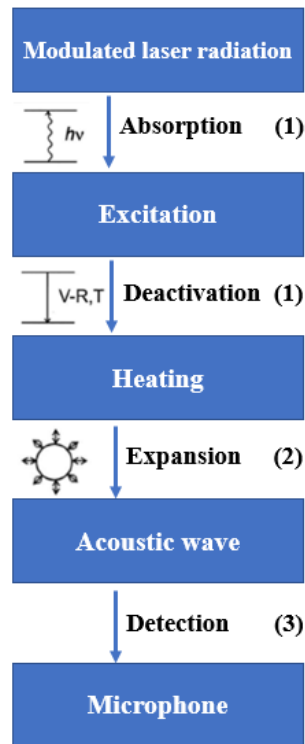
The photoacoustic effect resulting from the absorption of photons by gaseous molecules or aerosol particles can be described by three main steps summarized in Figure 2.2 <sup>96</sup>:

- 1) Localized heat release resulting from the absorption of photons by the irradiated species (absorption and deactivation processes in Figure 2.2)
- 2) Periodical thermal expansion of the sample and the surrounding gas due to the light modulation, which results in an acoustic wave proportional to the absorbed energy (expansion process in Figure 2.2)
- 3) Measurement of the generated acoustic signal (detection process in Figure 2.2).

For a PA setup equipped with microphones as acoustic transducers, the measured PA signal,  $S$  (V), depends on several parameters as presented by the following equation <sup>95</sup>:

$$S = P \times M \times C_{\text{cell}} \times \alpha_0 \times C + S_b \quad \text{Eq 2. 1}$$

where  $P$  (W) is the light power,  $M$  ( $\text{V Pa}^{-1}$ ) the microphones sensitivity, and  $C_{\text{cell}}$  ( $\text{Pa m W}^{-1}$ ) the PA cell constant, which represents the conversion efficiency of absorbed optical energy into an acoustic energy <sup>97</sup>. The PA cell constant is independent of the absorber (gas or PM) <sup>98</sup>.  $S_b$  (V) is the background PA noise, mainly generated by photons being absorbed either by the walls or the windows of the PA cell.  $\alpha_0$  ( $\text{Mm}^{-1} \text{ppb}^{-1}$ ,  $\text{Mm}^{-1} = 10^{-6} \text{m}^{-1}$ ) is the specific absorption coefficient of the detected trace gas and  $C$  (ppb) the gas concentration. In the case of aerosol measurements,  $\alpha_0$  [ $\text{m}^{-1} / (\mu\text{g m}^{-3})$ ] is the aerosol mass coefficient and  $C$  ( $\mu\text{g m}^{-3}$ ) the aerosol mass concentration <sup>95</sup>.



**Figure 2.2:** Schematic presentation of the laser-induced photoacoustic effect <sup>96</sup>.

## 2.2. Light sources

For the selection of a light source suitable for PAS applications, it is necessary to answer two main questions: <sup>96</sup> what is the spectral range where the targeted species absorb? and what is the targeted concentration range?

The light source is a crucial part in the PA spectrophone given its influence on the performances of the instrument, the detection sensitivity of the PA sensor being proportional to some extent to the light power. The optimal light source must (i) emit in a range of wavelengths where the targeted species strongly absorb photons and (ii) exhibit an output power in the range of ~ hundreds of mW <sup>66</sup>.

Different types of light sources can be used for PAS, namely black-body radiators <sup>99</sup>, supercontinuum lasers <sup>100</sup>, light-emitting diodes (LED) <sup>101</sup> and Hg arc lamps <sup>102</sup>, that in combination with bandpass filters, allow operation on a large range of wavelengths. Besides supercontinuum light, the disadvantage of these broadband light sources is the shape of the light beam and the difficulty of collimating it <sup>66</sup>. The selection of an appropriate light source relies on particular parameters, for instance the light beam divergence, broadband optical power, and more specifically, the spectral power density. The most frequently used light

sources are diode lasers and quantum cascade lasers <sup>66</sup>. In the present work, diode lasers emitting at 880 nm and 450 nm have been used as light sources for black carbon and NO<sub>2</sub> measurements, respectively.

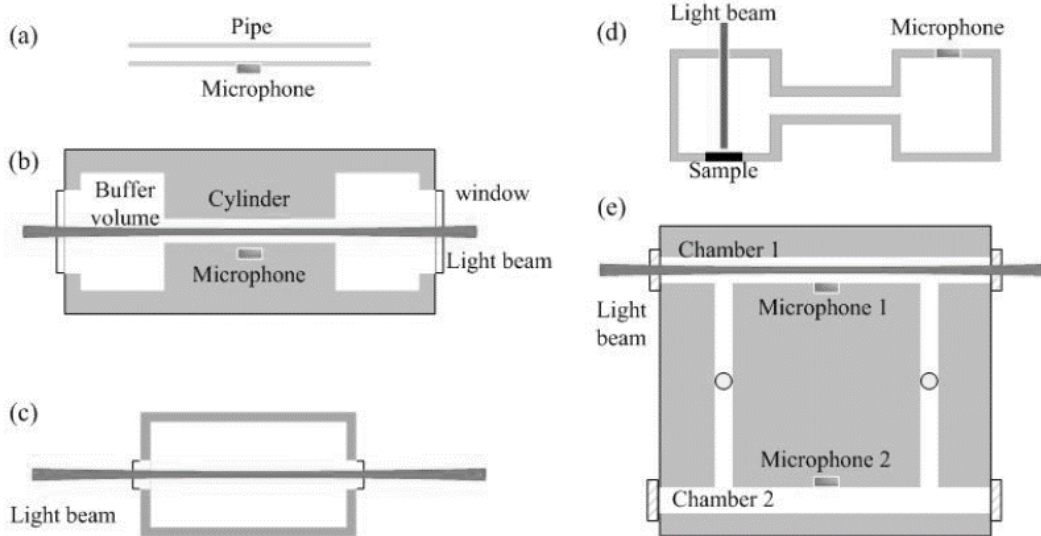
Light modulation is a key approach in PAS. It can be performed either by a mechanical chopper placed on the pathway of the laser beam or by modulating the diode current, which results in a modulation of the light emission <sup>66</sup>. A mechanical chopper is suitable for almost all type of light sources, capable of handling modulation frequencies up to a few kHz. However, the use of a chopper introduces mechanical vibrations and noise, practically noticeable at higher modulation frequencies <sup>66</sup>. As for electrical modulation, it involves modulating the current injected in the light source. This method is not appropriate for modulating a thermo-source such as blackbody radiation. In the present work, the two modulation methods were used: laser power is modulated using a mechanical chopper in the BC-PAS, and the laser power is electrically modulated for the dual-channel NO<sub>2</sub>-PAS.

### **2.3. Photo-acoustic cells**

In a PA spectrophone, the absorption of a periodically modulated laser light generates acoustic waves. A resonant PA cell is usually used to amplify the PA signal by adjusting the modulation frequency of the laser light to an acoustical resonance frequency of the PA cell <sup>97</sup>. Different designs can be used for the PA resonator as shown in Figure 2.3.

The simple pipe shown in Figure 2.3 (a) is treated as a one-dimensional acoustic resonator when the pipe size is smaller than the acoustic wavelength <sup>96</sup>. A cylindrical resonator without buffer volumes (Figure 2.3 (c)) has in general three acoustic modes including longitudinal, azimuthal and radial <sup>96</sup>. The Helmholtz resonator shown in Figure 2.3 (d) is mainly designed to create a separation between the microphone and the sample chamber. This configuration enables operation over a wide temperature range of the sample, while the microphone remains consistently operational at room temperature. However, the use of this type of resonator is limited given its low sensitivity <sup>96</sup>. This drawback is reduced in the case of a differential Helmholtz resonator (Figure 2.3 (e)), where the use of two identical resonators allows reducing background noise <sup>96</sup>.





**Figure 2.3:** Schematics of PAS cells - (a) Simple pipe <sup>96</sup>. (b) Cylinder equipped with two buffer volumes <sup>103</sup>. (c) Cylinder resonator <sup>104</sup>. (d) Helmholtz resonator with separate sample and detection chambers <sup>105</sup>. (e) Differential Helmholtz resonator <sup>106</sup>.

The PA resonator that is the most widely used is a cylinder equipped with two buffer volumes; they mainly consist in narrow and wide tubes connected together as shown in Figure 2.3 (b) <sup>96</sup>. The buffer volumes at each side help minimizing the acoustic noise resulting from (i) the external environment, (ii) the flowing gas, and (iii) light absorption from windows. In addition, the cell is equipped with gas inlet and outlet.

The resonance frequency of the acoustic resonator can be expressed by the following equation <sup>107</sup>:

$$f = \frac{c}{2 \times (L + \Delta L)} \quad \text{Eq 2. 2}$$

where  $c$  is the sound speed,  $L$  is the length of the resonator and  $\Delta L = \frac{16}{3\pi} \times R$  the so-called end correction factor ( $R$  being the resonator radius).

The amplification of the photoacoustic signal is characterized by a quality factor ( $Q$ ) of the acoustic resonance <sup>66</sup>. The quality factor is expressed by the ratio of the energy accumulated in the acoustic stationary wave divided by the energy losses per period, as shown in Eq 2. 3 <sup>108</sup>. In other terms, this factor represents the effect of losses <sup>96</sup>.

$$Q = \frac{2\pi \times \text{accumulated energy}}{\text{energy lost over one period}} \text{ or } Q = \frac{f}{\Delta f} \quad \text{Eq 2. 3}$$

where  $f$  is the resonance frequency and  $\Delta f$  is the half-width value of the resonance profile. The  $Q$  factor strongly depends on the cell design; it can vary from 10 up to several

hundreds, higher values indicating better performances. Therefore, the sensitivity of the photoacoustic instrument is related to the PA cell construction <sup>66</sup>.

The PA signal is inversely proportional to the cell volume and the modulation frequency of the laser beam. In order to achieve high PA signals, it is better to work with a small cell volume ( $\approx 10 \text{ cm}^3$ ) and a low modulation frequency. Nevertheless, the dominant noise sources are usually  $1/f$  frequency dependent, such as intrinsic noise of microphones, amplifier noise, and external acoustic noise, which requires to operate the PA cell at elevated modulation frequencies to improve the Signal-to-Noise Ratio (SNR) <sup>96</sup>. The best limit of detection will therefore depend on a tradeoff between a high PA signal and a low noise level.

The performances of PAS instruments will critically depend on the acoustic transducer's characteristics. Acoustic transducers usually used are conventional electrets <sup>95</sup> or condenser microphones <sup>109</sup>, quartz tuning forks (QTF) <sup>110</sup>, Cantilever <sup>111</sup>, or micro-electromechanical system (MEMS) microphones <sup>112</sup>.

The condenser and electret microphones are the most commonly used transducers in PA spectroscopy <sup>66</sup>. They are mainly made of a fixed metal back-plate and a flexible diaphragm. The distance between these two components changes in response to the acoustic signal, thereby altering the microphone's capacitance. This change in capacitance is then converted into an electric signal. Among the capacitive microphones, the electret microphones are particularly popular thanks to their small size, affordability, durability, reliability and compactness. They are suitable for a wide frequency range (from 20 Hz up to 20 kHz) <sup>113</sup>, making them ideal for automatic measurement systems. These microphones offer advantages such as low power consumption, high sensitivity (ranging from 10 to 50  $\text{mV Pa}^{-1}$ ), and low noise <sup>66</sup>. In the present work, electret microphones are used for both BC-PAS and  $\text{NO}_2$ -PAS.

To further enhance the PA signal, a multi-microphone approach can be employed, which results in an improvement by a factor of  $n^{1/2}$  ( $n$  represents the number of microphones) <sup>114</sup>.

## **2.4 Signal processing unit**

The microphone signal is first amplified with a preamplifier and then injected into a lock-in amplifier in order to improve the SNR by removing low-frequency noise, in particular

the  $1/f$  noise. A power meter is usually used to record the light power, thereby enabling normalization of the detected PA signal if needed. A data acquisition card is involved to sample the demodulated PA signal. A laptop is used to perform data processing and result display using a Labview program <sup>97</sup>.

### **3. Characterization and optimization of a photoacoustic spectrometer for measuring black carbon**

Carbonaceous particulate matter (PM) is a major combustion by-product and is characterized by strong absorption features in the visible and near-infrared radiation range. Black carbon (BC), a component of PM, is one of the main short-lived climate pollutants (SLCPs) <sup>14</sup>. PM plays an important role in Earth climate change and air quality. Accurate measurements of PM concentrations and absorption properties are highly needed to evaluate how PM impacts global warming and public health. Recently, PAS was found to be one of the best techniques for online, filter-free, measurements of absorbing PM. In contrast to traditional filter-based methods, PAS offers notable benefits such as high accuracy and portability, and reduced sensitivity to light scattering <sup>98</sup>.

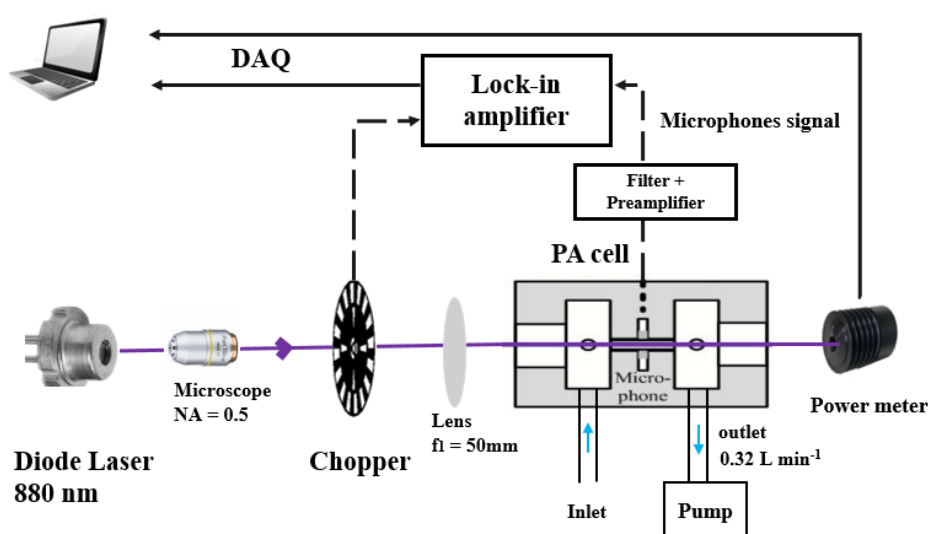
This section is devoted to the presentation of the progress made on an existing PAS for the measurement of carbonaceous particulate concentrations. The novelty of this instrument lies in the choice of the wavelength. At 880 nm, the detected particles are assimilated to BC, without interference from other molecules, especially organic carbon, that absorb mainly at shorter wavelengths <sup>115</sup>. This work was published in the special issue: Recent Advances in Photoacoustic and Photothermal Gas Spectroscopy of the journal *Molecules* <sup>116</sup>.

#### **3.1. Experimental setup**

The prototype of PA spectrophone is shown in Figure 2.4. As discussed above, it comprises a modulated light source, a photoacoustic resonator and a data processing module.

The light source is a high power TO-3 laser diode (Wave Spectrum, AL0880F1000, Beijing, China), emitting at  $880 \pm 5$  nm with an emission linewidth of  $\sim 1$  nm. It exhibits a maximum output optical power of 1 W at an operating current of 1.3 A and an operating

voltage of 2.2 V. Those parameters are controlled by a diode laser controller (6340 ComboSource, Arroyo Instruments, San Luis Obispo, CA, USA). A microscope with a numerical aperture (NA) of 0.5 is used to reshape and collimate the laser beam, which is then passed through a 100-slot mechanical chopper (New focus 3501, Newport/New Focus, Irvine, CA, USA). The chopper modulates the laser light at 6.09 kHz, which is the resonance frequency of the PA cell (see section 3.3.3 for optimization of this parameter). Afterwards, the modulated laser beam is focused into the PA cell using a plano-convex lens (focal length of 50 mm). The laser beam at the output of the cell is collected with a power meter (Coherent, Field Master GS, Saxonburg, PA, USA) to monitor the laser power.



**Figure 2.4:** Schematic representation of the PA spectrophone for BC measurements

The PA cell is a metallic cylindrical resonator, 23 mm long and 6 mm in diameter (see panel b in Figure 2.3). It is equipped with two buffer volumes (20 mm long and 50 mm in diameter each), with UV fused silica windows (transmission > 90% between 180 nm and 2.6  $\mu\text{m}$ ).

Four electret microphones (EK-23329-P07, Knowles, Itasca, IL, USA) are set up in the middle of the resonator to detect the PA signal with a sensitivity  $M$  of  $22.4 \text{ mV Pa}^{-1}$  at a sound frequency ranging from 100 to 10000 Hz.

As mentioned in section 2.4, the PA signal is first processed by a band-pass filter (5.5-7.5 kHz), then amplified using a home-made pre-amplifier with a gain of 10. In a second step, the acoustic signal is demodulated at the laser light modulation frequency using a lock-in amplifier (SR 830, Stanford Research Systems, Sunnyvale, CA, USA). The PA signal is

then sampled using a National Instrument data acquisition card (National Instrument PCI-6251, Austin, TX, USA), connected to a laptop allowing data processing and results display via a Labview program.

## 3.2. Optimization of operating conditions

To characterize the developed PAS instrument, a series of experiments was made in order to (1) calibrate the cell constant, (2) optimize operating parameters, including laser power, modulation frequency and sampling flow rate, and (3) evaluate the effect of ambient humidity on the PA signal.

### 3.2.1. Calibration of the PA cell constant

To calibrate the cell constant of a photoacoustic cell, an absorber (gas or particulate matter) with a known absorption cross section has to be introduced into the cell at a known concentration<sup>117</sup>. NO<sub>2</sub> is commonly used for this purpose at wavelengths ranging from the visible up to the near-infrared region<sup>118</sup>. At 880 nm, NO<sub>2</sub> exhibits small absorption cross sections (~10<sup>-23</sup> cm<sup>2</sup> molecules<sup>-1</sup> range), therefore, it is essential to work at a relatively high concentration.

For this calibration, a standard mixture of NO<sub>2</sub> in N<sub>2</sub> (3000 ± 60.6 ppm, Air Liquide) was sampled into the PA cell using a 1/4" PTFE tube (~1 m length) at a flow rate of 0.3 L min<sup>-1</sup>. Overnight flushing of the PA cell with N<sub>2</sub> was performed at the end of the calibration experiment to remove any potential contamination due to the use of elevated concentrations of NO<sub>2</sub>.

Eq 2. 1 was rearranged to derive C<sub>cell</sub> from the calibration experiment as shows below:

$$C_{\text{cell}} = \frac{S - S_b}{\alpha_0 \times C \times P \times M} \quad \text{Eq 2. 4}$$

The measured PA signal (S) for a NO<sub>2</sub> mixing ratio of 3000 ppm and the background signal (S<sub>b</sub>) observed when only pure N<sub>2</sub> is passed through the cell were 25.34 μV (± 0.20 μV) and 16.28 μV (± 0.22 μV), respectively. The specific absorption coefficient α<sub>0</sub> (Mm<sup>-1</sup> ppm<sup>-1</sup>) of NO<sub>2</sub> was derived from the following equation:

$$\alpha_0 = \frac{N \times \sigma(\lambda)}{C_{\text{NO}_2}} \quad \text{Eq 2. 5}$$

where  $N = 7.5 \times 10^{16}$  molecules  $\text{cm}^{-3}$  is the  $\text{NO}_2$  concentration at  $T = 293.5$  K and  $P = 1$  atm and  $C_{\text{NO}_2} = 3000 \pm 60.6$  ppm is the  $\text{NO}_2$  mixing ratio. According to the MPI-Mainz UV/VIS Spectral Atlas of Gaseous Molecules of Atmospheric Interest, the absorption cross section  $\sigma(\lambda)$  of  $\text{NO}_2$  at 880 nm is  $3.51 \times 10^{-23}$   $\text{cm}^2$  molecule $^{-1}$  <sup>119</sup>. The specific absorption coefficient  $\alpha_0$  of  $\text{NO}_2$  was then found to be  $0.088$   $\text{Mm}^{-1}$   $\text{ppm}^{-1}$ . Using a laser power of 173 mW, The PA cell constant was deduced to be  $C_{\text{cell}} = 2.21 \pm 0.05$   $\text{Pa m W}^{-1}$ . The uncertainty for the cell constant was calculated from a quadratic propagation of errors associated to the PA signal (precision), the  $\text{NO}_2$  mixing ratio and the laser power. The relative uncertainty is 0.8% on the PA signal ( $\frac{\Delta S_{\text{PA}}}{S_{\text{PA}}}$ , observed at the output of the lock-in amplifier), 2% on the  $\text{NO}_2$  concentration from the gas standard certification ( $\frac{\Delta C_{\text{NO}_2}}{C_{\text{NO}_2}}$ ) and 0.10% on the laser power ( $\frac{\Delta P}{P}$ ). The uncertainty values on the microphone sensitivity  $M$  and the specific absorption coefficient  $\alpha_0$  are considered as negligible. A value of 2.2% was estimated as the relative uncertainty on the cell constant, corresponding to a  $\Delta C_{\text{cell}} = 0.05$   $\text{Pa m W}^{-1}$ .

### 3.2.2. Laser power

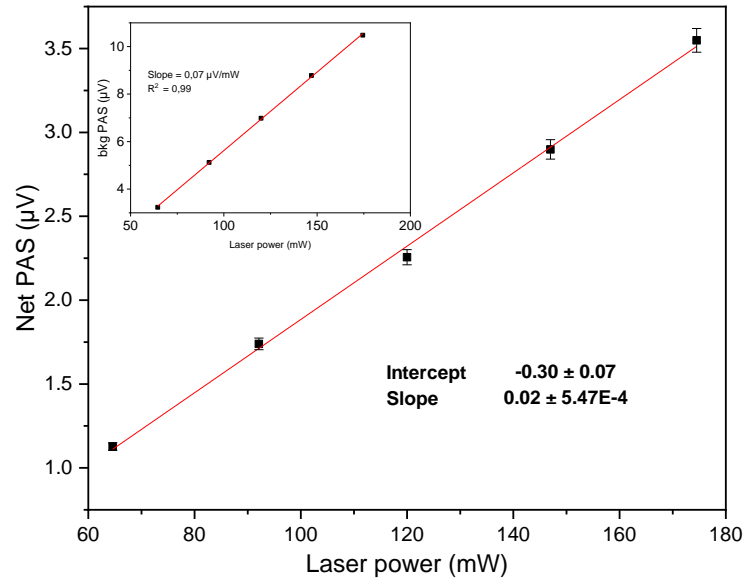
As mentioned above, the PA signal is proportional to the laser power, which means that an increase in the laser power would enhance the sensitivity of the instrument. In this regard, experiments were carried out to check this property and whether the sensor exhibits a linear response with the laser power. The laser power was adjusted by controlling the diode current intensity.

A sampling flow rate of  $0.4$   $\text{L min}^{-1}$  was used. By flushing dry  $\text{N}_2$  (Air Liquide, RH  $\sim 5\%$ ) into the PA cell, a background signal proportional to the laser power was observed, as shown in the inset of Figure 2.5 (bkg PAS vs laser power). This signal is due to the absorption of photons on the walls and windows of the PA cell, and the absorption of water-vapor. It is worth noting that high PM concentrations may contaminate the optical windows of the PA cell leading to higher background signal as well. Hence,  $\text{N}_2$  is regularly flushed after aerosol measurements to check the background signal.

Afterwards, ambient air was filtered through a PTFE membrane (Sartorius Stedium, Midisart 2000, porosity =  $0.2$   $\mu\text{m}$ ) to remove atmospheric aerosols and was sampled into

the PA cell. The mass concentration of particles with a size less than 0.2  $\mu\text{m}$  is assumed to be negligible ( $<1 \mu\text{g}\cdot\text{m}^{-3}$ ), as well as their effect on the PA signal.

After subtracting the background signal, the PA signal was found to be linearly proportional to the laser power as shown in Figure 2.5. This signal can be attributed to the absorption of water-vapor and other absorbing gases in ambient air, which was relatively constant along the experiment ( $\sim 18.5 \pm 0.5 \%$  at  $26^\circ\text{C}$ ).



**Figure 2.5:** Linear dependence of the net (net PAS) and background (bkg PAS in the inset) signals with laser power measured at the output of the PA cell. Error bars correspond to the Standard Deviation of the mean signal (1s measurements averaged over 240 s)

According to these results, showing that the net PA signal keeps increasing with the laser power, a modulated laser power of 175 mW (highest power measured at the output of the PA cell) was used in the present work, which corresponds to a current intensity of 1 A.

### 3.2.3. Modulation frequency

In the present photoacoustic spectrometer, modulation frequency of the laser beam was adjusted to the resonance frequency of the PA cell resonator, which is presented by Eq 2. 2. For an ideal gas, the sound speed  $c$  can be expressed as follows <sup>120</sup>:

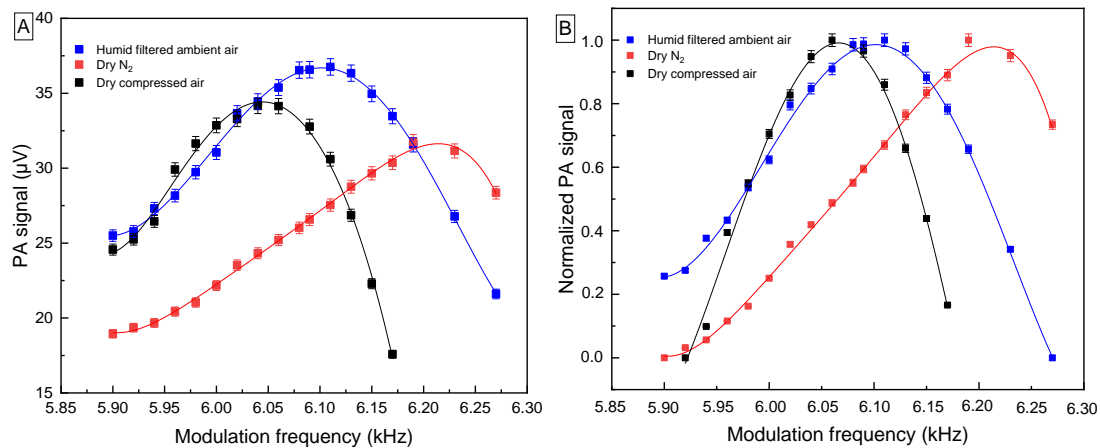
$$c = \sqrt{\frac{\Upsilon \times P}{\rho}} \quad \text{Eq 2. 6}$$

where  $\Upsilon$  is the adiabatic index also known as the isentropic expansion factor,  $P$  (Pa) and  $\rho$  ( $\text{kg m}^{-3}$ ) are the gas pressure and density, respectively. Hence, this parameter is dependent

on the medium composition, and in particular, on the molecular weight of molecules present in the carrier gas.

Therefore, to determine the optimal resonance frequency, experiments were carried out to monitor the variation of the PA signal at different modulation frequencies, and for three types of carrier gases: N<sub>2</sub> with low water content (RH = 9.5 ± 0.3 %, T = 27 ± 0.2 °C) - referred to as dry N<sub>2</sub> in the following sections; compressed air with low water content (RH = 12 ± 0.5 %, T = 27 ± 0.2 °C) - referred to as dry compressed air in the following sections; and humid filtered indoor ambient air (RH = 31 ± 1 %, T = 27 ± 0.5 °C), filtered by a PTFE membrane filter (0.2 µm) to remove particles.

Figure 2.6 (panels A and B) shows how the PA signal and the normalized PA signal ( $\frac{\text{PA signal}}{\text{peak value of PA signal}}$ ) vary with the modulation frequency in the range 5.90-6.27 kHz. This range of frequency covers the resonance frequency of dry N<sub>2</sub> (6.25 kHz) and dry compressed air (6.09 kHz) calculated using Eq 2. 2, where the sound speed in N<sub>2</sub> and air are 351.17 and 342.35 m s<sup>-1</sup>, respectively, with a cylinder length of 23 mm and a radius R of 3 mm ( $\chi = 1.4$ ,  $p = 1.013 \times 10^5$  Pa,  $\rho$  (N<sub>2</sub>) = 1.15 kg m<sup>-3</sup>,  $\rho$  (air) = 1.21 kg m<sup>-3</sup>). This test was carried out to compare the theoretical resonance frequencies to the optimal frequencies found experimentally.



**Figure 2.6:** Dependence of the PA signal on the modulation frequency for the different gases (A-raw data, B- normalized data). Error bars correspond to the Standard Deviation of the mean signal (1s measurements averaged over 60 s)

It has been noticed that dry N<sub>2</sub> and dry compressed air do not exhibit their maximum at the same frequency as expected since two different carrier gases are used, their peaks being observed at 6.19 kHz and at 6.06 kHz, respectively. They are within 1% and 0.5% of the

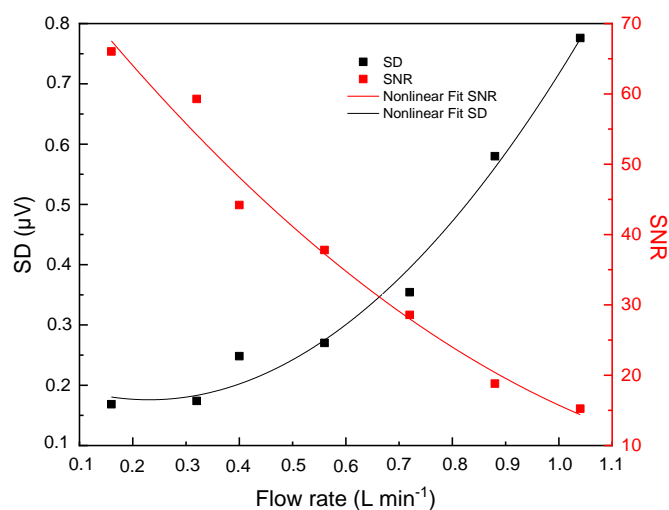


theoretical values, respectively. As the target absorber for the present PA spectrometer is BC, a modulation frequency of 6.06 kHz (“dry compressed air”) was chosen as operating parameter.

Figure 2.6 shows that at 6.06 kHz, an increase in RH from 12 to 34% would lead to a slight shift in the resonance frequency of about 0.8%, which results in a relative decrease in the instrument’s response of approximately 10%. This observation is roughly consistent with a shift of 1.6% in the resonance frequency which can be estimated by comparing the theoretical resonance frequencies calculated for humid air (6.19 kHz,  $\rho_{\text{air}} = 1.17 \text{ kg m}^{-3}$  <sup>121</sup>, 34% RH, 27°C) and dry compressed air (6.09 kHz). This implies that water-vapor has a significant impact on the resonance frequency <sup>122</sup> that should be taken into consideration for ambient measurements.

### 3.2.4. Sampling flow rate

Reducing acoustic noise is key for PA measurements since it limits the detection of low concentrations of targeted species <sup>96</sup>. Several factors can contribute to the noise level as mentioned above, one of which being the gas flow rate due to the generation of turbulences inside the PA cell. The dependence of the measurement noise (Standard Deviation observed during blank measurements: SD) and Signal-to-Noise ratio (SNR, net PA signal divided by SD) on the sampling flow rate was investigated within the range of 0.16 L min<sup>-1</sup> to 1.02 L min<sup>-1</sup> with ambient air (RH ~33 ± 1%, T = 28°C) filtered by a PTFE membrane (0.2 µm), as shown in Figure 2.7.



**Figure 2.7:** Dependence of the PA noise (SD) and signal-to-noise ratio (SNR) on the sampling flow rate

It has been noticed that the noise increases with a larger flow rate in a nonlinear way, while the SNR has an inverse behavior; it decreases with higher flow rates. In this regard, it is essential to indicate that in the PA system, above a certain value of the flow rate (typically about  $0.5 \text{ L min}^{-1}$ , in our case  $0.4 \text{ L min}^{-1}$ ), the apparition of turbulences inside the sampling cell generate some acoustic noise that worsen the precision of the measurements <sup>123</sup>.

A sampling flow rate of  $0.32 \text{ L min}^{-1}$  was selected since it represents a good compromise between the SNR and the air residence time in the PA resonator (0.12 s).

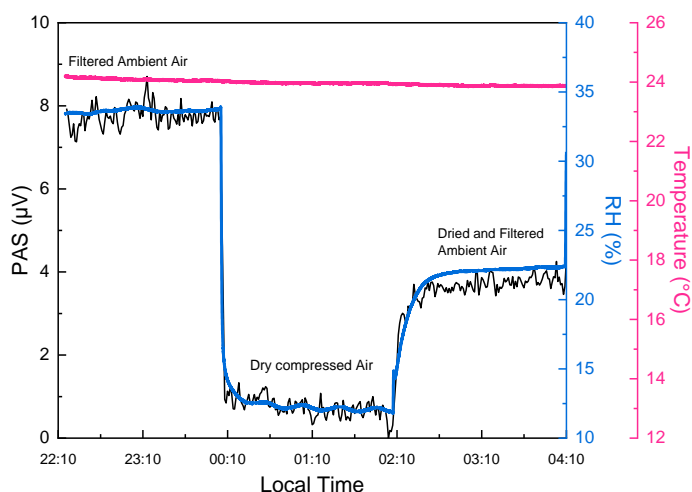
### **3.2.5. Management of sample humidity**

The PA signal depends on the vibrational-to-translation (V-T) relaxation rate of the targeted gas (or absorber in the particulate phase) <sup>122</sup>. In this regard, water-vapor is considered as a promoter to fasten this process and it can considerably enhance the PA signal <sup>124</sup>. In addition, water can absorb the laser light, which will also generate a PA signal. While the HITRAN database indicates that this molecule has a very weak absorption cross section at 880 nm ( $\sim 10^{-27} \text{ cm}^2 \text{ molecule}^{-1}$ ), its high concentration in the atmosphere can lead to a significant interference for the PAS measurements.

In the present work, water-vapor was monitored using a temperature & humidity sensor (Sensirion, SHT71, Stäfa, Switzerland) connected to the outlet of the PA cell. Figure 2.8 shows that an increase of RH from about 12% to about 34% at a relatively constant temperature, generates an increase of  $7 \mu\text{V}$  in the PA signal, which would be equivalent to a BC concentration of  $32.1 \mu\text{g m}^{-3}$  on the basis of the sensitivity reported later in Section 3.3.1. A correction procedure is hence essential to minimize this effect.

A Nafion dryer (Perma pure, 30 cm monotube MD-110-12S-4 dryer, Lakewood, NJ, USA) was chosen to continuously dry the sampled gas removing only water-vapor. Its operating principle consists on the transfer of moisture through the Nafion tubing wall, from the sample gas to a counter-flowing purge gas stream. Dry compressed air was used as a purge gas, injected at the optimal flow rate of the dryer of  $4 \text{ L min}^{-1}$ , as recommended by the manufacturer.

An experiment was carried out to monitor the variation of the PA signal with RH. Gases used in this experiment were dry compressed air (RH ~ 12%), ambient air filtered by a PTFE membrane to eliminate the effect of aerosol particulates on the PA signal (RH ~ 34%), and the previous filtered ambient air dried by the Nafion dryer (RH ~ 22%). A decrease of RH from 34% to 22% ( $T \sim 24\text{ }^{\circ}\text{C}$ ) was observed after drying ambient air by the Nafion dryer as shown in Figure 2.8, which generates a 57% reduction in the net PA signal from ambient air after subtracting the background signal from dry compressed air. While the sample is not dried completely, the use of a Nafion membrane will allow minimizing the impact of water-vapor on the PAS measurements. Since it stabilizes RH at a constant level of  $22 \pm 2\%$  in the samples (for an initial RH < 80%), the PA signal generated by the residual water-vapor is stable and can be considered as a background signal that needs to be subtracted. The effective PA signal derived after subtraction of the background signal, which is only due to the detection of BC, is referred to as EffPAS in the following.

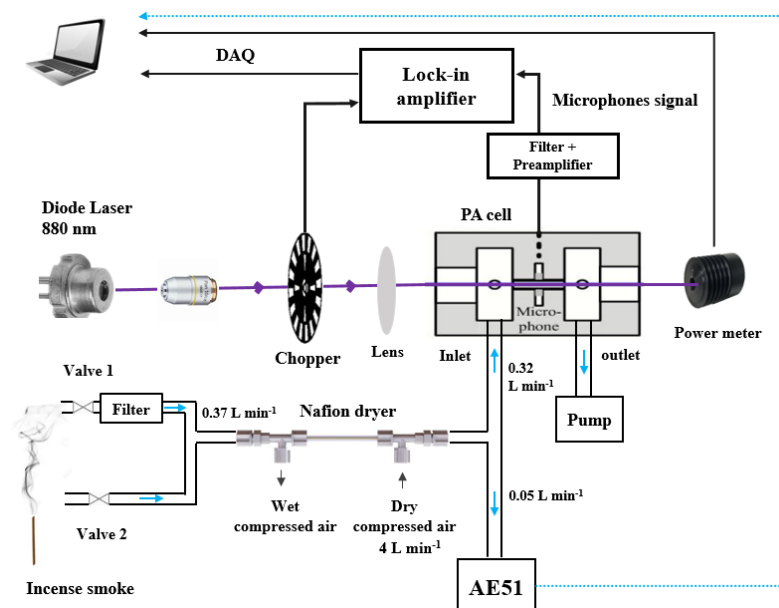


**Figure 2.8:** Time series of PAS measurements from filtered ambient air, dry compressed air, and dried and filtered ambient air

### 3.3. Calibration and figures of merit

#### 3.3.1. Relative calibration of the PAS signal

In the present work, carbonaceous particulate matter (PM) from incense smoke was sampled by the PAS to characterize and calibrate its response and to demonstrate its performances. Side-by-side measurements of the incense-generated PM have been performed using the developed PAS and a reference aethalometer instrument (microAeth, AE51) as shown in Figure 2.9.

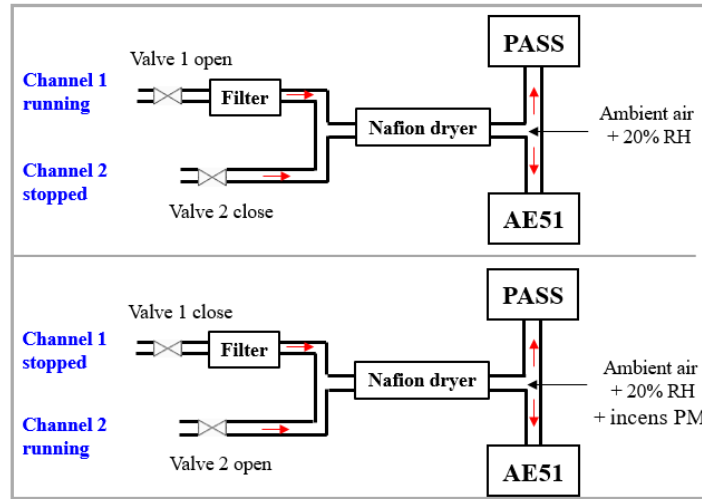


**Figure 2.9:** Schematic of the experimental setup for the measurement of incense-generated BC with the PAS instrument and a reference aethalometer (AE51)

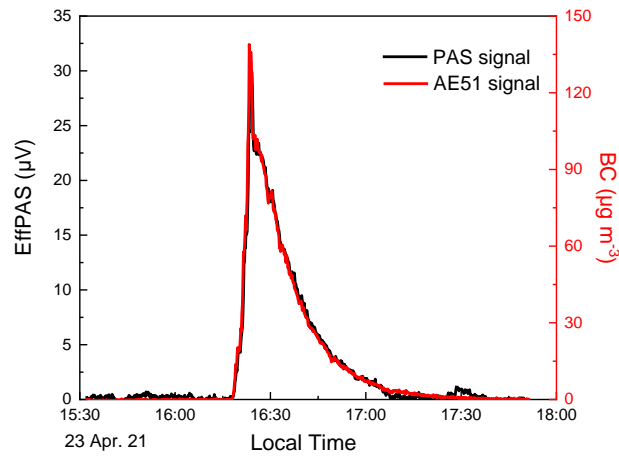
The inlets of both PAS and AE51 were connected to a Nafion dryer (same model as presented in the previous section), in order to reduce relative humidity, thus maintaining it stable at approximately 20%, and limiting the impact of its variation on the measured PA signal.

The aethalometer is a filter-based spectrometer operating at 880 nm. Its operation principle is based on the measurement of the rate of change in absorption of transmitted light due to continuous collection of particles on a filter. It is characterized by a 3- $\sigma$  LoD of  $0.216 \mu\text{g m}^{-3}$  at a time resolution of 1 min<sup>125</sup>. At this wavelength, the measurement is interpreted as BC.

To obtain the PA signal resulting only from BC absorption without the contribution of gaseous species, a two-channel measurement method (presented in Figure 2.10) was carried out: (1) channel 1, equipped with a particle matter PTFE membrane filter (same model as presented in section 3.2.2), allows measuring the potential contribution of gas species in air, including residual water; this measurement was considered as a background measurement; (2) channel 2, without a PM filter, allows measuring the contribution of both BC and gaseous species. The difference in signals between the two channels represents the absorption of BC (EffPAS in Figure 2. 11).



**Figure 2.10:** Schematic representation of the 2-channel measurement approach



**Figure 2. 11:** Time series of PAS and AE51 measurements of incense-generated BC

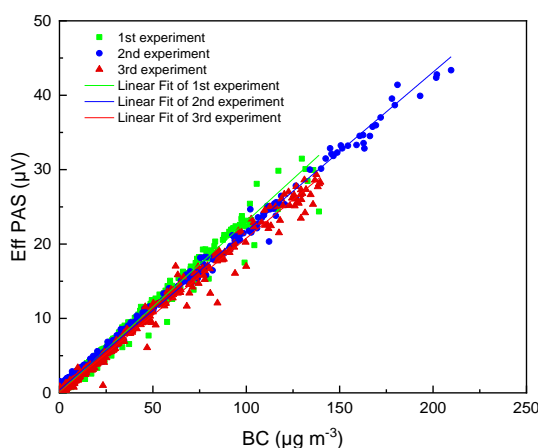
Measurement time series of incense-generated BC by PAS at a time resolution of 1 s (averaged to 10 s) and the AE51 at a time resolution of 10 s are shown in Figure 2. 11. The PAS signal was found to linearly correlate with the BC concentration over a range of 0-200  $\mu\text{g m}^{-3}$  (green plot Figure 2.12), with a determination coefficient  $R^2 = 0.99$ . The scatter plot indicates a sensitivity of  $0.23 \mu\text{V}/(\mu\text{g m}^{-3})$  for this instrument.

A  $3\text{-}\sigma$  (SNR=3) limit of detection (LoD) was calculated using the following equation:

$$\text{LoD} = \frac{3 \times \text{SD}}{S_{\text{slope}}} \quad \text{Eq 2. 7}$$

where SD is the standard deviation (noise) in the PA signal ( $0.20 \mu\text{V}$ ) during blank measurements (RH = 21%, T =  $24^\circ\text{C}$ ) and  $S_{\text{slope}}$  is the sensitivity of  $0.23 \mu\text{V}/(\mu\text{g m}^{-3})$

mentioned above. A  $3\text{-}\sigma$  LoD of  $2.5 \mu\text{g m}^{-3}$  is calculated and can be used to characterize the performance of the developed PA spectrophone at a time resolution of 1 s.

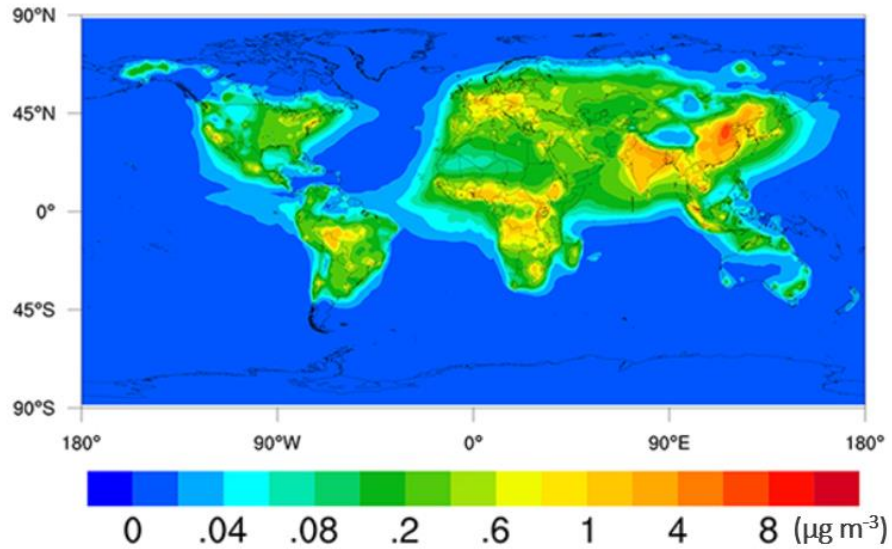


**Figure 2.12:** PA signals versus BC mass concentrations measured by the AE51 during three calibration experiments.

The repeatability of the measurements was also evaluated by repeating the experiment two more times using similar experimental conditions. Figure 2.12 shows a good repeatability between all experiments, with slopes ranging from 0.207-0.229 and  $3\text{-}\sigma$  LoDs in the range of  $2.3\text{-}2.7 \mu\text{g m}^{-3}$ .

With such limit of detection, this instrument can be employed for the detection of BC in the troposphere, especially in areas with moderate aerosol loadings and strong smog conditions, where the BC concentration can reach up to  $12 \mu\text{g m}^{-3}$ <sup>126</sup>, and  $60 \mu\text{g m}^{-3}$ <sup>126</sup>, respectively (orange and red zones in Figure 2.13). However, in regions with clean air masses, with BC concentrations less than  $1 \mu\text{g m}^{-3}$ <sup>126</sup> (green zones in Figure 2.13), an improvement of the LoD will be necessary before using this instrument.

The LoD can be further reduced to  $0.24 \mu\text{g m}^{-3}$  using a longer integration time of 1 min. Further improvements of the sensitivity can be achieved by increasing the number of microphones in the PAS cell and using higher laser power. For instance, using 8 microphones instead of 4 is expected to increase the sensitivity by a factor of  $\sqrt{2}$ . Using a new laser operating at 3.5 W instead of 1 W should also improve the sensitivity by a factor of 1.9. However, the dependence of the PA signal on the laser power will have to be investigated to ensure that the PA signal is not saturated<sup>55</sup>. These two improvements should lead to a LoD of  $0.06 \mu\text{g m}^{-3}$  at a time resolution of 1 min.



**Figure 2.13:** Annual-averaged surface BC concentrations for the year 2005 <sup>126</sup>

### 3.3.2. Assessment of the mass absorption coefficient of incense particles

In order to evaluate the ability of the BC-PAS on determining the optical properties of BC, calculations of the wavelength-dependent mass absorption coefficient ( $\alpha_{MAC}$ ) were performed based on Eq 2. 8. In fact, the determination of this parameter is crucial to quantify the radiative forcing effect of BC, which is an important information to predict temperature changes, cloud formation and other climate-related processes <sup>127</sup>.

$$\alpha_{MAC} = \frac{S_{slope}}{P \times M \times C_{cell}} \quad \text{Eq 2. 8}$$

where  $S_{slope} = 0.217 \mu V / (\mu g m^{-3})$  (derived from the three calibration experiments displayed in Figure 2.12),  $P = 175 \text{ mW}$ ,  $M = 4 \times 22.4 \text{ mV Pa}^{-1}$ ,  $C_{cell} = 2.21 \text{ Pa m W}^{-1}$ . The value of  $\alpha_{MAC}$  was determined to be  $6.3 \pm 0.44 \text{ m}^2 \text{ g}^{-1}$ , which corresponds to a minimum measurable absorption coefficient of  $5.23 \pm 0.36 \text{ Mm}^{-1} (1\sigma)$  (calculated as  $LoD \times \alpha_{MAC}$ ).

The uncertainty associated with the mass absorption coefficient was derived from a quadratic propagation of errors, including the PA signal precision, the power measurement accuracy, and errors associated to the cell constant and fluctuations in BC concentrations. The latter was calculated from the aethalometer measurements using the following equation <sup>128</sup>:

$$\frac{\Delta BC}{BC} = \sqrt{\left(\frac{\Delta \sigma_{ATN}}{\sigma_{ATN}}\right)^2 + \left(\frac{\Delta A}{A}\right)^2 + \left(\frac{\Delta Q}{Q}\right)^2 + \left(\frac{\Delta dt}{dt}\right)^2 + 2\left(\frac{\Delta I_0}{I_0}\right)^2 + 2\left(\frac{\Delta I_1}{I_1}\right)^2} \quad \text{Eq 2. 9}$$

where  $\frac{\Delta\sigma_{\text{ATN}}}{\sigma_{\text{ATN}}}$  is the relative uncertainty from the attenuation cross section, which is assumed to be negligible for the microAeth® AE51<sup>128</sup>.  $\frac{\Delta A}{A} = 2\%$  is the uncertainty from the spot area on the filter<sup>128</sup>.  $\frac{\Delta Q}{Q} = 5\%$  is the uncertainty related to the sampling flow rate<sup>128</sup>.  $\frac{\Delta dt}{dt}$  is the measurement time uncertainty, which is assumed to be negligible<sup>128</sup>.  $\frac{\Delta I_0}{I_0} = 2.1\%$  and  $\frac{\Delta I}{I} = 1.6\%$  are relative uncertainties on the reference and sensing signals (= SD/mean signal), respectively. The relative uncertainty associated to fluctuations in BC concentrations was evaluated to be 6.5%. The relative uncertainty on  $\alpha_{\text{MAC}}$  was found to be 6.9%, which corresponds to  $\Delta\alpha_{\text{MAC}} = 0.44 \text{ m}^2 \text{ g}^{-1}$ .

Values derived above for the mass absorption coefficient and the minimum measurable absorption coefficient are in good agreement with those reported by (Bond et al.)<sup>127</sup>, i.e.  $7.5 \pm 1.2 \text{ m}^2 \text{ g}^{-1}$  and  $6.23 \pm 1 \text{ Mm}^{-1}$ , respectively. However, these values are higher than those calculated on the basis of a power law as shown in the following equation<sup>129</sup>:

$$\alpha_{\text{MAC}} = k_0 \times \left(\frac{\lambda}{500 \text{ nm}}\right)^{-\text{AAE}} \quad \text{Eq 2. 10}$$

where  $k_0$  ( $7.0 \pm 0.4 \text{ m}^2 \text{ g}^{-1}$ ) is a constant derived from the soot mass specific absorption spectrum and AAE ( $1.2 \pm 0.4$ ) is the Absorption Angstrom Exponent that allows characterizing how the aerosol absorption varies with respect to the wavelength<sup>129</sup>.  $\alpha_{\text{MAC}}$  was found to be  $3.55 \pm 1.17 \text{ m}^2 \text{ g}^{-1}$ , corresponding to a minimum measurable absorption coefficient of  $2.94 \pm 0.97 \text{ Mm}^{-1}$ . The difference between our experimental value of  $6.3 \pm 0.44 \text{ m}^2 \text{ g}^{-1}$  and the theoretical values calculated above may be due to the use of  $k_0$  and AAE parameters (derived at RH = 1%) that are not suitable for the RH conditions of our experiments (21%). Indeed, it was shown that both  $k_0$  and AAE can be humidity dependent<sup>129</sup>.

### 3.4. Conclusions

A photoacoustic spectrophone operating at 880 nm was characterized and optimized for the measurement of black carbon in the atmosphere. The calibration of this instrument was performed by analyzing BC emitted from incense smoke using an aethalometer as a reference instrument. The sensitivity factor derived from these calibration experiments is  $0.22 \mu\text{V}/(\mu\text{g m}^{-3})$ . Taking into account the measurement noise, which was minimized



through the optimization of the sampling flow rate and a reduction of RH in the sample, a 3- $\sigma$  LoD (SNR = 3) of approximately  $2.5 \mu\text{g m}^{-3}$  at a time resolution of 1 s was obtained. This LoD can be improved to  $0.3 \mu\text{g m}^{-3}$  using a longer integration time of 1 min.

Further improvements in the sensitivity of the current PAS instrument can be achieved by increasing the number of microphones in the PA cell and using higher laser power. The RH effects can also be further reduced using a longer and more efficient Nafion dryer.

It is worth noting that the present instrument is the first PA spectrophone developed for the measurement of BC at 880 nm, after the one used by Hamasha et al. (<sup>130</sup>) in 2007 that operates at 870 nm and a time resolution of 2 min (LoD not reported).

Photoacoustic instruments exhibit the advantage of low uncertainties (< 10%) <sup>131</sup>, compared to filter-based techniques routinely used for aerosol measurements, where uncertainties can exceed 25% <sup>132</sup>, due to sampling artifacts. In addition, a faster time resolution of 1 s is achieved with this technology compared to aethalometers that usually operate at 10 s.

The characterization, calibration and measurement phases performed with the BC-PAS instrument have been useful in the development of the new NO<sub>2</sub>-PAS. This relied at first on the selection of pieces of equipment needed to build the new PAS instrument. For instance, it has been noticed that a higher laser power is useful to get a better sensitivity and lower LoD. In this regard, a high-powered diode laser (3.5 W) was purchased for the NO<sub>2</sub>-PAS instrument. The number of electret microphones was also increased (8 instead of 4) and the PA sampling cell was designed to incorporate these additional microphones.

The simplicity, the portability and the cost-effectiveness of the setup was also taken into consideration, mainly by simplifying the PAS setup. For example, the collimation of the laser beam on the BC-PAS was initially performed using a microscope and a lens. It is now replaced by the use of a collimator connected directly to a fiber-coupled laser. As for the modulation (see section 3.3.3), it was operated by a chopper, which might lead to additional noise in the measurements due to vibrations. Instead, it was chosen to perform it by modulating the laser current on the NO<sub>2</sub>-PAS, which allows a reduction of the acoustic noise, and therefore an enhancement of the SNR. All of these modifications are expected to result in a more compact PAS setup, more stable, more sensitive and more suitable for field deployment.

The optimization of the BC-PAS was also useful for designing characterization and calibration methods for the new NO<sub>2</sub>-PAS instrument.

## 4. Development of a 2-channel PAS for measuring NO<sub>2</sub>

This section presents the work made on the development and characterization of the 2-channel PAS for NO<sub>2</sub> measurements. This PAS was developed to be coupled to a chemical amplifier (CA) instrument, where the two channels would be used to perform simultaneous measurements of NO<sub>2</sub> at the outlet of the background and amplification reactors (chapter 1, section 2.1.1). This setup was planned to replace two Aerodyne (CAPS) analyzers previously used on the CA<sup>48</sup>. The construction cost of the PAS is estimated at 13 k€, i.e. 5 times lower than the cost of the 2 AERODYNE analyzers, which will therefore significantly reduce the price of a CA. The performance criteria necessary for utilizing the PAS instrument on the CA are detailed in Table 1. 3.

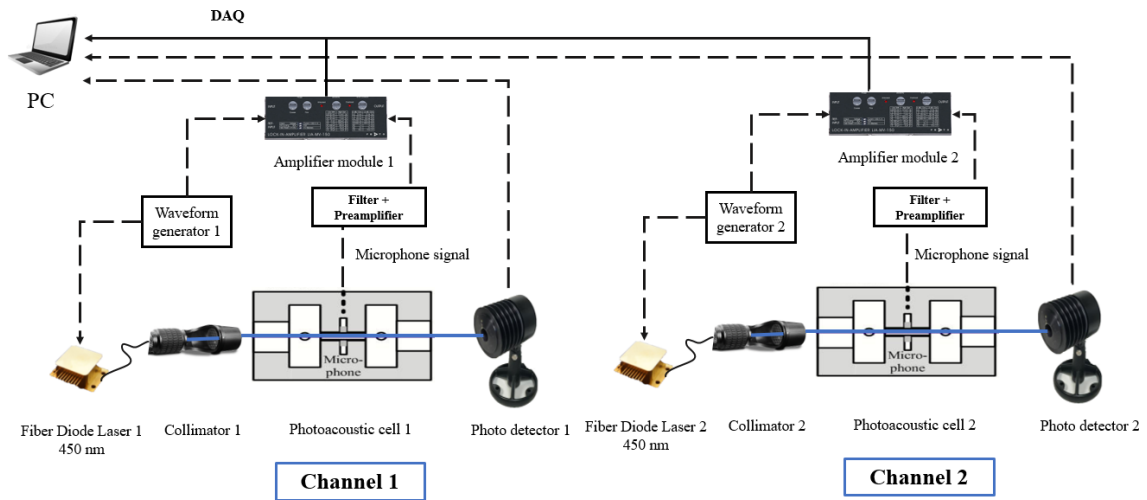
**Table 1. 3:** Required performance of the PAS instrument

<i>Time resolution</i>	< 5 s
<i>Min concentration range</i>	LoD-200 ppb
<i>Limit of detection (3-σ)</i>	< 100 ppt at 1 s
<i>Sensitivity</i>	- Not sensitive to humidity and temperature - Not sensitive to NO, CO and ethane (CA reagent gases)
<i>Sampling flow rate</i>	< 800 SCCM
<i>Drift in sensitivity</i>	< 5% over 1 month
<i>Baseline drift</i>	< 0.5 ppb over 1 day

The present work highlighted that the PAS performances are not good enough yet to couple it to the CA. Instead, we took advantage of the two-channel setup to propose an innovative approach for ambient NO<sub>2</sub> quantification. This approach lies on simultaneous measurements of the background and sample signals, which allows a better reduction of potential water-vapor effects, which represents one of the main issues in the PA system.

## 4.1. Experimental setup

A schematic presentation of the NO<sub>2</sub>-PAS is shown in Figure 2.14. The operating principle is similar to that of the PA spectrophone presented in the previous section and consists mainly in two diode laser modules, two PA resonators and a data processing module.



**Figure 2.14:** Schematic representation of the PAS for NO<sub>2</sub> measurements

The light sources are blue fiber-coupled diode lasers (WaveSpectrum, WS-9214266) emitting at approximately 450 nm with a max output optical power of 3.5 W when powered with a current of 3 A and a voltage of 4.3 V using laser diode drivers (Wavelength Electronics, PLD1 0K-CH). This laser source is almost 3 times more powerful than the laser used for the BC-PAS. In contrast to the latter, where the laser light was modulated using a chopper, the light here is modulated at the acoustic resonance frequency in the resonator based on an electrical modulation method (modulation of the laser current) using waveform generators (Multicomp, MP750510).

For each photoacoustic cell, the laser beam is collimated by a fiber collimator (Wave Spectrum, HPUCO-25-450-M-5BQ-HP) that contains an  $f = 5$  mm bi-convex lens. As mentioned previously, this collimator allows for a reduction of the number of optical devices. The laser beam is then directed into the PA cell whose geometry is similar to the one used for the BC-PAS. As mentioned above, it includes a cylindrical acoustic resonator, 2 buffer volumes but 8 electret microphones (FG-23329-P07, Knowles) instead of 4.

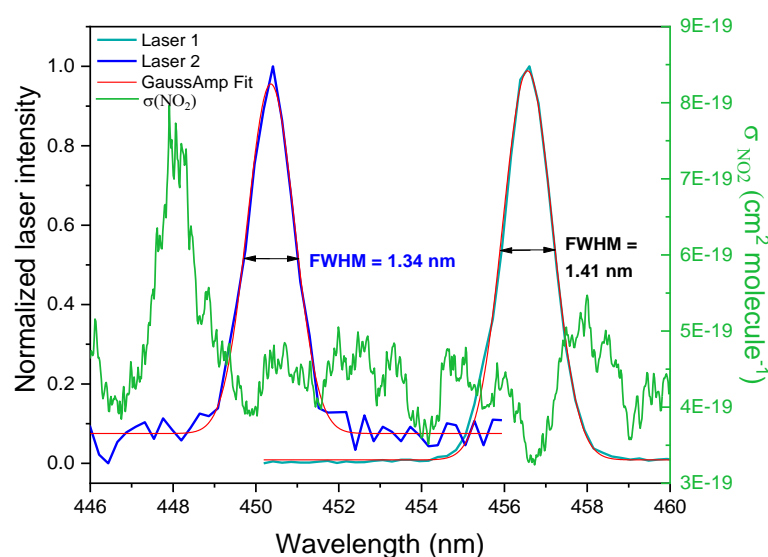
The PA signal is first processed by a band-pass filter (5.5-7.1 kHz), then amplified using a home-made pre-amplifier with a gain of 10. A lock-in amplifier (LIA-MV-150, Femto) is used for the demodulation of the PA signal at the laser light modulation frequency. The PA signal is then sampled using a National Instrument data acquisition card (USB-6003) that is connected to a laptop for data processing and results display via a Labview program.

## 4.2. Characterization and optimization of operating conditions

### 4.2.1. Emission spectra of the lasers

As mentioned above, the lasers are blue fiber-coupled diode lasers emitting at 450 nm as specified by the manufacturer. To check their emission profile, a spectrometer (Thorlabs, CCS200/M) with an accuracy of 2 nm was used to measure the emission spectra.

The obtained emission spectra and the absorption cross sections of NO<sub>2</sub> ( $\sigma_{\text{NO}_2}$ ,<sup>133</sup>) are overlaid in Figure 2.15. According to this figure, the spectra from the two lasers indicate emission peaks at 456.6 nm (referred to as laser 1 in the following) and 450.4 nm (referred to as laser 2), with Full Width at Half Maximum (FWHM) of 1.4 nm and 1.3 nm, respectively. These two wavelengths correspond to NO<sub>2</sub> absorption cross sections of  $3.73 \times 10^{-19} \text{ cm}^2 \text{ molecule}^{-1}$  and  $4.37 \times 10^{-19} \text{ cm}^2 \text{ molecule}^{-1}$ , respectively. These values were derived by averaging  $\sigma_{\text{NO}_2}$  over the FWHM of each laser emission line. The highest  $\sigma_{\text{NO}_2}$  value at 450.4 nm implies that the sensitivity of channel 2 (equipped with laser 2) will be higher by a factor of 1.38 compared to channel 1 (equipped with laser 1).

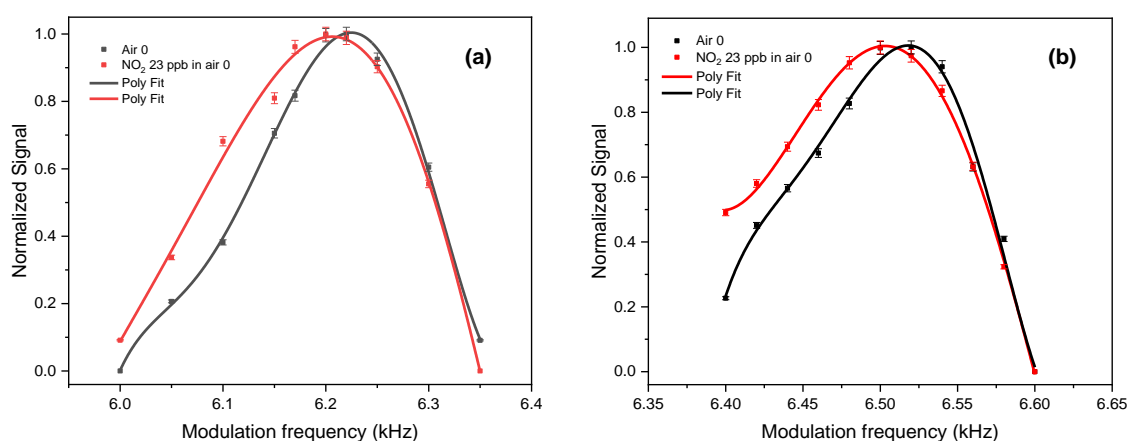


**Figure 2.15:** Emission spectra of the two diode lasers and NO<sub>2</sub> absorption cross sections between 446 and 460 nm

## 4.2.2. Modulation frequency

Similar to the BC-PAS, the modulation frequency of each laser beam was adjusted to the resonance frequency of the PA cells.

As this parameter depends on the medium composition, an experiment was carried out to investigate how the PA signal varies with the modulation frequency, using zero air and an air mixture containing 23 ppb of  $\text{NO}_2$  ( $\text{RH} = 13.5 \pm 0.5\%$ ,  $T = 20.5 \pm 0.1 \text{ }^\circ\text{C}$ ), the main goal being to determine the optimal resonance frequencies of the two channels. Figure 2.16 shows the variation of the normalized PA signal in an interval of modulation frequencies ranging from 6.0 to 6.35 kHz for channel 1 and from 6.4 to 6.6 kHz for channel 2.



**Figure 2.16:** Dependence of the PA signal on the modulation frequency for channels 1 (a) and 2 (b). Error bars correspond to the Standard Deviation of the mean signal (1s measurement averaged over 60 s)

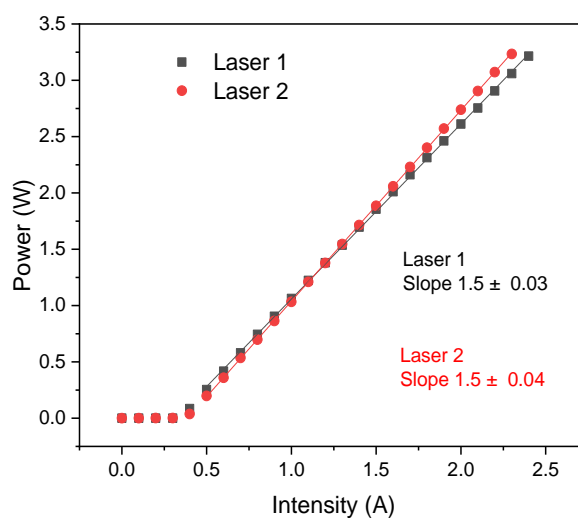
It was found that the two channels behave similarly, the black and red curves exhibiting the same shape, with a slight difference in frequency for the peak maximum. For channel 1, the optimal modulation frequencies are 6.22 and 6.20 kHz for zero air and the  $\text{NO}_2$  mixture, respectively. For channel 2, optimal modulation frequencies for zero air and the  $\text{NO}_2$  mixture are respectively 6.52 and 6.50 kHz. The operating modulation frequency was selected to be 6.22 kHz for channel 1 and 6.50 kHz for channel 2. The shift in Frequency observed between the two matrices (air zero and  $\text{NO}_2$  mixture) is likely due to a variation of pressure in the PA cell between the two experiments. On the basis of equations Eq 2. 2 and Eq 2. 6, a difference of about 20 Hz can be explained by a change in pressure of about 5 Torr (considering an initial atmospheric pressure of 760 Torr). If this type of pressure variation was occurring when the PAS is used for  $\text{NO}_2$  measurements (fixed modulation frequency), this would result in a reduction of the PA signal by 3.2%. Given that

atmospheric pressure can vary by  $\pm 25$  Torr at sea level, the cell pressure need to be precisely regulated to ensure no drift in sensitivity.

The theoretical value of the resonance frequency was found to be 6.05 kHz in air, calculated using equation (2.2) for a cylinder length of 23 mm and a radius R of 3 mm and a sound speed of  $340 \text{ m s}^{-1}$ . The difference between the two experimental values and the theoretical one is likely due to uncertainty in measuring the resonator dimensions. Indeed, assuming that this difference is due to uncertainties in the resonator's lengths, we calculated the lengths that would be needed to lead to the experimental values of the resonance frequency. It was found that the length of the resonator would have to be 21.06 mm instead of 23 mm for channel 1 (corresponding to an uncertainty of 8%), and 22.2 mm for channel 2 (corresponding to an uncertainty of 4%).

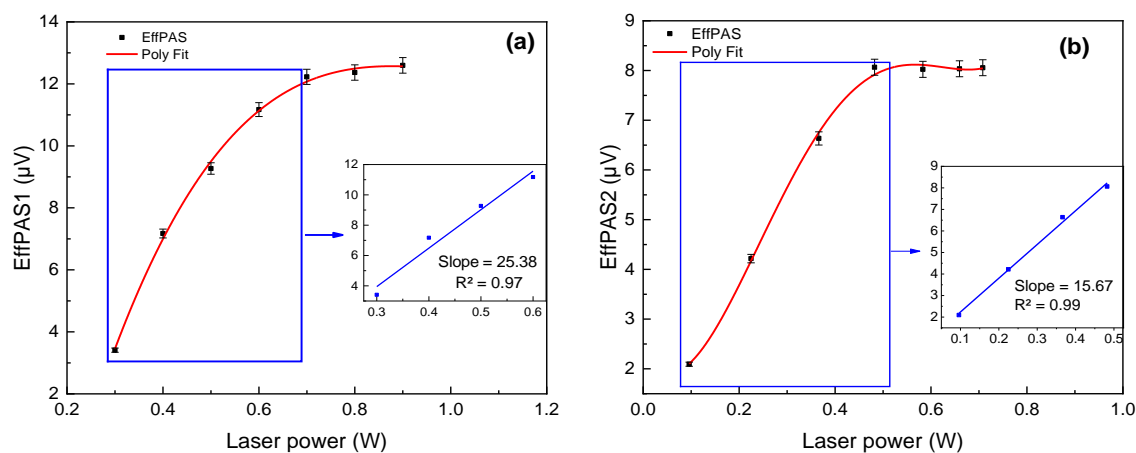
### 4.2.3. Laser power

As indicated previously, the PA signal is proportional to the laser power, which implies that an increase in the laser power would improve the instrument sensitivity. To check this property, an experiment was performed to monitor the variation of the PA signal generated by the absorption of a constant concentration of  $\text{NO}_2$  at different laser powers. The modulation frequencies of the two channels were set at the optimized values deduced in the previous section, and the gas flow rate at  $0.2 \text{ L min}^{-1}$ . The laser power was adjusted by controlling the current intensity, owing to the proportionality of these two parameters, as shown in Figure 2.17.



**Figure 2.17:** Dependence of the laser power (Laser 1: black squares, Laser 2: red circles) on the current intensity

The effective PA signal (EffPAS = PAS(bkg+NO<sub>2</sub>)-PAS(bkg), bkg: zero air) of channel 1 generated by the absorption of 125 ppb of NO<sub>2</sub> at RH = 8% and T = 22.7°C, and the one of channel 2 generated by the absorption of 80 ppb of NO<sub>2</sub> at RH = 7.4% and T = 22.5°C, are presented respectively in panel (a) and panel (b) of Figure 2.18, as a function of the modulated laser power measured in the output of the PA cell.



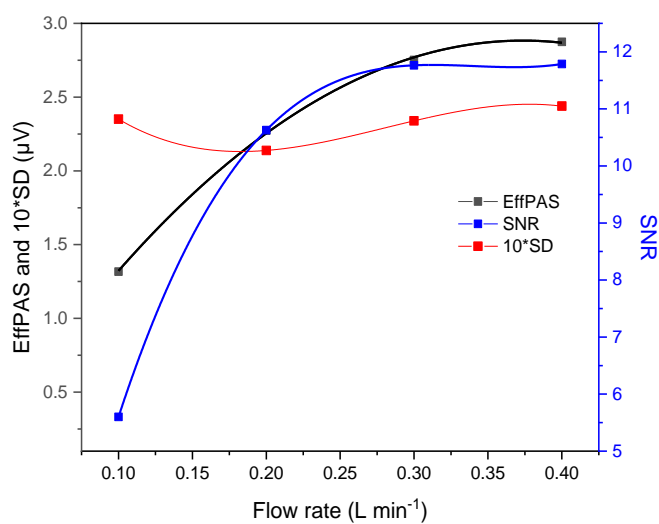
**Figure 2.18:** Dependence of the effective PA signal on laser power for channels 1 (a) and 2 (b) at constant NO<sub>2</sub> concentrations in zero air. Error bars correspond to the Standard Deviation of the mean signal (1s measurement averaged over 240 s)

We notice that between 0.3 and 0.7 W (channel 1) and 0.1 and 0.5 W (channel 2), the PA signal is increasing almost linearly with the laser power, with a slope of 25.4 µV W<sup>-1</sup> (channel 1) and 15.7 µV W<sup>-1</sup> (channel 2). Beyond 0.7 W (channel 1) / 0.5 W (channel 2), a saturation regime is reached, which suggests that no more molecules can be excited with increasing laser power and a depletion of the probed vibrational level<sup>55</sup>. The observation that a saturation regime is reached at lower laser power for channel 2 is consistent with a laser diode wavelength associated to a higher averaged  $\sigma_{\text{NO}_2}$  (section 4.2.1). The PAS signal will not benefit from a higher laser power. In the other hand, working in the region of saturation would be useful to avoid fluctuations in the PA signal due to variations in the laser power. The operating laser power was therefore set at 0.8 W for channel 1 and 0.7 W for channel 2.

#### 4.2.4. Sampling flow rate

Dependences of the EffPAS, the SD and SNR on the sampling flow rate were examined within the range of 0.1 L min<sup>-1</sup> to 0.4 L min<sup>-1</sup> with a mixture of 30 ppb NO<sub>2</sub> in zero air (RH = 15 ± 1.5 %, T = 23.4 ± 0.3 °C) as shown in Figure 2.19.

Until  $0.3 \text{ L min}^{-1}$ , EffPAS and SNR were found to increase with the sampling flow rate, whereas the noise was almost constant. Indeed, an increase in the sampling flow rate helps to refresh the PA cell faster with unexcited molecules<sup>55</sup>. As a result, the percentage of  $\text{NO}_2$  molecules in the upper state of energy relative to the ground state decreases, which in turn reduces the saturation effect and improves the net signal amplitude<sup>55</sup>. Above  $0.3 \text{ L min}^{-1}$ , SD increases together with the effective PA signal, leading to a SNR that levels off. A gas flow rate of  $0.4 \text{ L min}^{-1}$  was selected as operating parameter for the two channels.



**Figure 2.19:** Dependences of the net PA signal (EffPAS), PA noise (SD) and signal-to-noise ratio (SNR) on the sampling flow rate

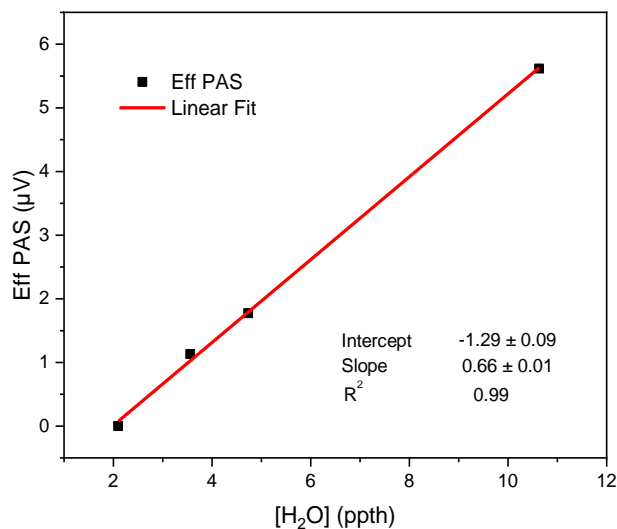
#### 4.2.5. Management of sample humidity

As mentioned previously for BC-PAS, and as observed in Figure 2.20, water-vapor impacts the PA signal both by enhancing the vibrational-to-translation (V-T) relaxation rate of the targeted absorber, and by absorbing the laser light. According to the HITRAN database<sup>133</sup>, the absorption cross section of water-vapor at 450 nm is approximately  $10^{-27} \text{ cm}^2 \text{ molecule}^{-1}$ .

Since the mixing ratio of water-vapor in ambient air can reach up to 3% and is varying over time, investigating the PAS response to water-vapor is required. In this regard, an experiment was carried out to monitor how the PA signal varies with water-vapor in zero air. The latter was controlled using a dilution system, allowing to generate water mixing ratios between 0.2 and 1.2%. Water-vapor mixing ratios were measured using a LI-840A  $\text{CO}_2/\text{H}_2\text{O}$  gas analyzer (LICOR).



As awaited, the PA signal was found to increase with water-vapor with a sensitivity of  $0.66 \mu\text{V ppth}^{-1}$  (ppth: part per thousand) as shown in Figure 2.20, which is equivalent to 7.3 ppb of  $\text{NO}_2$  per ppth of water. An ambient water mixing ratio of 1 - 2%, which is common in the atmosphere, would lead to the generation of a signal that would be equivalent to 73 - 147 ppb of  $\text{NO}_2$ . It is clear that the effect of water-vapor on the PAS response is huge and a strategy to reduce this measurement artifact is needed.



**Figure 2.20:** Dependence of the Eff PAS signal on  $\text{H}_2\text{O}$  concentration for channel 1

Among the potential strategies is the use of a Nafion dryer as done for the BC-PAS, which allows a significant reduction of water-vapor. While this strategy worked well for the BC-PAS and will likely work well for ambient measurements of  $\text{NO}_2$  using the PAS instrument described in this chapter, it will be less efficient for  $\text{NO}_2$  measurements from the chemical amplifier. Indeed, peroxy radical measurements with the chemical amplifier requires quantifying small differences in  $\text{NO}_2$  ranging from 20-5000 ppt between 2 measurement channels (see section 2.2 chapter 3). This strategy was not tested here due to a lack of time and the initial objective to couple the  $\text{NO}_2$ -PAS instrument to a PERCA was given up.

Instead, we tested another strategy for measuring  $\text{NO}_2$  in ambient air taking advantage of the 2-channel PAS configuration. This approach is based on performing simultaneous measurements of ambient  $\text{NO}_2$  (+ interfering water) and only interfering water. The  $\text{NO}_2$  component of the PAS signal could then be inferred by subtraction (this method will be presented more in details in the section 4.4).

### 4.3. Calibration and figures of merit

To characterize the PAS instrument, side-by-side measurements of  $\text{NO}_2$  were performed at different concentrations with a reference  $\text{NO}_2$  analyzer (CAPS monitor from Aerodyne, calibrated using a certified  $\text{NO}_2$  mixture at  $200 \pm 1(2\sigma)$  ppb from Air Liquid). A commercial mixture of  $\text{NO}_2$  (50 ppm, Messer) was diluted with humid zero air to obtain different  $\text{NO}_2$  concentrations ranging from 10-80 ppb as shown in the schematic of Figure 2.21. First, a constant flow of dry zero air was added to the system using a Mass Flow Controller (MFC) of  $50 \text{ L min}^{-1}$ . Part of it went directly to the air mixing chamber, and another part went to a bubbler containing water (flow rate regulated using different restrictors). The latter allowed saturating zero air with water-vapor, which was then sent to the air mixing chamber. The quantity of water-vapor generated was controlled by varying the quantity of zero air entering the water bubbler. The humid air mixture was then mixed with a constant flow of  $\text{NO}_2$  (50 ppm in  $\text{N}_2$ , transferred in a stainless-steel canister) ranging from 1-10  $\text{L min}^{-1}$ . The  $\text{NO}_2$ /water/air mixture is provided to the PAS and CAPS instruments, the excess going to a vent. In the experiment presented below, the concentrations of  $\text{NO}_2$  were generated at an RH of 12.5% ( $T = 26^\circ\text{C}$ ), i.e. 2.25 ppth of  $\text{H}_2\text{O}$  (measured using a LICOR monitor).

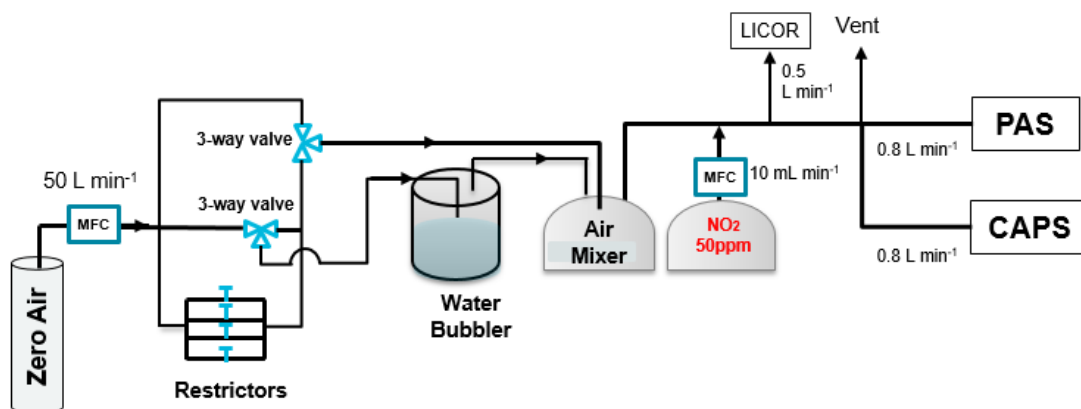
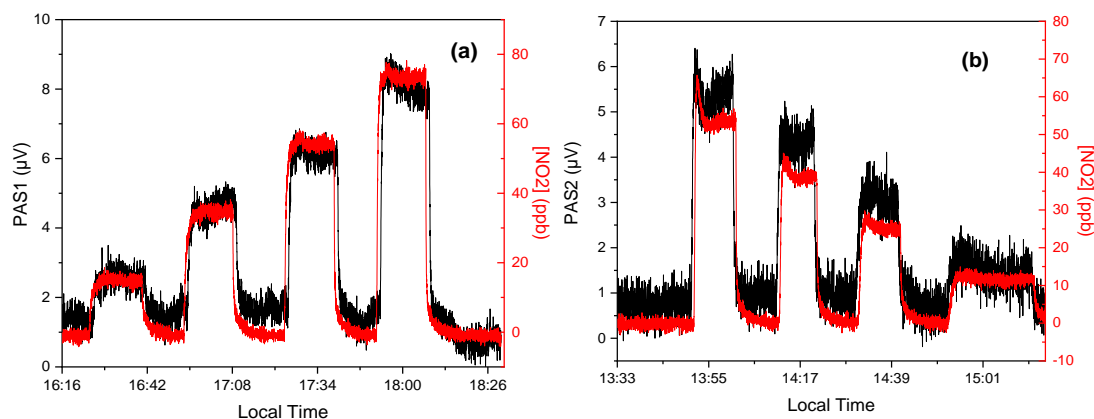


Figure 2.21: Setup for the generation of  $\text{NO}_2$ /water/air mixtures

The modulation frequencies were set at 6.22 kHz (channel 1) and 6.50 kHz (channel 2), the modulated laser power at the output of the PA cell was set to 0.8 W (channel 1) and 0.7 W (channel 2) and the gas flow rate at  $0.4 \text{ L min}^{-1}$ .

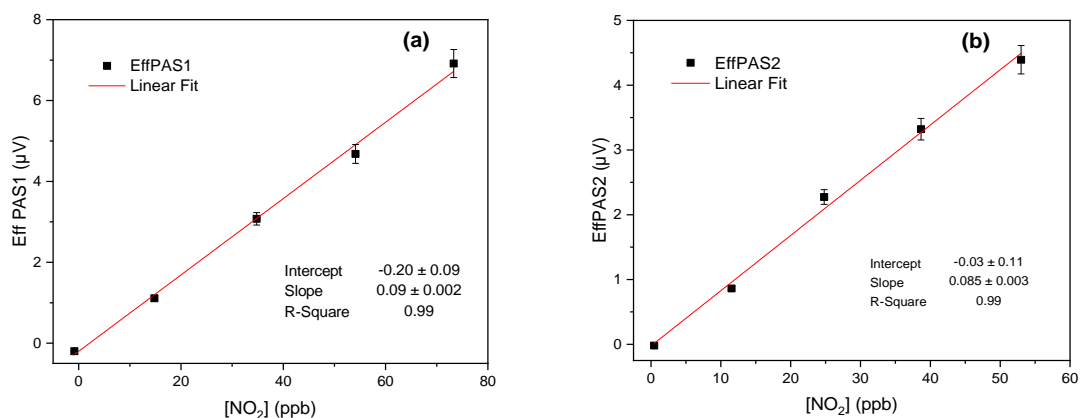
Time series of  $\text{NO}_2$  measurements performed by the PAS at a time resolution of 1 s are shown in Figure 2.22. The PA signal observed for zero air is generated by photons being absorbed on the walls or on the windows of the PA cell, and by the absorption of water-

vapor. This signal is considered as a background and was subtracted from the signal generated when  $\text{NO}_2$  is added in the mixture. The red plots in Figure 2.22 represent  $\text{NO}_2$  concentrations measured by the CAPS monitor. For this experiment, it was preferred to measure  $\text{NO}_2$  using a reference instrument instead of calculating its concentration from the performed dilution to avoid errors associated to its loss when transferred into the canister.



**Figure 2.22:** Calibration - Time series of  $\text{NO}_2$  measurements by PAS for channels 1 (a) and 2 (b) (black plot) and by CAPS (red plot)

Figure 2.23 displays scatter plots of the measured effective PAS signal vs.  $\text{NO}_2$  concentrations measured by CAPS. The correlation between these two signals was found to be linear up to 74 ppb for channel 1 (panel (a) Figure 2.23) and 53 ppb for channel 2 (panel (b) Figure 2.23), with a determination coefficient of 0.99. The y-intercepts are not significant at  $2\sigma$ . These experiments indicate a sensitivity of approximately  $0.09 \mu\text{V ppb}^{-1}$  for each channel.



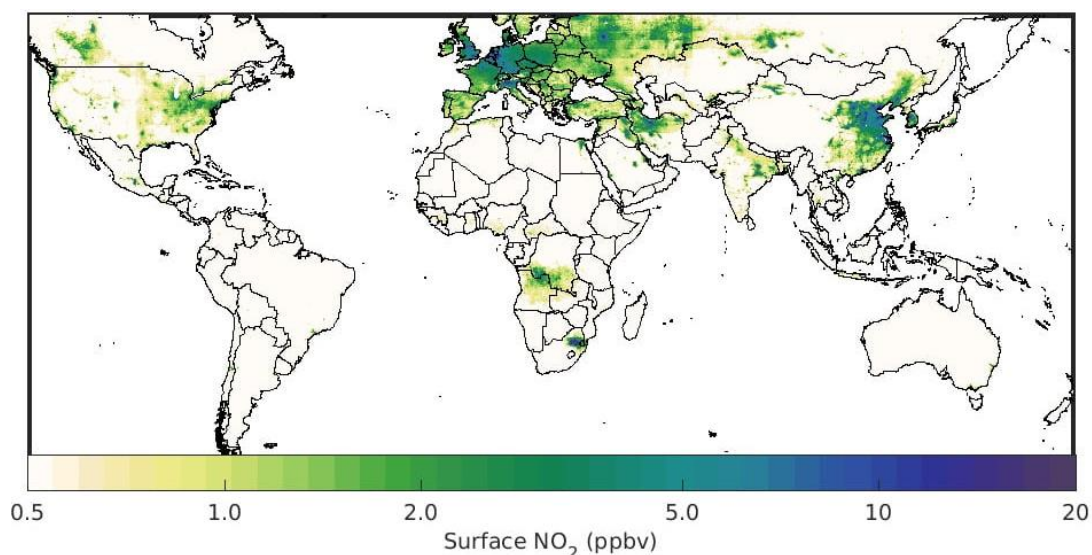
**Figure 2.23:** Calibration - Effective PAS signal versus  $\text{NO}_2$  for channels 1 (a) and 2 (b)

Limits of detection were calculated using Eq 2.7. The  $3\text{-}\sigma$  LoD for channel 1 was evaluated to be 6.9 ppb at the time resolution of 1 s from the measurement noise

(SD = 0.22  $\mu\text{V}$ ) and the sensitivity shown in panel (a) of Figure 2.23 ( $S_{\text{slope}} = 0.094 \mu\text{V ppb}^{-1}$ ). As for channel 2, the sensitivity was found to be  $0.085 \mu\text{V ppb}^{-1}$ , with a measurement noise SD of  $0.25 \mu\text{V}$ , corresponding to a  $3\text{-}\sigma$  LoD of 8.7 ppb (panel (b) of Figure 2.23).

Assuming that white noise is the main source of noise in the measurements, this LoD can be further reduced to 0.9 – 1.1 ppb using a longer integration time of 1 min. Additional improvement of the LoD is possible, by employing acoustic isolations in order to avoid external acoustic noise, or by improved filtering of the PA signal using low-noise lock-in and pre-amplifiers. The use of a Nafion dryer and an optimized lens system (for better collimation of the laser beam) would also allow reducing the background signal, hence improving the SNR. It is also possible to enhance the sensitivity by a factor of about 1.7 using a laser operating at 448.1 nm, where  $\sigma_{\text{NO}_2}$  is higher (Figure 2.15).

With such a limit of detection, this instrument can be employed for the detection of  $\text{NO}_2$  in the troposphere at a 1-min time resolution, especially in urbanized areas with moderate and strong  $\text{NO}_2$  conditions where  $\text{NO}_2$  can reach annual concentrations up to 20 ppb (blue zones in Figure 2.24). However, improvements of the LoD will be necessary to deploy this instrument in regions exhibiting cleaner air masses, where observed  $\text{NO}_2$  concentrations are less than 5 ppb (green and yellow zones in Figure 2.24).



**Figure 2.24:** Annual ground-level  $\text{NO}_2$  concentrations in the world for 2019 from the combination of TROPOMI satellite observations and the GEOS-Chem chemical transport model information and ground-based monitoring (estimations provided at  $\sim 1$  km resolution) <sup>134</sup>.

#### 4.4. Intercomparison of PAS and CAPS measurements in ambient air

To validate the performance of the 2-channel NO<sub>2</sub>-PAS, continuous measurements of ambient air were carried out in parallel to a reference instrument (CAPS, Aerodyne) at IMT Nord Europe (Bourseul site, Douai, France) from 20 to 24 June 2022. Part of these measurements were performed indoor (4 nights and 1 day), and the rest outdoor (2 days). For both types of measurements, the PAS instrument was housed indoor using a short Teflon tube of 0.5 m (1/4" OD) as inlet for indoor measurements and a 12.2 m long Teflon tube (1/4" OD) for exterior ambient air measurements.

Figure 2.25 shows a schematic of the PAS setup, where a strategy was implemented to account for the time-varying impact of water-vapor on the PA signal. This strategy is based on simultaneous measurements of ambient NO<sub>2</sub> + interfering water-vapor and only interfering water-vapor using the 2 channels. Ambient air is filtered with a 0.2 µm PTFE filter (Sartorius Stedium, Midisart 2000, porosity = 0.2 µm) to remove particles at a total flow rate of 1.6 L min<sup>-1</sup>, 0.8 L min<sup>-1</sup> of it being sampled by the CAPS, and the other 0.8 L min<sup>-1</sup> being sampled by the 2 PAS channels. One channel was operated in "ambient mode", i.e. measuring NO<sub>2</sub> + interfering water-vapor, and the other channel operated in "background (bkg) mode", where the sample goes through a NO<sub>2</sub> scrubber (Teledyne, PN 14697), which allows measuring only interfering water-vapor. The measurement modes were switched between the 2 channels every 10 min. This method allows tracking variations in the background signal due to water-vapor and the removal of its impact on the PA signal.

A pressure sensor (MKS, 722C13TCD2FA) was connected at the outlet of the setup to measure the sample pressure in the 2 channels when they were operating in ambient mode. Two temperature and humidity sensors (Sensirion SHT10) were also connected at the outlet of each channel to monitor water-vapor.

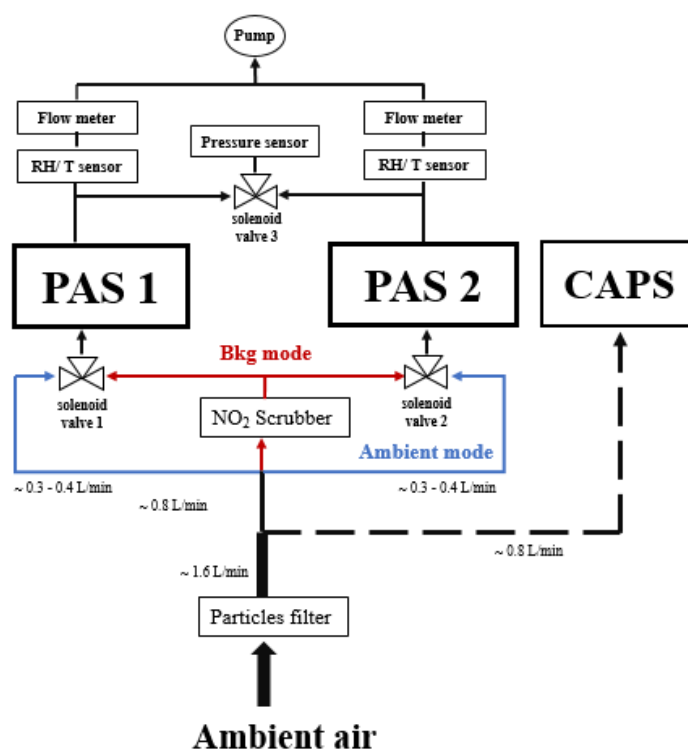
The effective PA signal generated by the absorption of NO<sub>2</sub> can be deduced using the following equation for each channel:

$$\text{EffPAS}(\text{NO}_2) = \text{PAS}(\text{bkg} + \text{NO}_2)_t - \left( \frac{\text{PAS}(\text{bkg})_{t-1} + \text{PAS}(\text{bkg})_{t+1}}{2} \right) \quad \text{Eq 2. 11}$$

Where t is a 10-min measurement step when the channel is operating in ambient mode, t -1 and t+1 are 10-min measurement steps when the channel is in background mode just before and after the ambient mode step, respectively.

The first 2 minutes of the PAS signal recorded during the ambient mode were removed to avoid the impact of electrical noise generated by the switching of the solenoid valves (valves 1 and 2 in Figure 2.25). For the background mode, only the last 2 minutes of the recorded PAS signal were used for the calculation of PAS (bkg). This was necessary to avoid a memory effect due to the desorption of NO<sub>2</sub> from the wall of the PA cell.

The calculated effective PAS signal generated by NO<sub>2</sub>, i.e. EffPAS(NO<sub>2</sub>), is then converted into a concentration using sensitivity factors deduced from the calibrations presented in section 4.3.

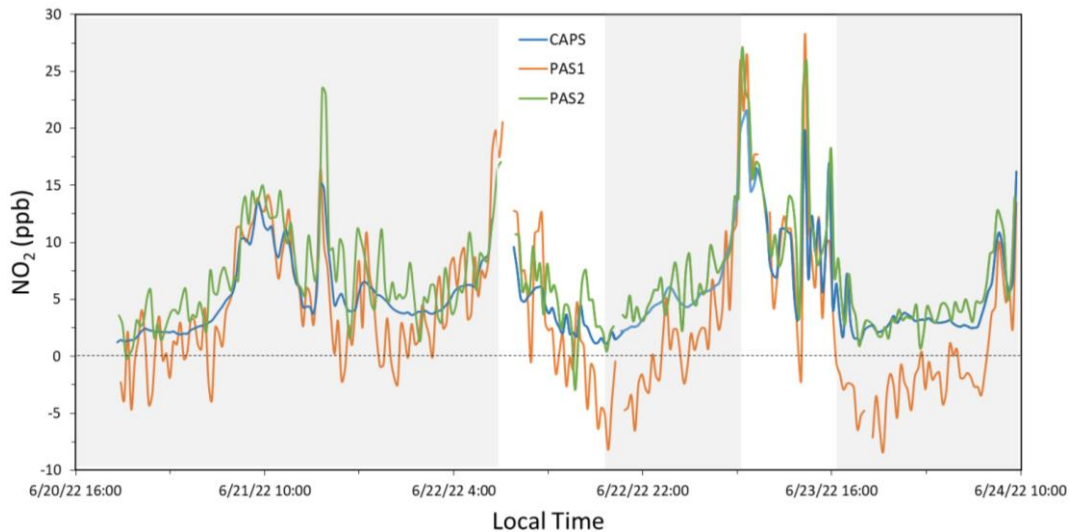


**Figure 2.25:** Schematic presentation of the NO<sub>2</sub>-PAS & CAPS setup for sequential measurements in ambient and background modes.

During this intercomparison exercise, the laser power of each diode was set at the optimum value determined in section 4.2.3, i.e. 0.8 and 0.7 W for channels 1 and 2, respectively. For channel 2, the laser power was continuously measured using the power meter, while for channel 1, it was checked daily. Continuous measurements of this parameter are not mandatory since the laser power is set at a value that is high enough to work in the saturation regime as discussed in section 4.2.3. In addition, the two lasers proved to be very stable over time (~ 0.06% variability during 2 hours of measurement).

Time-series of indoor and outdoor NO<sub>2</sub> measurements from 20 to 24 June 2022 using the 2 PAS channels, referred to as PAS1 and PAS2, and the CAPS analyzer are presented

in Figure 2.26. It is worth noting that the 2 channels of the PAS are complementary. When one channel measures the PAS signal from ambient air containing NO<sub>2</sub>, the second channel measures the background signal.



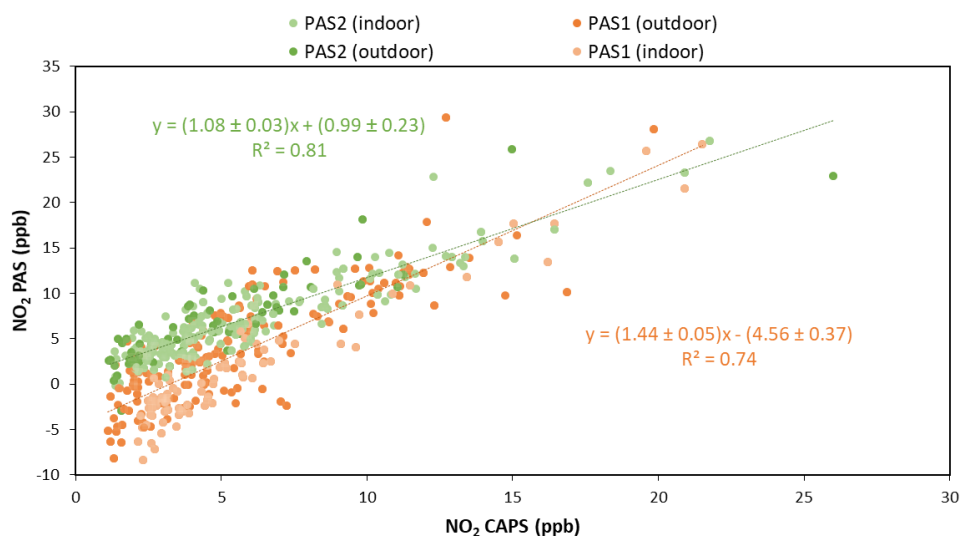
**Figure 2.26:** Time series of indoor (grey areas) and outdoor measurements of NO<sub>2</sub> using the two PAS channels (orange: channel 1, green: channel 2) and the CAPS monitor (blue). 1-s measurements have been averaged to 10 min.

On the basis of the CAPS data, an evident daily pattern can be observed in the variation of NO<sub>2</sub> concentrations, where it peaks in the mornings, reaching up to 23 ppb, and then decreases in the late afternoon and during the night to less than 1 ppb.

We notice that measurements from channel 2 (PAS2) are in good agreement with the CAPS measurements, with higher fluctuations due to the significant noise level in the PAS setup. In contrast, measurements from channel 1 (PAS1) exhibit a reasonable agreement with CAPS measurements only at the highest levels of NO<sub>2</sub>. Indeed, at low concentrations (e.g. afternoon and night of 22 June and 23 June), measurements from channel 1 are negative, which indicates an overestimation of the subtracted background signal.

The correlation between the measurements from channel 1 (PAS1) and CAPS seems to be linear as observed in Figure 2.27, with a linear fit of  $y = (1.44 \pm 0.05) x - (4.66 \pm 0.37)$  and a determination coefficient  $R^2 = 0.74$ . The negative intercept corresponds to the overestimation of the background signal mentioned above. Whereas for measurements from channel 2 (PAS2), the correlation with the CAPS measurements was found to be better, with a linear fit of  $y = (1.07 \pm 0.03) x + (0.99 \pm 0.22)$  and a determination coefficient  $R^2 = 0.81$ .

A close look at Figure 2.27 indicates that the agreement between the PAS and CAPS measurements does not change when sampling indoor and outdoor ambient air. Table 2.1 below summarizes the details of each time period, indicating the type of environment (indoor/ outdoor). As mentioned above, we notice that the different periods are consistent together, with the exception of 22 June (day) where a large slope of  $\sim 2.3$  is observed for the linear regression between PAS1 and CAPS. Average slopes for the linear regression between PAS and CAPS measurements are about 1.6 for channel 1 and 1.1 for channel 2.



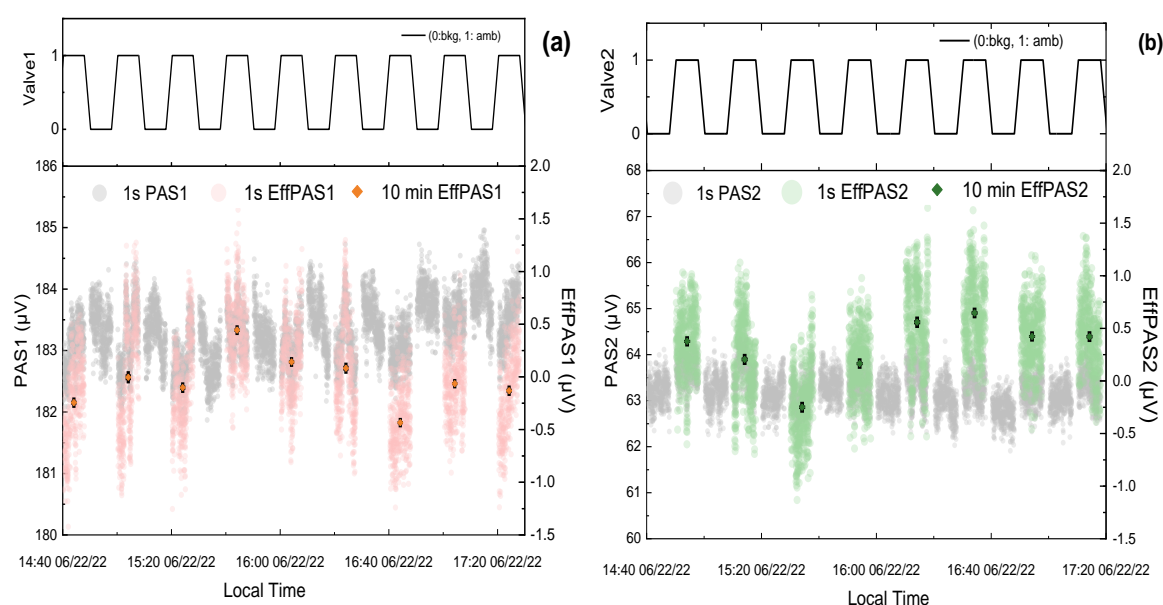
**Figure 2.27:** Correlation between  $\text{NO}_2$  concentrations measured by the two PAS channels (orange: channel 1, green: channel 2) and the CAPS instrument

**Table 2. 1:** Summary of ambient  $\text{NO}_2$  measurements by PAS and CAPS

<i>Date</i>	<i>20-22 June</i>	<i>22 June (day)</i>	<i>22-23 June (night)</i>	<i>23 June (day)</i>	<i>23-24 June (night)</i>
<b>Indoor/ Outdoor</b>	Indoor	Outdoor	Indoor	Outdoor	Indoor
<b>Average RH (%)</b>	45	47	66	66	60
<b>T (°C)</b>	25	26	26	26	26
<b>Average Absolute Humidity AH (<math>\text{g m}^{-3}</math>)</b>	9.4	12	13	15.4	13.5
<b>Pressure (Torr)</b>	751	746	748	745	744
<b>Average <math>\text{NO}_2</math> (ppb)</b>	30	10	23	28	16
<b>Slope PAS1 vs CAPS</b>	1.24	2.31	1.55	1.58	1.37
<b>Slope PAS2 vs CAPS</b>	1.06	1.19	1.09	0.99	1.15



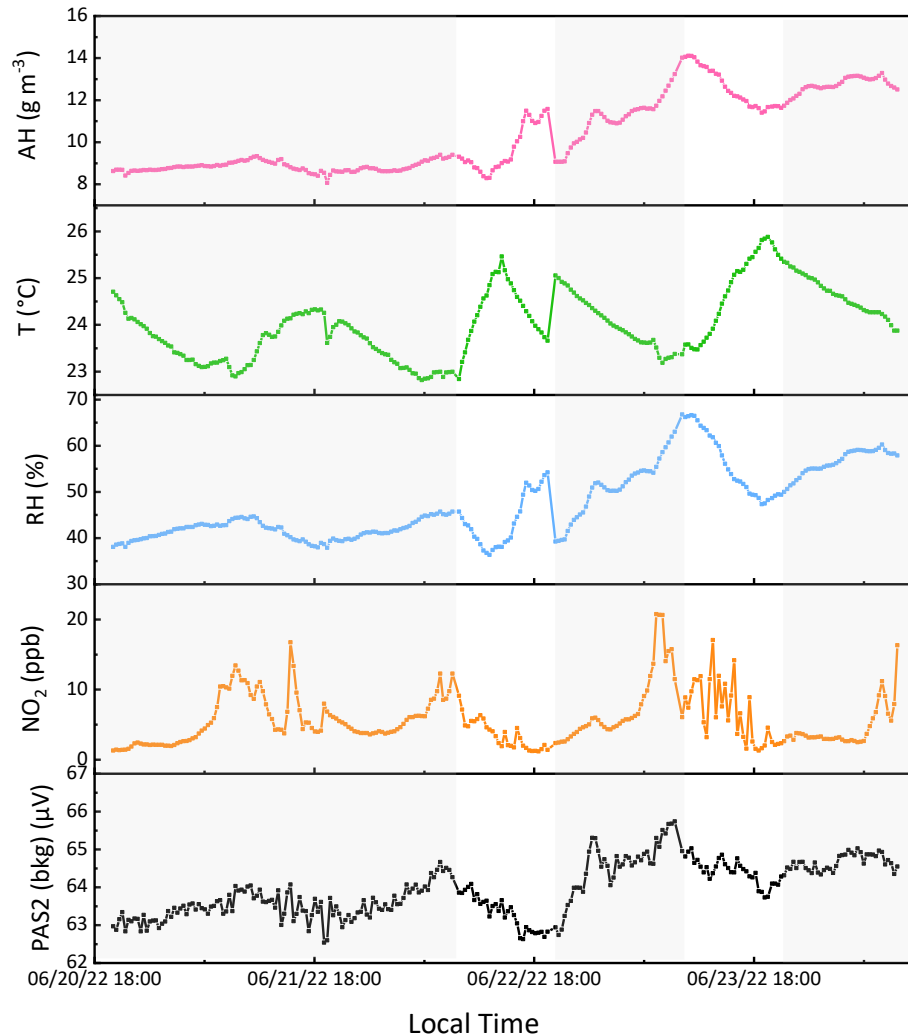
In order to investigate the negative signals observed during some time periods with channel 1 (PAS1), the raw PA signal monitored at a time resolution of 1 s during one of these time periods is shown in Figure 2.28 (a), as well as the corresponding effective signal (EffPAS1) at time resolutions of 1 s and 10 min. It is clear from this figure that during background mode (valve1 = 0), the signal is higher than in the ambient mode (valve1 = 1) most of the time. A systematic decreasing trend is usually observed on the background signal over the 10 min measurement duration, indicating that the background signal did not reach a stable level. In contrast, the background signal measured for PAS2 (Figure 2.28 (b)) mostly exhibited a stable behavior over the measurement duration. The behavior observed for PAS1 could be explained by a leak of indoor air into the PA cell of channel 1 or a memory effect, the latter being due to residual  $\text{NO}_2$  persisting in the cavity (desorption from the microphone, exchange of air with a dead volume where the microphones are located).



**Figure 2.28:** Time series of 1-s raw PA signals (grey symbols) for channels 1 (a) and 2 (b). Corresponding 1-s effective signal (EffPAS) shown in light orange for channel 1 and light green for channel 2. 10-min averaged effective signals shown in dark orange for channel 1 and dark green for channel 2.

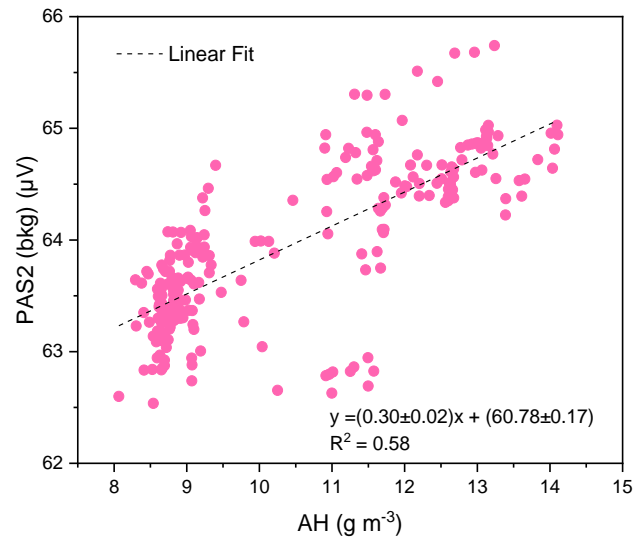
In order to better characterize the main parameters controlling the background signal on this PAS instrument, correlations of the background signal from channel 2 (channel 1 was not taken into account in the upcoming examinations given the memory effect/leak issue) with different atmospheric parameters such as temperature (T), relative humidity (RH), absolute humidity (AH) and  $\text{NO}_2$  concentration were investigated. This analysis is shown in Figure 2.29 and 2.30.

It was noted that the background signal, presented by the black curve, exhibits temporal fluctuations during the campaign, ranging between approximately 63  $\mu\text{V}$  and 66  $\mu\text{V}$ . These variations seem to correlate better with fluctuations observed in the AH signal.

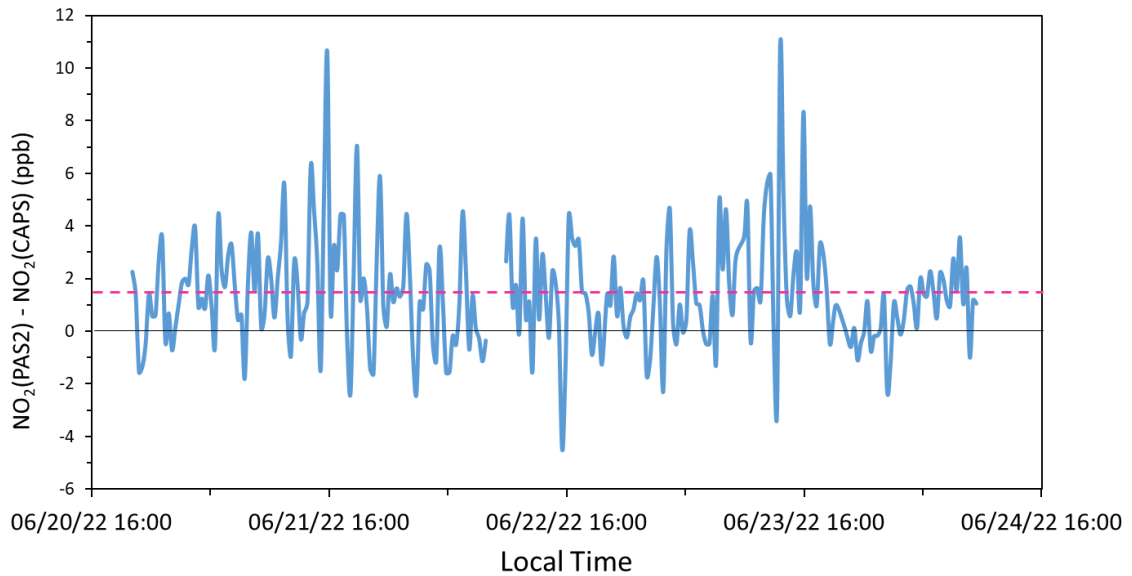


**Figure 2.29:** Time series of the background PA signal of channel 2 (black),  $\text{NO}_2$  concentrations (orange), relative humidity (RH, blue), temperature (T, green) and absolute humidity (AH, pink) measured at a time resolution of 1 s and averaged to 10 min.

Consistent with the expectations, the analysis revealed that the water-vapor predominantly contributed to the background signal. This was confirmed with the linear variation of the background signal with the AH as shown in Figure 2.30, with a determination coefficient of 0.58 (0.61 with RH). In contrast, the coefficients for the other parameters were comparatively lower: 0.004 for the temperature and 0.19 for  $\text{NO}_2$ .



**Figure 2.30:** Correlation of the background PA signal of channel 2 (PAS2 (bkg)) with absolute humidity (AH).



**Figure 2.31:** Time series of the residual NO<sub>2</sub> concentrations measured by channel 2 relative to the reference CAPS analyzer. Red dashed line: mean value of the time series

To ensure the effective removal of the background signal from ambient measurements, a time series of the difference between NO<sub>2</sub> concentrations measured by PAS (channel 2) and by CAPS is shown in Figure 2.31. This difference in concentrations was found to be relatively stable along the campaign, varying mainly between -3 and 7 ppb. Averaging this difference over the whole measurement period indicates a mean value of 1.4 ppb, showing the presence of an offset between the two instruments. This offset may be due to an underestimation of the PAS background or a zeroing issue on the CAPS monitor.

## 4.5. Conclusions

A 2-channel PAS was developed, characterized and calibrated for measuring NO<sub>2</sub>. Different parameters were optimized in order to reach the best sensitivity (optimization of the response) and the best limit of detection (reduction of the measurement noise). Among these parameters, the modulation frequency of the laser beam was found to be optimum at 6.22 kHz and 6.50 kHz for channels 1 and 2, respectively, while the optimum laser power was found to be 0.8 and 0.7 W for channels 1 and 2. The sampling flow rate leading to the highest signal-to-noise ratio was found to be 0.4 L min<sup>-1</sup> for the two channels.

Calibration experiments indicated a sensitivity of approximately 0.09 μV ppb<sup>-1</sup> for each channel, and a 3-σ LoD of 6.9 ppb and 8.7 ppb for channels 1 and 2, respectively, at a time resolution of 1 s. These detection limits can be improved to 0.9 and 1.1 ppb, respectively, by integrating the measurements over 1 min. The effect of water-vapor on the measurements was found to be important, with a sensitivity of about 0.65 μV ppth<sup>-1</sup>, which is equivalent to 6.5 ppb of NO<sub>2</sub> per ppth of H<sub>2</sub>O.

The work performed during this thesis mainly focused on assembling the device and assessing the performances. However, no tests were conducted to evaluate the stability of the sensitivity over a long time. Therefore, it will be necessary to conduct these tests during future characterization experiments to determine the frequency at which the instrument needs to be calibrated. Because of the high LoD and the important impact of water-vapor on the measurements, it has been concluded that the current version of the PAS instrument is not suitable for measuring NO<sub>2</sub> from the chemical amplifier and further improvements are needed on the PAS instrument. Therefore, the PAS instrument was not coupled to the chemical amplifier as initially planned in this Ph.D. The studies described in chapters 3 and 4 were conducted using a chemical amplifier coupled to two CAPS monitors.

Future improvements of the PAS instrument will focus on enhancing its limit of detection by reducing the noise level. This can be achieved through various means, including the implementation of acoustic isolations, the use of a Nafion dryer and an optimized lens system, and the incorporation of low-noise lock-in and pre-amplifiers. In addition, using diode lasers emitting at 448.1 nm would help improving the sensitivity.

A simplification of the setup is also included in the improvement plan, mainly by replacing the home-assembled laser, that requires multiple associated devices such as drivers, waveform generators, and power supplies, by a laser module allowing at the same time the control of its power and its modulation. New resonators with identical and highly precise geometries will be useful for operation at the same modulation frequencies, allowing the use of only one laser for both channels connected in series.



# **Chapter 3. Comparison of the IMT Chemical Amplifier to a Laser- Induced Fluorescence instrument during RO<sub>x</sub>Comp**

This chapter describes the deployment of the IMT Chemical Amplifier (CA) during the RO<sub>x</sub>Comp (RO<sub>x</sub> Comparison) campaign performed in August 2022 at SAPHIR (Simulation of Atmospheric Photochemistry In a large Reaction chamber), Jülich, Germany. A detailed comparison of IMT-CA to a Laser-Induced Fluorescence instrument was carried out in order to investigate its performance and its accuracy under contrasting chemical conditions.

# 1. Introduction

SAPHIR is an atmospheric simulation chamber operated by the Institute for Chemistry and Dynamics of the "Geosphere ICG-2: Troposphere" department, that is located on the campus of the Forschungszentrum Jülich (FZJ) research center in Germany <sup>135</sup>.

The aim of ROxComp was to evaluate the reliability of RO<sub>x</sub> (OH, HO<sub>2</sub> and RO<sub>2</sub>) measurement techniques developed by different international research groups, such as Chemical Amplification (CA: IMT Nord Europe, University of Bremen, Anhui University), Laser Induced Fluorescence (LIF-FAGE: University of Lille, University of Leeds, FZJ) and Chemical Ionization Mass Spectrometry (CIMS: Deutscher Wetterdienst, Leopold-Franzens Universität Innsbruck).

We took advantage of this intercomparison exercise to test the IMT Chemical Amplifier (IMT-CA) and to improve our understanding of uncertainties associated to CA measurements, which was an important aspect for developing and assessing the ozone production rate quantification approach proposed in chapter 4.

In the following sections, a presentation of the SAPHIR chamber is provided, along with the conducted experiments. Operating conditions, calibrations and testing of the IMT-CA instrument during the campaign are also described. Additionally, a detailed comparison between peroxy radical measurements performed with the IMT-CA and the laser-induced fluorescence instrument from the FZJ group (reference instrument) is provided.

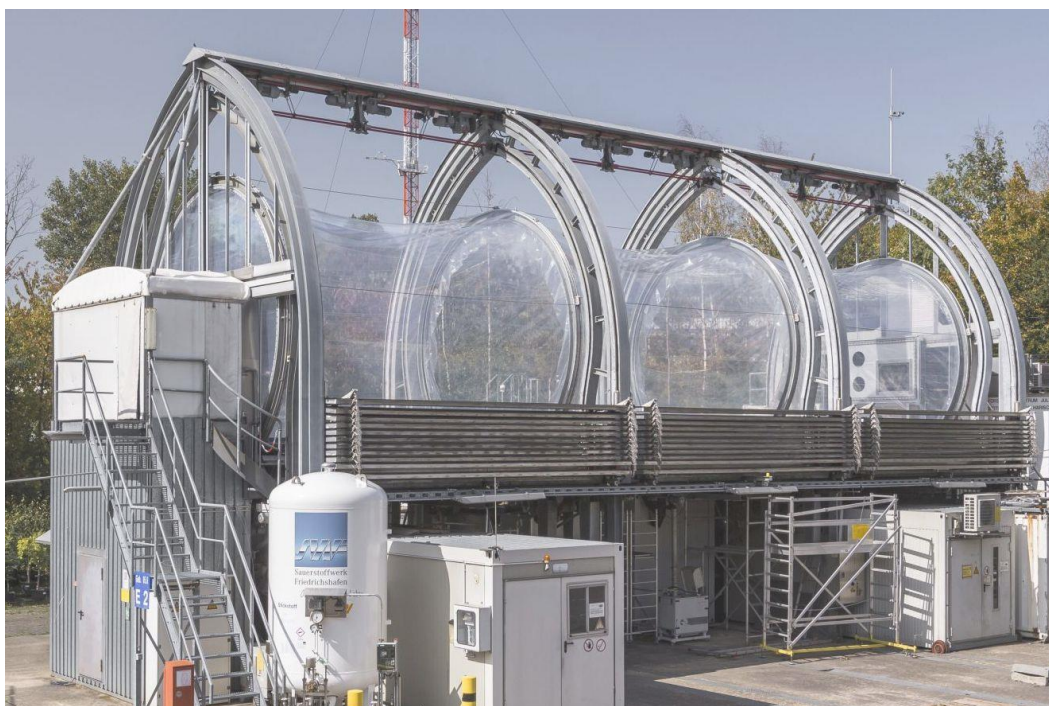
## 2. Description of the ROxComp campaign

The ROxComp campaign was carried out over a four-week period in August 2022, in the city of Jülich, Germany. Eight international research groups participated to this campaign, with different peroxy radical instruments as mentioned above and described in details in section 2.2. However, only data from the reference instrument employed by the FZJ group were considered for this study, data from instruments used by other groups are not discussed.



## 2.1. Characteristics of the SAPHIR chamber

The atmospheric simulation chamber SAPHIR shown in Figure 3.1 is part of EUROCHAMP, the European network of atmospheric chambers, which offers transnational access to its facilities<sup>136</sup>. SAPHIR was built with the purpose of conducting research on atmospheric chemistry, under simplified atmospheric-like conditions using ambient levels of trace gases. It also serves as an experimental site for intercomparisons between analytical instruments<sup>137</sup>.



**Figure 3. 1:** Picture of the SAPHIR chamber, FZJ, Germany  
(Copyright: Forschungszentrum Jülich / Sascha Kreklau)

The chamber has a cylindrical shape with a volume of  $270 \text{ m}^3$  (5 m diameter, 18 m length), and a volume-to-surface ratio of 0.83 m. In comparison to smaller chambers, the large volume-to-surface ratio makes surface effects less critical<sup>137</sup>. SAPHIR is equipped with a movable and opaque metallic curtain that can be opened/ closed within 1 min, allowing working either under dark, or irradiated conditions. This shutter system is also useful to protect the chamber from harsh weather conditions such as storms or hail<sup>138</sup>.

The simulation chamber consists of a double walled FEP Teflon foil secured on four steel frames, the inner and outer foils being  $125 \mu\text{m}$  and  $250 \mu\text{m}$  thick, respectively<sup>138</sup>. The space between the two Teflon sheets is continuously flushed with synthetic air to avoid a contamination of the inner volume of the chamber from the permeation of ambient trace

gases. The selection of the reactor material was based on its chemical inertness and its good transmission of UV light <sup>139</sup>.

Before starting any experiment, the chamber volume is purged during the previous night with a large flow rate of high purity synthetic air ( $\sim 500 \text{ m}^3 \text{ h}^{-1}$ ) to ensure the removal of residual trace gases that could arise from past experiments <sup>137</sup>. During an experiment, synthetic air is also injected inside the chamber, but at a smaller flow rate ( $\sim 15 \text{ m}^3 \text{ h}^{-1}$ ), to compensate for instruments' sampling and potential leaks <sup>138</sup>.

The replenishment flow results in the dilution of trace species within the chamber, the rate of dilution being calculated as follows <sup>136</sup>:

$$\text{Dilution rate (s}^{-1}\text{)} = \frac{\text{replenishment flow rate (m}^3 \text{ s}^{-1}\text{)}}{\text{chamber volume (m}^3\text{)}} \quad \text{Eq 3. 1}$$

A high replenishment flow rate is also needed when humidity is introduced into the chamber. For this purpose, high purity water (Milli-Q Gradient A10, Millipore Corporation) is vaporized and mixed to the flow of synthetic air ( $\sim 300 \text{ m}^3 \text{ h}^{-1}$ ) until reaching the desired relative humidity <sup>138</sup>.

For the experiments performed during ROxComp, trace gases ( $\text{O}_3$ ,  $\text{CO}$ ,  $\text{CH}_4$ , VOCs,  $\text{NO}$ ,  $\text{NO}_2$ , ...) were directly injected in the chamber <sup>136</sup>. Under sunlight conditions, trace gas mixing inside the chamber occurs within 10 minutes, while under dark conditions, homogenous mixing can take up to 30 minutes. Several fans installed inside the chamber can be used to reduce the mixing time to approximately 1 minute <sup>137</sup>. These fans were turned ON most of the time during ROxCOMP.

The SAPHIR chamber has the advantage of being operated under tropospheric conditions, since the experiments can be conducted at ambient trace gas concentrations and using solar irradiation. This was a great advantage for the ROxComp campaign since chemical systems used to generate peroxy radicals were representative of the troposphere.

## **2.2. Peroxy radical instruments coupled to SAPHIR**

An extensive set of highly sensitive instruments is continuously coupled to the SAPHIR chamber for measurement of radicals, traces gases, aerosols, and various physical parameters. During ROxComp, additional techniques for measuring peroxy radicals were also connected to the chamber (listed in Table 3.1), including chemical Amplification, Laser

Induced Fluorescence and Mass Spectrometry. These techniques were presented in Chapter 1.

**Table 3. 1:** Peroxy radical instruments coupled to SAPHIR during ROxComp

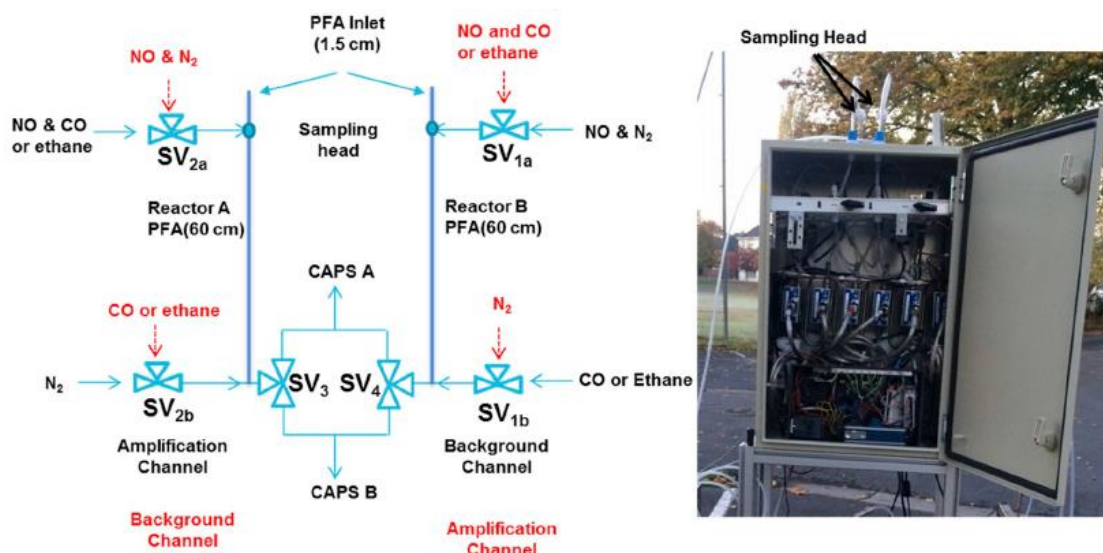
<i>Group</i>	<i>Technique</i>	<i>Time resolution*</i>	<i>3-<math>\sigma</math> LoD*</i>	<i>1-<math>\sigma</math> Accuracy*</i>
IMT Nord Europe	PERCA	6 min	0.3 ppt (RH=10 %) $0.8 \times 10^7 \text{ cm}^{-3}$	15.7 %
Universität Bremen	PERCA	60 s	<3 ppt (RH < 3%) $< 7.9 \times 10^7 \text{ cm}^{-3}$	15 %
Anhui University	PERCA	60 s	2.7 ppt (RH=10 %) $7.2 \times 10^7 \text{ cm}^{-3}$	-
Lille University	FAGE	40 s	$8.6 \times 10^7 \text{ cm}^{-3}$	15 %
Forschungszentrum Jülich	FAGE	47 s	HO <sub>2</sub> : $3 \times 10^7 \text{ cm}^{-3}$ RO <sub>2</sub> : $6 \times 10^7 \text{ cm}^{-3}$	18 %
University of Leeds	FAGE	30 s	HO <sub>2</sub> : $4 \times 10^6 \text{ cm}^{-3}$ RO <sub>2</sub> : $5.1 \times 10^6 \text{ cm}^{-3}$	13 %
Deutscher Wetterdienst	CIMS	5 min	$< 1.5 \times 10^6 \text{ cm}^{-3}$	28.5 %

\*Provided from the presentation of each group during the ROxComp workshops on Aug. 2022

Among the Chemical Amplifiers, the IMT Nord Europe CA was operated using the PERCA (PERoxy Radical Chemical Amplifier) approach as described in section 2.1 of chapter 1. As shown in Figure 3.2, the sampling unit consists in two PerFluoroAlkoxy (PFA) reactors, one operating in amplification mode and one in background mode, two NO<sub>2</sub> analyzers (CAPS from AERODYNE Research Inc) positioned at the reactors outlets, and two groups of solenoid valves (SV). The first group of valves (SV1a, SV1b, SV2a and SV2b) allows switching between the two measurement modes within each reactor. The second group (SV3, SV4) allows switching the NO<sub>2</sub> analyzers between the reactors. The setup is also equipped with mass flow controllers (MFC) to regulate flow rates of the reagent gases <sup>48</sup>.

The CAPS monitors are equipped with internal Nafion dryers to remove water-vapor, an 82 cm<sup>3</sup> stainless steel absorption cell containing high reflectivity mirrors and blue Light Emission Diodes (LED) emitting around 450 nm. The light passing through the cell is modulated and focused onto a vacuum photodiode. The phase-shift induced in the detected

signal by the absorption of  $\text{NO}_2$  is used to retrieve its concentration<sup>48</sup>. These CAPS instruments exhibit detection limits of approximately 50 ppt at a time resolution of 10 seconds.

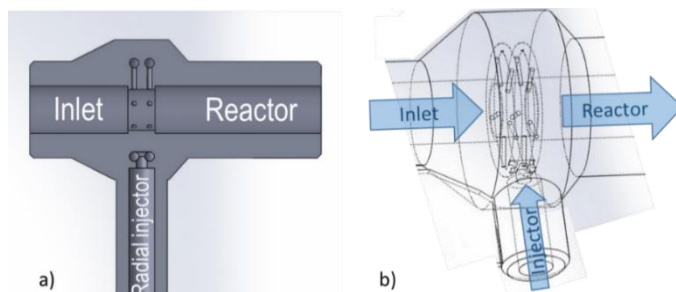


**Figure 3.2:** Schematic presentation of the IMT Nord Europe CA<sup>48</sup>

Ambient air is sampled into each reactor at a flow rate of  $\sim 800 \text{ cm}^3 \text{ min}^{-1}$  via a short PFA inlet (1/4", 1.5 cm long). The latter is connected with the reactor using home-made 3D printed nylon couplers (Figure 3.2), enabling the addition and mixing of reagent gases with ambient air. In the amplification reactor, a mixture of NO (22 sccm, 50 ppm in  $\text{N}_2$ ) and CO (80 sccm, pure) is introduced upstream when the PERCA approach is used. Simultaneously, a flow of  $\text{N}_2$  ( $\sim 80$  sccm) is added downstream the reactor. These flow rates were optimized to get the highest Chain Length (CL) as discussed in section 2.1 of chapter 1. The amount of  $\text{NO}_2$  present in ambient air and generated from (1) the ambient titration of  $\text{O}_3$  ( $\text{O}_3 + \text{NO} \rightarrow \text{NO}_2$ ) and (2) the amplification of  $\text{HO}_2 + \text{RO}_2$  is then quantified by one of the CAPS monitors. For the background reactor, an inversion is made between the introduction points of CO and  $\text{N}_2$  in order to only measure the amount of  $\text{NO}_2$  present in ambient air and generated from ambient  $\text{O}_3$  titration. The amount of  $\text{NO}_2$  generated by radical amplification, referred to as  $\Delta\text{NO}_2$  in the following, is then inferred by subtracting the  $\text{NO}_2$  measured at the exit of the background reactor from the  $\text{NO}_2$  measured at the exit of the amplification reactor ( $\text{NO}_2_{\text{amp}} - \text{NO}_2_{\text{bkg}}$ ).

In order to eliminate potential biases in  $\Delta\text{NO}_2$ , which could arise from (1) a drift in monitors' zero, (2) a contamination from the addition of the NO mixture that can result in the generation of different amounts of  $\text{NO}_2$  in each reactor, or (3) different amounts of  $\text{O}_3$

losses (wall effects) in each reactor before its titration into NO<sub>2</sub>, we used a measurement sequence as described in Duncianu et al. <sup>48</sup>. This sequence, which implies switching the operating modes (background or amplification) and the CAPS sampling between the two reactors, led to a measurement time resolution of 6-min.



**Figure 3.3:** Schematics of the home-made 3D printed nylon coupler in a transversal cut (a) and zoom of the double ring injector mixing area (b) <sup>48</sup>

Peroxy radical concentrations are deduced using the following equation:

$$[\text{HO}_2] + \sum[\text{RO}_2] = \frac{\Delta\text{NO}_2}{\text{CL}} \quad \text{Eq 3. 2}$$

This equation assumes that [OH] and [RO] are negligible, which is always true in the troposphere and under conditions used during ROxComp.

As mentioned in the first chapter in section 2.1, the CL is RH-dependent, therefore the limit of detection also depends on RH. For the IMT-CA and the PERCA approach, the 3 $\sigma$  LoD is 0.3, 0.6 and 1.4 ppt at 10, 50 and 80% RH, respectively, at a time resolution of 6 min <sup>48</sup>.

Another chemical amplifier deployed during ROxComp is the Peroxy Radical Chemical Enhancement and Absorption Spectrometer (PerCEAS) developed by the Institute of Environmental Physics of the University of Bremen <sup>45</sup>. Similar to the IMT-CA instrument, it consists in a dual channel instrument using the PERCA approach. Specificities of this instrument compared to the IMT-CA rely on operating the two reactors at low pressure (< ambient pressure) and using two CEAS NO<sub>2</sub> detectors. The latter are based on Cavity Ring Down Spectroscopy operating at a wavelength of 408 nm <sup>45</sup>. This setup exhibits a 3 $\sigma$ -LoD for HO<sub>2</sub> +  $\sum$ RO<sub>2</sub> < 3 ppt at RH < 3% and a time resolution of 60 s <sup>45</sup>.

The third chemical amplifier used in this campaign is a Nafion dryer based dual-channel CA developed by the Anhui University <sup>47</sup>. In this instrument, Nafion dryers serve at the same time as conversion reactors and sample dryers. The advantage of this setup compared

to the two other chemical amplifiers is a lower impact of humidity on the CL. NO<sub>2</sub> is quantified at the outlet of the reactors using two broadband cavity enhanced spectroscopy (BBCES) detectors<sup>140</sup>. This setup has a 3 $\sigma$ -LoD of approximately 2.7 ppt at a relative humidity of 10% and a time resolution of 60 s<sup>47</sup>.

During ROxComp, three laser-induced fluorescence instruments using the FAGE (Fluorescent Assay by Gas Expansion) approach were deployed for the speciated detection of OH, HO<sub>2</sub> and RO<sub>2</sub>. The University of Lille instrument (UL-FAGE) is characterized by 3 $\sigma$ -LoDs of 1.4 $\times 10^6$ , 1.7 $\times 10^7$  and 8.6 $\times 10^7$  cm<sup>-3</sup> for OH, HO<sub>2</sub> and RO<sub>x</sub>, respectively, at a time resolution of 40 s. The Forschungszentrum Jülich instrument (FZJ-FAGE) has 3 $\sigma$  LoDs of 3 $\times 10^7$  and 6 $\times 10^7$  cm<sup>-3</sup> for HO<sub>2</sub> and RO<sub>2</sub>, respectively, at a time resolution of 47 s, and 2.1 $\times 10^6$  cm<sup>-3</sup> for OH at a time resolution of 270 s. As for the University of Leeds instrument (Leeds-FAGE), it exhibits 3 $\sigma$ -LoDs of 4.1 $\times 10^6$  cm<sup>-3</sup> and 5.1 $\times 10^6$  cm<sup>-3</sup> for HO<sub>2</sub> and RO<sub>2</sub> respectively, when operated at a time resolution of 30 s. Figures of merit for these instruments, as well as the chemical ionization mass spectrometer below, were provided during personal presentations made during ROxComp (Aug. 2022).

The only Chemical Ionization Mass Spectrometer (CIMS) deployed during ROxComp was operated by the DWD (Deutscher Wetterdienst) group. It exhibits 3 $\sigma$ -LoDs of 7.5 $\times 10^4$  cm<sup>-3</sup> for OH and < 1.5 $\times 10^6$  cm<sup>-3</sup> for HO<sub>2</sub> +  $\Sigma$  RO<sub>2</sub> at a measurement time resolution of 5 min.

All these instruments were calibrated using the water-photolysis approach, each group using its own calibrator. While the operating principle is similar, there were differences in the calibrators' designs, the type of VOCs used to generate RO<sub>2</sub> (CH<sub>4</sub> or isoprene) and operating conditions (laminar or turbulent flow regimes). Cross calibrations between the different groups were performed at the end of ROxComp to check whether all instruments were well calibrated (details presented in section 3.2 for IMT-CA).

### **2.3. Ancillary measurements performed in SAPHIR**

The SAPHIR chamber is also equipped with a large variety of gas-phase instruments to provide a detailed chemical characterization when performing kinetic experiments. Instruments used during ROxComp are reported in Table 3.2<sup>141</sup>.

Cavity Ring-Down Spectrometers were used for the detection of inorganic species, for instance CO, CO<sub>2</sub>, H<sub>2</sub>O and also organic molecules such as CH<sub>4</sub> and HCHO. A Proton-Transfer Reaction-Time of Flight Mass Spectrometer (PTR-ToFMS) and a Gas Chromatograph (GC) were used to monitor volatile organic compounds <sup>135</sup>. A chemiluminescence monitor (CLD) equipped with a photolytic converter was used for the quantification of NO and NO<sub>2</sub>. This type of monitor provides a higher degree of specificity for NO<sub>2</sub> measurements than monitors equipped with a molybdenum converter <sup>141</sup>. A UV-absorption monitor was used for the measurement of O<sub>3</sub> <sup>135</sup> and a Differential Optical Absorption Spectrometer (DOAS) was used as a reference instrument for the measurement of OH <sup>135</sup>.

**Table 3. 2:** Ancillary measurements during ROxComp

<i>Species</i>	<i>Technique*</i>	<i>Time resolution*</i>	<i>3-σ LoD*</i>	<i>1- σ Accuracy*</i>
CO, CH <sub>4</sub>	CRDS	60s	3 ppb	5 %
CO <sub>2</sub>		60s	75 ppb	5%
H <sub>2</sub> O		60s	0.3 %	5%
HCHO		300s	0.3 ppb	10 %
VOCs	PTR-ToFMS	30s	45 ppt	14 %
NO	CLD	60 s	60 ppt	5 %
NO <sub>2</sub>			90 ppt	7 %
O <sub>3</sub>	UV photometry	60 s	1.5 ppb	2 %
OH	DOAS	134 s	2.4×10 <sup>6</sup> cm <sup>-3</sup>	6.5 %
J values	spectroradiometer	60 s	-	18 %

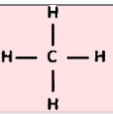
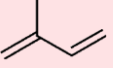
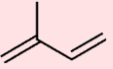
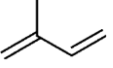
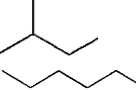
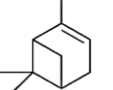
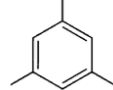
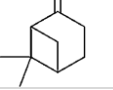
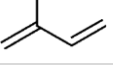
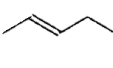
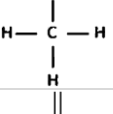

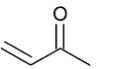
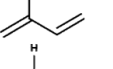
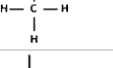
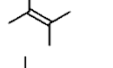
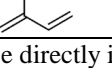
\*The reported values are available elsewhere <sup>141</sup>

As for photolysis frequencies, they were derived from measurements of the solar actinic flux using a spectroradiometer positioned on the roof of the adjacent institute building <sup>139</sup>. The photolysis frequencies within the chamber are similar to that measured on the roof of the building, the light transmission through the chamber walls being close to 100%.

## 2.4. Conducted experiments

During ROxComp, 16 experiments were performed under different experimental conditions (Table 3.3) in order to challenge the peroxy radical instruments.

**Table 3. 3:** Experimental conditions for ROxComp experiments

<i>Date</i>	<i>VOC</i>	<i>Structural formula</i>	<i>O<sub>3</sub></i>	<i>NO<sub>x</sub>*</i>	<i>H<sub>2</sub>O</i>	<i>Main oxidant</i>	<i>Sunlight</i>	<i>Chapter section</i>
8 Aug. 22	CH <sub>4</sub> (+CO)		x	x	✓	OH	✓	-
9 Aug. 22	Isoprene		x	x	✓	OH	✓	-
10 Aug. 22	Isoprene		✓	x	✓	OH	✓	-
11 Aug. 22	Isoprene		✓	NO	✓	OH	✓	4.3
12 Aug. 22	I-pentane n-hexane		x	NO	✓	OH	✓	4.3
13 Aug. 22	α-pinene		✓	NO	✓	O <sub>3</sub> & OH	✓	4.3- 4.4.2
14 Aug. 22	Mesitylene		x	NO	✓	OH	✓	4.3
16 Aug. 22	β-pinene		✓	x	✓	OH	✓	4.3
17 Aug. 22	Isoprene		✓	NO <sub>2</sub>	x	NO <sub>3</sub> & OH	x & ✓	4.4.1
19 Aug. 22	Trans-2-Hexene		✓	x	✓	O <sub>3</sub>	x	4.1-4.2 -4.4.2
20 Aug. 22	CH <sub>4</sub> (+CO)		x	NO	✓	OH	✓	4.1-4.3
22 Aug. 22	β-pinene		✓	NO <sub>2</sub>	✓	NO <sub>3</sub> & OH	x & ✓	4.4.1
23 Aug. 22	- (Ambient air)		x	x	✓	OH	✓	4.4.3
24 Aug. 22	MVK		✓	x	✓	OH	✓	4.2
25 Aug. 22	Isoprene		x	x	✓	Cl <sub>2</sub>	✓	-
	CH <sub>4</sub>							
26 Aug. 22	TME		✓	x	✓	O <sub>3</sub> & OH	x & ✓	4.2- 4.4.2
	Isoprene							

\*The stated compounds are those directly injected into the chamber



Part of these experiments were focused on testing instruments' responses to matrix constituents such as O<sub>3</sub>, NO and H<sub>2</sub>O. The other part was devoted to investigate instruments' sensitivity to various peroxy radicals generated from the oxidation of organic compounds (CH<sub>4</sub>, alkanes, alkenes) using different oxidants (OH, O<sub>3</sub>, NO<sub>3</sub>, Cl). The first three experiments performed during RO<sub>x</sub>Comp (red rows in Table 3.3), were not taken into consideration in this study, given that a technical issue occurred on the IMT-CA instrument (leakage of reagent gases).

As already mentioned, it is important to note that experimental conditions were representative of ambient air conditions, with trace gas concentrations similar to what is usually observed in the troposphere. For instance, when the concentrations are averaged over the whole experiment, water-vapor levels varied from 1 to 15 ppth and RO<sub>x</sub> were in the range of 4 - 14×10<sup>6</sup>, 0.2 - 1.3×10<sup>9</sup> and 0.3 - 1.3×10<sup>9</sup> cm<sup>-3</sup> for OH, HO<sub>2</sub> and RO<sub>2</sub>, respectively. We also notice that average NO<sub>x</sub> concentrations ranged from < LoD up to 3 ppb for NO and from 0.2 - 7 ppb for NO<sub>2</sub>. The averaged concentrations of O<sub>3</sub> and VOCs ranged from 12 to 80 ppb and approximately 0.4 to 7 ppb, respectively.

The experiments described above were grouped together as follows in the results discussion section (4.1-4.4) to investigate different aspects for IMT-CA:

- Assessment of humidity effects:
  - Dark ozonolysis of hexene (19 Aug. 22)
  - Photooxidation of CO and CH<sub>4</sub> (20 Aug. 22)
- Assessment of O<sub>3</sub> effects:
  - 19 Aug. 22 experiment (described above)
  - Photooxidation of MVK (24 Aug. 22)
  - Dark oxidation of isoprene by OH and photooxidation (26 Aug. 22)
- Assessment of NO effects:
  - Photooxidation of isoprene (11 Aug. 22)
  - Photooxidation of i-pentane and n-hexane (12 Aug. 22)
  - Dark Ozonolysis of α-pinene and photooxidation (13 Aug. 22)
  - Photooxidation of Mesitylene (14 Aug. 22)

- Photooxidation of  $\beta$ -pinene (16 Aug. 22)
  - 20 Aug. 22 experiment (described above)
- Assessment of the sensitivity to functionalized peroxy radicals:
- 13 Aug. 22 experiment (described above)
  - Dark oxidation of isoprene by  $\text{NO}_3$  and photooxidation (17 Aug. 22)
  - 19 Aug. 22 experiment (described above)
  - Dark oxidation of  $\beta$ -pinene by  $\text{NO}_3$  (22 Aug. 22)
  - Photooxidation of ambient air (23 Aug. 22)
  - Dark oxidation of isoprene by OH then photooxidation (26 Aug. 22)

### 3. Setup and calibration of the IMT-CA instrument

#### 3.1. Setup of the Chemical Amplifier

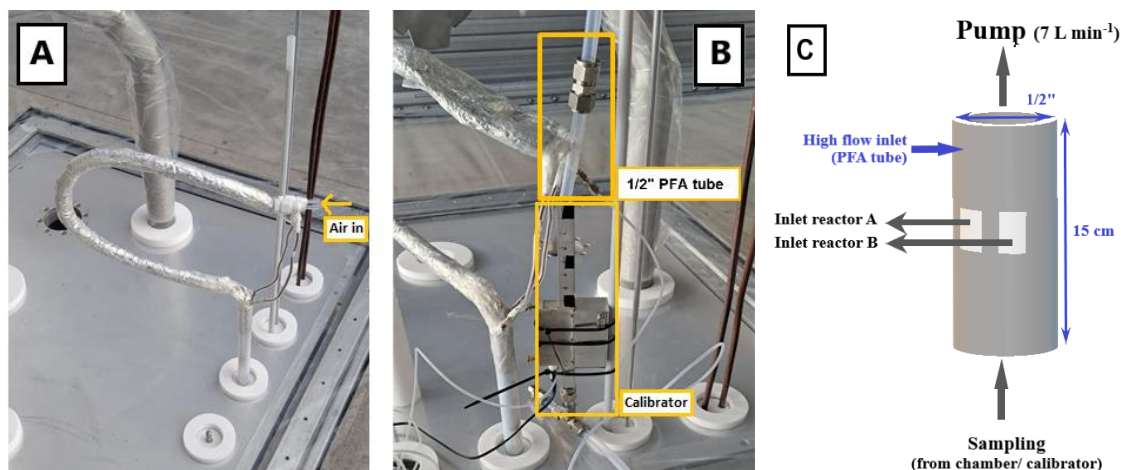
To couple IMT-CA to the SAPHIR chamber, the sampling reactors were installed inside the chamber as shown in Figure 3.4 (A), and then connected to the sampling system through a flange in the chamber floor. The sampling system was lifted on a container roof as we see in Figure 3.4 (B), while the  $\text{NO}_2$  analyzers were housed inside the container, presented in Figure 3.4 (C). The sampling reactors were kept under dark conditions and the outer surface was covered with Teflon.



**Figure 3. 4:** IMT-CA coupling to SAPHIR, **A-** CA sampling reactors inside SAPHIR, **B-** CA sampling system lifted on the container's roof below the chamber's floor, **C-** Two  $\text{NO}_2$  monitors housed inside the container

Two sampling approaches were employed during this campaign. The first consisted in direct sampling through the CA inlets (Figure 3.5 (A)), while the second involved the use of an additional high flow inlet (Figure 3.5 (B)). The second approach was used when we realized that turbulences generated by the use of fans within the chamber was affecting the

CA sampling process, leading to the release of a small amount of the CA reagent gases (CO and NO) inside the chamber. To address this problem, a 1/2 inch 15 cm long PFA tube was added to the reactors' inlets and was pumped at a high flow rate of about 7 L min<sup>-1</sup>, aiming to reduce turbulences and to avoid the release of CO/NO inside the chamber.



**Figure 3.5:** IMT-CA inlets, **A-** direct inlet, **B-** high flow inlet using a 1/2" PFA tube, **C-** schematic presentation of the high flow inlet and reactors' inlets coupling

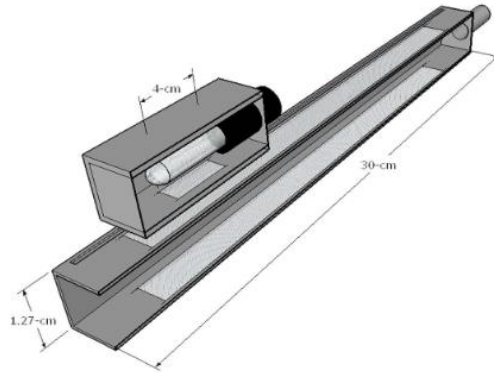
This additional inlet resulted in a loss of peroxy radicals of 20% (characterized in section 3.2 below), which was accounted in the retrieval of the CA measurements. The high flow inlet was used during experiments conducted between 11 and 16 Aug. 22.

### 3.2. Calibration of the Chemical Amplifier

Calibrating a RO<sub>x</sub> instrument is difficult since it requires to produce known concentrations of reactive radicals at low levels with a high accuracy.

To calibrate the IMT-CA instrument, a calibrator based on water-vapor photolysis in air at 185 nm was used. This calibrator has been described elsewhere<sup>142</sup>. A cross section of the calibration source is shown in Figure 3.6. It comprises an aluminum rectangular flow reactor featuring two suprasil windows. A low-pressure mercury lamp serves as the light source and is enclosed in an aluminum cartridge. The latter undergoes constant purging with dry nitrogen to prevent oxygen photolysis within the lamp housing, that could generate ozone and potentially affect the transmission of photons into the flow reactor. A bandpass filter (FWHM=20 nm, Acton Research) located between the lamp housing and the flow reactor allows filtering the lamp emission bands other than 185 nm.

During a calibration experiment, humid air is flown within the calibration cell where both water and oxygen undergo photolysis as shown by the following reactions <sup>142</sup>:



**Figure 3.6:** Cross-section of the IMT-CA calibrator <sup>142</sup>

Concentrations of OH and HO<sub>2</sub> are determined from the following equation:

$$[\text{HO}_2] = [\text{OH}] = [\text{H}_2\text{O}] \times \sigma_{\text{water}} \times \Phi_{\text{OH+H}} \times (\text{Fxt}) \quad \text{Eq 3. 3}$$

where  $\sigma_{\text{water}} = 7.14 \times 10^{-20} \text{ cm}^2$  is the absorption cross section of water at 185 nm <sup>143</sup>,  $\Phi_{\text{OH+H}} = 1$  the photo-dissociation quantum yield of water into OH and H <sup>144</sup>, F the photon flux, and t the photolysis time. The product (Fxt) is derived from O<sub>2</sub> actinometry as shown in the following equations:

$$[\text{O}_3] = [\text{O}_2] \times \sigma_{\text{O}_2} \times \Phi_{\text{O}_3} \times (\text{Fxt}) \quad \text{Eq 3. 4}$$

$$(\text{F} \times \text{t}) = \frac{[\text{O}_3]}{2 \times [\text{O}_2] \times \sigma_{\text{O}_2}} \quad \text{Eq 3. 5}$$

where  $\sigma_{\text{O}_2} = 1.2 \times 10^{-20} \text{ cm}^{-2}$  is the effective absorption cross section of O<sub>2</sub> at 185 nm [10] and  $\Phi_{\text{O}_3} = 2$ .

By adding a VOC inside the calibrator, isoprene in this work, all OH radicals are converted into HO<sub>2</sub> and RO<sub>2</sub> <sup>145</sup>. The concentrations of these two radicals at the exit of the calibrator are determined as follows:

$$[\text{HO}_2] = (1 + X) \times [\text{H}_2\text{O}] \times \sigma_{\text{water}} \times \Phi_{\text{OH}+\text{H}} \times \frac{[\text{O}_3]}{2 \times [\text{O}_2] \times \sigma_{\text{O}_2}} \quad \text{Eq 3. 6}$$

$$[\text{RO}_2] = (1 - X) \times [\text{H}_2\text{O}] \times \sigma_{\text{water}} \times \Phi_{\text{OH}+\text{H}} \times \frac{[\text{O}_3]}{2 \times [\text{O}_2] \times \sigma_{\text{O}_2}} \quad \text{Eq 3. 7}$$

X represents the prompt yield of HO<sub>2</sub> from VOC+OH, the expressions (1 + X) and (1 – X) standing for the non-unity yield of HO<sub>2</sub> and RO<sub>2</sub>, with X=0.06 for isoprene<sup>48</sup>.

The concentration of isoprene was adjusted to 6.2×10<sup>12</sup> cm<sup>-3</sup> in order to convert 99% of OH into peroxy radicals in less than 2 ms, ensuring a negligible loss of OH on the calibrator inner surface. To introduce isoprene in the calibrator, a diluted mixture of the pure compound was prepared in a 6 L stainless steel canister filled with zero air at 3 bars in order to get a concentration of 3500 ppm. Then, 2.5 mL min<sup>-1</sup> of the obtained mixture was added to a flow rate of 35 L min<sup>-1</sup> of dry or humid zero air before entering the calibrator. Flow rates were regulated using mass flow controllers (MFC, MKS).

As mentioned in chapter 1, the CL of a chemical amplifier depends on RH. This issue was addressed by conducting calibration experiments at variable RH. The RH ranged between 10 and 50% (T = 21 – 32°C), resulting in peroxy radical concentrations in the range of 4×10<sup>9</sup> – 2×10<sup>10</sup> cm<sup>-3</sup>. The accuracy of the calibrated CL depends on uncertainties associated to the measured ΔNO<sub>2</sub> and the generated concentrations of peroxy radicals. The uncertainty on ΔNO<sub>2</sub> can be disregarded due to the generation of high concentrations of peroxy radicals during calibrations. Dusanter et al. (2008)<sup>142</sup> reported a 2-σ accuracy of 31% for peroxy radical concentrations generated by this calibrator. This results in a 2-σ accuracy of 31% for the CL.

The water-vapor concentration was measured using a LICOR 840A instrument based on infrared absorption. The amount of ozone generated in the calibration cell was quantified as NO<sub>2</sub> using the CAPS monitor, after being titrated by NO in one of the CA reactors operated in background mode. The NO mixing ratio was maintained at the level used when the CA is used for ambient measurements, which ensure an ozone conversion higher than 99.9%.

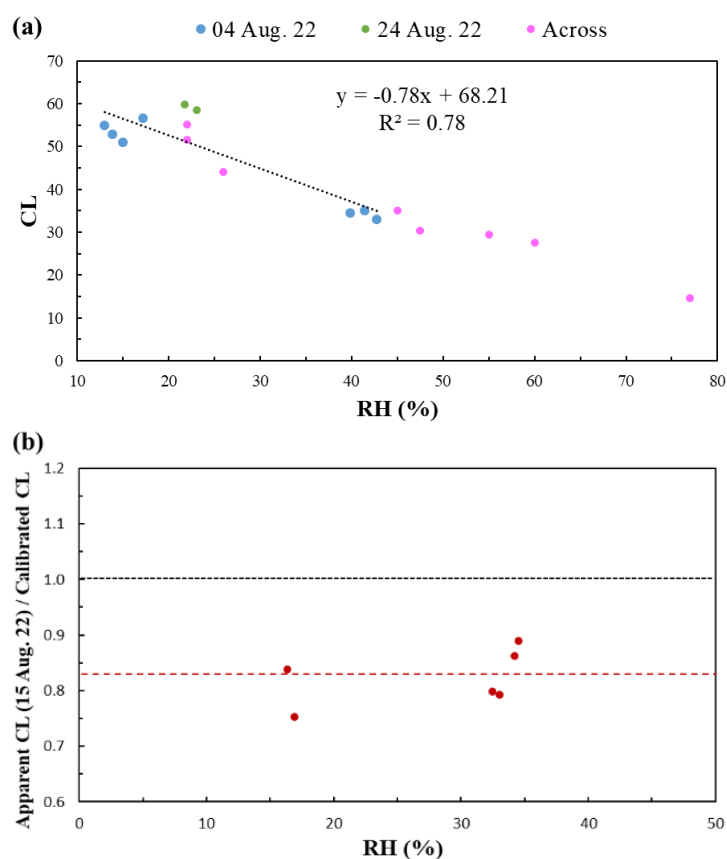
When generating a specific concentration of HO<sub>2</sub>+RO<sub>2</sub>, air from the calibrator is drawn through the CA inlets. The CA measurement is switched back and forth between background and amplification modes, with a duration of 10 min for each mode. The

difference in NO<sub>2</sub> measured between these two modes, ΔNO<sub>2</sub>, is used to calculate the CL as follows:

$$CL = \frac{\Delta NO_2}{[HO_2] + [RO_2]} \quad \text{Eq 3. 8}$$

Three calibrations were performed during ROxComp. These calibrations were compared to calibrations from the ACROSS field campaign, made in the French Rambouillet forest during June-July 2022, in order to check the stability of the CA's response.

The calibration results are presented in Figure 3.7 (a). Calibrations performed on 4 and 24 August were done using the direct sampling approach described in section 3.1 while the calibration from 15 August was done using the additional high flow inlet.



**Figure 3.7:** Calibration of the chain length for IMT–CA during ROxComp (04 and 24 Aug. 2022) and Across (a) and determination of radical losses in the high flow rate inlet (b)

The good agreement observed between ACROSS and ROxComp calibrations, using the direct sampling approach, indicates a good stability of the IMT instrument over time. A parameterization of the chain length,  $CL = -0.78 RH + 68.21$ , was deduced for the

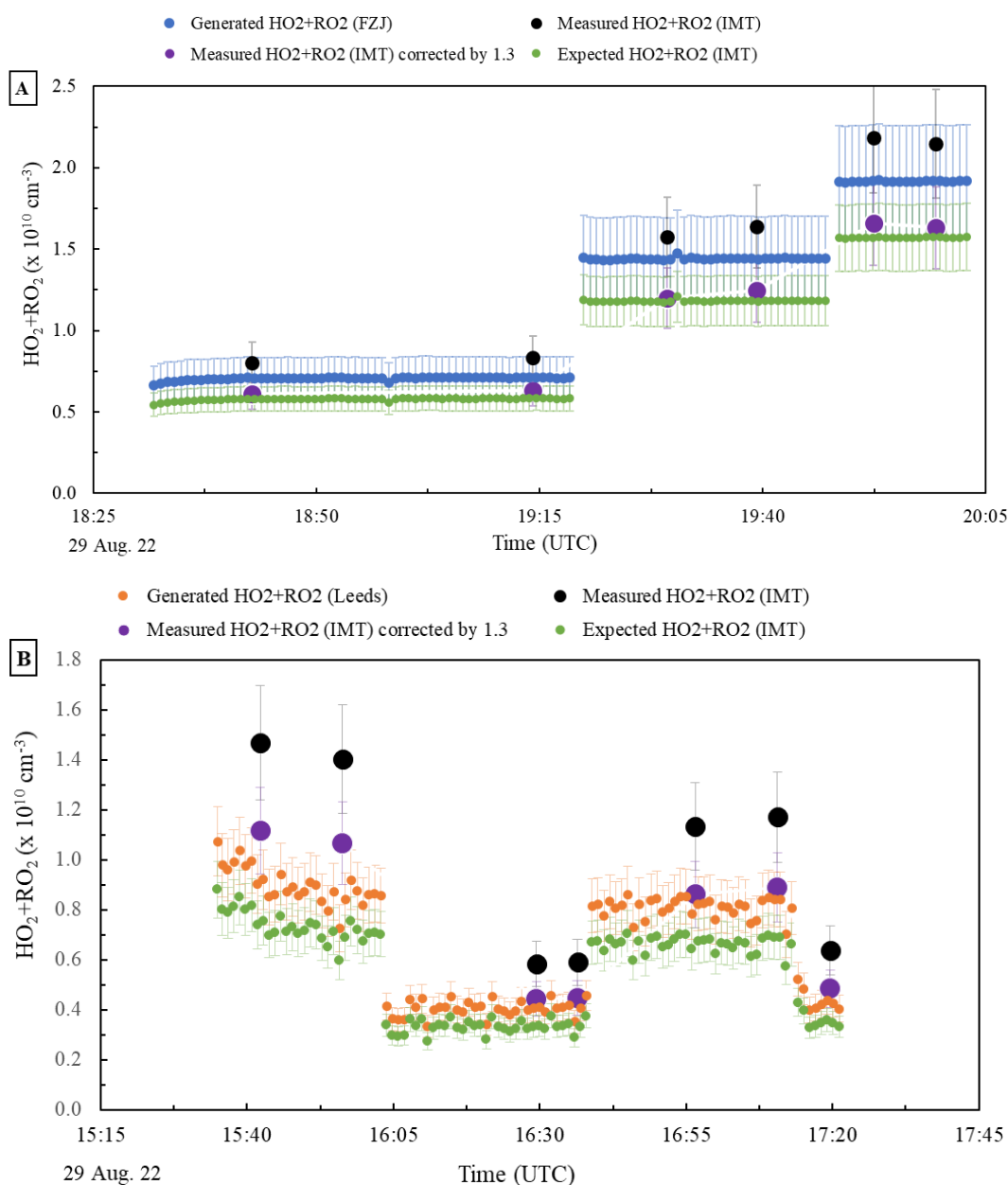
quantification of peroxy radical concentrations produced during the ROxComp experiments when the direct sampling approach was used.

The calibration made on 15 August led to lower "apparent" CL values due to the use of the high flow rate inlet that led to radical losses on its inner surface. Comparing calibrations performed with and without the high flow rate inlet in Figure 3.7 (b) leads to a correction factor of 1.2 (corrected concentration = measured concentration  $\times$  1.2), indicating a radical loss of 20%. This correction was taken into consideration for the retrieval of radical concentrations for all experiments performed between 11 and 16 August, during which the high flow rate inlet was used.

At the end of the ROxComp campaign, cross calibrations were made for each RO<sub>x</sub> instrument using calibrators from other groups in order to identify any potential calibration issues. IMT-CA was cross-calibrated using the Leeds and Jülich radical sources. As already mentioned, these two calibrators are based on the same operating principle as the IMT calibrator, i.e. water-vapor photolysis. However, there are notable differences such as the type of VOC added in the calibrator (methane instead of isoprene for the Leeds and Jülich calibrators) and the flow regime (laminar for Jülich instead of turbulent for IMT and Leeds).

The peroxy radical concentrations measured by the IMT-CA at the outlet of the Leeds and Jülich calibrators are expected to be 18% lower than the generated concentrations. This is due to the partial propagation of CH<sub>3</sub>O<sub>2</sub> radicals (formed by the oxidation of CH<sub>4</sub>) into HO<sub>2</sub> in the CA. Indeed, as the first step of the amplification chemistry is based on converting RO<sub>2</sub> into HO<sub>2</sub>, the formation of organic nitrates and nitrites from RO<sub>2</sub>+NO and RO+NO reactions limits the fraction of RO<sub>2</sub> detected<sup>48</sup>. In the case of CH<sub>3</sub>O<sub>2</sub>, while the CH<sub>3</sub>ONO<sub>2</sub> yield is low from the CH<sub>3</sub>O<sub>2</sub>+NO reaction (approx. 0.1%), the CH<sub>3</sub>ONO yield from the competition between CH<sub>3</sub>O+O<sub>2</sub> and CH<sub>3</sub>O+NO is about 36% for a NO mixing ratio of 6 ppm as used in the CA reactors<sup>48</sup>. In contrast, both the organic nitrate and nitrite yields for isoprene-based radicals (C<sub>5</sub>H<sub>7</sub>O<sub>2</sub>) generated in the IMT calibrator are low (< 10.7%)<sup>48</sup>.

The cross-calibration results presented in Figure 3.8 show that peroxy radical concentrations measured by IMT-CA (black dots) are higher by a factor of 1.38 and 1.72 than expected when using FZJ (A) and Leeds (B) calibrators, respectively.



**Figure 3.8:** Cross calibration of IMT-CA with: A) FZJ calibrator and B) Leeds calibrator. Error bars represent 1- $\sigma$  uncertainties stated for calibration sources

These cross-calibrations demonstrated the existence of a bias in the calibration of IMT-CA when using the IMT calibrator. Laboratory testing performed after ROxComp indicated that the isoprene concentration in the IMT calibrator was high enough to generate a significant amplification of radicals during the background mode, leading to an underestimation of the chain length. Decreasing the isoprene concentration from  $6.2 \times 10^{12} \text{ cm}^{-3}$  to  $1.2 \times 10^{12} \text{ cm}^{-3}$  leads to an increase of the calibrated CL by a factor of 1.3.

Taking this issue into account, peroxy radical concentrations measured by IMT-CA at the exit of the FZJ and Leeds calibrators are in better agreement with expected values, the



measurements being a factor of 1.19 larger on average. While this difference is within the stated  $2\sigma$  accuracy of the calibrators (31% for IMT, 26% for Leeds and 36% for FZJ), a correction factor of 1.19 was applied to the peroxy radical concentrations measured by the IMT-CA for two reasons: (1) the calibrated CL may still be underestimated when using the lower concentration of isoprene in our calibrator and (2) a new mercury lamp was recently installed on the IMT calibrator whose effective  $O_2$  absorption cross section was assumed to be  $1.2 \times 10^{-20} \text{ cm}^2$  (not determined experimentally). For the latter, the effective  $O_2$  absorption cross section could be wrong by up to 24%<sup>146</sup>, and so the calculated  $HO_2+RO_2$  concentrations from our calibrator. These two issues need to be further investigated in the laboratory.

### 3.3. Assessment of measurement biases from ozone

The IMT-CA has the advantage of operating simultaneously in background and amplification modes, which allows cancelling out  $NO_2$  formation processes other than radical amplification in the calculation of  $\Delta NO_2$ . However, a bias in peroxy radical measurements is observed when ozone is sampled under dry and humid conditions, that seems to be due to the amplification of spurious radicals, and that cannot be removed by a simple difference between the amplified and background modes. To quantify this interference, experiments were made in the laboratory during and after ROxComp using different experimental conditions. During ROxComp, the PERCA approach was used to assess this  $O_3$  interference under dry conditions, while after the campaign, the ECHAMP approach was employed in the laboratory for similar tests, under both, dry and humid conditions.

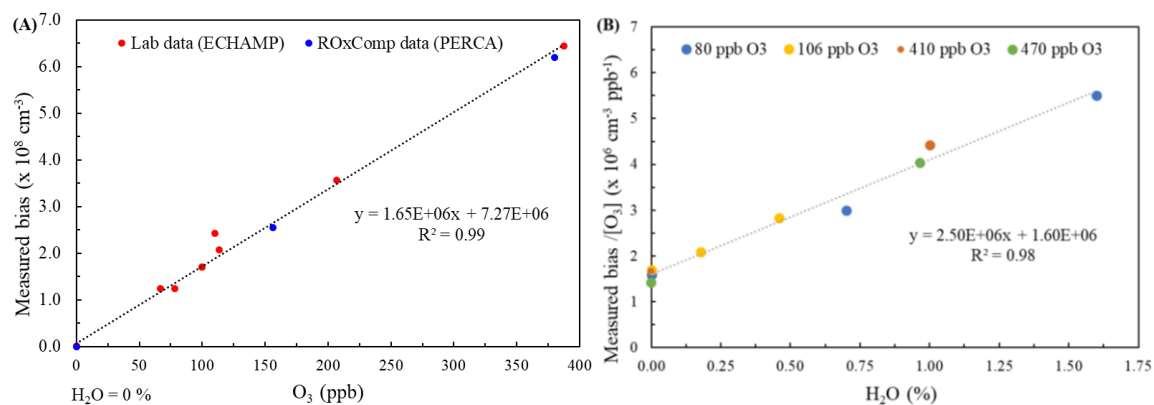
During ROxComp and in the laboratory, experiments were performed under dry conditions at different  $O_3$  concentrations.  $O_3$  was generated by passing a low flow rate of dry zero air ( $1 - 10 \text{ ml min}^{-1}$ ) through a UV lamp in order to produce  $O_3$  by oxygen photolysis at 185 nm (R 3. 3-R 3. 4). The generated amount of  $O_3$  was next added to a large flow of dry zero air ( $4 \text{ L min}^{-1}$ ), leading to ozone concentrations in the range of 67-390 ppb. The  $O_3$  concentration was varied by adjusting the air flow rate passing to the UV lamp. This ozone mixture was then directly sampled by the CA.

The results presented in Figure 3.9 (A) show a linearity between the measured bias and the  $O_3$  concentration, for both approaches, with a linear regression slope of  $1.65 \times 10^6 \text{ cm}^{-3}$

ppb<sup>-1</sup>. The determination coefficient was found to be 0.99. Since the same level of interferences is observed using the PERCA and ECHAMP approaches, this suggests that a radical species is generated inside the CA, which is then amplified as peroxy radicals.

Experiments were also performed under humid conditions for the ECHAMP approach only, by passing the flow of dry synthetic air (4 L min<sup>-1</sup>) through a humidification system and then mixing it with O<sub>3</sub> generated using dry air as described above. For each test, O<sub>3</sub> was fixed at a stable concentration (80, 106, 410 and 470 ppb). The results shown in Figure 3.9 (B) reveals that the level of interferences increases with water. The same behavior is observed at the four O<sub>3</sub> concentrations, which led to the determination of a measurement bias of 2.5×10<sup>6</sup> cm<sup>-3</sup> per ppb of ozone and % of water-vapor, with a good linear regression characterized by a determination coefficient of 0.98.

Given the similar results observed between the PERCA and ECHAMP approaches when operating under dry conditions, it is assumed that a similar behavior is likely to be observed under humid conditions. Nevertheless, these tests should also be conducted and validated for the PERCA approach under humid conditions. It is noteworthy that preliminary measurements in the laboratory showed similar behaviors for the two approaches.



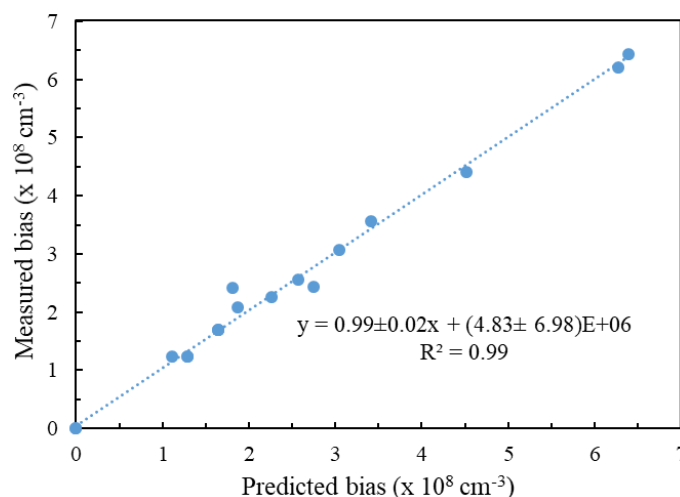
**Figure 3.9:** Peroxy radical measurement bias at (A) variable O<sub>3</sub> concentrations and dry conditions, and (B) constant O<sub>3</sub> concentrations and varying humidity conditions

An empirical model was deduced from these experiments to predict biases in peroxy radical measurements for the different experimental conditions of ROxComp. This model can be presented by the following equation:

$$\text{Bias} = 1.65 \times 10^6 [\text{O}_3] + 2.5 \times 10^6 [\text{O}_3][\text{H}_2\text{O}] \quad \text{Eq 3.9}$$

Where this bias is expressed in cm<sup>-3</sup>, [O<sub>3</sub>] in ppb and [H<sub>2</sub>O] in %.

To confirm the efficiency of this model, a comparison between the model-predicted biases for all the tests presented above and values measured experimentally is shown in Figure 3.10. The scatter plot shows a good correlation with a determination coefficient of 0.99 and a slope of unity. The y-intercept is not statistically significant at  $1\sigma$ . This implies that the proposed model is able to predict the IMT-ECHAMP/PERCA bias generated by the presence of  $O_3$  under dry and humid conditions.



**Figure 3.10:** Measured vs predicted  $O_3$  biases in IMT-CA measurements using the empirical model

This model was used during ROxComp to remove biases generated by ozone when measuring peroxy radical concentrations. For instance, a bias of  $4.5 \times 10^8 \text{ cm}^{-3}$  was observed when  $O_3$ , water-vapor and peroxy radical concentrations were 104 ppb, 1.4 % and  $2.1 \times 10^9 \text{ cm}^{-3}$ , respectively, for the 11 Aug. experiment. Those are amongst the worst conditions encountered during ROxComp for the generation of this  $O_3$ -water bias. Examples of calculated biases that were subtracted from IMT-CA measurements are shown in section 4.2 (Figure 3.13).

The physicochemical process at the origin of this bias is not well understood yet. This may be linked to the formation of excited state  $NO_2$  ( $NO_2^*$ ) and  $NO_3$  ( $NO_3^*$ ) in the CA inlet when ambient  $O_3$  is titrated into  $NO_2$  due to the addition of  $NO$ . It has been reported in the literature that  $NO_2^*$  and  $NO_3^*$  could react with water-vapor to form  $OH$  and  $HO_2$ <sup>147</sup>. While the recent study of Dillon et al. (2018) indicates that the formation of  $OH$  from  $NO_2^* + H_2O$  and  $NO_3^* + H_2O$  is not significant, the formation of  $HO_2$  from  $NO_3^* + H_2O$  has not been ruled out.

## 4. Comparison: IMT-CA vs FZJ-FAGE

During RO<sub>x</sub>Comp, experimental conditions were set in order to investigate the influence of specific parameters on the performance of the different RO<sub>x</sub> instruments. The comparison between peroxy radical concentrations measured by the IMT-CA and the FZJ-FAGE instrument is made below on the basis of specific parameters, i.e. RH, O<sub>3</sub>, NO and the type of generated peroxy radicals.

It is important to note that the measurement datasets used in this section were not yet finalized at the time this chapter was written and the conclusions drawn from the intercomparison are preliminary.

### 4.1. Assessment of humidity effects

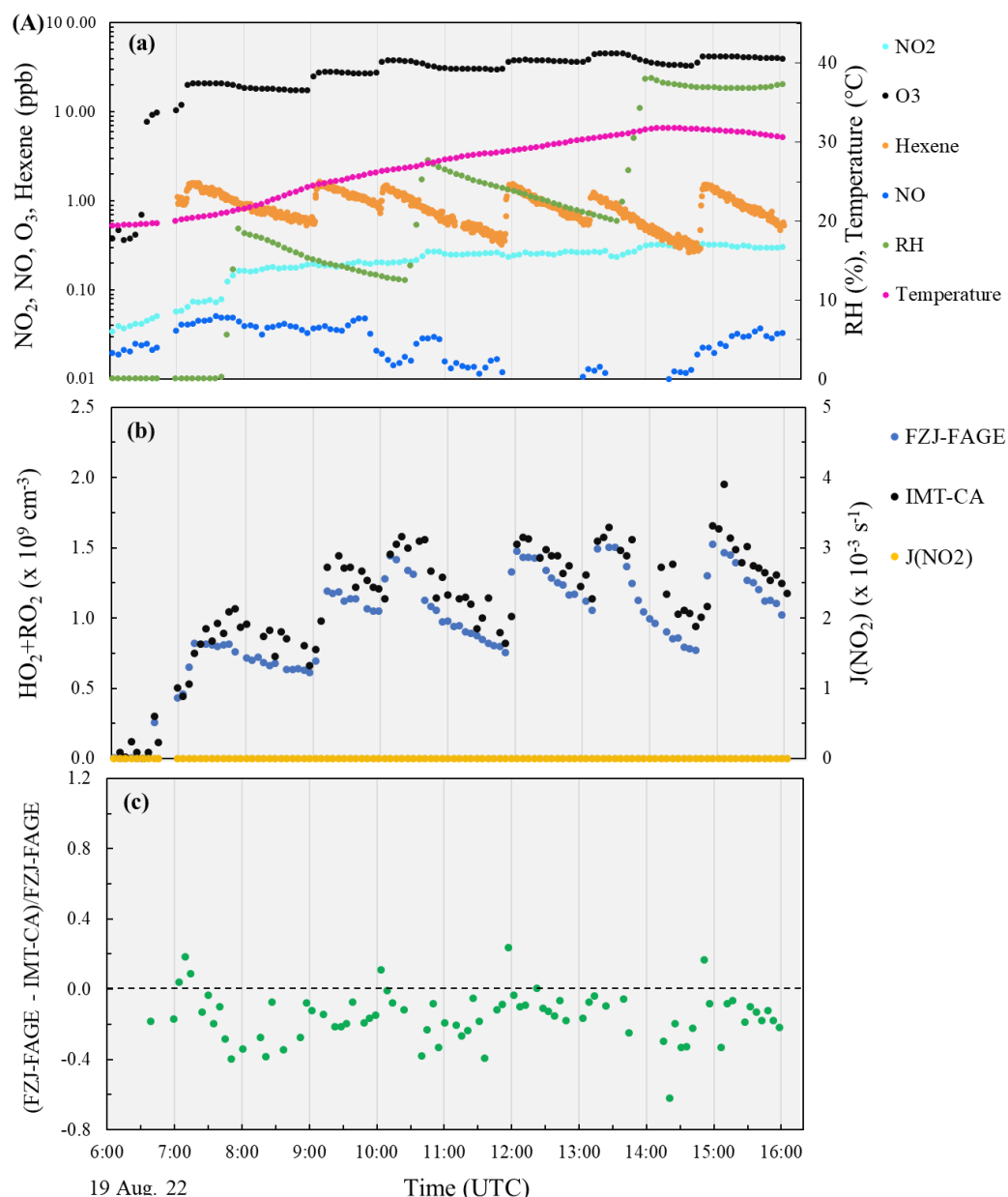
To evaluate a potential impact of RH on IMT-CA measurements and ensure proper calibration of the CL versus humidity, two experiments were selected from Table 3.3 for the comparative analysis between our instrument and FZJ-FAGE. These experiments were selected since water-vapor was added during the course of the experiments.

1. The experiment performed on 19 Aug. 22, focusing on the dark ozonolysis of hexene, during which three humidification steps were made to reach 3 different levels of RH (20, 30 and 39%),
2. The experiment carried out on 20 Aug. 22, focusing on CH<sub>4</sub> photooxidation, which exhibits 2 humidification steps (reaching 10 and 35%).

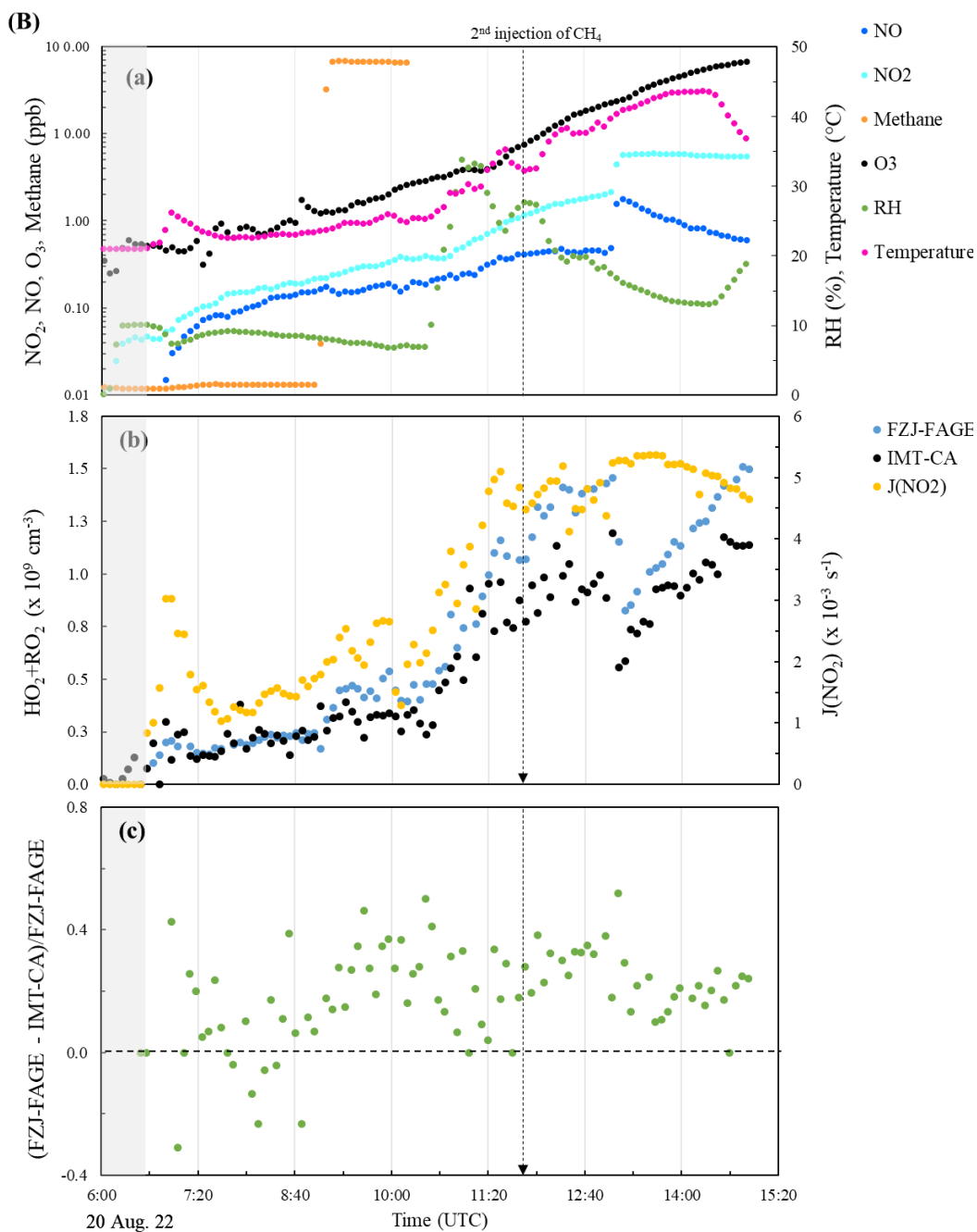
Figure 3.11 presents the results for each experiment, including HO<sub>2</sub>+RO<sub>2</sub> concentrations measured by the two radical instruments, time series of parameters of interest (NO<sub>x</sub>, O<sub>3</sub> and VOC concentrations, RH, temperature and J(NO<sub>2</sub>)) as well as the relative agreement between IMT-CA and FZJ-FAGE. The latter is shown as the difference in HO<sub>2</sub>+RO<sub>2</sub> concentrations measured by the two instruments normalized to the FZJ-FAGE measurements.

During the dark experiment conducted on 19 Aug., which consisted in the ozonolysis of trans-2-hexene, a good agreement is observed between IMT-CA and FZJ-FAGE when water-vapor was introduced into the chamber at three distinct times (7:40, 10:27 and 13:36). The IMT-CA measurements are systematically higher by approximately 18%, which is

within the combined uncertainties from the two instruments. No change in the agreement was noticeable each time water-vapor was added in the chamber. The scatter plot in Figure 3.12 (a) indicates a slope of  $1.05 \pm 0.04$  and an intercept of  $(9.5 \pm 3.7) \times 10^7 \text{ cm}^{-3}$ , with a coefficient of determination of 0.91. This slope of 1.05, when compared to the 18% averaged overestimation of IMT-CA mentioned above, seems to indicate that the difference between the 2 instruments is mainly due to a constant offset in one (or both) measurement datasets.



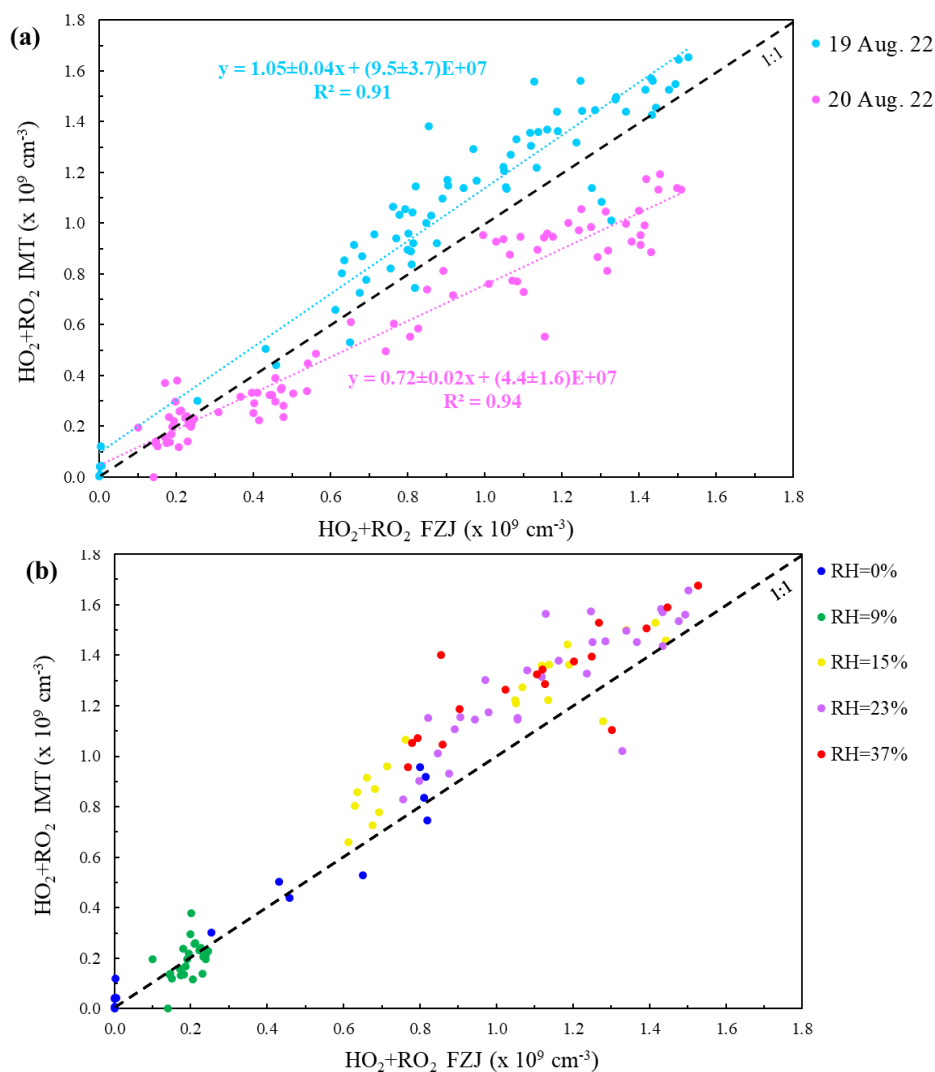
**Figure 3.11:** Results from selected RH-relevant experiments - (A) 19 Aug. 22 and (B) 20 Aug. 22. For each experiment, panel (a): temporal variation of different parameters (NO, NO<sub>2</sub>, O<sub>3</sub>, VOC, RH, temperature), panel (b): HO<sub>2</sub>+RO<sub>2</sub> concentrations measured by IMT-CA and FZJ-FAGE and photolysis rate measurements of NO<sub>2</sub> (J(NO<sub>2</sub>)), and panel (c): ratio of HO<sub>2</sub>+RO<sub>2</sub> concentrations (FZJ-FAGE-IMT-CA)/ FZJ-FAGE. The gray area indicates dark conditions.



**Figure 3.11(continued)**

The absence of an RH effect on the IMT-CA measurements is confirmed by the experiment performed on 20 Aug., where the addition of water-vapor at 10:29 did not change the agreement between the 2 instruments. It should be noted that the agreement between IMT-CA and FZJ-FAGE for this experiment is not as good as on 19 Aug., likely due to the injection of methane at 09:03 and 11:48. Indeed, the photooxidation of methane leads to the formation of methyl peroxy radicals (CH<sub>3</sub>O<sub>2</sub>), whose detection is hampered by a poor conversion into HO<sub>2</sub> in the CA reactors, as already discussed in section 3.2.

The scatter plot for this experiment, shown in Figure 3.12 (a), indicates a slope of  $0.72 \pm 0.02$ , which would be consistent with a large fraction of peroxy radicals being  $\text{CH}_3\text{O}_2$ . For instance, if the pool of peroxy radicals was partitioned into 25% of  $\text{HO}_2$  and 75% of  $\text{CH}_3\text{O}_2$ , we would expect IMT-CA to underestimate the FZJ-FAGE measurements by 27% (detection of only 64% of  $\text{CH}_3\text{O}_2$  by IMT-CA, see page 125). This aspect will be further investigated through 0-D box modeling, which will allow assessing the partitioning between peroxy radicals.



**Figure 3.12:** Correlation between IMT-CA and FZJ-FAGE measurements for the RH-relevant experiments. Color coding based on (a) the dates: 19 Aug. 22 (blue dots) and 20 Aug. 22 (pink dots), and (b) RH level: 0% (blue dots), 9% (green dots), 15% (yellow dots), 23% (purple dots) and 37% (red dots)

Figure 3.12 (b) depicts scatter plots of IMT-CA vs. FZJ-FAGE for the two experiments together, with a color coding based on the RH level. Data from the 20 Aug. experiment acquired after the methane injections is not taken in consideration for the reason mentioned

above. This plot reveals a good correlation between the two instruments for the different levels of RH with an average agreement within 11%. This further validates the absence of a significant RH effect on the IMT-CA measurements, highlighting that the CL is correctly calibrated as a function of RH (section 3.2).

In summary, these experiments have demonstrated a strong correlation between the IMT-CA and FZJ-FAGE measurements. Absolute concentrations measured by the two instruments are within measurement uncertainty, i.e 31% for IMT-CA and 32/36% for HO<sub>2</sub>/RO<sub>2</sub> from FZJ-FAGE at 2 $\sigma$ <sup>94</sup>, and significant humidity effects are not observed. Overall, the comparison discussed in this section allowed validating the calibration procedure used to infer the CL dependence on water and the reliability of the IMT-CA instrument under the range of RH conditions used in the selected experiments.

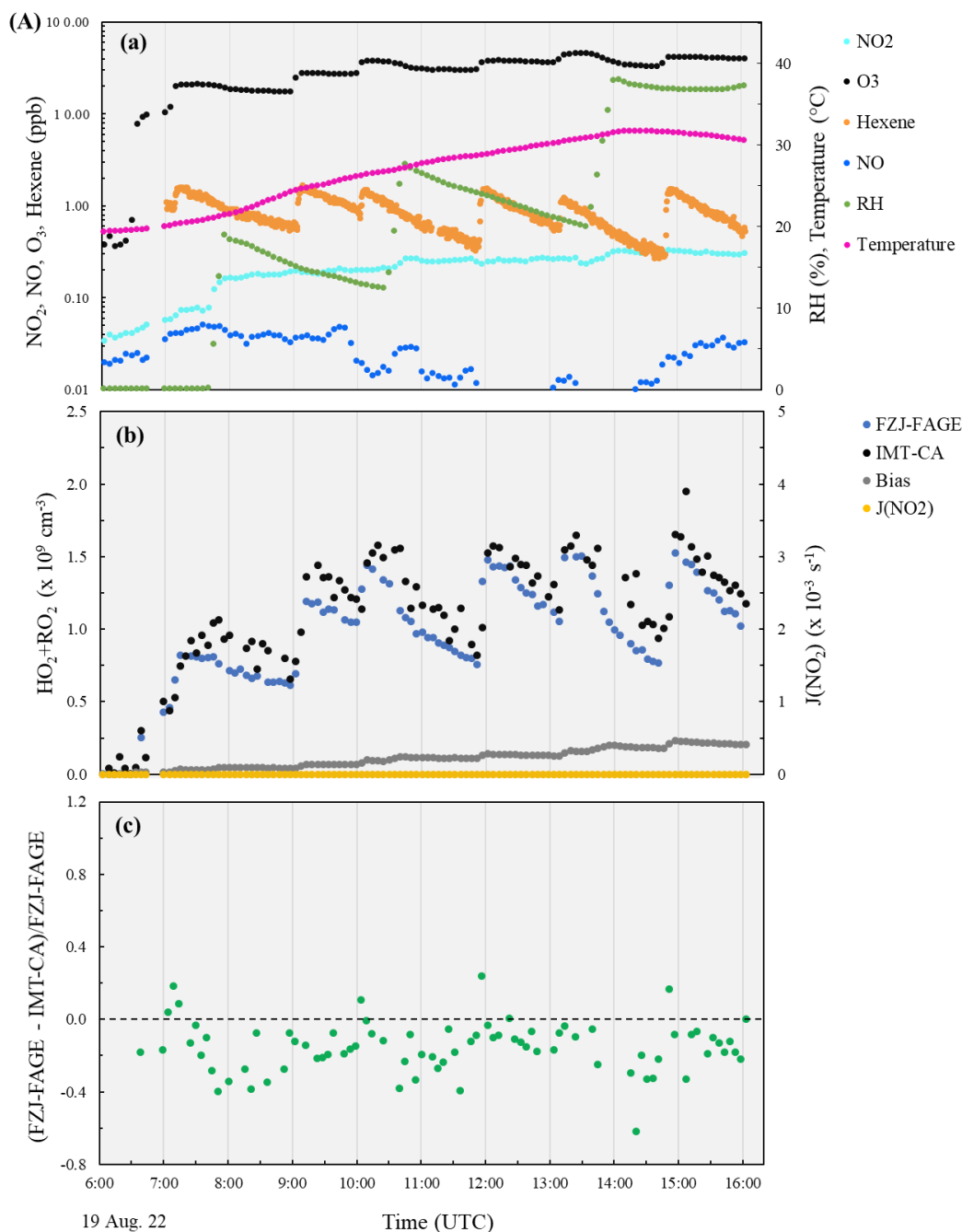
## 4.2. Assessment of O<sub>3</sub> effects

As described in section 3.3, IMT-CA was found to be impacted by a measurement bias when ozone is present. While this bias is accounted when retrieving ambient concentrations of peroxy radical, its origin is not well understood. A second series of comparison was made to check whether this O<sub>3</sub>-water bias is well corrected and to assess potential other impacts of O<sub>3</sub> on the IMT-CA measurements. Two experiments were selected for this study:

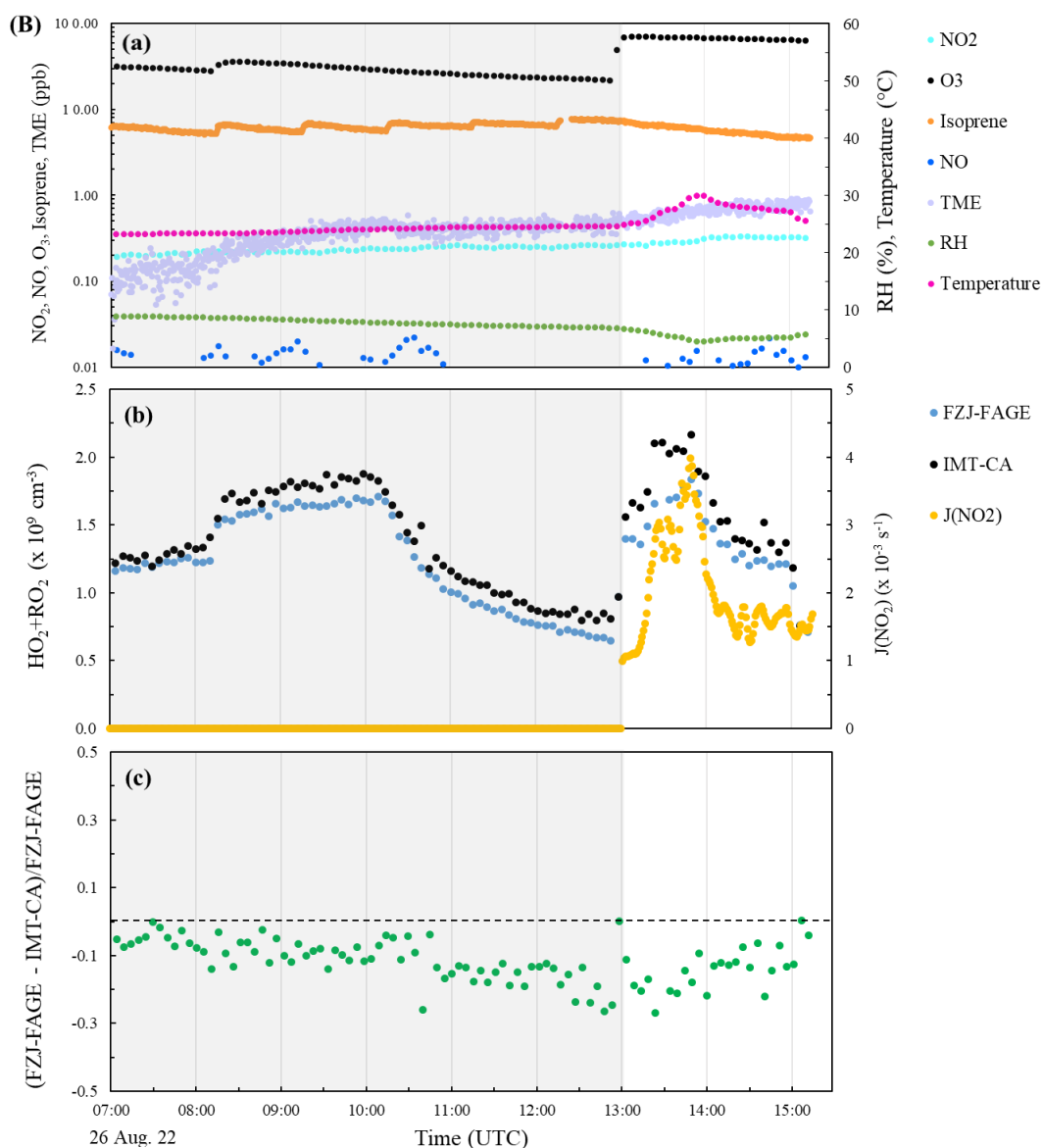
1. The experiment carried out on 19 Aug. 22, already presented in the previous section. This experiment involves the ozonolysis of hexene under dark conditions, during which seven injections of O<sub>3</sub> were performed to reach levels of 10, 20, 28, 30, 38, 46 and 42 ppb.
2. The experiment performed on 26 Aug. 22, consisting in the oxidation of isoprene by OH under dark and dry conditions, OH being produced from the reaction between O<sub>3</sub> and TME. During this experiment 3 injections of O<sub>3</sub> were performed under dark conditions (30, 35 and 70 ppb) and the chamber was irradiated by the solar light during the last 2 hours.

Figure 3.13 presents time series of different parameters (RH, temperature and J(NO<sub>2</sub>)), species concentrations (NO<sub>x</sub>, O<sub>3</sub>, VOC, HO<sub>2</sub>+RO<sub>2</sub> measured by IMT-CA and FZJ-FAGE), the O<sub>3</sub>-water bias that was subtracted from IMT-CA measurements (calculated from O<sub>3</sub> and H<sub>2</sub>O as described in section 3.3), as well as the relative agreement between IMT-CA and FZJ-FAGE measurements.





**Figure 3.13:** Results from selected O<sub>3</sub>-relevant experiments - (A) 19 Aug. 22 and (B) 26 Aug. 22. For each experiment, panel (a): temporal variation of different parameters (NO, NO<sub>2</sub>, O<sub>3</sub>, VOC, RH, temperature), panel (b): HO<sub>2</sub>+RO<sub>2</sub> concentrations measured by IMT-CA and FZJ-FAGE, the bias in the IMT-CA measurements related to the presence of O<sub>3</sub> and photolysis rate measurements of NO<sub>2</sub> (J(NO<sub>2</sub>)), and panel (c): the ratio of HO<sub>2</sub>+RO<sub>2</sub> concentrations (FZJ-FAGE-IMT-CA)/FZJ-FAGE. The gray shadow is an indication of dark conditions.



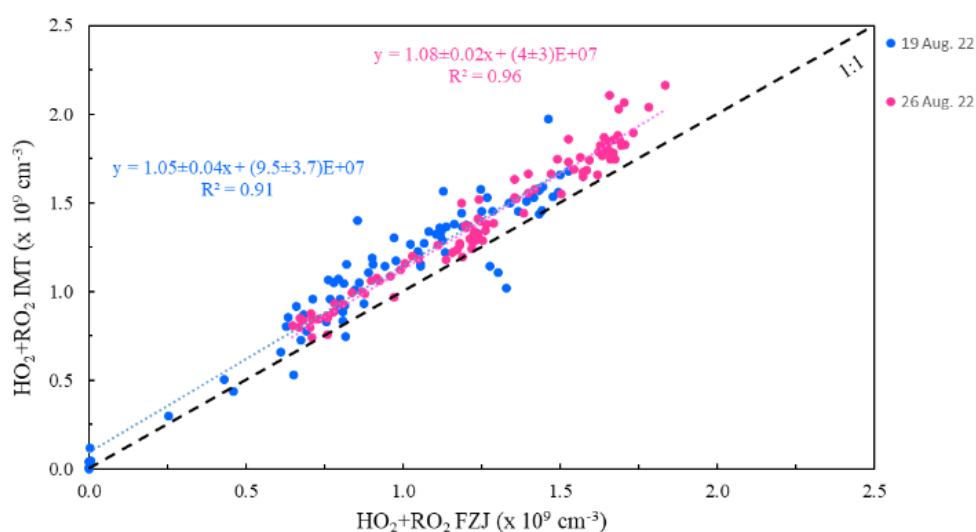
**Figure 3.13 (continued)**

The results for the 19 Aug. experiment are presented in Figure 3.13 (A). When focusing on the times where O<sub>3</sub> was added in the chamber (6:30, 7:05, 9:00, 10:00, 11:52, 13:08 and 14:46), we notice a good agreement between IMT-CA and FZJ-FAGE. The relative agreement does not change significantly between the 2 instruments when O<sub>3</sub> is added. As mentioned in the previous section, a systematic difference is observed between the two radical instruments, with IMT-CA measurements being higher by approximately 18% all along the experiment, despite variations in the O<sub>3</sub> concentration. The correlation between IMT-CA and FZJ-FAGE measurements depicted in Figure 3.14 reveals a slope of  $1.05 \pm 0.04$  and an intercept of  $(9.5 \pm 3.7) \times 10^7 \text{ cm}^{-3}$ , with a determination coefficient of 0.91.

Similar conclusions are drawn from the 26 Aug. experiment, where a good agreement is observed between IMT-CA and FZJ-FAGE at the different times that O<sub>3</sub> was injected. It was found that the IMT-CA measurements are systematically higher than the FZJ-FAGE measurements by approximately 12% on average. While a slight increase in this difference was observed at the opening of the shutter system, up to 19%, it rapidly decreased to approximately 11%, despite the presence of a high concentration of O<sub>3</sub> (~ 70 ppb).

The scatter plot between the two radical instruments shown in Figure 3.14 reveals a slope of  $1.08 \pm 0.02$  and an intercept of  $(4 \pm 3) \times 10^7 \text{ cm}^{-3}$ , with a good determination coefficient of 0.96. Similarly to the 19 Aug. experiment, this slope of 1.08, when compared to the 12% averaged overestimation of IMT-CA, seems to indicate that the difference between the 2 instruments is mainly due to a constant offset in one (or both) measurement datasets.

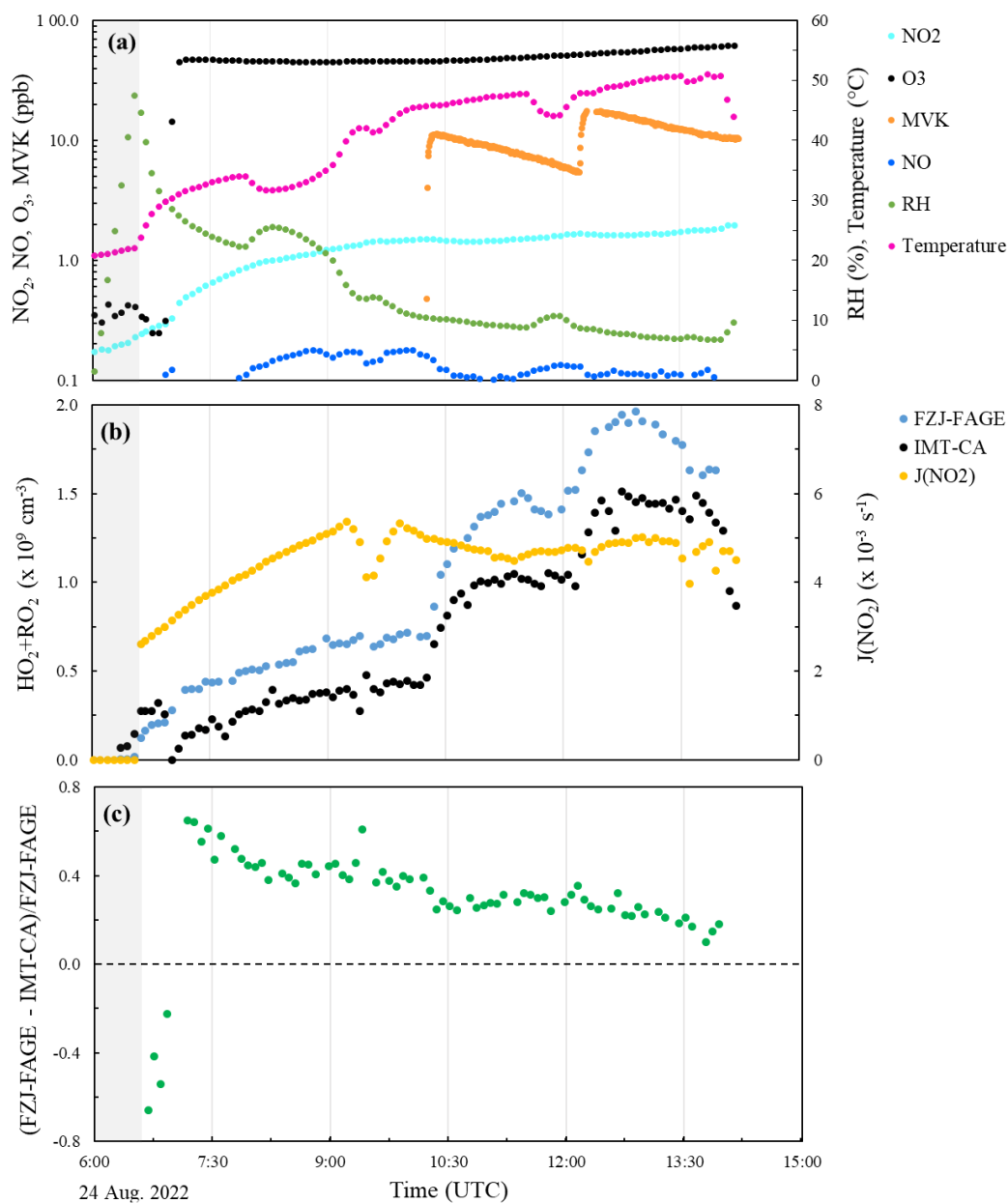
These findings confirm the absence of a significant O<sub>3</sub> effect on the IMT-CA measurements, under varying conditions of humidity and irradiation, and suggest a successful removal of the O<sub>3</sub>-water bias characterized in section 3.3.



**Figure 3.14:** Correlation between IMT-CA and FZJ-FAGE measurements for the experiments of 19 Aug. 22 (blue dots) and 26 Aug. 22 (pink dots)

However, one experiment performed during ROxComp on 24 Aug., seems to indicate that the O<sub>3</sub>-water bias was not subtracted correctly. During this day, O<sub>3</sub> was injected shortly after the beginning of the experiments. A close look at Figure 3.15 indicates that after the injection, the HO<sub>2</sub>+RO<sub>2</sub> concentration measured by FZJ-FAGE increases slightly while the bias-corrected concentration from IMT-CA decreases significantly. A systematic difference is then observed between the two instruments all along the experiment, this difference being

close to the O<sub>3</sub>-water bias that was subtracted from the IMT-CA measurements. This point is puzzling and requires further testing of IMT-CA to determine whether the disagreement observed in this experiment is due to an inaccurate subtraction of the O<sub>3</sub>-water bias.



**Figure 3.15:** Results from 24 Aug. experiment. Panel (a): temporal variation of different parameters (NO, NO<sub>2</sub>, O<sub>3</sub>, VOC, RH, temperature), panel (b): HO<sub>2</sub>+RO<sub>2</sub> concentrations measured by IMT-CA and FZJ-FAGE and photolysis rate measurements of NO<sub>2</sub> (J(NO<sub>2</sub>)), and panel (c): the ratio of HO<sub>2</sub>+RO<sub>2</sub> concentrations (FZJ-FAGE - IMT-CA)/FZJ-FAGE. The gray shadow is an indication of dark conditions.

### 4.3. Assessment of NO effects

Nitrogen monoxide (NO) has a significant impact on the chemistry of peroxy radicals in ambient air as discussed in section 1.2.1 (chapter 1) and section 2.1 (chapter 4). Two

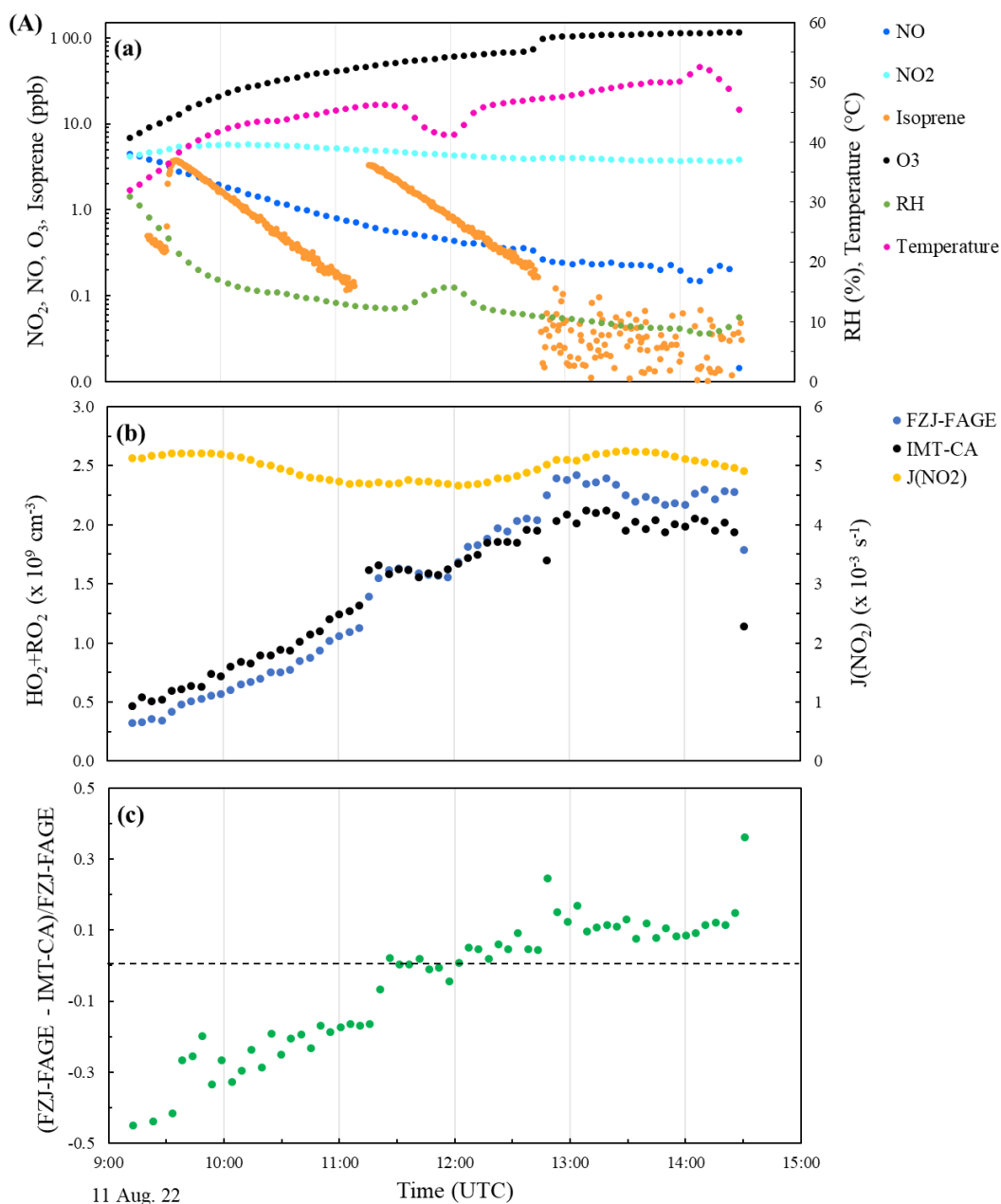
chemical regimes of oxidation are usually referred to as low-NO and high-NO. It is therefore interesting to assess whether there is a potential influence of NO on IMT-CA measurements. Four experiments involving the injection of NO in the chamber were selected for this comparison:

1. The 11 Aug. 22 experiment, which consisted in the photooxidation of isoprene, under humid conditions, with an injection of NO at the beginning of the experiment,
2. The 12 Aug. 22 experiment, focusing on the photooxidation of iso-pentane and hexane under humid conditions, with two injections of NO at the beginning and halfway the experiment,
3. The 14 Aug. 22 experiment, consisting in a photooxidation experiment using Mesitylene, under humid conditions, with an injection of NO at the beginning of the experiment,
4. The 20 Aug. 22 experiment, already presented in section 4.1, focusing on the photooxidation of methane under humid conditions with the injection of NO towards the end of the experiment.

The experimental results, depicted in Figure 3.16, led to several significant findings summarized below for each experiment:

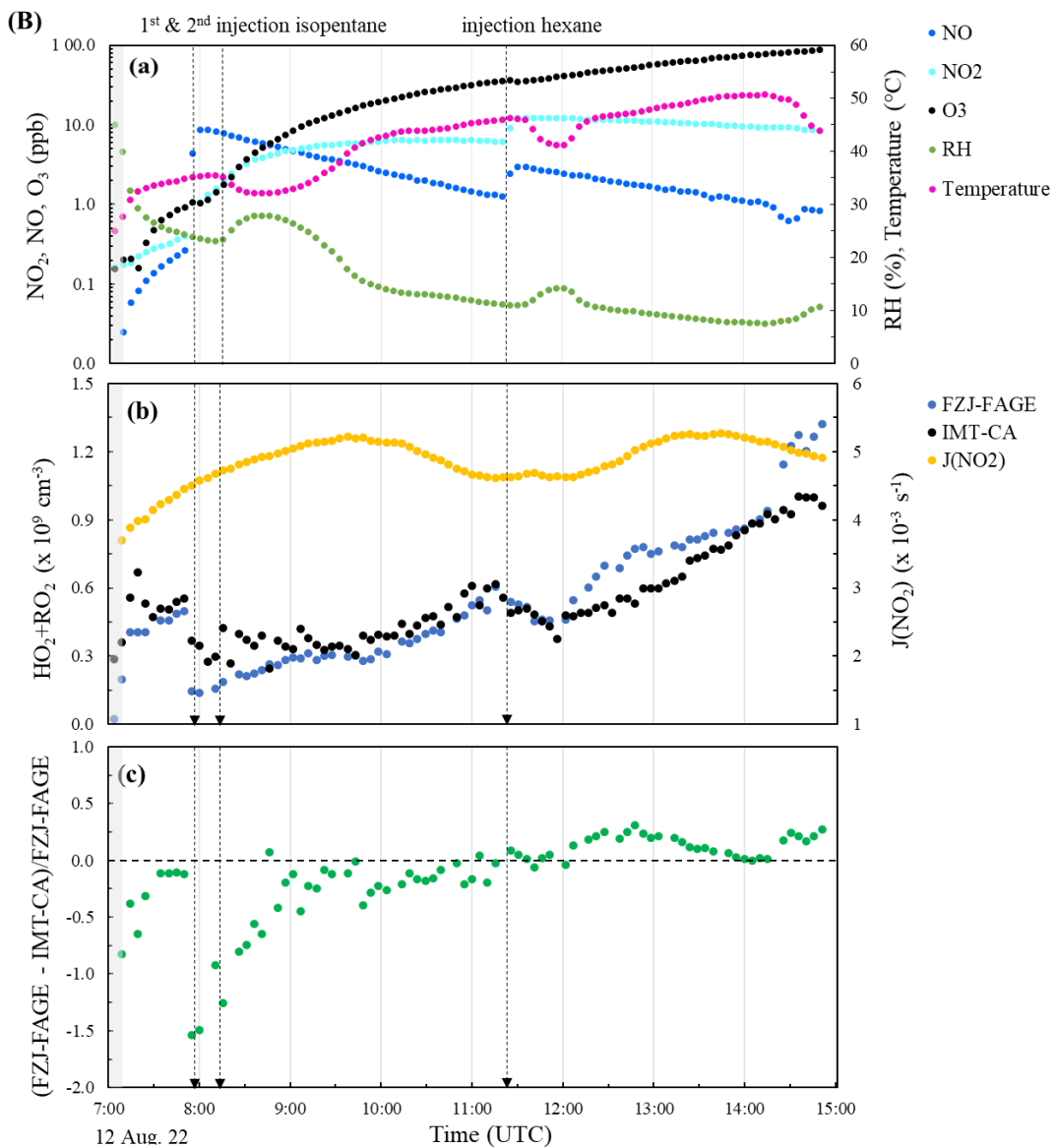
- 11 Aug. experiment (Figure 3.16 (A)): The agreement between IMT-CA and FZJ-FAGE is within 30% most of the time. While the difference between the 2 instruments is within the combined measurement uncertainty, it is clear that a systematic dependence on NO is observed. An overestimation of about 30% is seen for IMT-CA at the beginning of the experiment after the injection of 10 ppb of NO. Then a good agreement is achieved between the two radical instruments for NO concentrations ranging from 0.3-1 ppb. The agreement worsens afterwards when NO decreases below 300 ppt, with an underestimation of 11% on average for IMT-CA.
- 12 Aug. experiment (Figure 3.16, (B)): A similar trend with NO is observed for the agreement between IMT-CA and FZJ-FAGE. The first injection of 10 ppb of NO at 07:53 resulted in lower HO<sub>2</sub>+RO<sub>2</sub> concentrations in the chamber as shown by both instruments, which is due to the fast reaction between peroxy radicals and NO. An average overestimation of IMT-CA by approximately 30% is observed after this

injection of NO, which is consistent with the previous experiment. This overestimation decreases over time, together with NO, and a good agreement is observed around 11:30 when NO is close to 1 ppb. An underestimation from IMT-CA is then observed from 12:00 until almost the end of the experiment when NO is lower than 2.3 ppb.



**Figure 3.16:** Results from selected NO-relevant experiments - (A) 11 Aug. 22, (B) 12 Aug. 22, (C) 14 Aug. 22 and (D) 20 Aug. 22. For each experiment, panel (a): temporal variation of different parameters (NO, NO<sub>2</sub>, O<sub>3</sub>, VOC, RH, temperature) and panel (b): HO<sub>2</sub>+RO<sub>2</sub> concentrations measured by IMT-CA and FZJ-FAGE and photolysis rate measurements of NO<sub>2</sub> (J(NO<sub>2</sub>)). (c): the ratio of HO<sub>2</sub>+RO<sub>2</sub> concentrations: (FZJ-FAGE-IMT-CA)/FZJ-FAGE. The gray shadow is an indication of dark conditions.

- 14 Aug. experiment (Figure 3.16 (C)): By the opening of the shutter system, significant peroxy radical concentrations of about  $5.5 \times 10^8 \text{ cm}^{-3}$  and  $6.5 \times 10^8 \text{ cm}^{-3}$  are measured by FZJ-FAGE and IMT-CA, respectively. Similarly to the two other experiments discussed above, the injection of 10 ppb of NO at 08:50 led to an average overestimation of  $\text{HO}_2 + \text{RO}_2$  of approximately 23% by IMT-CA. This difference decreased with NO overtime and a good agreement between the two instruments is observed from 9:30 to 11:20 when NO ranges from 0.2-1.0 ppb. A small but systematic underestimation of 5% is then observed after 11:20 for IMT-CA when NO is lower than 200 ppt.



**Figure 3.16 (continued)**

- 20 Aug. experiment (Figure 3.16 (D)): A good agreement between the two instruments is initially observed for NO concentrations lower than 200 ppt, which

later on is worsened by injections of  $\text{CH}_4$ . These injections led to an underestimation of IMT-CA due to the formation of  $\text{CH}_3\text{O}_2$  that is not efficiently detected by the CA as discussed in sections 3.2 and 4.1. The addition of 5 ppb of NO at 13:04 impacted the relative agreement between IMT-CA and FZJ-FAGE, the IMT-CA underestimation being reduced from approximately 30% to 20% on average. This behavior is consistent with the 3 previous experiments since it indicates that IMT-CA measurements increase faster with NO than FZJ-FAGE measurements.

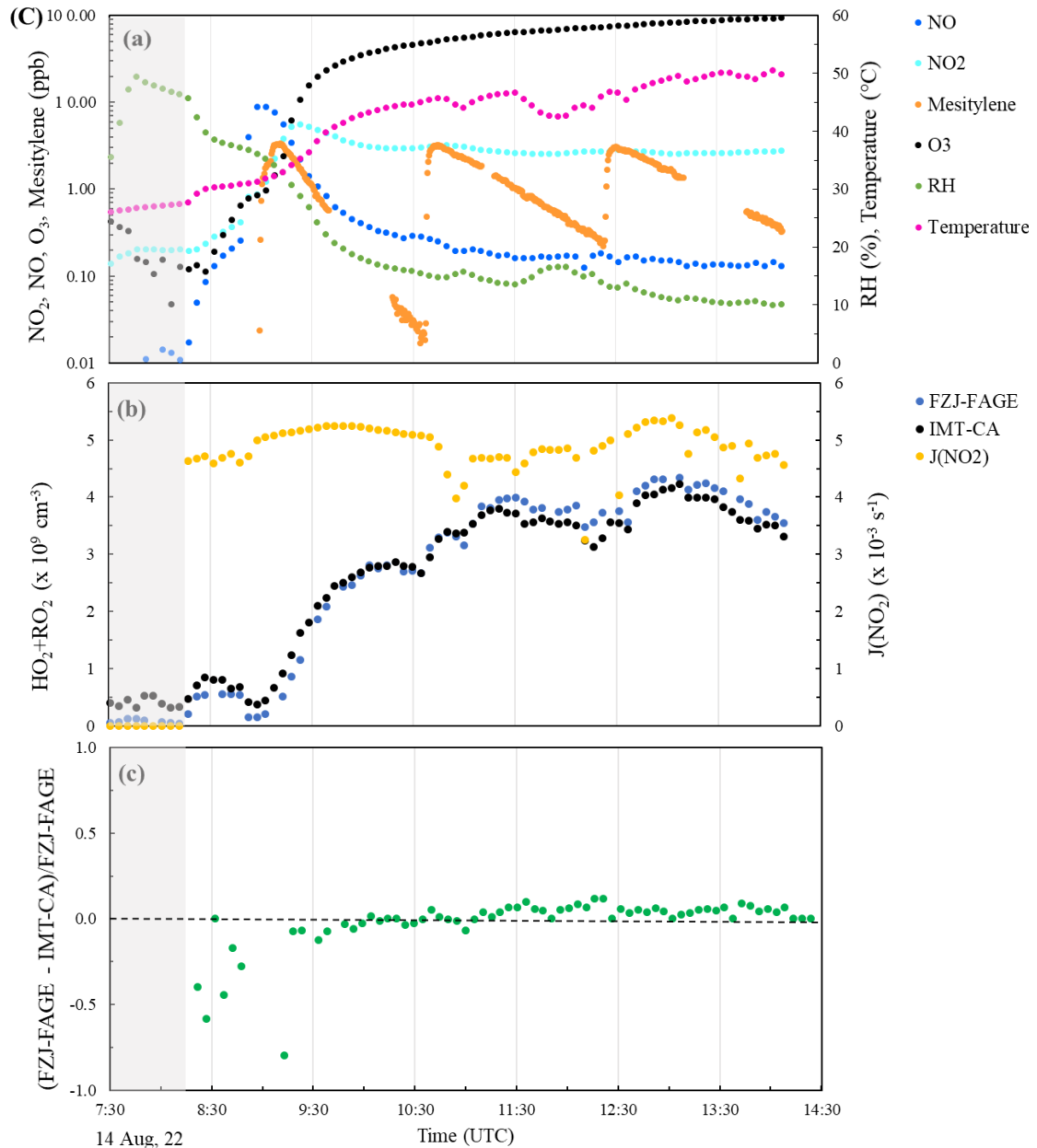


Figure 3.16 (continued)



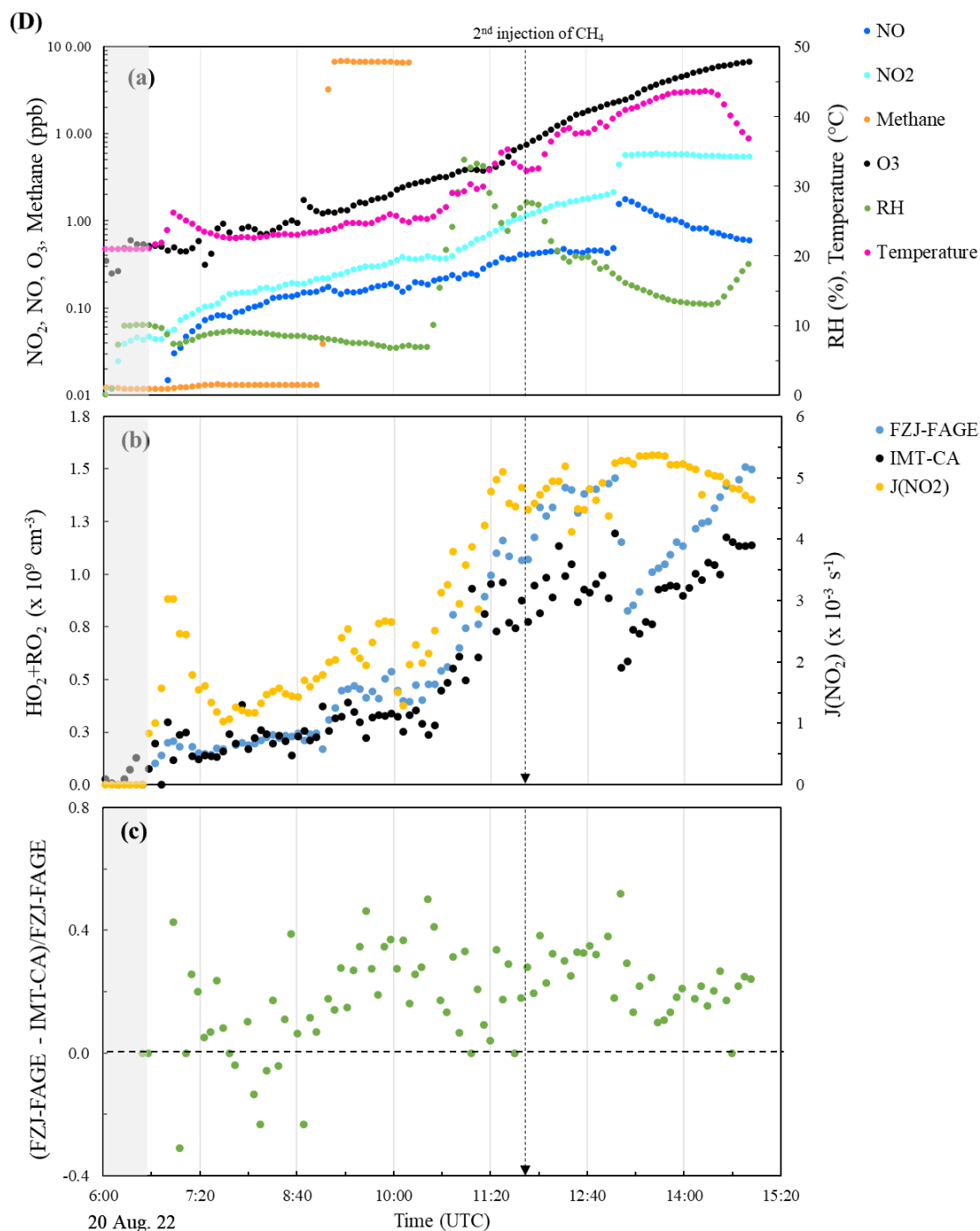
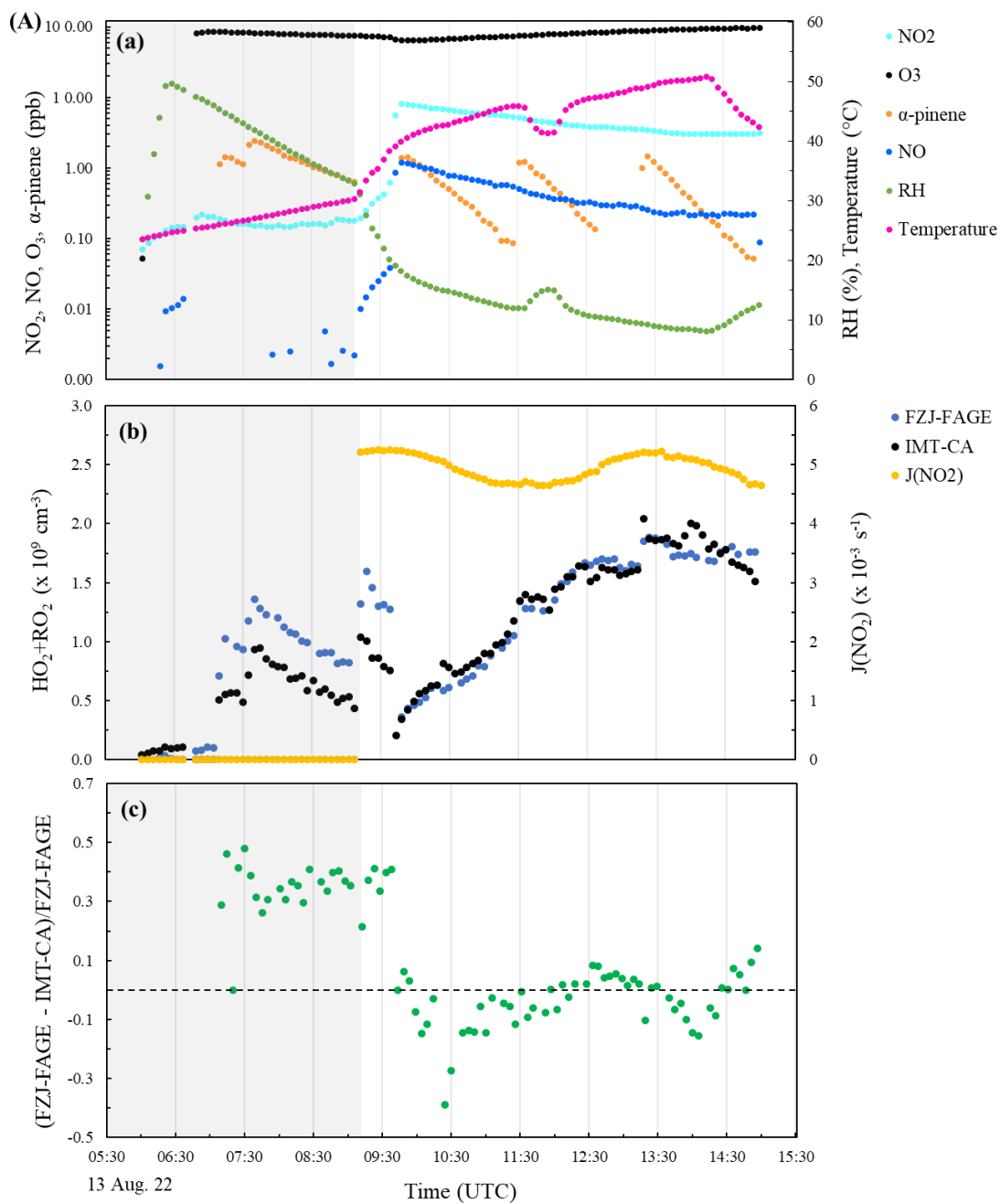
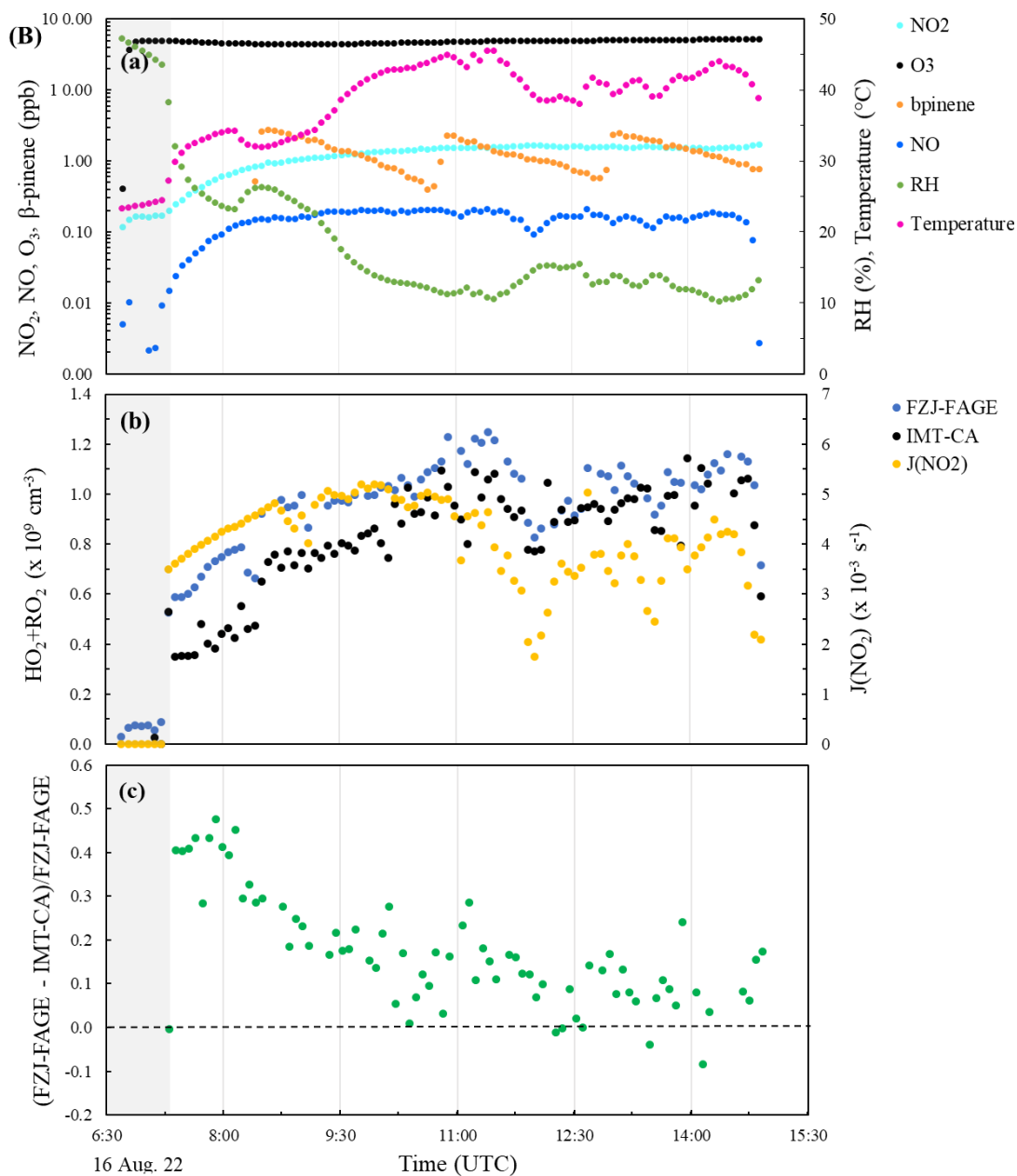


Figure 3.16 (continued)

In addition to the experiments discussed above, it is interesting to note that other experiments (NO ranging from < LoD -1 ppb) are consistent with this NO trend. Both the 13 Aug. experiment, which partly consisted in the dark ozonolysis of  $\alpha$ -pinene, and the 16 Aug. experiment, which consisted in the photooxidation of  $\beta$ -pinene under humid and low NO<sub>x</sub> conditions, show that IMT-CA measures lower concentrations than FZJ-FAGE (Figure 3.17).



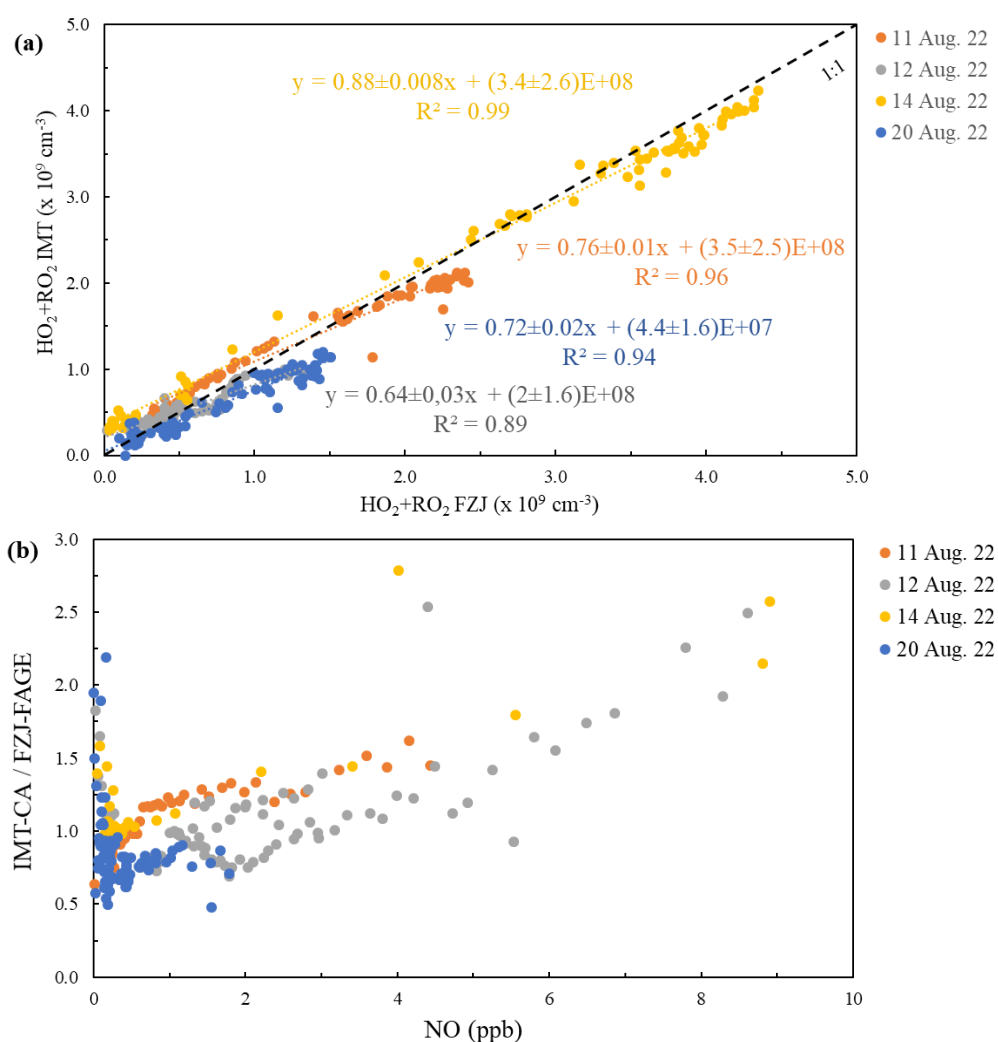
**Figure 3.17:** Results from selected Low  $\text{NO}_x$ -relevant experiments - (A) 13 Aug. 22 and (B) 16 Aug. 22. For each experiment, panel (a): temporal variation of different parameters ( $\text{NO}$ ,  $\text{NO}_2$ ,  $\text{O}_3$ , VOC, RH, temperature) and panel (b):  $\text{HO}_2 + \text{RO}_2$  concentrations measured by IMT-CA and FZJ-FAGE and photolysis rate measurements of  $\text{NO}_2$  ( $J(\text{NO}_2)$ ). (c): the ratio of  $\text{HO}_2 + \text{RO}_2$  concentrations:  $(\text{FZJ-FAGE} - \text{IMT-CA})/\text{FZJ-FAGE}$ . The gray shadow is an indication of dark conditions.



**Figure 3.17 (continued)**

By analyzing how IMT-CA and FZJ-FAGE measurements correlates across the four selected experiments in Figure 3.18 (a), it is clear that a strong correlation is observed for all experiments, with determination coefficients higher than 0.89. On the other hand, significant differences are noted between the linear regressions, with slopes ranging from 0.64 to 0.88. Assuming that FZJ-FAGE detect all the  $\text{RO}_2$  radicals with the same efficiency, one would expect the slopes from the linear regressions to scale with the CA detection efficiency of the detected  $\text{RO}_2$  radicals, i.e. with  $(1-Y)$ ,  $Y$  being the fraction of  $\text{RO}_2$  radicals converted into nitrate and nitrite organic compounds during the  $\text{RO}_2$ -to- $\text{HO}_2$  conversion step in the CA as discussed in section 3.2. Duncianu et al. (2020) showed that this

relationship is observed when IMT-CA is calibrated using different mixtures of HO<sub>2</sub>+RO<sub>2</sub> by adding different VOCs in the calibrator. According to the MCM<sup>148</sup>, Y varies as follows: Isoprene-RO<sub>2</sub>: 8.7% (11 Aug.) < Mesitylene-RO<sub>2</sub>: 15.7% (14 Aug.) < Pentane- and hexane-RO<sub>2</sub>: 18% on average (12 Aug.) < Methane-RO<sub>2</sub>: 36% (20 Aug.). The ranking of the linear regression slopes should therefore be as follows: Isoprene-RO<sub>2</sub> > Mesitylene-RO<sub>2</sub> > Pentane- and hexane-RO<sub>2</sub> > Methane-RO<sub>2</sub>, which is not consistent with Figure 3.18 (a). It is believed that part of this inconsistency is also due to the impact of NO on the IMT-CA/FZJ-FAGE agreement, but also to detection efficiencies that could be RO<sub>2</sub>-dependent on the FAGE instrument as reported in Fuchs et al. (2008)<sup>52</sup>. Indeed, the authors reported relative sensitivities of 0.91, 0.59 and 1.21 for ethane-, isobutane- and isoprene-based peroxy radicals when methyl peroxy radicals are taken as a reference.



**Figure 3.18:** Correlations between (a) IMT-CA and FZJ-FAGE measurements and (b) the IMT-CA/FZJ-FAGE ratio and NO for the NO-relevant experiments of 11 Aug. 22 (isoprene, orange dots), 12 Aug. 22 (isopentane+hexane, grey dots), 14 Aug. 22 (mesitylene, yellow dots) and 20 Aug. 22 (methane, blue dots).

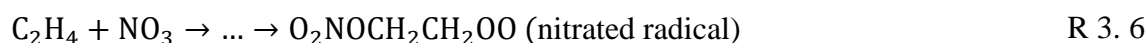
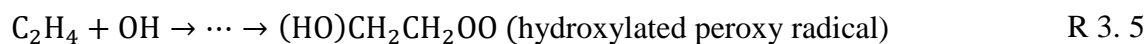
The IMT-CA/FZJ-FAGE measurement ratio is depicted as function of NO in Figure 3.18 (b). It is noteworthy that when the ratio is plotted as a function of NO<sub>x</sub> instead of NO, no correlation is observed. It is clear from this figure that, as discussed above, all experiments exhibit a similar trend with NO. The difference noticed between two groups of experiments, i.e. 11 Aug./14 Aug. and 12 Aug./20 Aug., is likely due to the former group being characterized by peroxy radicals that are more efficiently detected by the CA (organic nitrate and nitrite yields of 8.7-15.7%) than the later (yields of 18-36%).

In summary from this series of comparisons, it has been deduced that the presence of high NO concentrations in the medium (>1 ppb) led to an overestimation of HO<sub>2</sub>+RO<sub>2</sub> concentrations measured by IMT-CA when compared to the FZJ instrument. In contrast, IMT-CA systematically measured lower peroxy radical concentrations than FZJ-FAGE at NO concentrations lower than 200 ppt. A good agreement is only observed when NO ranges from 300ppt-1ppb. While this systematic behavior needs to be further investigated, and needs to be understood, these results indicate that the IMT-CA measurements are within ±30% of the FZJ-FAGE measurements when NO ranges from 0.003-8.9 ppb.

#### **4.4. Detection efficiency for various types of peroxy radicals**

As already mentioned, peroxy radicals were produced through the oxidation of various VOCs as indicated in Table 3.3. To simulate natural atmospheric oxidation processes, three different oxidants were used for initiating oxidation reactions in SAPHIR. The main oxidant was OH (photooxidation, 10 experiments reported in Table 3.3). Additionally, two other oxidants, namely O<sub>3</sub> (3 experiments) and NO<sub>3</sub> (2 experiments), were used to assess the capability of the various instruments in detecting a large range of peroxy radicals.

To illustrate this aspect, we used ethylene as an example below, since it reacts with the three oxidants mentioned above. This VOC was not used in any of the RO<sub>x</sub>Comp experiments, but it is used here for simplicity compared to other VOCs that involves more reaction pathways, for instance β-pinene. When ethylene is oxidized by OH, NO<sub>3</sub> and O<sub>3</sub>, different types of radicals are generated, such as hydroxylated and nitrated peroxy radicals, as shown in the following reactions:



The Criegee biradical formed in reaction R 3. 7 will then lead to the formation of OH and HO<sub>2</sub>. Larger Criegee intermediates will lead to the formation of organic peroxy radicals, usually carbonylated RO<sub>2</sub> radicals (C=O function).

In the upcoming sections, an analysis of these different types of oxidation is conducted, underlying the potential radicals that were formed during selected experiments. The last section is devoted to investigate the photooxidation in ambient air, which represents the most complex matrix, giving rise to a large variety of peroxy radicals.

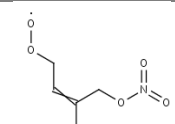
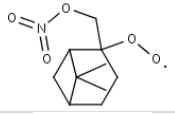
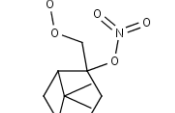
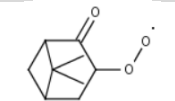
#### 4.4.1. Detection efficiency of nitrooxy-peroxy radicals

To evaluate the IMT-CA performance towards nitrooxy-peroxy radicals, two experiments involving the oxidation of a VOC by NO<sub>3</sub> were selected:

1. The 17 Aug. 22 experiment (Figure 3.19 (A)) consisted in the oxidation of isoprene under dry conditions. This experiment was performed in two distinct stages. The oxidation was first initiated by NO<sub>3</sub>, which was formed through the reaction of O<sub>3</sub> with NO<sub>2</sub> under dark conditions. Then, the oxidation was continued through photooxidation after opening the shutter system,
2. The 22 Aug. 22 experiment (Figure 3.19 (B)) represents another instance of dual oxidation of a VOC using β-pinene. The oxidation was initiated by NO<sub>3</sub> under dark and humid (5% RH) conditions, followed by a period of photooxidation.

Table 3.4 reports first-generation peroxy radicals that are produced when isoprene and β-pinene are oxidized by NO<sub>3</sub> and O<sub>3</sub>. The NO<sub>3</sub> radical adds on a C=C doublebond, which leads to the formation of β-nitrooxy-peroxy radicals for β-pinene and a δ-nitrooxy-peroxy radical for isoprene. The O<sub>3</sub> reaction with β-pinene can also lead to the formation of carbonylated radicals.

**Table 3. 4:** Radicals produced from isoprene and  $\beta$ -pinene oxidation by  $\text{NO}_3$  and  $\text{O}_3$  (dark conditions)

<i>Date</i>	<i>VOC</i>	<i>Radical name*</i>	<i>Structural formula</i>
17 Aug. 22	isoprene	NISOPO2 ( $\text{NO}_3$ )	
22 Aug. 22	$\beta$ -pinene	NBPINAO2 ( $\text{NO}_3$ )	
		NBPINBO2 ( $\text{NO}_3$ )	
		NOPINDO2 ( $\text{O}_3$ )	

\*Radical names from MCM v3.3.1. The oxidant leading to the formation of the radical is reported in parenthesis.

A good agreement between IMT-CA and FZJ-FAGE is observed for the 17 Aug. experiment, with measurements from both instruments being within 20% most of the time. This is particularly evident during the dark oxidation period as shown in Figure 3.19 (A). Throughout this experiment, four injections of approximately 5 ppb of isoprene were performed at different times. Each isoprene injection was consistently accompanied by injections of  $\text{NO}_2$  and  $\text{O}_3$  (amounts ranging from 1 to 6.5 ppb for  $\text{NO}_2$  and from 10 to 50 ppb for  $\text{O}_3$ ).

When the chamber roof was opened, we notice a rapid consumption of isoprene compared to the dark conditions. This is due to the formation of OH ( $3.8 \times 10^6 \text{ cm}^{-3}$  on average from FZJ measurements) and the fast isoprene-OH reaction ( $k_{\text{OH}+\text{isoprene}} = 1 \times 10^{-10} \text{ cm}^3 \text{ molecule}^{-1} \text{ s}^{-1}$ ) compared to the slower isoprene- $\text{NO}_3$  reaction occurring under dark conditions ( $k_{\text{NO}_3} = 6.96 \times 10^{-13} \text{ cm}^3 \text{ molecule}^{-1} \text{ s}^{-1}$ ).

At the beginning of the photooxidation period, we notice an overestimation of IMT-CA by 31% on average compared to the FZJ instrument, which is likely due to the fast change in temperature inside the chamber when the shutter was opened and the CA reactors were quickly warmed by the solar light. This effect was observed during other experiments when the shutter system was opened (12, 14, 24 and 26 Aug.). Indeed, the chemical amplifier's CL strongly depends on RH, which in turn depends on temperature. The current version of

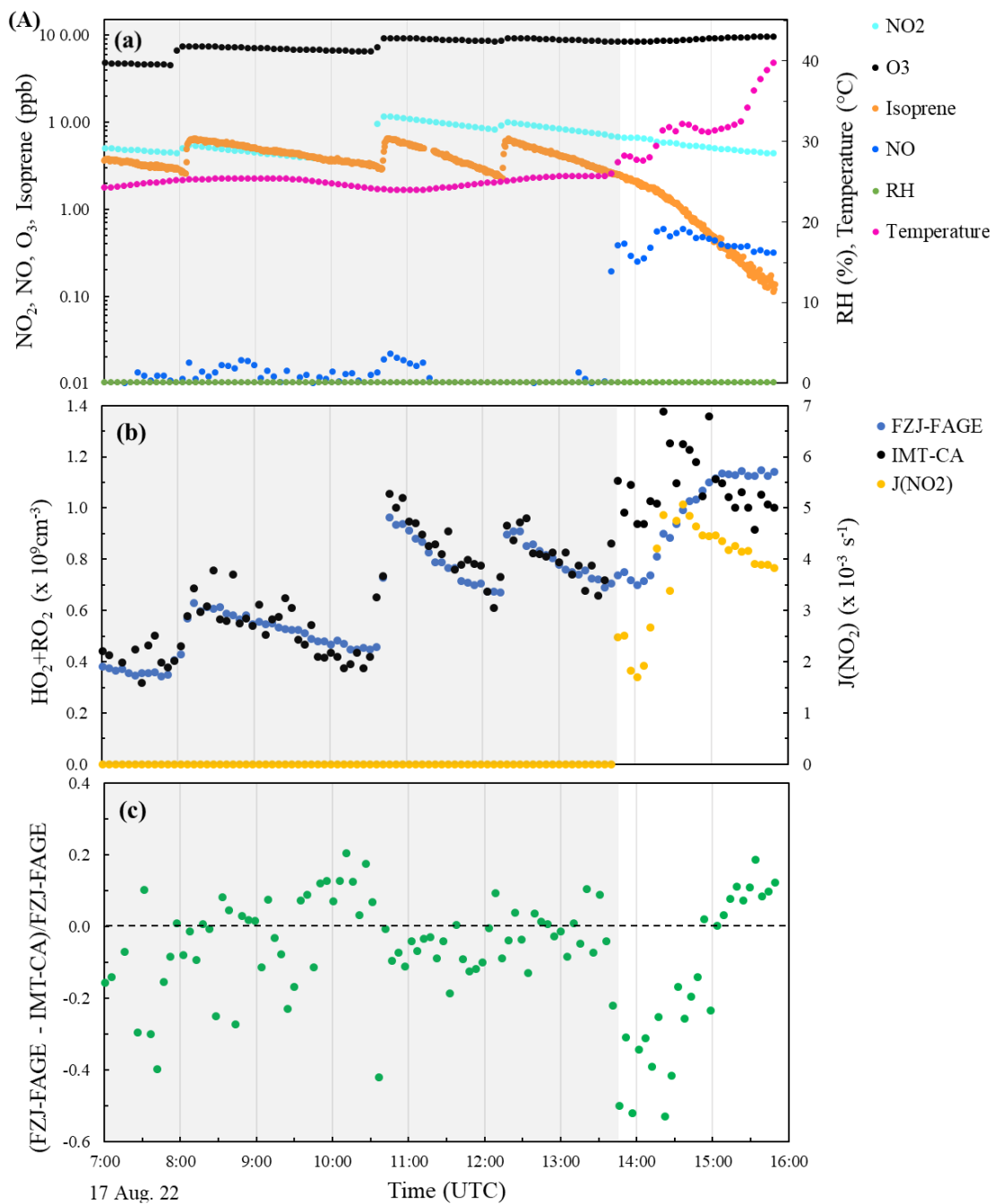
IMT-CA is not equipped with temperature sensors on the CA reactors and RH inside the reactors may diverge from RH measurements performed in the surrounding chamber when the temperature is quickly changing after opening the shutter. Using RH values from the chamber's sensors could lead to a miscalculation of the CL during a short period of time until the CA reactors are thermalized with the surrounding air. Future versions of IMT-CA will need to implement temperature sensors on both reactors.

While the agreement between the two instruments is not as good during the last hour of the experiment, measurements are still within 10%. The cause of this larger disagreement is not well understood yet and will require box modeling for further investigations.

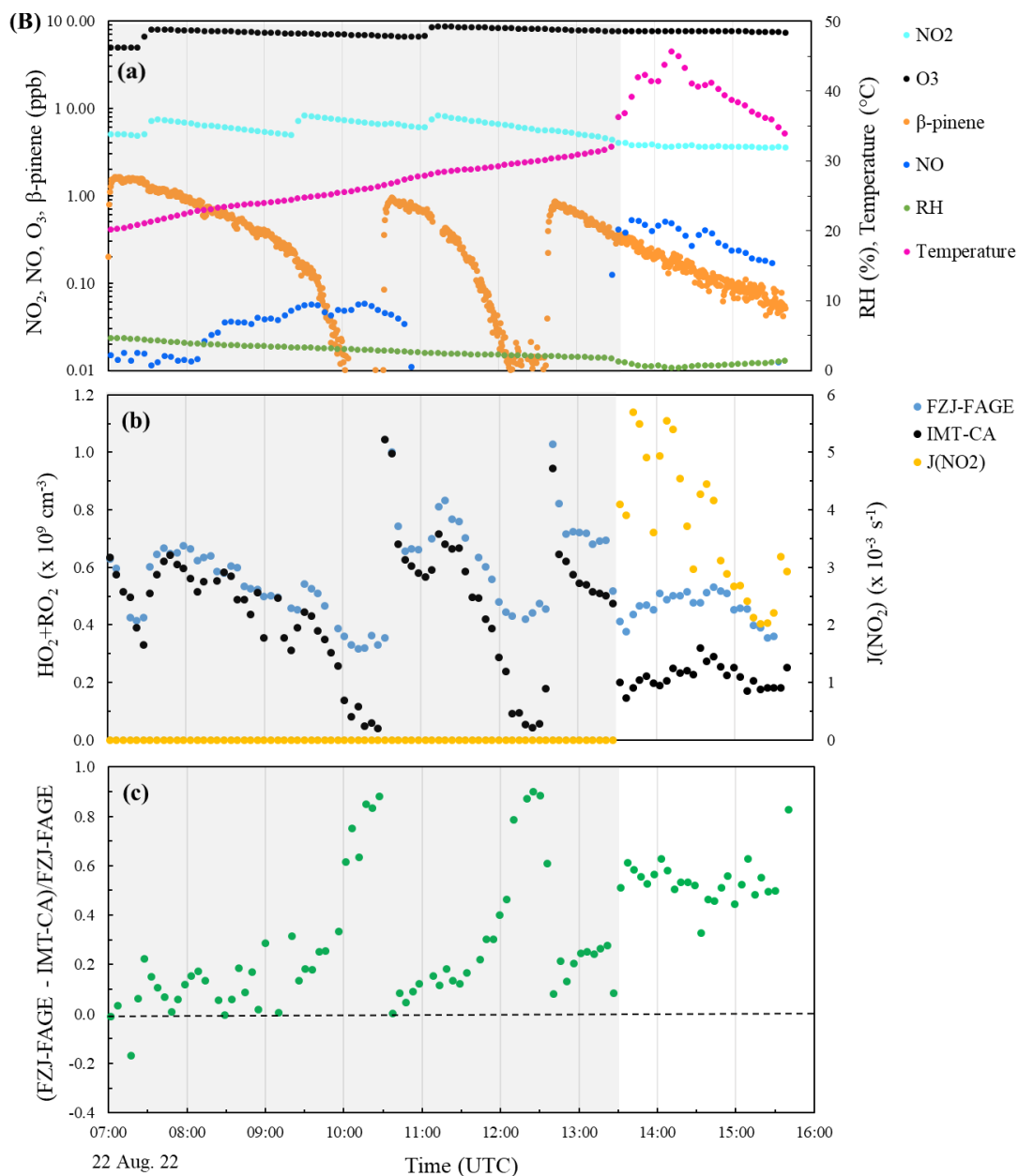
For the 22 Aug. experiment (Figure 3.19 (B)), different amounts of  $\beta$ -pinene (1.6, 0.9 and 0.8 ppb) were injected into the chamber at various times relative to the injections of  $O_3$  and  $NO_2$ . A total of three  $O_3$  injections were made (approximately 50, 30 and 20 ppb), along with corresponding  $NO_2$  injections (5, 3 and 2.7 ppb). An additional injection of  $NO_2$  was made at 09:24 (3 ppb). For this experiment, we notice a rapid consumption of  $\beta$ -pinene after each addition of  $NO_2$ , this is likely due to its oxidation by  $NO_3$  ( $k_{NO_3+\beta\text{-pinene}} = 2.5 \times 10^{-12} \text{ cm}^3 \text{ molecule}^{-1} \text{ s}^{-1}$ ) compared to the photooxidation period ( $k_{OH+\beta\text{-pinene}} = 7.89 \times 10^{-11} \text{ cm}^3 \text{ molecule}^{-1} \text{ s}^{-1}$ , OH concentration of  $1.9 \times 10^6 \text{ cm}^{-3}$  on average from FZJ measurements). During these events, we notice that the  $HO_2+RO_2$  concentration measured by IMT-CA decreases faster than that measured by FZJ-FAGE, reaching almost the detection limit of  $0.5 \times 10^8 \text{ cm}^{-3}$  for IMT-CA while concentrations measured by FZJ-FAGE are an order of magnitude higher ( $\sim 4 \times 10^8 \text{ cm}^{-3}$ ). This observation may indicate that higher-generation species generated through the oxidation of secondary VOCs by  $NO_3$  (possible according to the MCM database) impact the IMT-CA or FZJ-FAGE measurements (or both).

Over the photooxidation period, a significant underprediction of 53% is also noticed for IMT-CA on average. During this period, NO concentrations are relatively low (0.17 – 0.52 ppb), and close to the concentration range where an underestimation of IMT-CA was observed during other photooxidation experiments (section 4.3).





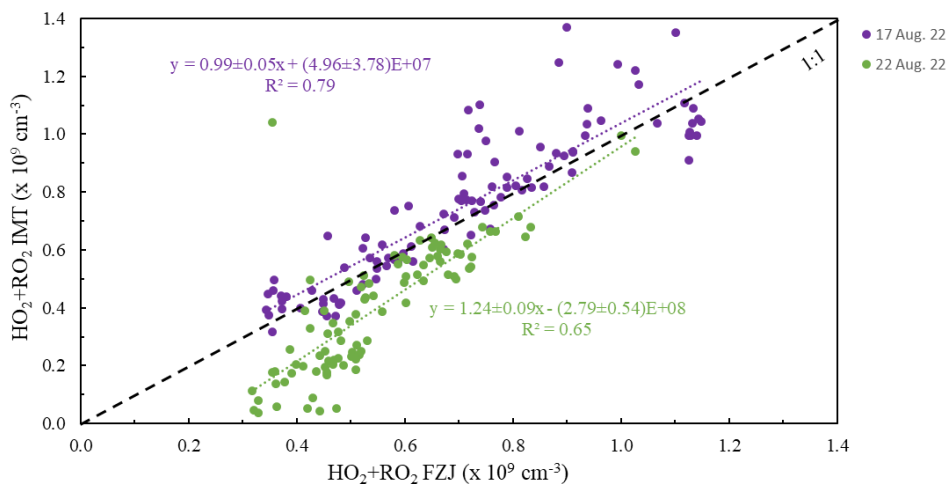
**Figure 3.19:** Results from selected NO<sub>3</sub>-relevant experiments - (A) 17 Aug. 22 and (B) 22 Aug. 22. For each experiment, panel (a): temporal variation of different parameters (NO, NO<sub>2</sub>, O<sub>3</sub>, VOC, RH, temperature), panel (b): HO<sub>2</sub>+RO<sub>2</sub> concentrations measured by IMT-CA and FZJ-FAGE and photolysis rate measurements of NO<sub>2</sub> (J(NO<sub>2</sub>)) and panel (c): the ratio of HO<sub>2</sub>+RO<sub>2</sub> concentrations: (FZJ-FAGE-IMT-CA)/FZJ-FAGE. The gray shadow is an indication of dark conditions.



**Figure 3.19 (continued)**

A good correlation was observed between the 2 instruments for the 17 Aug. experiment (depicted in Figure 3.20), with a slope of approximately unity and a non-significant intercept. This correlation is characterized by a moderate determination coefficient of  $\sim 0.8$ , which is improved to  $\sim 0.9$  when only considering the measurements made under dark conditions, outlining the deviation observed during the photooxidation process. A worse agreement was noticed for the 22 Aug. experiment, characterized by a slope of  $1.24 \pm 0.09$ , a significant intercept of  $(-2.8 \pm 0.5) \times 10^8 \text{ cm}^{-3}$ , and a moderate determination coefficient of 0.65. A better agreement between the two instruments is obtained when only accounting for the measurements conducted under dark conditions and at  $\beta$ -pinene concentrations higher

than 300 ppt. The slope of the linear regression was found to be around a unity under these conditions, with a less significant intercept of  $(-1.6 \pm 0.6) \times 10^8 \text{ cm}^{-3}$ , and a higher determination coefficient of 0.82.



**Figure 3.20:** Correlation between IMT-CA and FZJ-FAGE measurements for the NO<sub>3</sub>-relevant experiments of 17 Aug. 22 (purple dots) and 22 Aug. 22 (green dots)

In summary, it was concluded that HO<sub>2</sub>+RO<sub>2</sub> measurements by IMT-CA are as accurate than FZJ-FAGE when first generation nitrooxy-peroxy radicals are produced under dark conditions, through the oxidation of a VOC by NO<sub>3</sub>, and under low NO<sub>x</sub> conditions. However, the strong disagreement observed when β-pinene is low (<300 ppt) suggests that higher-generation species impact the IMT-CA and/or the FZJ-FAGE measurements. The origin of this issue and its impact on ambient measurements of HO<sub>2</sub>+RO<sub>2</sub> under tropospheric conditions needs to be further investigated using box modeling.

#### 4.4.2. Detection efficiency of O-functionalized peroxy radicals

This section investigates whether IMT-CA detects efficiently O-functionalized peroxy radicals (carbonyl and hydroxyl functions) generated during the ozonolysis of VOCs. Three experiments were selected for this purpose:

1. The 13 Aug. 22 experiment, consisting in a dual oxidation of α-pinene. At the beginning of the experiment, peroxy radicals were generated by the ozonolysis of α-pinene under dark and humid conditions (up to 50% RH). During the second part of the experiment, the aged mixture present in the chamber undergoes photooxidation in the presence of NO<sub>x</sub> and O<sub>3</sub>,

2. The 19 Aug. 22 experiment, focusing on the oxidation of trans-2-hexene by O<sub>3</sub> under dark conditions, with injections of water vapor,
3. The 26 Aug. 22 experiment, consisting in the OH-oxidation of isoprene under dark and dry conditions, OH being produced from the reaction between O<sub>3</sub> and TME, and later by solar irradiation in the presence of high O<sub>3</sub> concentrations.

Table 3.5 reports first-generation peroxy radicals that were produced during these experiments. Peroxy radicals generated when  $\alpha$ -pinene, trans-2-hexene and isoprene react with the selected oxidants are reported in blue, while additional peroxy radicals that arises from unavoidable secondary chemistry are reported in orange. This secondary chemistry is due to the generation of OH during ozonolysis experiments (i.e. trans-2-hexene+O<sub>3</sub>) as well as the oxidation of radical precursors (i.e. TME+O<sub>3</sub>, TME+OH). It is however expected that the former will be present at higher concentrations than the latter when the VOC injected in the chamber is present at a significant concentration.

During the dark conditions of the 13 Aug. experiment displayed in Figure 3.21 (A), an underestimation of about 32% is observed in the IMT-CA measurements. Based on Table 3.5, the main peroxy radicals formed during this time period are characterized by a carbonyl function. A similar underestimation of 34% by IMT-CA is observed right after the opening of the shutter, despite an expected change in the oxygenated function attached to the peroxy radical (hydroxyl instead of carbonyl). After the addition of 1.2 ppb of NO at 09:40, a better agreement is observed between the two instruments, the measurements from the two instruments being within 10%. The underestimation of IMT-CA when NO is lower than 200-300 ppt, the larger increase of IMT-CA measurements compared to FZJ-FAGE measurements when NO is added in the chamber, and the good agreement between the 2 instruments when NO is close to 1 ppb are consistent with the findings of section 4.3. Therefore, we concluded that (i) the detection efficiency of IMT-CA towards carbonylated and hydroxylated peroxy radicals is similar and that (ii) IMT-CA detects these radicals as efficiently than FZJ-FAGE.

During the 19 Aug. experiment displayed in Figure 3.21 (B), trans-2-hexene and O<sub>3</sub> were injected 7 times simultaneously. According to Table 3.5, the ozonolysis of trans-2-hexene leads to the formation of non-functionalized RO<sub>2</sub>. However, this reaction also generates OH, which in turn reacts with trans-2-hexene to form hydroxylated peroxy radicals. From the low NO conditions observed during this experiment (NO < 0.1 ppb), an underestimation of IMT-CA would be expected, similar to that observed for the 13 Aug. experiments when

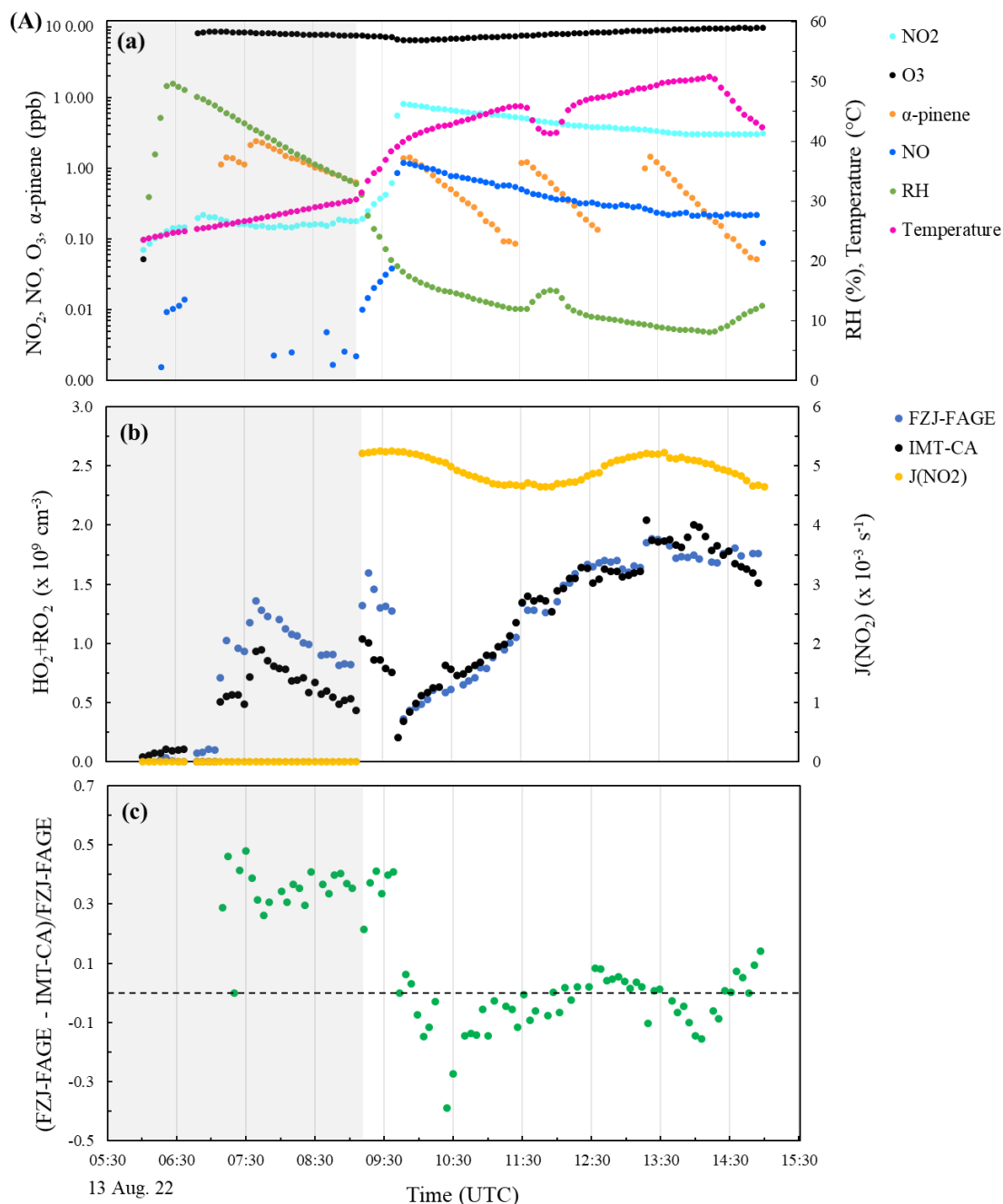
NO is lower than 200 ppt. On the contrary, an overestimation of 18% is observed. A similar behavior was found for the 26 Aug. experiment displayed in Figure 3.21 (C), where IMT-CA also overestimates the FZJ-FAGE measurements by 10-20%, despite the low NO concentrations (< 0.1 ppb).

**Table 3. 5:** Peroxy radicals produced from the oxidation of  $\alpha$ -pinene, trans-2-hexene, TME and isoprene by  $O_3$  and OH

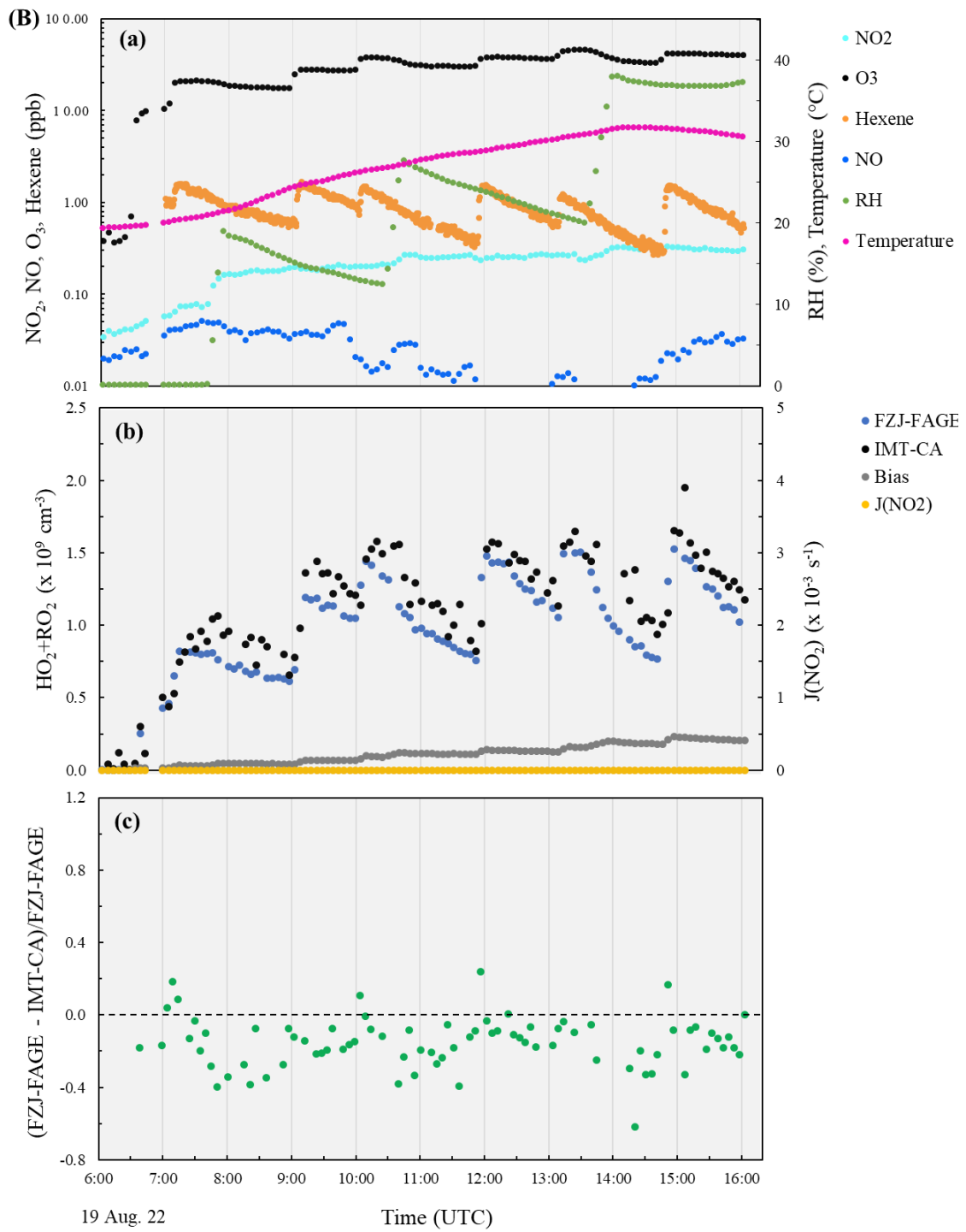
<i>Date</i>	<i>Reaction</i>	<i>Radical name*</i>	<i>Structural formula</i>
13 Aug. 22	$\alpha$ - pinene + $O_3$	C96O2	
		C107O2	
		C109O2	
	$\alpha$ - pinene + OH	APINAO2	
		APINBO2	
		APINCO2	
19 Aug. 22	Trans - 2 - hexene + $O_3$	CH <sub>3</sub> O <sub>2</sub>	
		NC3H7O2	
	Trans - 2 - hexene + OH	C64OH5O2	
		C65OH4O2	
26 Aug. 22	TME + $O_3$	CH <sub>3</sub> COCH <sub>2</sub> O <sub>2</sub>	
	TME + OH	C4ME2OHO2	
	Isoprene + OH	CISOPAO2	
		ISOPBO2	
		CISOPCO2	
		ISOPDO2	
		ISOP34O2	
		ISOPAO2	
		ISOPCO2	

\*Radical names from MCM v3.3.1. Peroxy radicals from VOC reactions with selected oxidants are presented in blue, and additional peroxy radicals from secondary chemistry in orange

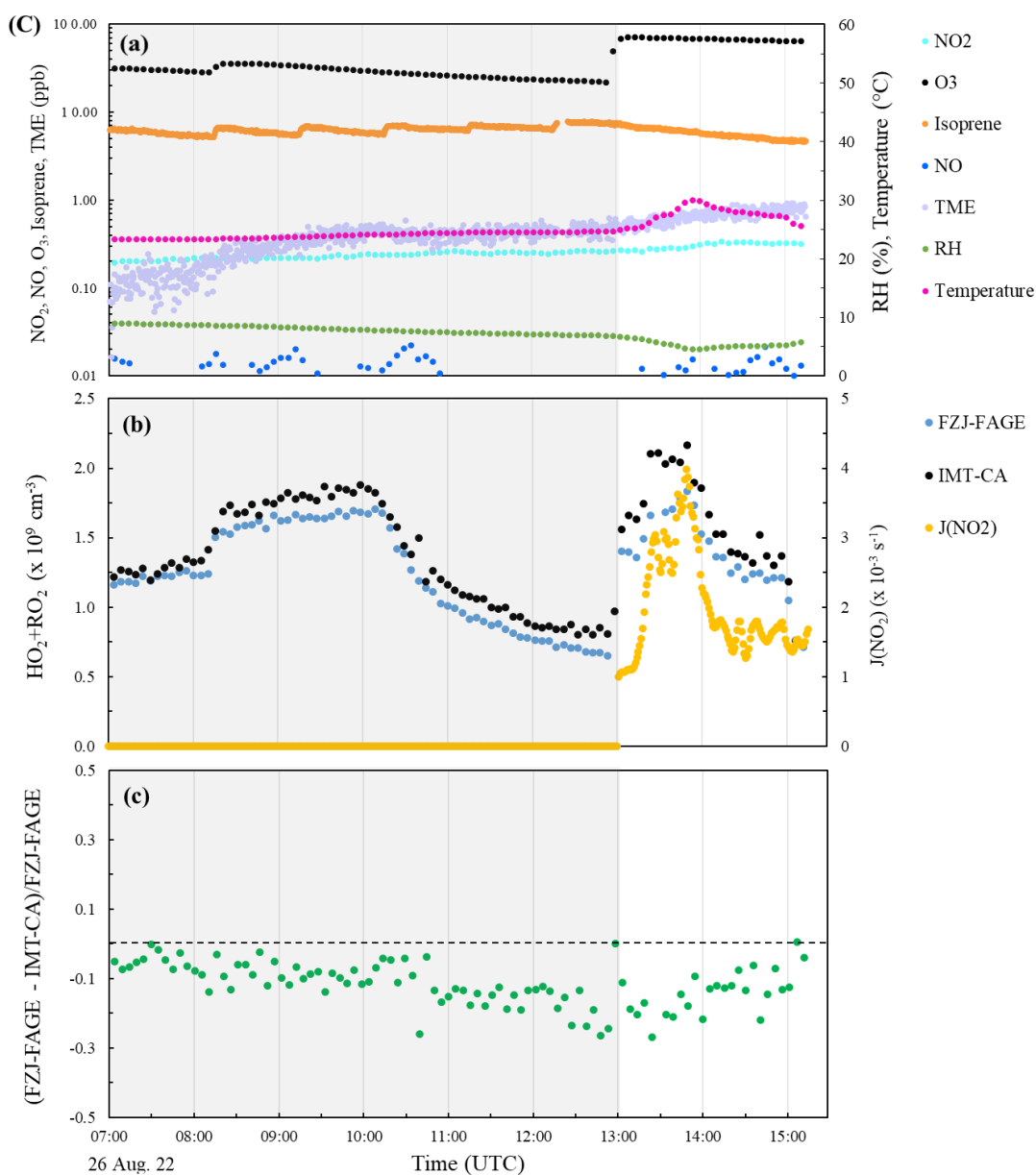
While the reason for the different behavior observed during the 19 Aug. and 26 Aug. 22 experiments is not yet identified, there is no evidence indicating that carbonylated and hydroxylated peroxy radicals generated during these experiments are not well detected by the IMT-CA.



**Figure 3.21:** Results from selected ozonolysis-experiments - (A) 13 Aug. 22, (B) 19 Aug. 22 and 26 Aug. 22. For each experiment, panel (a): temporal variation of different parameters ( $\text{NO}$ ,  $\text{NO}_2$ ,  $\text{O}_3$ , VOC, RH, temperature), panel (b):  $\text{HO}_2 + \text{RO}_2$  concentrations measured by IMT-CA and FZJ-FAGE and photolysis rate measurements of  $\text{NO}_2$  ( $J(\text{NO}_2)$ ) and panel (c): the ratio of  $\text{HO}_2 + \text{RO}_2$  concentrations:  $(\text{FZJ-FAGE} - \text{IMT-CA})/\text{FZJ-FAGE}$ . The gray shadow is an indication of dark conditions.



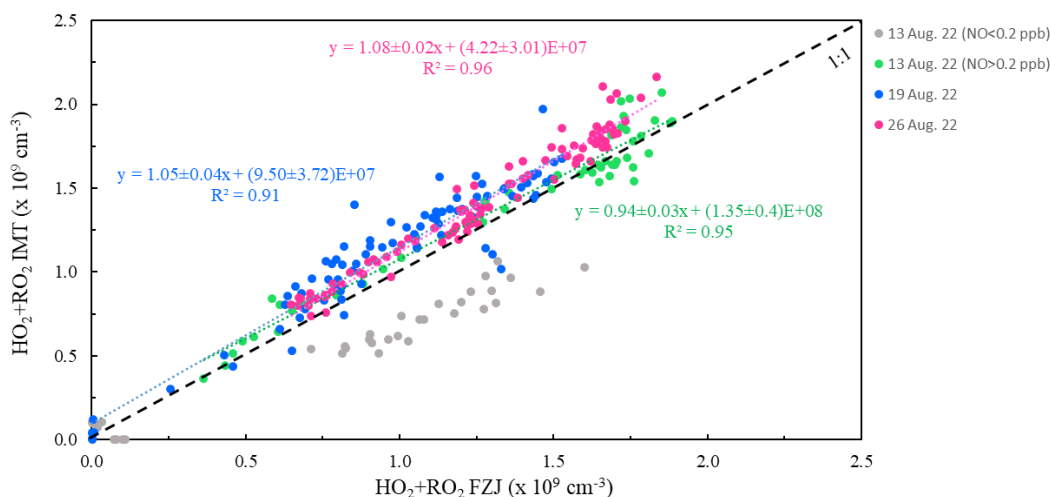
**Figure 3.21 (continued)**



**Figure 3.21 (continued)**

As depicted in Figure 3.22, strong correlations are evident between IMT-CA and FZJ-FAGE for the three experiments, with the exception of the 13 Aug. experiment when NO is lower than 200 ppt (not included in the regression fit shown in Figure 3.22). The determination coefficients are 0.95, 0.91 and 0.96 and the linear regressions' slopes  $0.94 \pm 0.03$ ,  $1.05 \pm 0.04$  and  $1.08 \pm 0.02$ , for the 13 Aug., 19 Aug. and 26 Aug. experiments, respectively. These results indicate that the two instruments measured concentrations that are within measurement uncertainties (31% for IMT-PERCA and 32/36% for HO<sub>2</sub>/RO<sub>2</sub> from FZJ-FAGE at  $2\sigma$ ). The intercepts observed for the 19 Aug. and 26 Aug. experiments are not statistically significant, while the intercept is slightly above the  $3\sigma$  upper bound for the 13 Aug. experiment.





**Figure 3.22:** Correlation between IMT-CA and FZJ-FAGE measurements for the ozonolysis-experiments of 13 Aug. 22 (green and grey dots), 19 Aug. 22 (blue dots) and 26 Aug. 22 (pink dots)

The results presented in this section indicate that IMT-CA measurements are within 20% of that measured by the FZJ instrument, when O-functionalized peroxy radicals are produced under dark conditions through the ozonolysis of a VOC. The conversion efficiency of some functionalized peroxy radicals generated from the oxidation of alkenes by OH was also studied in Duncianu et al.<sup>48</sup>. It was found that the fraction of RO<sub>2</sub> radicals propagated into HO<sub>2</sub> was consistent with the fraction of RO<sub>2</sub> lost through the formation of organic nitrate and nitrite compounds.

#### 4.4.3. Photooxydation of ambient air

During this experiment, which took place on 23 Aug. 22, ambient air was sampled through the SAPHIR chamber at an averaged flow rate of 72 L min<sup>-1</sup> while irradiated by the solar light. The aim of this experiment was to evaluate the performance of the different radical instruments when a complex mixture of peroxy radicals is produced in ambient air during the photooxidation of VOCs from biogenic and anthropogenic origins.

The results presented in Figure 3.23 reveals a humid environment with changing RH and temperature, in the range of 11-57% and 20-48 °C, respectively. NO<sub>x</sub> concentrations were found to be variable along the experiment, ranging from 1.8 to 9.9 ppb for NO<sub>2</sub> and from approximately 100 ppt up to 2.7 ppb for NO. Elevated NO<sub>x</sub> concentrations were observed during the morning and a decrease was observed in the afternoon. In contrast, O<sub>3</sub> exhibited the opposite trend, its concentration increasing along the day from approximately 28 to 62 ppb.

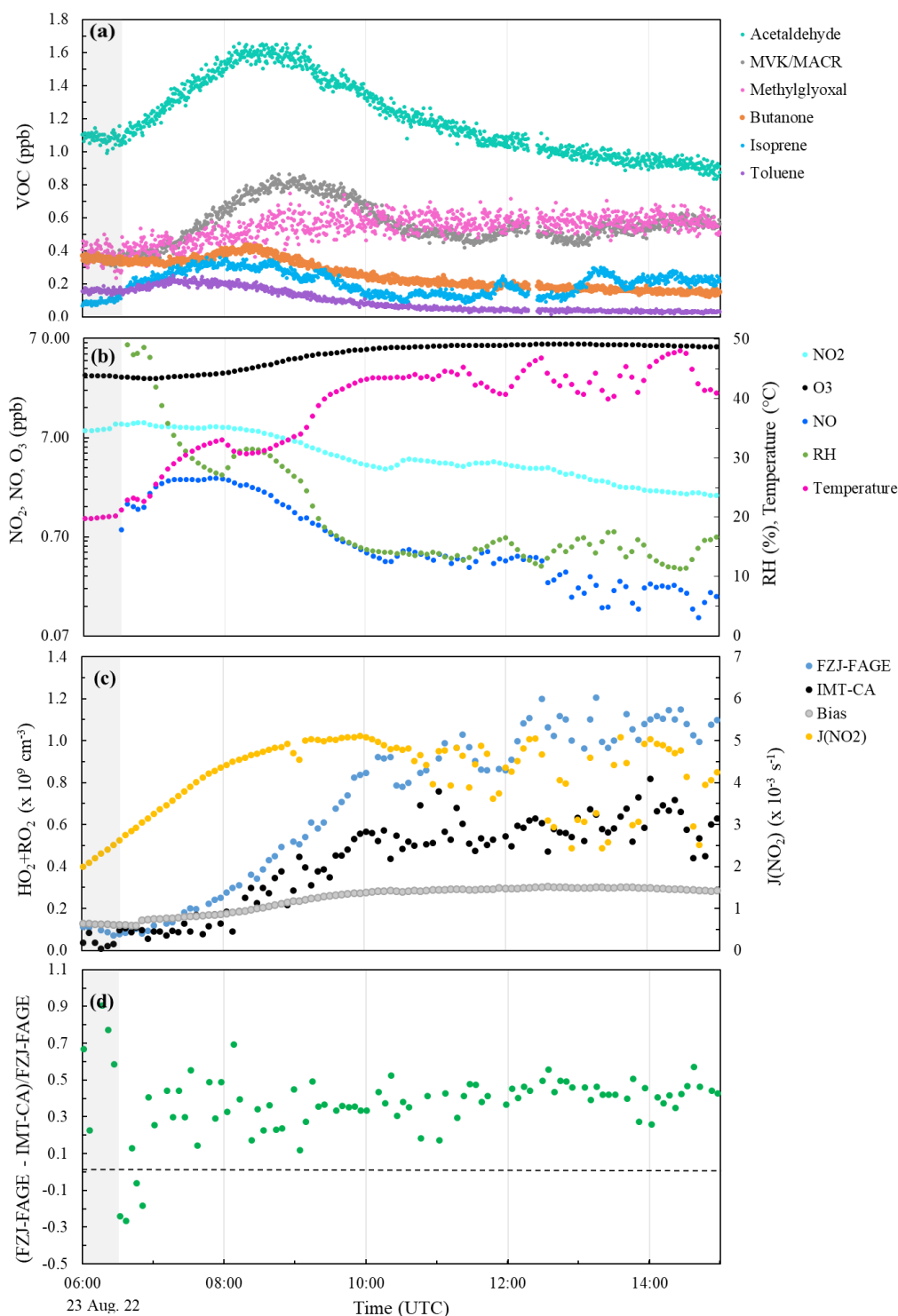
Various VOCs were quantified by PTR-ToFMS, the most abundant ones being presented in Figure 3.23 (a). This figure shows that the most abundant VOC is acetaldehyde, with an averaged contribution of 42% to the total amount of VOCs depicted in this figure. This species is directly emitted (primary origin) by anthropogenic activities, mostly from vehicular emissions and industrial activities, but is also produced during oxidation processes in the atmosphere (secondary origin). Other anthropogenic and biogenic VOCs, of both primary and secondary origins, were also detected, such as methylglyoxal, methacrolein (MACR) + methylvinylketone (MVK), butanone and toluene, with averaged contributions of 19%, 20%, 9% and 3%, respectively. Among the biogenic VOCs, we notice the presence of isoprene, contributing to around 7% to the total concentration of VOCs displayed in Figure 3.23, as well as some of its oxidation products MACR + MVK (20%). It is clear from Figure 3.23 (a) that the majority of the measured VOCs are present at higher concentrations during the morning, between 7 and 10 am. Formaldehyde (HCHO) was unfortunately not reported during these experiments since its measurement by PTR-MS is not straightforward due to a strong humidity-dependent response.

During this experiment,  $\text{HO}_2+\text{RO}_2$  concentrations were found to increase throughout the day as shown in Figure 3.23 (c), which is expected from the increase in J-values that leads to larger initiation rates of  $\text{RO}_x$  radicals from photolytic processes. Figure 3.23 (d) shows that IMT-CA measurements significantly underestimates the FZJ-FAGE measurements by 20-50%. The correlation between IMT-CA and FZJ-FAGE measurements was found to be good, with a determination coefficient of 0.92 as depicted in Figure 3.24 (a). The slope of  $0.57\pm 0.2$  indicates that IMT-CA underestimate the FZJ-FAGE measurements by 43% on average.

This behavior does not seem to be linked to the  $\text{NO}_x$  level as discussed in section 4.3 since the same underestimation is observed at NO concentrations ranging from 0.3 up to 2.6 ppb as shown in Figure 3.24 (b). This figure reveals an absence of correlation between the IMT-CA/FZJ-FAGE ratio and the NO concentration.

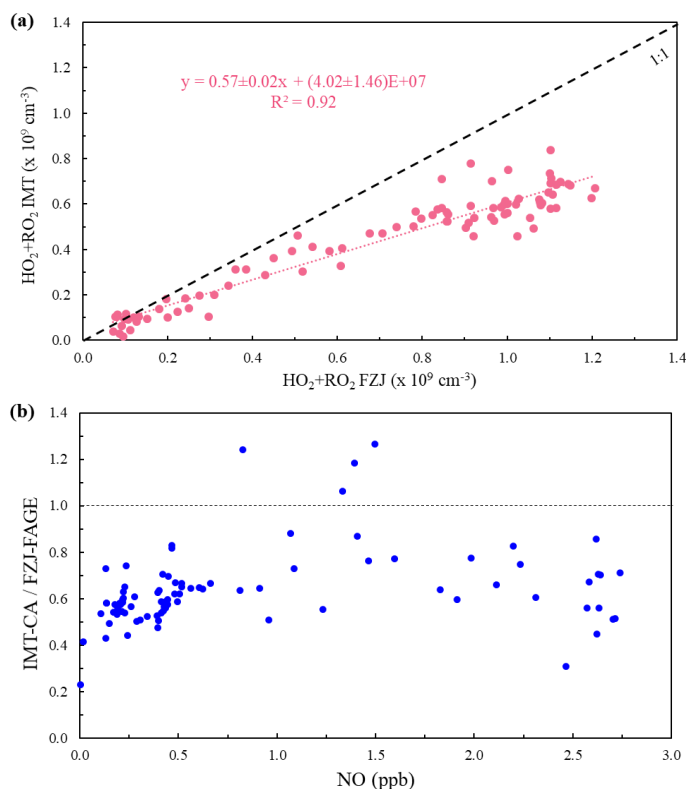
According to Table 3.6, different types of peroxy radicals are likely generated during this experiment, mainly carbonylated and hydroxylated radicals. Based on the findings of the previous sections, carbonylated and hydroxylated radicals produced during this experiment should be well quantified by the CA. However, some of these functionalized

peroxy radicals exhibits several oxygenated functions and the detection efficiency of these radicals by IMT-CA should be further studied.



**Figure 3.23:** Results from the 23 Aug. 22 experiment for the measurement of ambient air under irradiated conditions, panel (a): time series of the concentrations of most abundant VOCs, panel (b): temporal variation of different parameters (NO, NO<sub>2</sub>, O<sub>3</sub>, RH, temperature), panel (c): HO<sub>2</sub>+RO<sub>2</sub> concentrations measured by IMT-CA and FZJ-FAGE, the bias in the IMT-CA measurements related to the presence of O<sub>3</sub> and photolysis rate measurements of NO<sub>2</sub> (J(NO<sub>2</sub>)) and panel (d): the ratio of HO<sub>2</sub>+RO<sub>2</sub> concentrations: (FZJ-FAGE-IMT-CA)/FZJ-FAGE. The gray shadow is an indication of dark conditions.

The O<sub>3</sub>-water bias that was subtracted from IMT-CA measurements is shown in grey in Figure 3.23 (c). It is interesting to note that it can reach up to  $2.5 \times 10^8 \text{ cm}^{-3}$ , which represent 44% of the reported IMT-CA concentration on average during the last 5 hours of this experiment. As already mentioned in section 4.2, an issue may be associated to the subtraction of this bias, which could cause part of the differences observed between IMT-CA and FZJ-FAGE. Additional work is necessary to understand whether the O<sub>3</sub>-water bias is real and whether it should be subtracted from IMT-CA measurements.

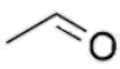
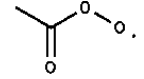
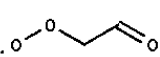
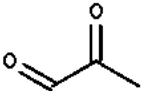
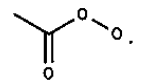
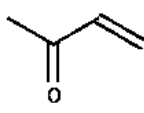
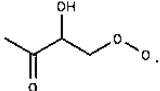
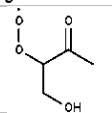
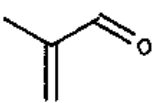
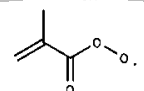
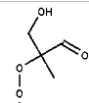
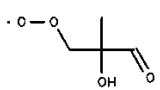
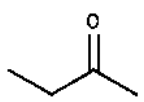
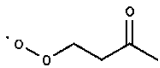
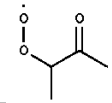
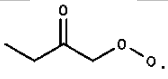
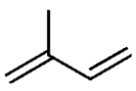
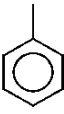
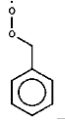
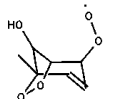


**Figure 3.24:** Correlation between (a) IMT-CA and FZJ-FAGE measurements and (b) the ratio IMT-CA/FZJ-FAGE and NO for the experiment of 23 Aug. 22

It is worth noting that the two most abundant measured VOCs, acetaldehyde and methylglyoxal, contribute to the formation of  $\text{CH}_3\text{CO}_3$ , whose reaction with NO, HO<sub>2</sub> and RO<sub>2</sub> leads to the formation of  $\text{CH}_3\text{O}_2$ . One of the most abundant trace gases in the atmosphere, i.e. methane (not shown in Figure 3.23), reacts with OH to also form  $\text{CH}_3\text{O}_2$ . Results from box models indicate that  $\text{CH}_3\text{O}_2$  is usually the most abundant organic peroxy radical, which was also likely the case during this chamber experiment. As explained in section 3.2,  $\text{CH}_3\text{O}_2$  is only partially detected in the CA, due to a high  $\text{CH}_3\text{ONO}$  yield of about 36% from the competition between  $\text{CH}_3\text{O} + \text{NO}$  and  $\text{CH}_3\text{O} + \text{O}_2$  in the CA reactors<sup>48</sup>.

Therefore, part of the IMT-CA underestimation observed here is likely due to the poor detection of  $\text{CH}_3\text{O}_2$ .

**Table 3. 6:** Tentative list of peroxy radicals produced during the 23 Aug. 22 experiment from reactions of VOCs with OH

VOC	Structural formula	Radical name*	Structural formula
Acetaldehyde		$\text{CH}_3\text{CO}_3$	
		$\text{HCOCH}_2\text{O}_2$	
Methylglyoxal		$\text{CH}_3\text{CO}_3$	
MVK		ISOP34O2	
		ISOPDO2	
MACR		$\text{MACO}_3$	
		MACRO2	
		MACROHO2	
Butanone		MEKAO2	
		MEKBO2	
		MEKCO2	
Isoprene		See Table 3.5 (experiment 26 Aug. 22)	
Toluene		$\text{C}_6\text{H}_5\text{CH}_2\text{O}_2$	
		TLBIPERO2	

\*Radical names from MCM v3.3.1

Box modeling is necessary here to get more information on the type of organic peroxy radicals present in the chamber and their abundance in order to investigate whether the IMT-

CA measurements are consistent with the modeled HO<sub>2</sub>+RO<sub>2</sub> concentrations where the concentration of each RO<sub>2</sub> radical is scaled on the basis of its detection efficiency in the CA, which can be determined from known organic nitrate and nitrite yields.

## 5. Conclusions

The ROxComp campaign was a unique opportunity for cross-comparison of different peroxy radical instruments, which will help improving the technological understanding and the accuracy of Chemical Amplification, Laser Induced Fluorescence and Mass Spectrometry techniques.

This chapter presents how IMT-CA compares to FZJ-FAGE for a large range of experimental conditions. It should be noted that the measurement datasets used here were not finalized yet at the time this chapter was written and the conclusions presented here are preliminary. Nevertheless, these results have provided new insights into the performance of IMT-CA, which allowed to identify areas of agreement and potential sources of discrepancies.

Among the knowledge gained from this campaign, a miscalibration of IMT-CA was identified through cross calibrations using radical sources from other groups. This issue was further investigated in our laboratory and it was found that the concentration of isoprene added in the IMT calibrator, used to convert OH into RO<sub>2</sub> radicals, was high enough to generate a significant amplification of peroxy radicals when the CA reactors were operated in background mode, which in turn led to an underestimation of the radical chain length. This issue was corrected for and will be easily solved for future calibrations by decreasing the isoprene concentration.

The ROxComp experiments allowed investigating whether RH could have an impact on IMT-CA measurements. It was found that the addition of humidity during different experiments did not impact the agreement between IMT-CA and FZJ-FAGE. In addition, these measurements were useful to ensure that the IMT-CA chain length is properly parameterized as a function of relative humidity.

From laboratory testing, it was found that a correction in the IMT-CA measurements is necessary to remove a measurement bias that scales with ozone under dry and humid conditions. A parameterization of this bias was derived as a function of ambient O<sub>3</sub> and

water-vapor. By investigating how IMT-CA measurements respond to changing conditions of O<sub>3</sub> and humidity during ROxComp, it was found that this O<sub>3</sub> bias seems to be properly removed for most experiments. However, the results from a few experiments suggest the opposite. This point is puzzling and requires further testing of IMT-CA to better understand the origin of the potential O<sub>3</sub> bias and whether it is well accounted for.

The ROxComp experiments allowed investigating whether NO impacts the IMT-CA/FZJ-FAGE comparison. While the agreement between the two instruments is within 30% most of the time, experiments conducted at NO concentrations ranging from hundreds of ppt to several ppb revealed a systematic discrepancy. It was found that IMT-CA measures (1) lower peroxy radical concentrations than FZJ-FAGE when operating at NO concentrations lower than 200-300 ppt, (2) higher concentrations when operating at NO concentrations larger than 1 ppb, and (3) similar concentrations in intermediate conditions. This trend on NO is not easy to understand and may be due to the use of preliminary datasets of HO<sub>2</sub>+RO<sub>2</sub> measurements.

The point discussed above needs to be further investigated when datasets are finalized. If the trend is still observed, careful investigations of the changes in other parameters in all the experiments that were selected to show this trend will have to be carried out to ensure that NO is at the origin of the observed discrepancy. It would be useful to confirm these results by conducting new experiments in atmospheric chambers where we could gradually vary NO during the oxidation of targeted VOCs. Box modeling of the reported chamber experiments should also provide additional information that will help understanding this discrepancy.

The ROxComp experiments also allowed investigating whether various types of peroxy radicals (i.e. nitrooxy-peroxy and O-functionalized peroxy radicals) are efficiently detected by IMT-CA. Experiments performed using different types of oxidants (OH, O<sub>3</sub>, NO<sub>3</sub>) showed that IMT-CA is able to detect carbonylated, hydroxylated and nitrooxy-peroxy radicals with a good efficiency. However, it was found that species generated through the oxidation of secondary VOCs by NO<sub>3</sub> impact the IMT-CA or FZJ-FAGE measurements (or both).

In summary, while several aspects highlighted above needs further scrutiny, IMT-CA demonstrated reasonable performances, with an agreement within 30% with FZJ-FAGE.

However, it is important to consider the necessity of conducting additional studies to better characterize the stated deficiencies, which should help improving again the accuracy of IMT-CA.





# **Chapter 4. Evaluation of a methodology to quantify ozone production rates using a Chemical Amplifier**

This chapter presents the work performed to evaluate the ozone production rate quantification methodology. The analysis presented here takes advantage of chamber experiments performed during ROxComp and builds on findings from chapter 3.

# 1. Introduction

As presented in Chapter 1, section 2,  $P(O_3)$  can be determined following two different approaches. A direct approach is based on using a MOPS (Measurement of Ozone Production Sensor) or an OPR (Ozone Production Rates) instrument, where  $P(O_3)$  is derived from differential measurements of  $O_3$  between a reference chamber exempt of  $O_3$  production and a sample chamber reproducing ambient  $O_3$  formation, both sampling ambient air. The indirect approach is based on computing  $P(O_3)$  from ambient measurements of peroxy radicals and NO. In this work, we have adopted the indirect approach, where peroxy radicals were measured using the CA developed at IMT and NO was quantified using a chemiluminescence based  $NO_x$  analyzer.

In this chapter, several ROxComp experiments presented in Chapter 3 were selected to evaluate the  $P(O_3)$  quantification methodology. These experiments, performed in the SAPHIR chamber, consisted in the photooxidation of VOCs under atmospheric conditions. During these experiments, the chamber was exposed to the sunlight, which resulted in ozone formation at varying production rates and under different chemical regimes.

The following sections provide a comprehensive overview of the methodologies, a detailed presentation of the selected experiments and an evaluation of the CA-based  $P(O_3)$  quantification approach.

## 2. Description of $P(O_3)$ quantification methodologies

As mentioned above, the present work involves the quantification of  $P(O_3)$  from measurements of both  $HO_2+RO_2$  and NO concentrations. The resulting value represents the gross  $O_3$  production rate, denoted as  $p(O_3)$ . The net  $O_3$  production rate,  $P(O_3)$ , is then deduced by subtracting  $O_3$  losses,  $l(O_3)$ , from  $p(O_3)$ . To validate the reliability of this approach,  $P(O_3)$  values were compared to those inferred from another method, which is based on calculating the rate of change of  $O_x$  species ( $O_3+NO_2$ ) from their temporal variation.  $O_x$  is used instead of  $O_3$  in these calculations due to the rapid interconversion between these two species in the atmosphere. We therefore refer to  $P(O_3)$  as  $P(O_x)$  in the following.

In this manuscript, a bold capital letter is used to refer to the net  $O_x$  production rate,  $P(O_x)$ , while a normal lowercase letter is used for the gross production rate,  $p(O_x)$ , or destruction rate,  $l(O_x)$ .

## 2.1. $P(O_x)$ inferred from ambient measurements of $HO_2+RO_2$ and NO

The principle of this method, previously introduced in the first chapter, is briefly summarized in this section. In this approach, the gross  $O_x$  production rate,  $p(O_x)$ , is computed as the reaction rate between  $HO_2+RO_2$  and NO, as shown in Eq 4. 1:

$$p(O_x) = (r k_{NO+HO_2} + (1 - r)k_{NO+RO_2})[HO_2 + RO_2][NO] \quad \text{Eq 4. 1}$$

where:

- $r = \frac{[HO_2]}{[HO_2]+[RO_2]}$
- $k_{NO+HO_2}$  and  $k_{NO+RO_2}$  are the reaction rate coefficients for  $NO + HO_2$  and  $NO + RO_2$ , respectively.

Since the CA measures the sum of  $HO_2+RO_2$ , we assumed that  $[HO_2] = [RO_2]$ , allowing us to simplify the calculation of  $p(O_x)$  as follows:

$$p(O_x) = k_{NO+peroxy}[NO][HO_2 + RO_2] \quad \text{Eq 4. 2}$$

where  $k_{NO+peroxy} = \frac{1}{2}(k_{HO_2+NO} + k_{RO_2+NO})$ .

This hypothesis is validated in section 4, where  $p(O_x)$  values derived from Eq 4. 2 were compared to values inferred from the measured  $\frac{[HO_2]}{[HO_2]+[RO_2]}$ . The latter was derived from speciated radical measurements performed by a laser-induced fluorescence instrument.

It is important to note that for the quantification of  $p(O_x)$ , IMT-CA has the advantage of only measuring the fraction of  $HO_2$  and  $RO_2$  radicals leading to  $O_3$  formation (Chapter 1, section 1.2). Therefore, it was not necessary to include the branching ratio for organic nitrate formation in the reaction of  $RO_2+NO$  in the  $p(O_x)$  equations (Eq 4. 1 and Eq 4. 2).

The net  $O_x$  production rate,  $P(O_x)$ , is then inferred by subtracting the total  $O_x$  loss rate,  $l(O_x)$ , calculated from ancillary measurements made during chamber experiments. The two quantities were determined using the following equations:

$$l(O_x) = j(O^1D)[O_3]f + k_{OH+NO_2}[OH][NO_2] + k_{HO_2+O_3}[HO_2][O_3] + \quad \text{Eq 4. 3}$$

$$k_{OH+O_3}[OH][O_3] + \Sigma k_{O_3+\text{alkene},i}[O_3][\text{alkene}]_i + O_3 \text{ wall loss rate} +$$

$O_x$  dilution rate

$$P(O_x)^{HO_2+RO_2} = p(O_x) - l(O_x) \quad \text{Eq 4. 4}$$

where:

- $j(O^1D)$  is the photolysis rate of  $O_3$  for the photolytic pathway leading to  $O(^1D)$  atoms,
- $f$  is the fraction of  $O(^1D)$  atoms that reacts with  $H_2O$  to produce  $OH$  (the other fraction,  $1-f$ , reproduces  $O_3$  and therefore neutral in terms of  $O_3$  loss),
- " $O_x$  wall loss rate" is the first order loss rate of  $O_3$  on the chamber walls, the loss rate of  $NO_2$  being negligible,
- " $O_x$  dilution rate" is the first order dilution rate of  $O_x$  due to the continuous addition of zero air during chamber experiments.

It is interesting to note that under dark conditions, i.e without solar irradiation,  $l(O_x)$  is only due to dilution and wall losses when only  $O_3$  is present in the chamber. Therefore, by monitoring the  $O_x$  loss rate under such conditions, it is possible to determine the contribution of  $O_3$  wall losses since the dilution rate is known. In fact, the latter was inferred in the present study from previous SAPHIR experiments published in the literature, and was verified during the  $\beta$ -pinene photooxidation experiment presented in section 4.1.

## 2.2. $P(O_x)$ inferred from temporal variations of $O_x$

This method consists in calculating the net  $O_x$  production rate, denoted as  $P(O_x)^{O_x}$ , from changes in  $O_x$  concentrations ( $\Delta O_x$ ) in the SAPHIR chamber. The change in  $O_x$  is then divided by the time difference between two measurements ( $\Delta t$ ), as presented in the following equation:

$$P(O_x)^{O_x} = \frac{\Delta O_x}{\Delta t} \quad \text{Eq 4. 5}$$

As previously stated (Chapter 3, section 2.3), O<sub>3</sub> and NO<sub>2</sub> were quantified using a UV-absorption monitor and a chemiluminescence detector (CLD), respectively, both coupled to SAPHIR.

The comparison between  $P(O_x)^{HO_2+RO_2}$  and  $P(O_x)^{O_x}$  can be seen as a critical test to assess (i) the reliability of the CA-based methodology and (ii) the completeness of O<sub>x</sub> production and loss processes.

### 3. Description of selected chamber experiments

#### 3.1. SAPHIR chamber

Seven experiments from the ROxComp campaign were carefully selected to conduct the  $P(O_x)$  evaluation. As presented earlier in Chapter 3, section 2, SAPHIR is a simulation chamber characterized by a volume of 270 m<sup>3</sup>, which is equipped with a large number of analytical instruments. This chamber is also equipped with a shutter system enabling working under either dark or irradiated conditions. A double FEP Teflon wall, whose interstice is flushed with zero air, allows reaching very clean conditions.

Teflon chambers have the particularity of producing radical precursors when only flushed with zero air. In fact, under typical tropospheric H<sub>2</sub>O concentrations, HONO molecules are released from the chamber walls<sup>138</sup>. When the chamber is irradiated by the solar light, HONO undergoes photolysis, leading to the formation of OH and NO. While the mechanism underlying HONO formation remains uncertain, it explains the permanent presence of a background concentration of OH and NO within the chamber. The concentrations of HONO measured in SAPHIR are similar to those observed in ambient air and are dependent on humidity, solar radiation, and temperature<sup>138</sup>.

For the ROxComp experiments, it is essential to consider that chemical species are continuously diluted from the addition of zero air in the chamber. For all experiments, the dilution rate was calculated from the known flow rate of zero air that is continuously injected in the chamber. For a few experiments, the dilution rate was also determined from the injection of a tracer (CO<sub>2</sub>) and its real-time monitoring. The two methods were

consistent within 11%. On average, the SAPHIR chamber exhibits a dilution rate of approximately  $10^{-5} \text{ s}^{-1}$ .

It was also reported that  $\text{O}_3$  is lost on the chamber walls at a rate of  $3.9 \times 10^{-6} \text{ s}^{-1}$ <sup>137</sup>. During ROxComp,  $\text{O}_3$  measurements performed under dark conditions when SAPHIR is only filled with zero air, allowed a direct quantification of the  $\text{O}_3$  loss rate. The obtained value was found to be within 0.5% of the value reported above (details about these calculations are presented in section 4.2).

In section 4, calculations of ozone production rates and their interpretation are based on a diverse set of parameters, including  $\text{NO}_x$  (CLD),  $\text{O}_3$  (UV-absorption), OH,  $\text{HO}_2$  and  $\text{RO}_2$  (FZJ-FAGE), J-values (spectroradiometer), VOCs (PTR-ToFMS),  $\text{H}_2\text{O}$  (PICARRO analyzer), temperature and RH (VAISALA RH and T sensors). These measurements were provided by the FZJ group and more details about the analytical techniques are provided in Chapter 3, section 2.2.

### 3.2. Experimental conditions

The selected experiments are photooxidation reactions of various biogenic and anthropogenic VOCs exhibiting different reactivities towards OH, as shown in Table 4.1 from the reported  $k_{\text{VOC}+\text{OH}}$  values. The range of reactivity with OH covers 4 orders of magnitude, where methane is the less reactive VOC ( $k_{\text{CH}_4+\text{OH}} \sim 6.4 \times 10^{-15} \text{ cm}^3 \text{ molecule}^{-1} \text{ s}^{-1}$ <sup>149</sup>) and isoprene the most reactive one ( $k_{\text{C}_5\text{H}_8+\text{OH}} \sim 1 \times 10^{-10} \text{ cm}^3 \text{ molecule}^{-1} \text{ s}^{-1}$ <sup>150</sup>). In addition, we notice that a few VOCs exhibit a significant reactivity towards  $\text{O}_3$ , such  $\alpha$ -pinene and  $\beta$ -pinene. Each of these experiments was performed under controlled conditions, including well-defined temperature and RH ranges, and specific duration/timing of sunlight exposure.

During these experiments, the chamber was irradiated with sunlight instead of artificial lamps, leading to experimental conditions representative of oxidation phenomenon occurring in the atmosphere. A close inspection of Table 4.1 shows that measured OH concentrations, varying from  $1 \times 10^6$  to  $20 \times 10^6 \text{ cm}^{-3}$ , are similar to values reported from field campaigns<sup>91</sup>. In addition, the  $\frac{[\text{HO}_2]}{[\text{HO}_2]+[\text{RO}_2]}$  ratio varies from 0.4 to 0.5, which is in the range of the observed ratios in the atmosphere<sup>94</sup>.

Table 4.1 also shows that the production of  $O_x$  in the chamber, calculated from the amount of  $O_x$  produced over several hours of oxidation, is in the range of 0.6 – 21 ppb h<sup>-1</sup> (no correction for dilution and wall losses). This covers the range of the ambient  $P(O_x)$  values that is usually reported in the literature <sup>93</sup>.

It is important to highlight that some experiments were conducted without the addition of NO, thereby representing low NO<sub>x</sub> conditions typical of rural sites, namely the  $\beta$ -pinene, methane and MVK experiments. In contrast, the remaining experiments were performed with the addition of NO, simulating moderate-to-high NO<sub>x</sub> conditions typically observed in or near urban centers: isoprene, i-pentane+n-hexane,  $\alpha$ -pinene and mesitylene experiments.

**Table 4. 1:** Selected RO<sub>x</sub>Comp experiments for  $P(O_x)$  quantification

<i>Date</i>	<i>VOC</i>	<i>NO</i>	<i>O<sub>3</sub></i>	<i>OH</i> (10 <sup>6</sup> cm <sup>-3</sup> ) <i>min-max</i>	$\frac{HO_2}{HO_2+RO_2}$	$\Delta O_x$ /h	$k_{VOC+OH}$ (cm <sup>3</sup> molecule <sup>-1</sup> s <sup>-1</sup> )* <i>Ref</i> <sup>151</sup>	$k_{VOC+O_3}$ (cm <sup>3</sup> molecule <sup>-1</sup> s <sup>-1</sup> )* <i>Ref</i> <sup>151</sup>
11 Aug. 22	Isoprene	✓	-	4-6	0.50 ± 0.06	63 ppb/3h	1×10 <sup>-10</sup>	1.3×10 <sup>-17</sup>
12 Aug. 22	i-pentane Hexane	✓	-	1-10	0.40 ± 0.11	98 ppb/8h	3.7×10 <sup>-12</sup> 1.8×10 <sup>-14</sup>	-
13 Aug. 22	$\alpha$ -pinene	✓	✓	2-8	0.48 ± 0.04	20 ppb/8h	5.3×10 <sup>-11</sup>	9.4×10 <sup>-17</sup>
14 Aug. 22	Mesitylene	✓	-	7-20	0.48 ± 0.10	97 ppb/7h	5.7×10 <sup>-11</sup>	-
16 Aug. 22	$\beta$ -pinene	-	✓	3-9	0.47 ± 0.04	4 ppb/7h	7.9×10 <sup>-11</sup>	1.9×10 <sup>-17</sup>
20 Aug. 22	Methane	-	-	1-7	0.47 ± 0.10	75 ppb/9h	6.4×10 <sup>-15</sup>	-
24 Aug. 22	MVK	-	✓	5-10	0.49 ± 0.04	15 ppb/9h	2.0×10 <sup>-11</sup>	0.5×10 <sup>-17</sup>

\* value reported at 298 K. A tick (✓) in the NO and O<sub>3</sub> columns indicate an injection in the chamber.

## 4. Evaluation of the CA-based $P(O_x)$ quantification approach

To evaluate the  $P(O_x)$  quantification approach relying on the measurement of peroxy radicals using IMT-CA, a comparison between the previously defined quantities  $P(O_x)^{HO_2+RO_2}$  and  $P(O_x)^{O_x}$  was performed for each experiment reported in Table 4.1.



## 4.1. Rational of low vs high NO conditions

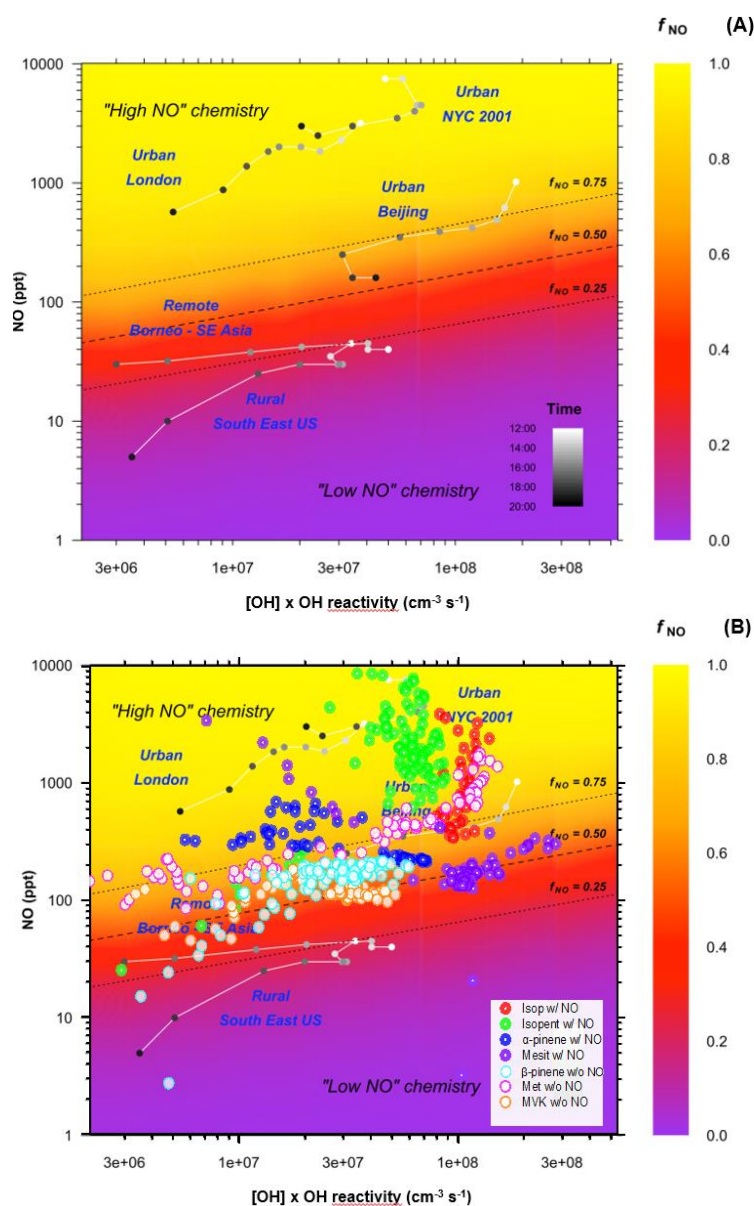
A preliminary look at the results revealed a significant correlation between NO and the level of agreement between  $P(O_x)^{HO_2+RO_2}$  and  $P(O_x)^{O_x}$ . It was therefore decided to class the experiments into two groups. The first group involves experiments conducted without any addition of NO (Table 4.1, cross in the NO column), while the second group comprises experiments during which a specific amount of NO was injected in the chamber. This categorization enables a more thorough analysis to assess the influence of NO on (i) the  $P(O_x)$  quantification and (ii) the mechanisms governing ozone formation.

For the experiments reported in Table 4.1, low NO conditions refer to NO concentrations ranging from 0.04–1.2 ppb, while high NO conditions refer to NO concentrations in the range of 1.2–9.0 ppb. In order to put these experiments in perspective with the definition of "low" and "high" NO oxidation regimes found in the literature, the chemical regimes observed during ROxComp were placed onto a two-dimensional plot proposed by Newland et al.<sup>152</sup>. Figure 4.1 (A) was generated by Newland et al. from box modeling (Dynamically Simple Model of Atmospheric Chemical Complexity / Master Chemical Mechanism v3.3.1) and using field measurements performed in a polluted megacity (Beijing, China) during summer 2017. This two-dimensional space defines the "low" and "high" NO regimes using NO and  $[OH] \times OH$  reactivity as chemical coordinates. The color coding,  $f_{NO}$ , represents the fraction of peroxy radicals reacting with NO, a value of one indicating that all peroxy radicals reacts with NO. The transition between "high" and "low" NO regimes occurs when  $f_{NO}$  is close to 0.5,  $f_{NO} > 0.75$  and  $f_{NO} < 0.25$  being the "high" and "low" NO regimes, respectively.

Results from field measurements performed at different locations in the world are presented with colored symbols, where the color refers to specific periods of the day. We notice that urban sites (London, New York City and Beijing) are mainly characterized by the "high NO" chemistry regime, while remote and rural sites (Borneo-SE Asia<sup>54</sup> and South East US<sup>154</sup>) are characterized by the "low NO" regime.

In Figure 4.1 (B), the results from ROxComp experiments are overlaid onto the original plot of Newland et al. to identify the NO chemistry regime for each experiment. Experiments conducted without NO addition are shown by thin edge circles, while thick edge circles are experiments where NO was added in the chamber.

We clearly notice in Figure 4.1 (B) that most of the experiments where NO was injected in the chamber, i.e. isoprene, i-pentane+n-hexane and  $\alpha$ -pinene experiments, are located in the "high NO" regime. Conversely, for the mesitylene experiment, part of the dataset is located in the transition region, and the other in the high NO regime. On the other hand, the experiments where NO was not injected in the chamber (or injected at the end of the experiment), i.e. the MVK,  $\beta$ -pinene and methane (excluding the last 2 hours) experiments were found to be located in the transition region. We notice that a significant part of the methane experiment is in the high NO chemistry region, due to the injection of  $\sim 1.5$  ppb of NO two hours before the end of the experiment (see Figure 4.2).



**Figure 4. 1:** Two-dimensional space defining "low" and "high" NO VOC oxidation regimes - Variation of  $f_{NO}$  (fraction of peroxy radicals reacting with NO) as a function of OH reactivity and NO. (A) original graph from reference <sup>152</sup>, (B) adapted with results from ROxComp experiments reported in Table 4.1.

It is therefore important to note that the denominations of "high NO" and "low NO" experiments in this study is mainly related to VOC oxidation regimes referred to as "high NO" and "high/low NO transition regime" in the literature.

## 4.2. P(O<sub>x</sub>) quantification under low NO conditions

The datasets presented in this section includes the  $\beta$ -pinene, methane (excluding the last 2 hours) and MVK photooxidation experiments from Table 4.1 during which NO was not injected in SAPHIR. Figure 4.2 displays time series of environmental conditions (T, RH, J-values) for the three experiments, as well as measured concentrations of NO<sub>x</sub>, O<sub>3</sub>, HO<sub>2</sub>+RO<sub>2</sub> (IMT-CA), VOC and the  $\frac{[\text{HO}_2]}{[\text{HO}_2]+[\text{RO}_2]}$  ratio deduced from the speciated FZJ-FAGE measurements.

Panels (A) from Figure 4.2 indicates that each experiment was performed under humid conditions with RH ranging from 10-47%, 10-34% and 8-47% for the  $\beta$ -pinene, methane and MVK experiments, respectively, and a temperature ranging from 20 to 50°C. The photolysis rate of NO<sub>2</sub>, J(NO<sub>2</sub>), was found to be  $(3.8\pm 1.3)\times 10^{-3} \text{ s}^{-1}$ ,  $(3.2\pm 1.6)\times 10^{-3} \text{ s}^{-1}$  and  $(4.4\pm 0.9)\times 10^{-3} \text{ s}^{-1}$  on average for the  $\beta$ -pinene, methane and MVK experiments, respectively.

During these experiments, NO (Figure 4.2, panel B) corresponds to the background concentration generated within the chamber from HONO photolysis as explained earlier. The NO concentration was close to 0.2 ppb for the  $\beta$ -pinene and MVK experiments, and 0.4 ppb during the majority of the methane experiment until a concentration of about 1.5 ppb of NO was injected in SAPHIR for the last two hours of the experiment.

Regarding the NO<sub>2</sub> concentration, it exhibited a relatively similar pattern throughout the three experiments. NO<sub>2</sub> increased from approximately 0.2 ppb at the beginning of the experiments up to 1.7-2.0 ppb towards the end. During the methane photooxidation experiment, the late addition of 1.5 ppb of NO resulted in an increase of NO<sub>2</sub> up to 6 ppb. Approximately 50 ppb of ozone was added in SAPHIR before the opening of the shutter for the  $\beta$ -pinene experiment and shortly after the opening for the MVK experiment. In contrast, ozone was not injected in the chamber for the methane experiment.

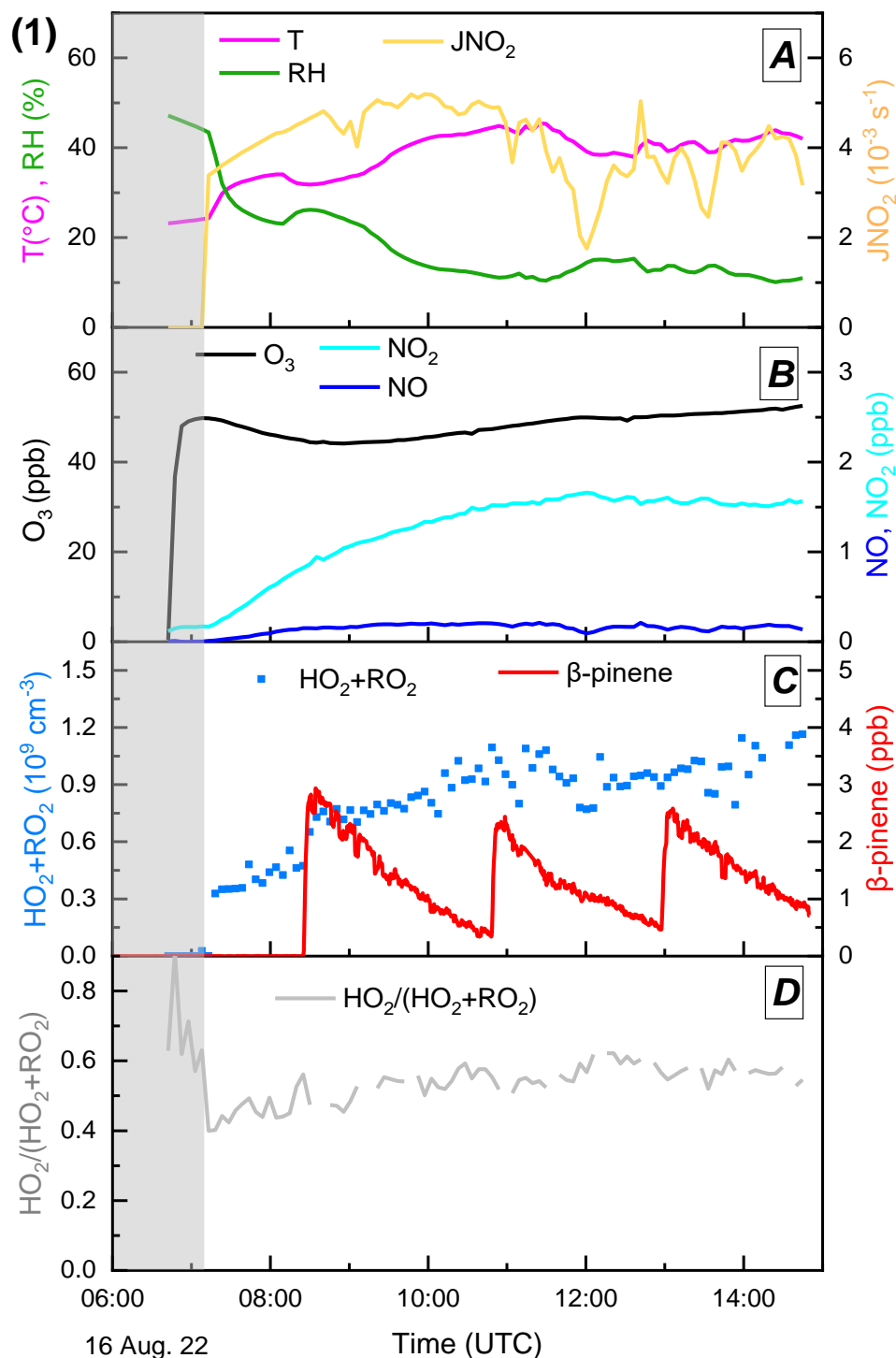
For the VOC addition, three injections were conducted for  $\beta$ -pinene, with concentrations of approximately 3, 2 and 2 ppb observed at 08:25, 10:47 and 12:58, respectively. For the methane experiment, two injections led to concentrations of approximately 70 ppb at 09:03 and 11:48. It should be noted that an injection of 1 ppm of CO was performed before the methane injections at 07:30 am. Unfortunately, methane and CO concentrations were not reported for the whole experiment due to technical issues with the monitor. As for MVK, two injections leading to concentrations of approximately 12 ppb were performed at 10:15 and 12:12.

Throughout these experiments,  $\text{HO}_2+\text{RO}_2$  concentrations reached relatively close maxima of  $1.2 \times 10^9$ ,  $1.3 \times 10^9$  and  $1.5 \times 10^9 \text{ cm}^{-3}$  for the  $\beta$ -pinene, methane and MVK experiments, respectively. These concentrations were variable along the experiments, in response to the addition of different components to the chamber and to changes in environmental conditions.

The  $\frac{[\text{HO}_2]}{[\text{HO}_2+\text{RO}_2]}$  ratios derived from FZJ-FAGE measurements ranged from 0.4 to 0.6. For the  $\beta$ -pinene experiment, this averaged ratio was  $0.54 \pm 0.05$  ( $1\sigma$ ) under irradiated conditions. For the methane experiment, this ratio varied between 0.58 and 0.71 after the CO injection and just before the addition of methane. A ratio higher than 0.5 is consistent with the production of  $\text{HO}_2$  from the reaction of CO with OH, where CO is likely the main species reacting with OH. Upon the injection of methane, this ratio decreased due to the formation of  $\text{CH}_3\text{O}_2$  from the reaction between methane and OH and remained relatively constant at an average value of  $0.42 \pm 0.04$  ( $1\sigma$ ). As for the MVK experiment, the  $\frac{[\text{HO}_2]}{[\text{HO}_2]+[\text{RO}_2]}$  ratio was almost constant along the experiment with an average value of  $0.49 \pm 0.04$  ( $1\sigma$ ). It is worth noting that these ratios are close to values usually observed in ambient measurements<sup>52</sup>. These observations validate the assumption made in section 2.1, i.e. that  $\frac{[\text{HO}_2]}{[\text{HO}_2]+[\text{RO}_2]} = 0.5$ , for the calculation of  $\text{P}(\text{O}_x)$  using  $\text{HO}_2+\text{RO}_2$  measurements from IMT-CA.

Time series of ozone production rates calculated using the methodologies presented in sections 2.1 and 2.2 are depicted in Figure 4.3 for the  $\beta$ -pinene (A), methane (B) and MVK (C) experiments. In this figure  $\text{p}(\text{O}_x)$  represents the gross  $\text{O}_x$  production rate calculated from IMT-CA measurements of  $\text{HO}_2+\text{RO}_2$  (Eq 4. 2), while  $\text{p}(\text{O}_x)_{\text{obs.HO}_2/(\text{HO}_2+\text{RO}_2)}$

represents the gross  $O_x$  production rate calculated from the same  $HO_2+RO_2$  data but using  $\frac{[HO_2]}{[HO_2]+[RO_2]}$  ratios derived from FZJ-FAGE data (Eq 4. 1).



**Figure 4.2:** Experimental chamber observations for the (1)  $\beta$ -pinene, (2) methane and (3) MVK experiments: A - Chamber's environmental conditions (T, RH, J- $NO_2$ ), B -  $O_3$  and  $NO_x$  concentrations, C -  $HO_2+RO_2$  from IMT-CA and VOC concentrations (technical issues occurred when measuring CO and  $CH_4$ ), D -  $\frac{[HO_2]}{[HO_2]+[RO_2]}$  ratios calculated from FZJ-FAGE measurements. The grey shadow is an indication of dark conditions.

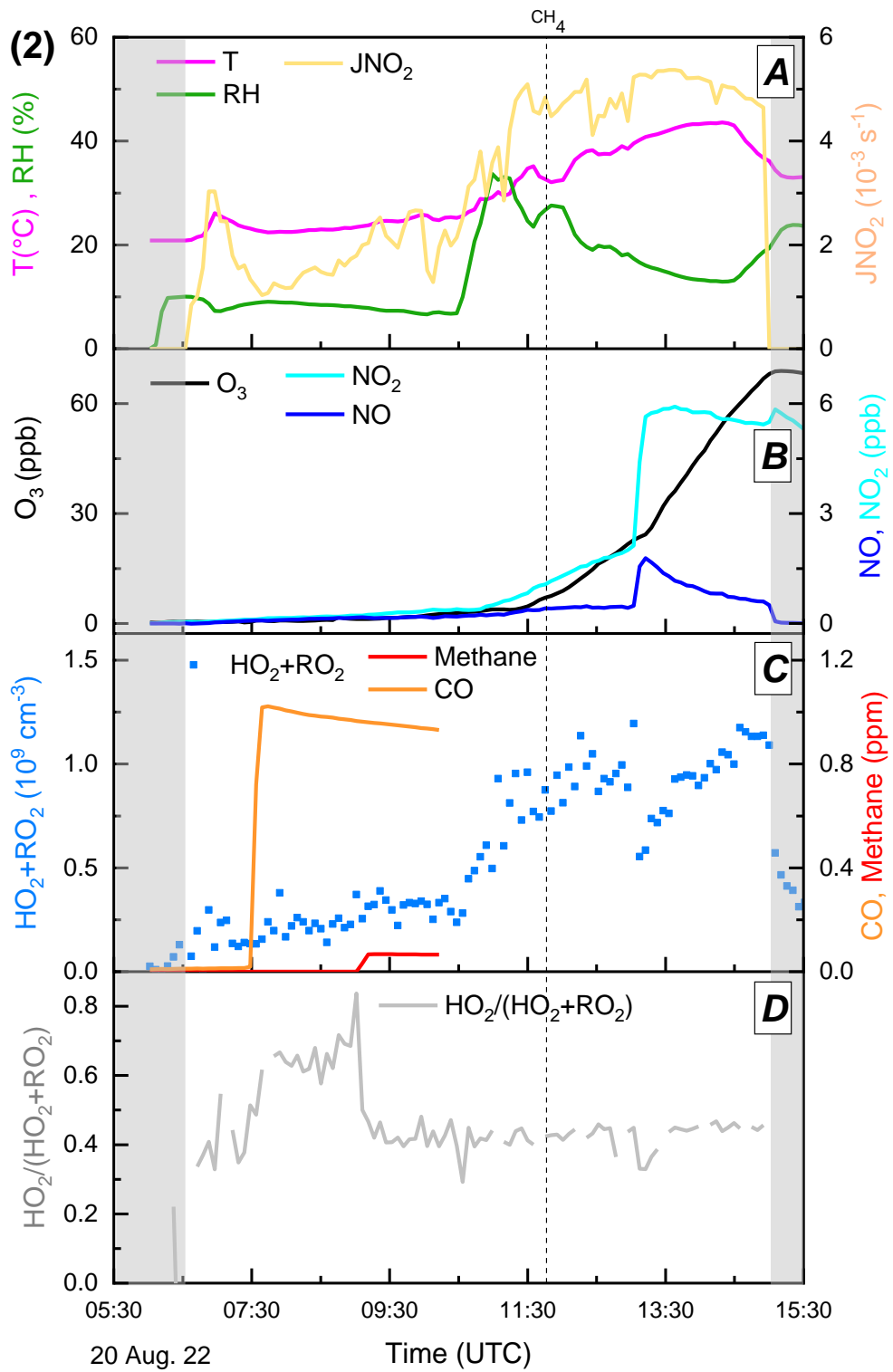
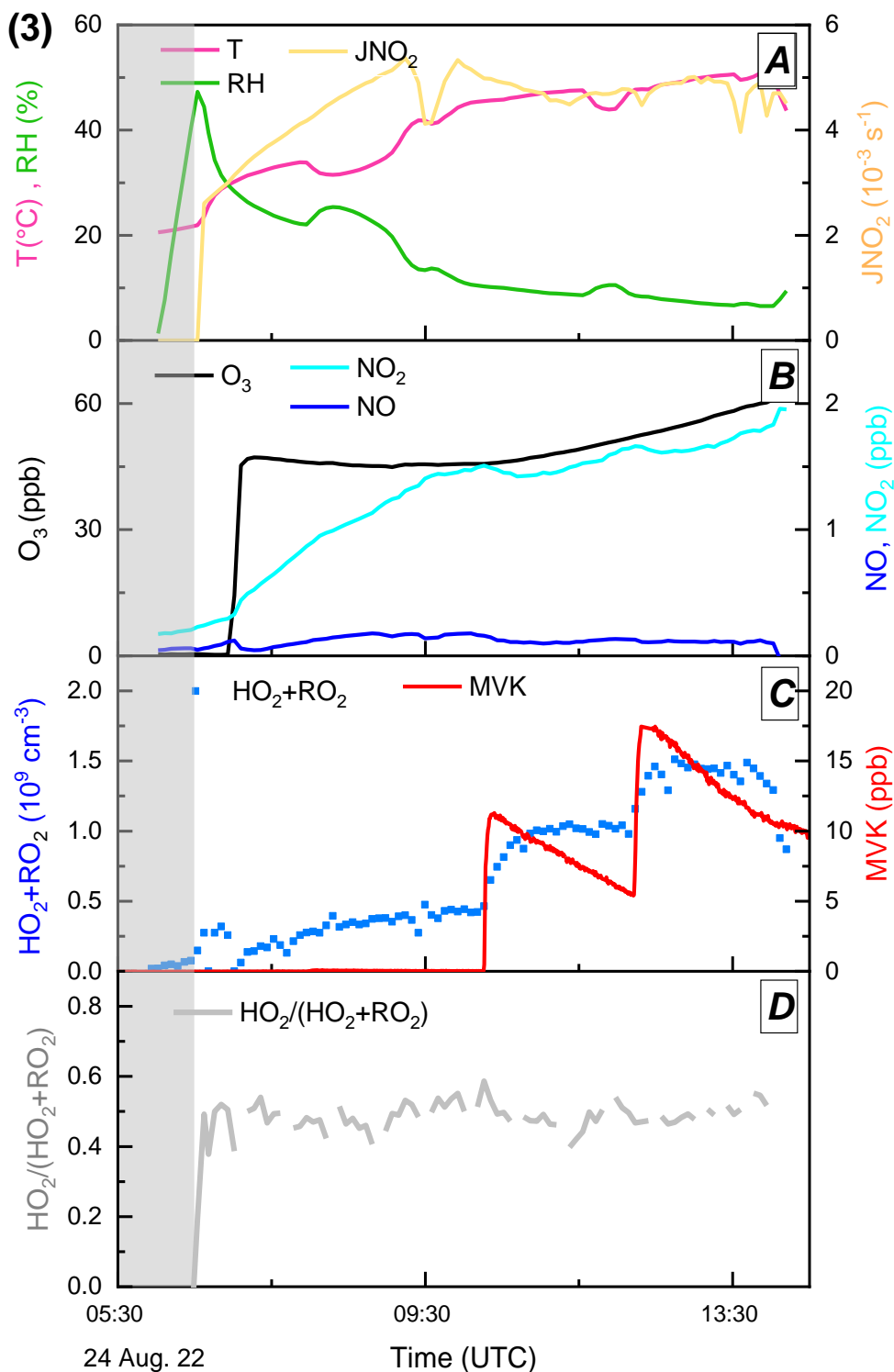


Figure 4.2 (continued)

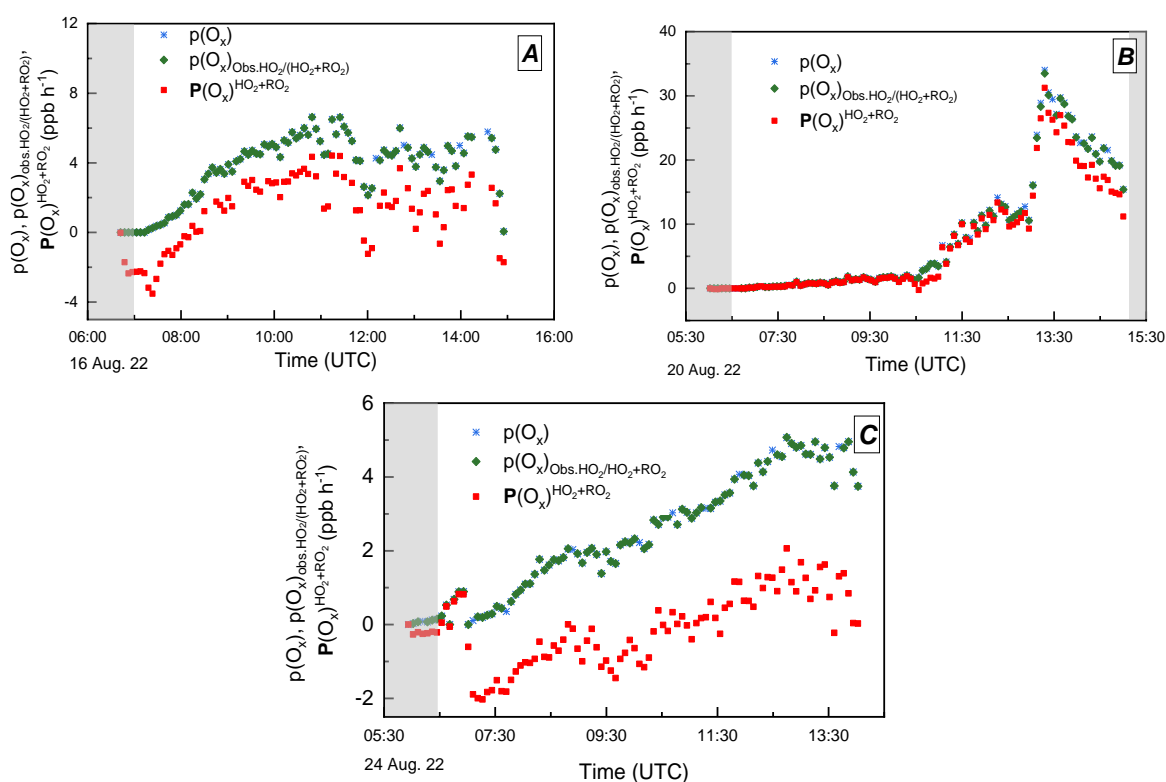


**Figure 4.2 (continued)**

A close look at the three panels of Figure 4.3 reveals a very good agreement between the two gross O<sub>3</sub> production rates  $p(O_x)$  and  $p(O_x)_{\text{obs.HO}_2/(\text{HO}_2+\text{RO}_2)}$ . This observation confirms that using the sum of HO<sub>2</sub>+RO<sub>2</sub> measured by IMT-CA and an average rate coefficient ( $k_{\text{peroxy}+\text{NO}}$ ) to calculate the gross  $p(O_x)$ , instead of speciated concentrations of

HO<sub>2</sub> and RO<sub>2</sub> and individual rate coefficients, leads to a relative bias lower than 1%. A similar difference is expected for p(O<sub>x</sub>) quantification in ambient air, since experimental conditions used in the SAPHIR chamber mimic atmospheric conditions.

During the β-pinene experiment (Figure 4.3 (A)), the net  $\mathbf{P}(\text{O}_x)^{\text{HO}_2+\text{RO}_2}$  was found to be lower than the gross p(O<sub>x</sub>) by approximately  $2.8 \pm 0.6 \text{ ppb h}^{-1}$  (76%). For the methane experiment (Figure 4.3 (B)), these two quantities were close during the first half of the experiment. A small difference (< 18%) is observed after 13:04 when NO is added to the chamber, which can be explained by an increase of the NO<sub>2</sub> loss rate through its reaction with OH. As for the MVK experiment, a significant difference between  $\mathbf{P}(\text{O}_x)^{\text{HO}_2+\text{RO}_2}$  and p(O<sub>x</sub>) appeared when O<sub>3</sub> was injected in the chamber at 07:00, up to  $4.1 \text{ ppb h}^{-1}$ . Differences observed between  $\mathbf{P}(\text{O}_x)^{\text{HO}_2+\text{RO}_2}$  and p(O<sub>x</sub>) are due to O<sub>x</sub> losses within the chamber, indicating that l(O<sub>x</sub>) can be significant compared to p(O<sub>x</sub>) and that  $\mathbf{P}(\text{O}_x)$  cannot be accurately estimated from p(O<sub>x</sub>) determinations only.

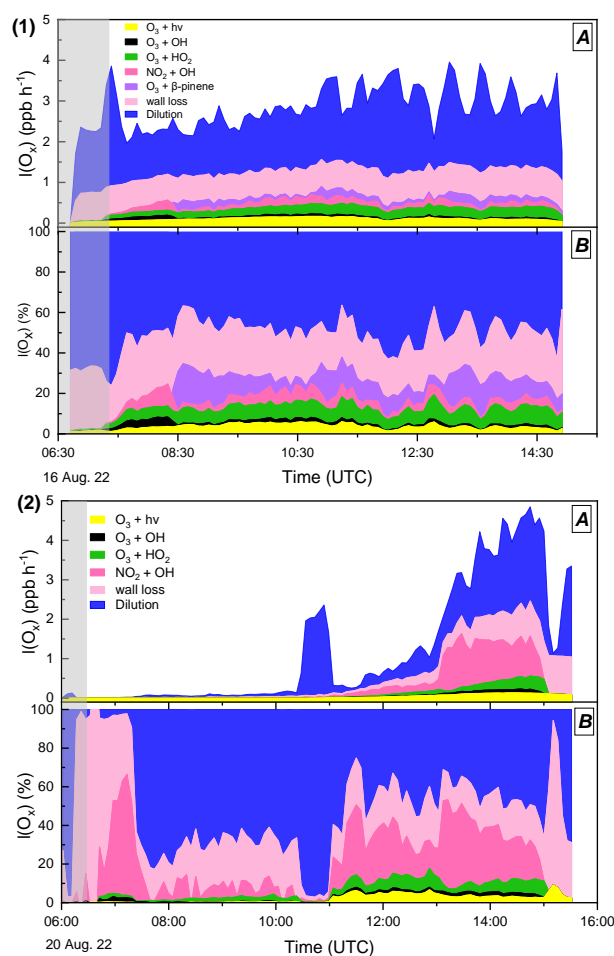


**Figure 4.3:** Ozone production rates for the (A) β-pinene, (B) methane and (C) MVK experiments: p(O<sub>x</sub>) from IMT-CA measurements of HO<sub>2</sub>+RO<sub>2</sub> (blue stars), p(O<sub>x</sub>)<sub>obs.HO<sub>2</sub>/(HO<sub>2</sub>+RO<sub>2</sub>)</sub> from IMT CA measurements of HO<sub>2</sub>+RO<sub>2</sub> and  $\frac{[\text{HO}_2]}{[\text{HO}_2]+[\text{RO}_2]}$  ratios from FZJ-FAGE (green diamonds) and net  $\mathbf{P}(\text{O}_x)^{\text{HO}_2+\text{RO}_2}$  (red squares). The grey shadow is an indication of dark conditions.

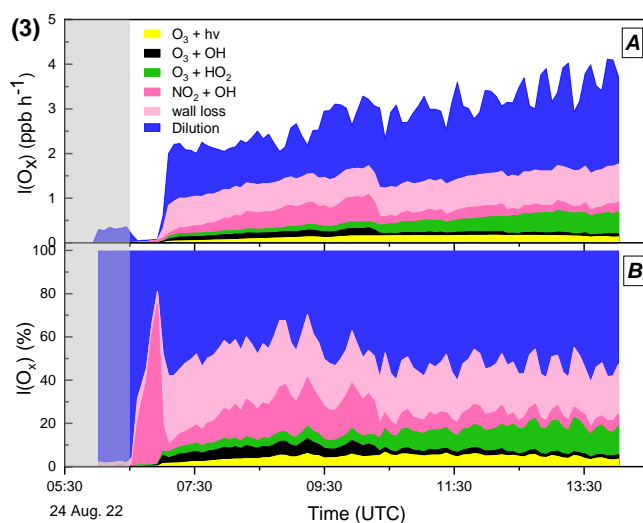


To determine the contribution of each  $O_x$  loss process, calculations were conducted on the basis of Eq 4. 4 (section 2.1) for the three experiments. Figure 4.4 shows that the main processes contributing to  $O_x$  losses are related to the use of a simulation chamber. The contributions of dilution and  $O_3$  wall losses to the total  $O_x$  loss rate were found to be 54% and 23% on average for the three experiments, respectively.

Gas-phase chemical loss processes only account for approximately 19%, 26% and 24% of the total  $O_x$  loss rate on average for the  $\beta$ -pinene, methane and MVK experiments, respectively. Among the chemical processes, we note the predominance of the  $O_3+HO_2$  and  $NO_2+OH$  reactions, accounting for 6.3 and 8.3% on average for the three experiments, respectively. A moderate loss from  $O_3$  photo-dissociation is also observed. It is worth noting that during the  $\beta$ -pinene experiment, a significant additional loss process is observed. It consists on the  $O_3+\beta$ -pinene reaction, contributing to about 22% to the total chemical loss rate on average.



**Figure 4.4:** A - Stacked  $O_x$  loss rates in  $ppb\ h^{-1}$  for the (1)  $\beta$ -pinene, (2) methane and (3) MVK experiments, B - Contribution of each  $O_x$  loss process to the total loss. The grey shadow is an indication of dark conditions.

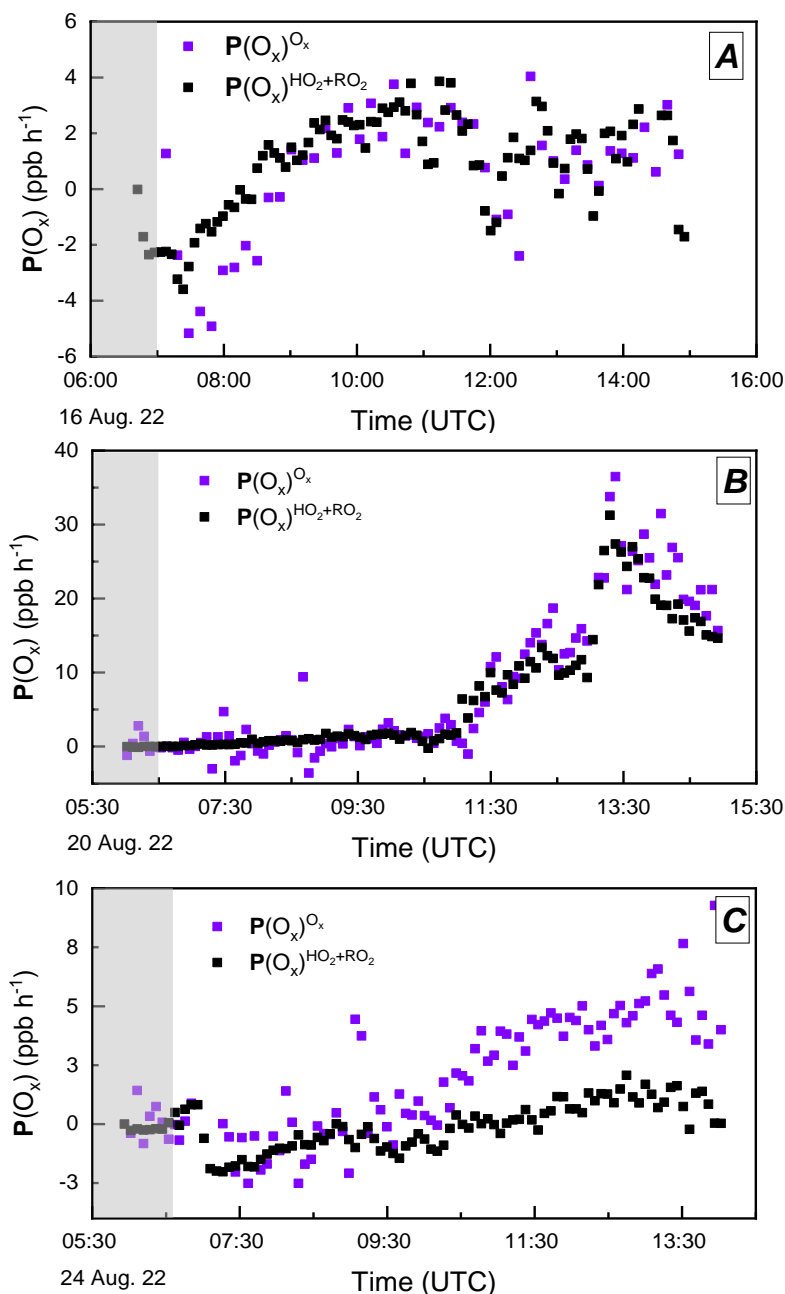


**Figure 4.4 (continued)**

The difference between the net  $\mathbf{P}(\text{O}_x)^{\text{HO}_2+\text{RO}_2}$  and the gross  $p(\text{O}_x)$  is expected to be lower during ambient measurements than during chamber experiments, due to the absence of the dilution effect and  $\text{O}_x$  wall losses. On the basis of the loss rates displayed in Figure 4.4, this difference should range from 5-24%, which corresponds to the contribution of chemical loss processes to the total loss of  $\text{O}_x$  species.

Figure 4.5 contrasts the two net  $\text{O}_3$  production rates calculated from radical measurements, i.e.  $\mathbf{P}(\text{O}_x)^{\text{HO}_2+\text{RO}_2}$ , and from changes in  $\text{O}_x$  concentrations over time,  $\mathbf{P}(\text{O}_x)^{\text{O}_x}$ . A good agreement is observed for the  $\beta$ -pinene and methane experiments, with averaged differences of only 8% and 9%, respectively.

For the MVK experiment, a good agreement was observed during the first half of the experiment. A significant difference appears when MVK is injected in the chamber at 10:15,  $\mathbf{P}(\text{O}_x)^{\text{O}_x}$  increasing over time while  $\mathbf{P}(\text{O}_x)^{\text{HO}_2+\text{RO}_2}$  remains constant. The difference between the two quantities went up to about 75% by the end of the experiment. While the source of this disagreement is not yet understood, this is likely related to the disagreement observed between  $\text{HO}_2+\text{RO}_2$  concentrations reported by the IMT-CA and FZJ-FAGE instruments in chapter 3 (section 4.2), which could be due to an issue in the subtraction of the  $\text{O}_3$ -water bias for the CA measurements.



**Figure 4.5:** Comparison between  $\text{P}(\text{O}_x)^{\text{HO}_2+\text{RO}_2}$  and  $\text{P}(\text{O}_x)^{\text{O}_x}$  for the (A)  $\beta$ -pinene, (B) methane and (C) MVK experiments. The grey shadow is an indication of dark conditions.

### 4.3. $\text{P}(\text{O}_x)$ quantification under high NO

The group of experiments used to evaluate the ozone production rate quantification methodology under high NO conditions includes the photooxidation reactions of isoprene, i-pentane+n-hexane,  $\alpha$ -pinene and mesitylene. Time series of temperature, RH,  $\text{NO}_x$ ,  $\text{O}_3$ ,  $\text{HO}_2+\text{RO}_2$  from IMT-CA and VOC concentrations, as well as the  $\frac{[\text{HO}_2]}{[\text{HO}_2]+[\text{RO}_2]}$  ratio are depicted in Figure 4.6 for the four experiments.

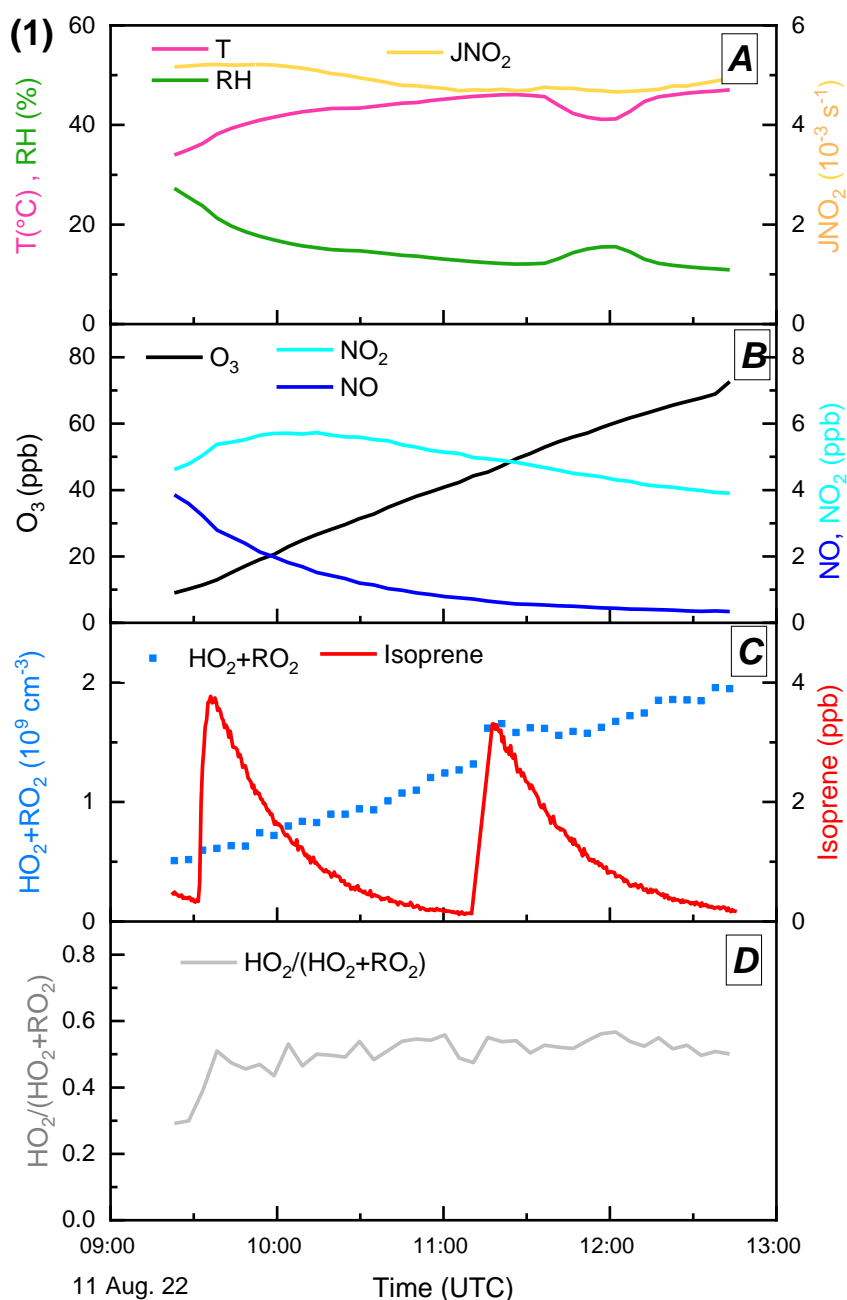
Similarly to the previous section, these experiments were conducted under humid conditions as shown in panels A, with RH varying from 11-27%, 7-45%, 8-50% and 10-49%, for isoprene, i-pentane+n-hexane,  $\alpha$ -pinene and mesitylene, respectively. Temperature was in the range of 23-51°C. The solar irradiance was similar during these experiments, with an average  $J(\text{NO}_2)$  value of about  $5 \times 10^{-3} \text{ s}^{-1}$ .

During the isoprene experiment (Figure 4.6 (1)), NO was injected at the beginning and its concentration decreased from 3.9 to 0.3 ppb over 3.5 hours.  $\text{NO}_2$  slowly varied over the course of this experiment and was about  $4.9 \pm 0.6$  ppb ( $1\sigma$ ) on average. The addition of  $\sim 3.5$  ppb of isoprene at 09:30 and 11:30 led to a monotonous increase of  $\text{HO}_2$  and  $\text{RO}_2$ , the sum of which went up to  $\sim 2 \times 10^9 \text{ cm}^{-3}$  towards the end of the experiment. The reaction of these radicals with NO resulted in the production of large amounts of  $\text{O}_3$ , whose concentration increased from 9 to 73 ppb.

For the i-pentane+n-hexane experiment (Figure 4.6 (2)), two injections of NO were made throughout the experiment, the first one at 07:53 leading to a concentration of approximately 8.5 ppb, and the second at 11:23 with a concentration of about 2 ppb.  $\text{NO}_2$  mostly increased all along the experiment within the range of 0.2 – 12.2 ppb. The oxidation of  $\sim 69$  ppb of i-pentane injected between 07:56-08:10 resulted in the production of  $\sim 3 \times 10^8 \text{ cm}^{-3}$  of  $\text{HO}_2 + \text{RO}_2$ . This concentration slowly increased to about  $9 \times 10^8 \text{ cm}^{-3}$  after the injection of 96 ppb of n-hexane at 11:26. Unfortunately, GC measurements of i-pentane and n-hexane were not available for this analysis. During this experiment, we notice that the peroxy radical concentrations were low compared to the other experiments. This can be explained to some extent by the low reactivity of i-pentane and n-hexane with OH compared to the other VOCs, as reported in Table 4.1. The reaction of these peroxy radicals with NO led to an increase of  $\text{O}_3$  from  $< \text{LoD}$  up to about 80 ppb.

In the case of the  $\alpha$ -pinene experiment (Figure 4.6 (3)), a concentration of  $\sim 84$  ppb of  $\text{O}_3$  was added in the chamber before opening the shutter. This concentration gradually decreased until the shutter system was opened and approximately 1 ppb of NO was injected at 09:40. This was accompanied by an increase in  $\text{NO}_2$  reaching a maximum value of about 8 ppb. Both NO and  $\text{NO}_2$  then decreased along the experiment. Several injections of  $\alpha$ -pinene were made at different times when the chamber was irradiated (09:46, 11:28, 13:17), with peak concentrations in the range of 1.4-2.7 ppb. The chemistry resulted in the

production of  $\text{HO}_2+\text{RO}_2$  with a total concentration ranging from  $(0.2-2.0)\times 10^9 \text{ cm}^{-3}$ . Ozone slowly increased along the experiment from  $\sim 74$  ppb to  $\sim 97$  ppb during the irradiated period.



**Figure 4.6:** Experimental chamber observations for the (1) isoprene, (2) i-pentane+n-hexane, (3)  $\alpha$ -pinene and (4) mesitylene experiments: A - Chamber's operating conditions (T, RH,  $\text{JNO}_2$ ), B -  $\text{O}_3$  and  $\text{NO}_x$  concentrations, C -  $\text{HO}_2+\text{RO}_2$  from IMT-CA and VOC concentrations, D -  $\frac{[\text{HO}_2]}{[\text{HO}_2]+[\text{RO}_2]}$  calculation from FZJ-FAGE measurements. The grey shadow is an indication of dark conditions.

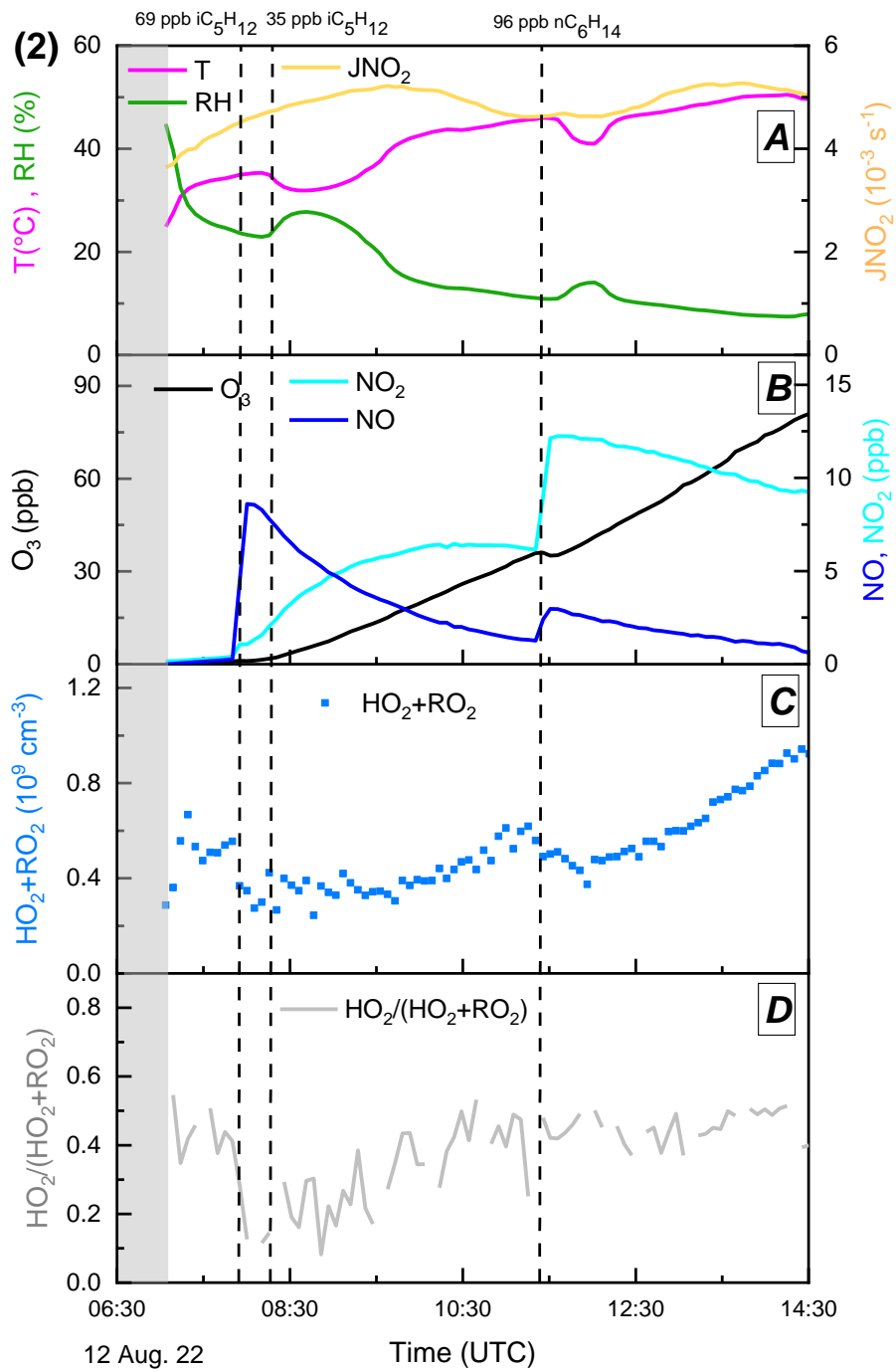
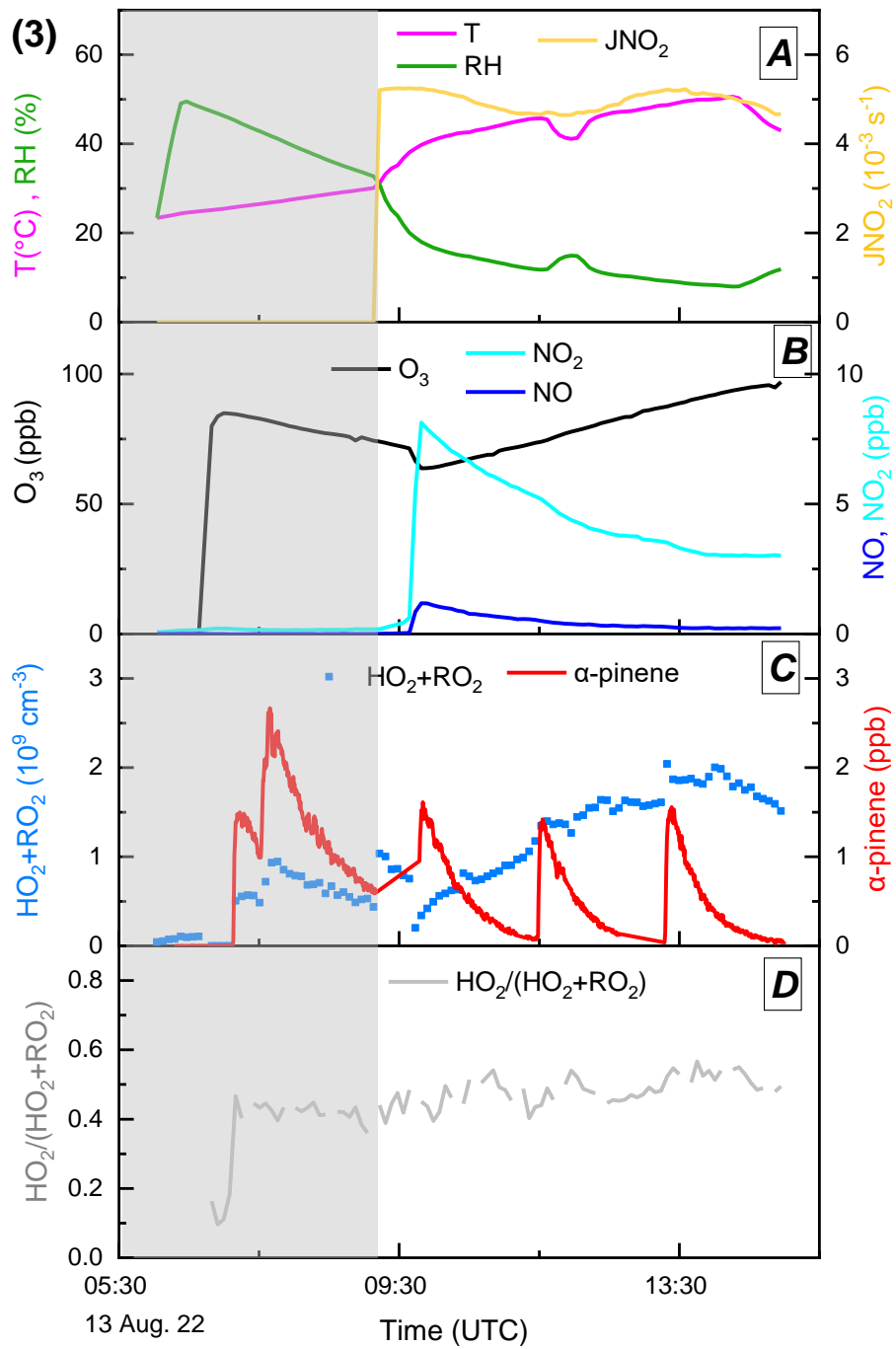
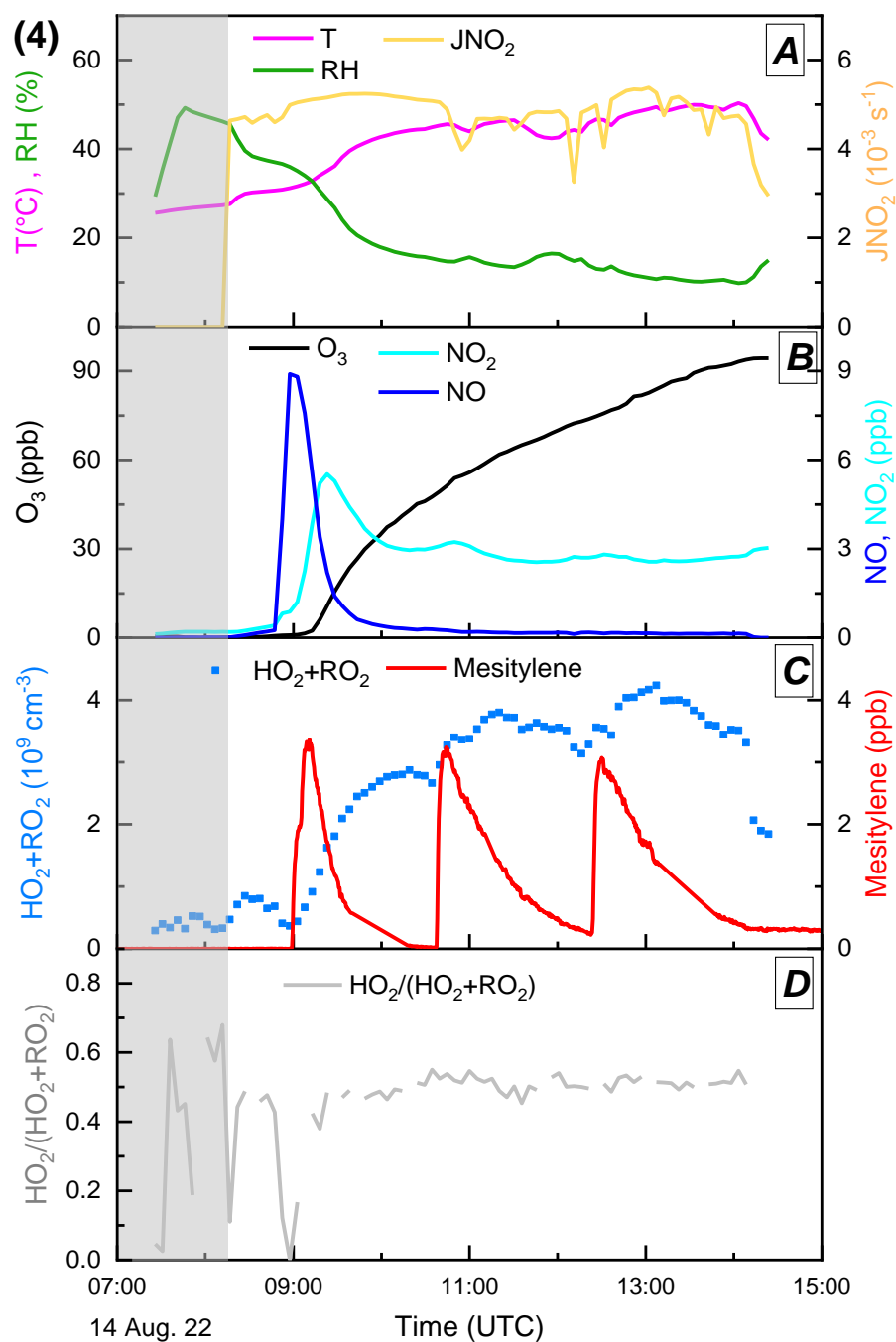


Figure 4.6 (continued)



**Figure 4.6 (continued)**



**Figure 4.6 (continued)**

For mesitylene (Figure 4.6 (4)), a high concentration of NO of about 9 ppb was introduced in the chamber around 9 am after the opening of the shutter. This resulted in an increase in [NO<sub>2</sub>] from 0.4 up to 5.5 ppb, which then decreased to ~2.6 ppb within an hour. It is worth reminding that among these four VOCs, mesitylene has the second highest reactivity with OH, which likely explain the observation of high concentrations of HO<sub>2</sub>+RO<sub>2</sub>. The latter increased at each injection of mesitylene, to reach a maximum value of about  $4.2 \times 10^9 \text{ cm}^{-3}$ . The simultaneous presence of high concentrations of NO and



HO<sub>2</sub>+RO<sub>2</sub> led to a fast production of O<sub>3</sub>, which increased from < LoD at the beginning of the experiment up to 94 ppb at the end.

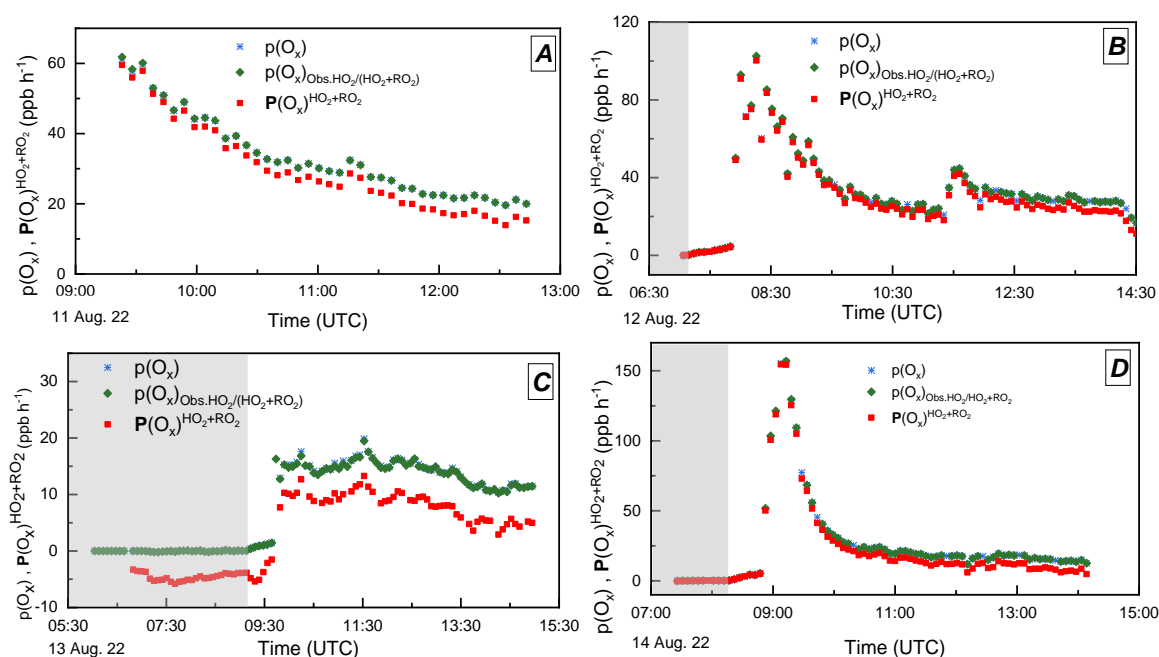
According to the FZJ-FAGE data, the  $\frac{[\text{HO}_2]}{[\text{HO}_2]+[\text{RO}_2]}$  ratio along the four experiments was in the range of 0.4-0.5 on average, which is similar to that observed for the low NO experiments. For the i-pentane+n-hexane experiment, we notice that this ratio was lower in the middle of the experiment, with an average value of 0.33, revealing that RO<sub>2</sub> was produced at a higher rate than HO<sub>2</sub> from the oxidation of i-pentane. This ratio increased progressively with the decrease of i-pentane, reaching an average and stable value of about 0.46 after the addition of n-hexane.

Figure 4.7 displays a comparison between the net and gross O<sub>3</sub> production rates calculated from radical and ancillary measurements. Similar to the low NO experiments, a good agreement is observed between  $p(\text{O}_x)$  and  $p(\text{O}_x)_{\text{obs.HO}_2/(\text{HO}_2+\text{RO}_2)}$  during the four experiments, confirming that using the sum of HO<sub>2</sub>+RO<sub>2</sub> measured by the CA and an average rate coefficient (hypothesis from section 2.1) is suitable to quantify  $p(\text{O}_x)$  under high NO conditions.

An examination of the four panels of Figure 4.7 reveals significant deviations between  $\mathbf{P}(\text{O}_x)^{\text{HO}_2+\text{RO}_2}$  and  $p(\text{O}_x)$ . For instance, during the isoprene experiment (Figure 4.7 (A)), a notable difference between these two quantities emerges over time, ranging from 1.6 to 5.7 ppb h<sup>-1</sup> (2.7 - 29 %). In contrast, during the i-pentane+n-hexane experiment (Figure 4.7 (A)), this difference was small along the majority of the experiment, increasing only during the last 2 h, to less than 6.2 ppb h<sup>-1</sup> (33%). Although the total O<sub>x</sub> loss rates during these two experiments are comparable as presented in Figure 4.8 (1 & 2), higher gross ozone production rates observed during the i-pentane+n-hexane experiment led to a lower relative difference between  $\mathbf{P}(\text{O}_x)^{\text{HO}_2+\text{RO}_2}$  and  $p(\text{O}_x)$ .

For the  $\alpha$ -pinene experiment shown in Figure 4.7 (C), we notice the presence of negative values in  $\mathbf{P}(\text{O}_x)^{\text{HO}_2+\text{RO}_2}$  under dark conditions. This is due to the large loss rate of O<sub>3</sub> (initially injected in the chamber) due to dilution and wall losses, with no concurrent ozone production occurring at that time. In fact, significant O<sub>x</sub> production was only initiated when the shutter system was opened and NO was injected at 09:40. The difference between  $p(\text{O}_x)$  and  $\mathbf{P}(\text{O}_x)^{\text{HO}_2+\text{RO}_2}$  steadily increased along the experiment up to 7.5 ppb h<sup>-1</sup> (62%).

This particular experiment served as means to check the wall loss rate of O<sub>3</sub> reported in the literature for SAPHIR ( $3.9 \times 10^6 \text{ s}^{-1}$ <sup>137</sup>). In fact, between 06:45 and 07:07, only O<sub>3</sub> was present in the chamber, implying that the O<sub>3</sub> loss during this period is only attributed to wall losses and dilution (as depicted in Figure 4.8 (3)). Knowing the dilution rate ( $0.028 \text{ h}^{-1}$ , calculated from the air flow rate continuously added in SAPHIR and the chamber volume), the  $P(\text{O}_x)^{\text{Ox}}$  value ( $-3.52 \text{ ppb h}^{-1}$ , calculated from the change in O<sub>x</sub> over time) and considering an O<sub>3</sub> concentration of 83.4 ppb, the O<sub>3</sub> wall loss rate was found to be  $3.93 \times 10^6 \text{ s}^{-1}$ , which is in good agreement with the value reported in the literature<sup>137</sup>.

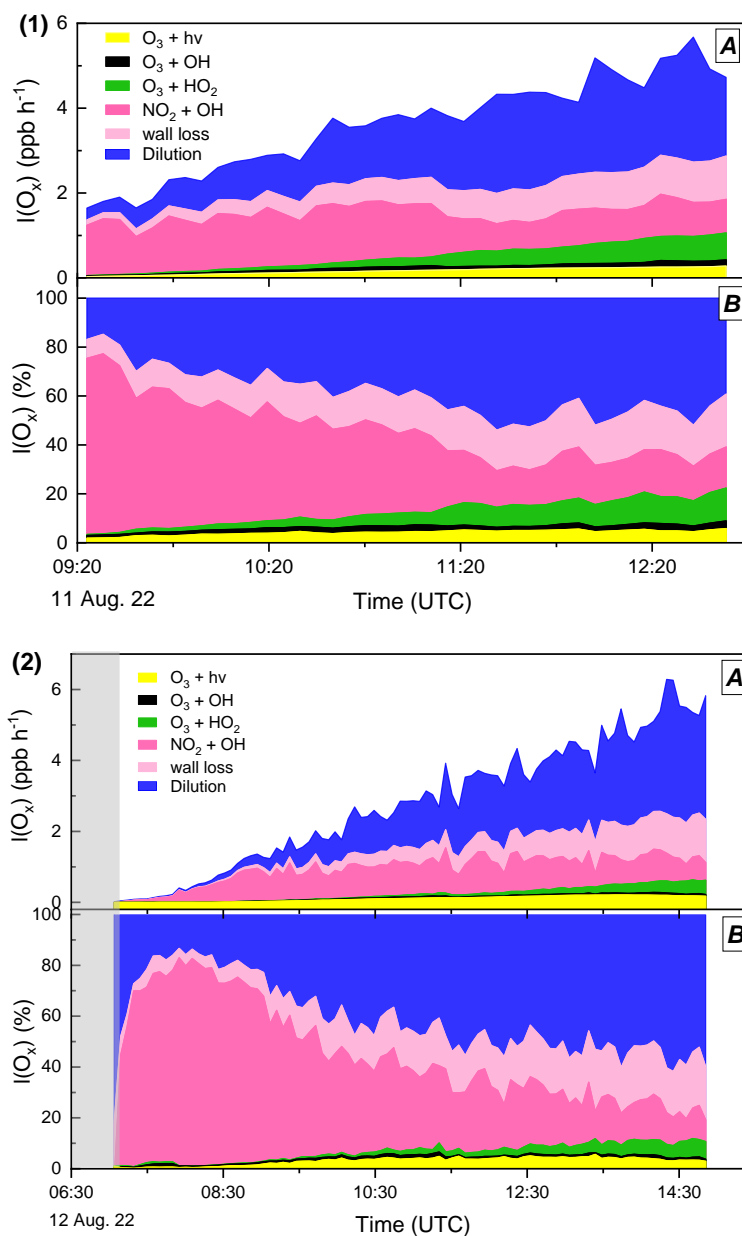


**Figure 4.7:** Ozone production rates for the (A) isoprene, (B) i-pentane+n-hexane, (C)  $\alpha$ -pinene and (D) mesitylene experiments:  $p(\text{O}_x)$  from HO<sub>2</sub>+RO<sub>2</sub> measured by IMT CA (blue stars),  $p(\text{O}_x)_{\text{obs.HO}_2}/(\text{HO}_2+\text{RO}_2)$  calculated from HO<sub>2</sub>+RO<sub>2</sub> measured by the CA and  $\frac{[\text{HO}_2]}{[\text{HO}_2]+[\text{RO}_2]}$  ratio from FZJ-FAGE (green diamonds) and net  $P(\text{O}_x)^{\text{HO}_2+\text{RO}_2}$  (red squares). The grey shadow is an indication of dark conditions.

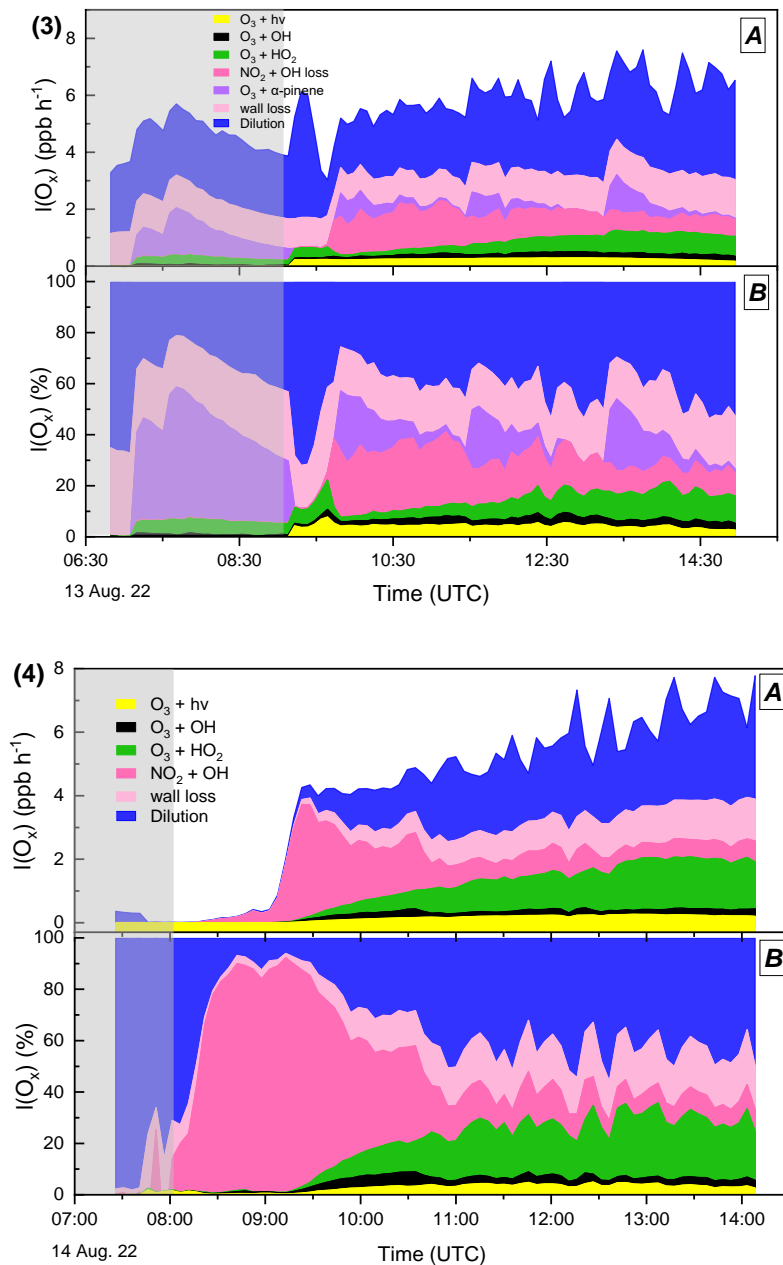
During the mesitylene experiment, a high gross production rate of O<sub>x</sub> was observed compared to the other experiments, reaching a peak value of  $155 \text{ ppb h}^{-1}$  (Figure 4.7 (D)). The difference between  $p(\text{O}_x)$  and  $P(\text{O}_x)^{\text{HO}_2+\text{RO}_2}$  was negligible during the first half of the experiment, and was only notable by the end of the experiment where it reaches a value of  $7.8 \text{ ppb h}^{-1}$  (62%).

According to panels B in Figure 4.8, the two main processes contributing to O<sub>x</sub> losses during these experiments are dilution and O<sub>3</sub> wall losses as observed for the low NO experiments. Dilution was the predominant process with an average contribution to the total

loss rate of about 39-45% for these four experiments. The  $O_3$  wall loss was significant with an average contribution ranging from 13-19%. Interestingly, the  $NO_2+OH$  reaction is also important, with averaged contributions of 15-38%, due to the high  $NO_2$  concentrations present during these experiments compared to the low  $NO$  experiments. Finally, the  $O_3+\alpha$ -pinene reaction contributes significantly for the  $\alpha$ -pinene experiment with an average contribution of 8%.



**Figure 4.8:** A -Stacked  $O_x$  loss rates in  $ppb\ h^{-1}$  for the (1) isoprene, (2) i-pentane+n-hexane, (3)  $\alpha$ -pinene and (4) mesitylene experiments, B - Contribution of each  $O_x$  loss process to the total loss. The grey shadow is an indication of dark conditions.

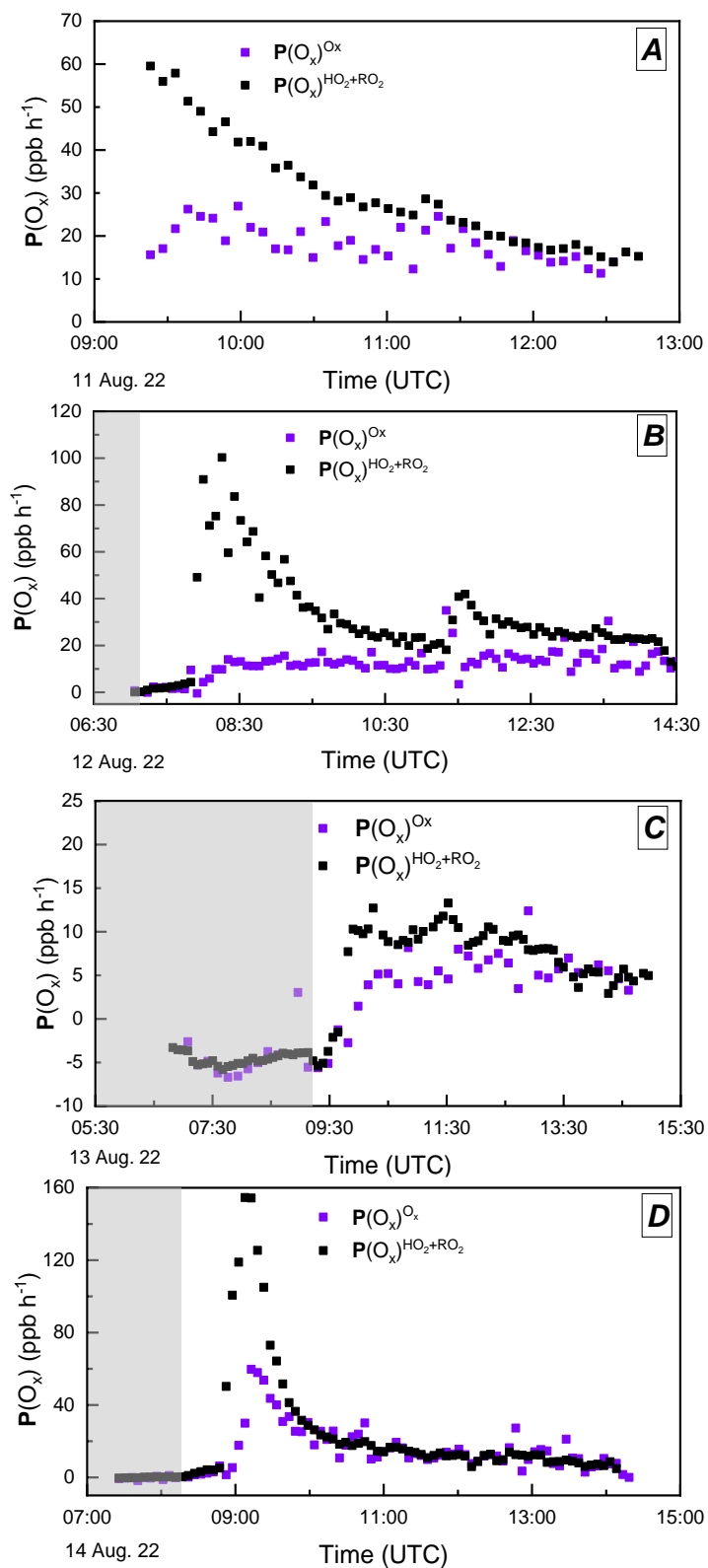


**Figure 4.8 (continued)**

Similar to low NO experiments, the difference between the net  $P(O_x)^{HO_2+RO_2}$  and the gross  $p(O_x)$  during high NO conditions is expected to be lower during field measurements. Based on the observed losses in Figure 4.8, this difference is awaited to be in the range of 24 to 44%, when only considering the contribution of chemical loss processes, which is higher than the one estimated for low NO conditions (5-24%).

When comparing the two net  $O_x$  production rates:  $P(O_x)^{HO_2+RO_2}$  and  $P(O_x)^{O_x}$  in Figure 4.9, a satisfactory agreement was found during some time periods, e.g. after 10:00 for the

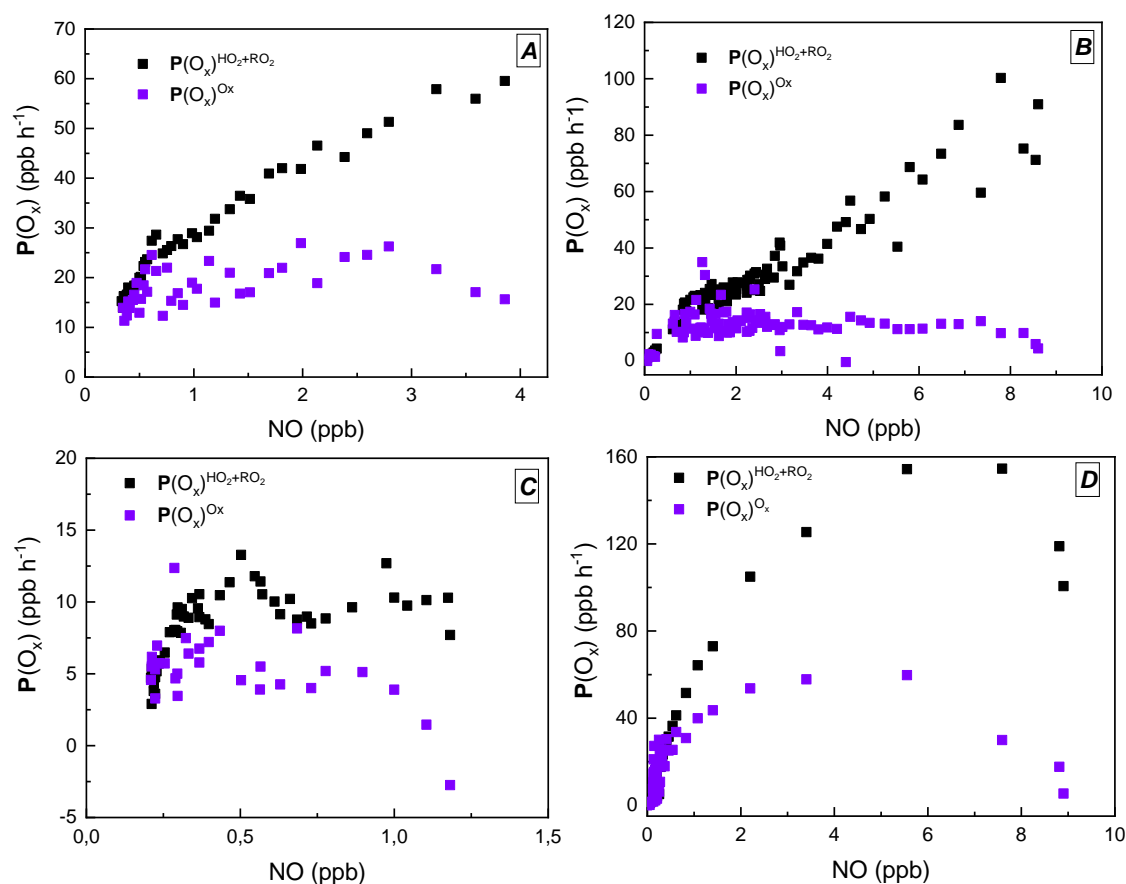
mesitylene experiment as illustrated in panel D. However, a significant difference appears between these two quantities for other time periods.



**Figure 4.9:** Comparison between  $P(O_x)^{HO_2+RO_2}$  and  $P(O_x)^{O_x}$  for the (A) isoprene, (B) i-pentane+n-hexane (C)  $\alpha$ -pinene and (D) mesitylene experiments. The grey shadow is an indication of dark conditions.

A close look at these results revealed that the disagreements coincide with NO injections. For the isoprene experiment (panel A, Figure 4.9), an important difference of about 74% between the two  $P(O_x)$  quantities is observed at the beginning of the experiment when NO is the highest (3.9 ppb), progressively decreasing over time with NO. Conversely, in the case of i-pentane+n-hexane (panel B, Figure 4.9), a good agreement is observed in the very beginning of the experiment until NO is injected in SAPHIR around 07:50, a significant difference of almost one order of magnitude being observed afterward. A similar behavior was observed in the case of  $\alpha$ -pinene and mesitylene experiments. For  $\alpha$ -pinene, the disagreement was observed after the NO injection at 09:40, reaching up to 86%, while for the mesitylene, it appeared after the NO injection at 08:50 for a short period of time (about 1 h) during which NO quickly decreased from 8.9 to less than 0.5 ppb, the two  $P(O_x)$  quantities agreeing after that until the end of the experiment.

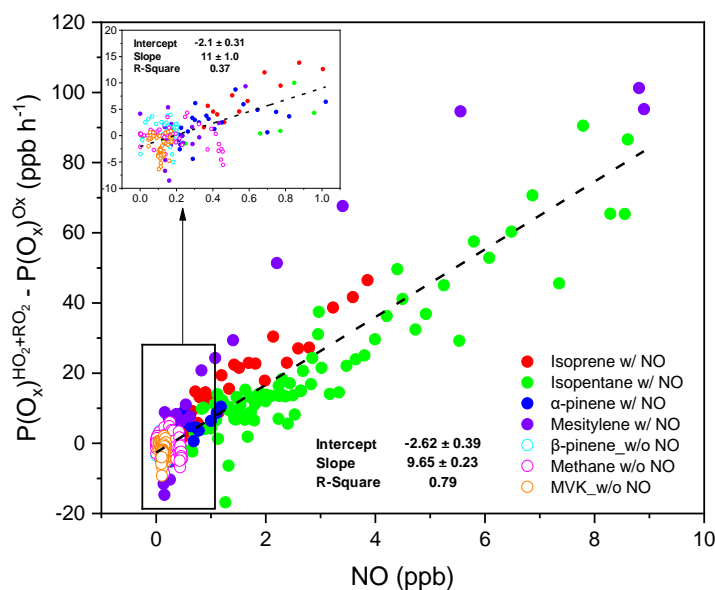
To better understand these observations,  $P(O_x)^{HO_2+RO_2}$  and  $P(O_x)^{O_x}$  were plotted together as a function of NO in Figure 4.10.



**Figure 4.10:** Dependence of  $P(O_x)^{HO_2+RO_2}$  and  $P(O_x)^{O_x}$  on NO for the (A) isoprene, (B) i-pentane+n-hexane (C)  $\alpha$ -pinene and (D) mesitylene experiments.

As expected, these two quantities increase with NO when its concentration is in the low ppb range, which is characteristic of a  $\text{NO}_x$ -limited regime. While a turnover seems to be observed above a certain threshold of NO for some experiments, e.g 0.8-1.0 ppb for the  $\alpha$ -pinene experiment and 5-7 ppb for the mesitylene experiment. However, there is no clear indication of a turnover for the isoprene and i-pentane+n-hexane experiments. In addition, Figure 4.10 clearly shows that both  $\mathbf{P}(\text{O}_x)$  quantities increase at different rates with NO,  $\mathbf{P}(\text{O}_x)^{\text{HO}_2+\text{RO}_2}$  increasing faster than  $\mathbf{P}(\text{O}_x)^{\text{O}_x}$ . It is worth noting that along the four experiments, and for low NO concentrations ( $< 0.5$  ppb) a relatively good agreement is observed between  $\mathbf{P}(\text{O}_x)^{\text{HO}_2+\text{RO}_2}$  and  $\mathbf{P}(\text{O}_x)^{\text{O}_x}$ .

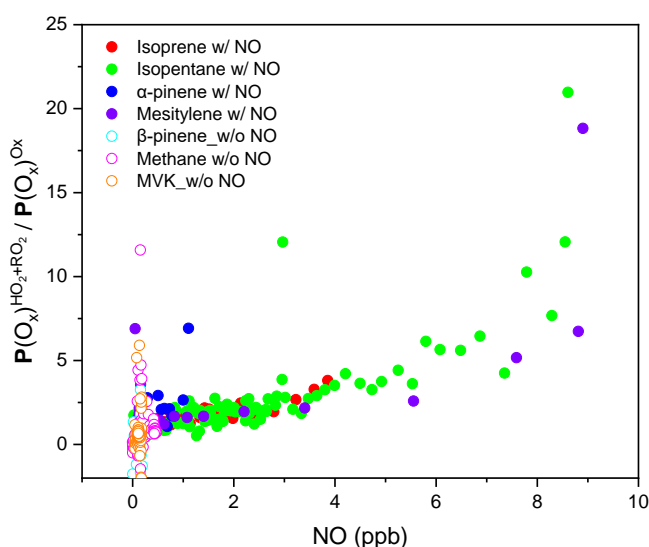
The difference between  $\mathbf{P}(\text{O}_x)^{\text{HO}_2+\text{RO}_2}$  and  $\mathbf{P}(\text{O}_x)^{\text{O}_x}$  at varying NO concentrations for both low and high NO experiments is depicted in Figure 4.11, where all experiments seem to be consistent together. In fact, during the  $\beta$ -pinene, methane and MVK experiments, where NO concentration was lower than 0.5 ppb, the difference between the two  $\mathbf{P}(\text{O}_x)$  quantities is not significant. For the methane experiment, only data acquired before the NO injection was included in this figure. Besides, for experiments performed at higher NO concentrations (isoprene, i-pentane+n-hexane,  $\alpha$ -pinene and mesitylene), a similar NO-dependent difference is observed between  $\mathbf{P}(\text{O}_x)^{\text{HO}_2+\text{RO}_2}$  and  $\mathbf{P}(\text{O}_x)^{\text{O}_x}$ . Indeed,  $[\mathbf{P}(\text{O}_x)^{\text{HO}_2+\text{RO}_2} - \mathbf{P}(\text{O}_x)^{\text{O}_x}]$  seems to correlate linearly with NO with a similar slope for each experiment.



**Figure 4.11:** Dependence of  $\mathbf{P}(\text{O}_x)^{\text{HO}_2+\text{RO}_2} - \mathbf{P}(\text{O}_x)^{\text{O}_x}$  on NO for all experiments from Table 4.1. The insert represents a zoom of the results at  $[\text{NO}]$  below 1 ppb.

A linear regression applied to the data points shown in Figure 4.11 provide a slope of about  $9.7 \pm 0.2$  ppb  $\text{h}^{-1}$  per ppb of NO, with a moderate determination coefficient of approximately 0.79. A zoom on the region where [NO] is lower than 1 ppb (insert in Figure 4.11) reveals a similar linear correlation with a slope of  $11 \pm 1.0$  ppb  $\text{h}^{-1}$  per ppb of NO and a poor determination coefficient of 0.37. From this insert, a significant disagreement between  $\mathbf{P}(\text{O}_x)^{\text{HO}_2+\text{RO}_2}$  and  $\mathbf{P}(\text{O}_x)^{\text{O}_x}$  is observed for NO concentrations larger than 0.5 ppb.

Figure 4.12 displays how the  $\mathbf{P}(\text{O}_x)^{\text{HO}_2+\text{RO}_2}/\mathbf{P}(\text{O}_x)^{\text{O}_x}$  ratio varies with NO. This figure indicate that the ratio does not change significantly below 2 ppb of NO. For higher concentrations, a significant increase of this ratio is observed, up to a factor of 8-20 for  $[\text{NO}] \sim 9$  ppb.



**Figure 4.12:** Trend of the  $\mathbf{P}(\text{O}_x)^{\text{HO}_2+\text{RO}_2}/\mathbf{P}(\text{O}_x)^{\text{O}_x}$  ratio with NO for all experiments reported in Table 4.1.

#### 4.4. Contrasting chamber results to ambient observations

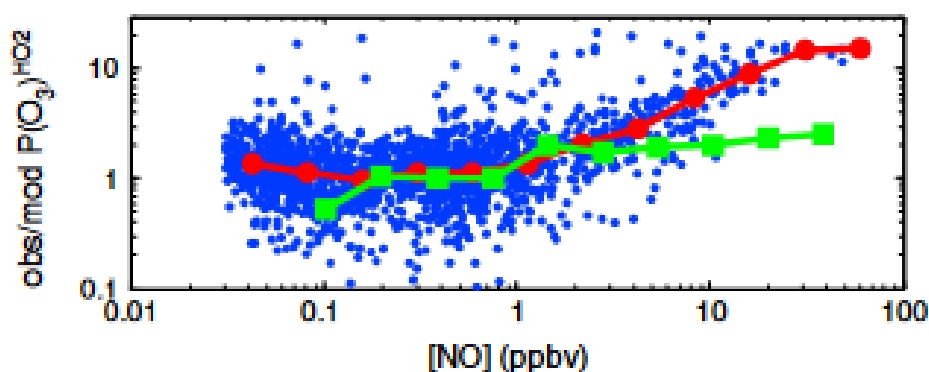
To assess the relevance of our experimental observations, a comparison was carried out with prior investigations reported in literature.

Several field campaigns report similar observations regarding the NO-dependence of ozone production rates inferred from ambient measurements of radicals. For instance, during the SHARP (Study of Houston Atmospheric Radical Precursor) field campaign conducted in 2009 in Houston, USA (presented earlier in Chapter 1), a significant difference was observed between directly measured  $\mathbf{P}(\text{O}_x)$  values, using the MOPS technique, which



would be similar to  $\mathbf{P}(\text{O}_x)^{\text{Ox}}$  in the sections above, and values calculated from  $\text{HO}_2$  and  $\text{NO}$  measurements, as well as modeled  $\text{RO}_2$ , similar to the  $\mathbf{P}(\text{O}_x)^{\text{HO}_2+\text{RO}_2}$  quantity defined in our study. During SHARP, the radical-calculated  $\mathbf{P}(\text{O}_x)$  values were found to be twice higher than the MOPS ones at high  $\text{NO}$  concentrations ( $> 10$  ppb) <sup>75</sup>. Conversely, at low  $\text{NO}$  concentrations, a good agreement between the two quantities was observed.

A follow-up paper concerning the SHARP campaign <sup>155</sup> reported a good agreement at low  $\text{NO}$  concentrations between the radical-calculated values, values measured by MOPS (green squares Figure 4.13), and values inferred from a box model. However, significant differences emerged at  $\text{NO}$  concentrations larger than 1 ppb. The discrepancy between the radical-calculated values and the modeled ones reaches approximately a factor of 10 at  $\text{NO}$  concentrations of 20-50 ppb, as shown in Figure 4.13 (red circles). While these observations cannot be directly compared to our results, the outcome seems consistent. Despite the difference between the comparison made in our work and the one reported in Figure 4.13, a common behavior is observed in the calculated ozone production rate using measured peroxy radicals indicating its fast increase at high  $\text{NO}$  concentrations compared to either (i) the one derived from a box model or (ii) the one calculated from the temporal variation of  $\text{O}_x$ .



**Figure 4.13:** Trends in ozone production rate ratios with  $\text{NO}$  for the 2009 SHARP campaign. Ratios of ozone production rates calculated from measured and modelled  $\text{HO}_2$  and  $\text{NO}$  concentrations ( $\text{obs } \mathbf{P}(\text{O}_3)^{\text{HO}_2} / \text{mod } \mathbf{P}(\text{O}_3)^{\text{HO}_2}$ ). Blue dots: 10 min average data, red circles: median values in  $\log(\text{NO})$  bins. Green squares: ratios of MOPS  $\mathbf{P}(\text{O}_3)$  values to modeled  $\mathbf{P}(\text{O}_3)$  (calculated from modeled  $\text{HO}_2+\text{RO}_2$ ) <sup>155</sup>.

This phenomenon was also documented in several other field studies. In a first group of studies, comparisons between  $\mathbf{P}(\text{O}_3)$  values measured by the MOPS technique and simulated by a box model are reported <sup>156, 157, 158</sup>. In a second group, comparisons between  $\mathbf{P}(\text{O}_3)$  values calculated from measured  $\text{HO}_2+\text{RO}_2$  <sup>94</sup> or only  $\text{HO}_2$  <sup>159</sup> using a LIF-FAGE

technique and modeled one using RACM 2 box model revealed a significant difference that increases with higher NO concentrations.

#### 4.5. Discussion on potential raisons leading to the $\mathbf{P(O_x)^{HO_2+RO_2} / P(O_x)^{O_x}}$ disagreement at high NO

Different reasons were proposed as potential explanations for this discrepancy. For field measurements, i.e.  $\mathbf{P(O_x)^{HO_2+RO_2}}$  from ambient measurements of peroxy radicals (or only HO<sub>2</sub>) and that predicted from model simulations, one possible reason would be the presence of atmospheric peroxy radicals produced from the oxidation of “unmeasured/unknown” VOCs that are co-emitted with NO<sup>158</sup>. These radicals being not considered by the models, it would lead to a model underestimation of HO<sub>2</sub> and RO<sub>2</sub> concentrations, which would translate into an underestimation of  $\mathbf{P(O_x)}$  values. However, this cannot explain the disagreement observed in our study since additional VOCs are not introduced into the SAPHIR chamber when NO is injected.

Another proposed reason would be the presence of instruments’ artifacts, either in the peroxy radical or NO measurements techniques<sup>158</sup>. This could lead to an overestimation of these species, hence an overestimation of  $\mathbf{P(O_x)^{HO_2+RO_2}}$ . Considering an instrument artifact, and based on the  $\mathbf{P(O_x)}$  equations rewritten below, different hypothesis can be formulated:

$$\mathbf{P(O_x)^{HO_2+RO_2}} = \mathbf{p(O_x)} - \mathbf{l(O_x)} \quad \text{Eq 4. 6}$$

$$\mathbf{p(O_x)} = k_{\text{NO+peroxy}}[\text{NO}][\text{HO}_2 + \text{RO}_2] \quad \text{Eq 4. 7}$$

$$\mathbf{l(O_x)} = j(\text{O}^1\text{D})[\text{O}_3]f + k_{\text{OH+NO}_2}[\text{OH}][\text{NO}_2] + k_{\text{HO}_2+\text{O}_3}[\text{HO}_2][\text{O}_3] + \quad \text{Eq 4. 8}$$

$$k_{\text{OH+O}_3}[\text{OH}][\text{O}_3] + \Sigma k_{\text{O}_3+\text{alkene},i}[\text{O}_3][\text{alkene}]_i + \text{O}_3 \text{ wall loss rate} +$$

$\text{O}_x$  dilution rate

$$\mathbf{P(O_x)^{O_x}} = \frac{\Delta \text{O}_x}{\Delta t} \quad \text{Eq 4. 9}$$

◆ Hypothesis 1: Miscalibration of IMT-CA or the NO monitor

We can invoke i) a miscalibration of either the CA or of the NO analyzer, which would result in an overestimation of  $\mathbf{P(O_x)^{HO_2+RO_2}}$ , and ii) a miscalibration of either the O<sub>3</sub> or

NO<sub>2</sub> analyzers, resulting in an underestimation of  $\mathbf{P}(\text{O}_x)^{0x}$ . These potential issues would bias the  $\mathbf{P}(\text{O}_x)^{\text{HO}_2+\text{RO}_2}$  or  $\mathbf{P}(\text{O}_x)^{0x}$  calculations from Eq 4. 6 and 4. 9 by a constant multiplying factor. In this case, the  $\mathbf{P}(\text{O}_x)^{\text{HO}_2+\text{RO}_2}/\mathbf{P}(\text{O}_x)^{0x}$  ratio should not change with NO. However, Figure 4.12 shows that the ratio is changing with NO, indicating that the disagreement between  $\mathbf{P}(\text{O}_x)^{\text{HO}_2+\text{RO}_2}$  or  $\mathbf{P}(\text{O}_x)^{0x}$  cannot be explained by a simple calibration issue.

It should be noted that an error associated to  $k_{\text{NO+peroxy}}$  would have the same impact than a miscalibration of one of the instruments, and this can also be ruled out.

◆ Hypothesis 2: An artifact in the HO<sub>2</sub>+RO<sub>2</sub> or NO measurements

We can propose the presence of an artifact that would (1) add a constant offset in the measurement of either HO<sub>2</sub>+RO<sub>2</sub> or NO, or (2) an artifact in either HO<sub>2</sub>+RO<sub>2</sub> or NO that scales with NO.

- An offset in the CA measurements (referred to as [A]) would be taken into consideration as follows:

$$p(\text{O}_x) = k_{\text{NO+peroxy}}[\text{NO}]([A] + [\text{HO}_2 + \text{RO}_2]_{\text{True}}) \quad \text{Eq 4. 10}$$

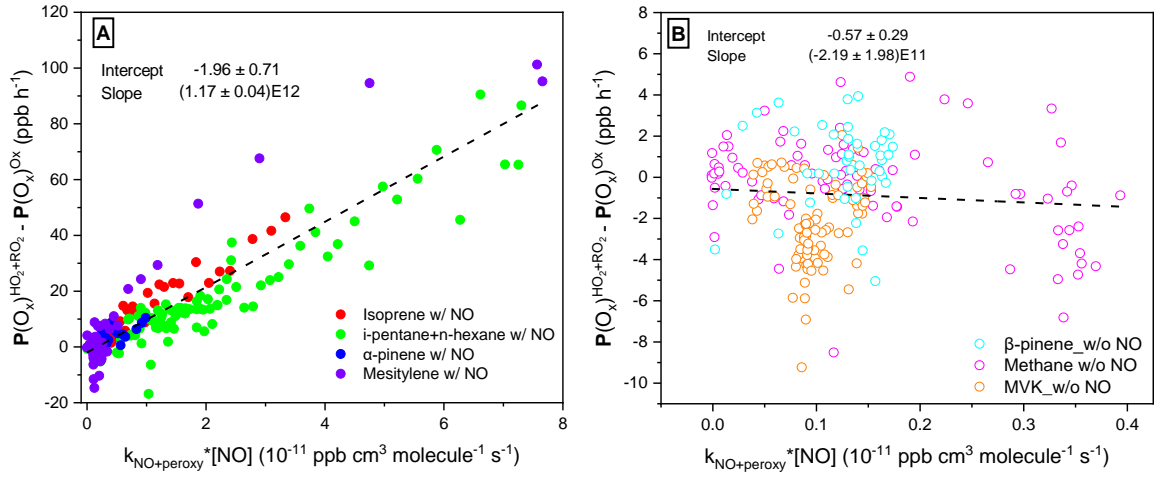
$$\mathbf{P}(\text{O}_x)^{\text{HO}_2+\text{RO}_2} = k_{\text{NO+peroxy}}[\text{NO}][A] + k_{\text{NO+peroxy}}[\text{NO}][\text{HO}_2 + \text{RO}_2]_{\text{True}} - \quad \text{Eq 4. 11}$$

$$l(\text{O}_x)$$

If the origin of the difference between  $\mathbf{P}(\text{O}_x)^{\text{HO}_2+\text{RO}_2}$  and  $\mathbf{P}(\text{O}_x)^{0x}$  is only due to this artifact,  $\mathbf{P}(\text{O}_x)^{0x} = k_{\text{NO+peroxy}}[\text{NO}][\text{HO}_2 + \text{RO}_2]_{\text{True}} - l(\text{O}_x)$ . Therefore, Eq 4. 11 can be rearranged as:

$$\mathbf{P}(\text{O}_x)^{\text{HO}_2+\text{RO}_2} - \mathbf{P}(\text{O}_x)^{0x} = k_{\text{NO+peroxy}}[\text{NO}][A] \quad \text{Eq 4. 12}$$

If this hypothesis is correct, the artifact [A] should be the slope of the linear correlation between  $\mathbf{P}(\text{O}_x)^{\text{HO}_2+\text{RO}_2} - \mathbf{P}(\text{O}_x)^{0x}$  and the product of  $k_{\text{NO+peroxy}}$  and [NO]. In addition, the linear regression should exhibit a zero intercept. Figure 4.14 shows that this trend is indeed observed when plotting data from the high NO experiments, while no trend is observed for the low NO experiments. According to Figure 4.14 (A), a constant artifact of  $3.3 \times 10^8$  molecules cm<sup>-3</sup> in the IMT-CA measurements could explain the discrepancy observed between  $\mathbf{P}(\text{O}_x)^{\text{HO}_2+\text{RO}_2}$  and  $\mathbf{P}(\text{O}_x)^{0x}$  when NO is injected in the chamber.



**Figure 4.14:** Scatter plot of  $P(O_x)^{HO_2+RO_2} - P(O_x)^{O_x}$  vs.  $k_{NO+peroxy}[NO]$  for A) high NO experiments and B) low NO experiments.

Removing a bias of  $3.3 \times 10^8$  molecules  $cm^{-3}$  from  $HO_2+RO_2$  concentrations measured during the low NO experiments would lead to negative values and indicate that if an artifact is present, it would only be present when NO is high. Given that these experiments were conducted in the same period, the presence of an artifact in the CA measurements for only the high NO experiments is difficult to explain. It would require the formation of an interfering species, produced only when NO is injected in the chamber, and whose concentration does not scale on NO. Such possibility seems very unlikely.

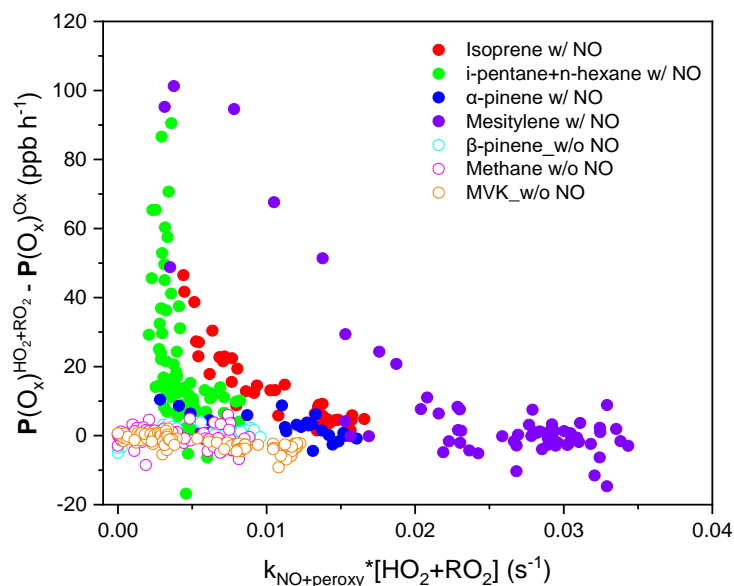
➤ An offset in the NO measurements (referred to as [B]):

Following the same reasoning as above, a constant offset in the NO measurements would lead to the following equations:

$$p(O_x) = k_{NO+peroxy}[HO_2 + RO_2]([B] + [NO]_{True}) \quad \text{Eq 4. 13}$$

$$P(O_x)^{HO_2+RO_2} - P(O_x)^{O_x} = k_{NO+peroxy}[HO_2 + RO_2][B] \quad \text{Eq 4. 14}$$

If the proposed hypothesis is correct, the artifact [B] would correspond to the slope of a linear regression between  $P(O_x)^{HO_2+RO_2} - P(O_x)^{O_x}$  and the product of  $k_{NO+peroxy}$  and  $[HO_2 + RO_2]$ . However, Figure 4.15 reveals a non-linear relationship between these two quantities, mainly in the case of high NO experiments, where the difference  $P(O_x)^{HO_2+RO_2} - P(O_x)^{O_x}$  is only significant at high [NO] and low  $[HO_2+RO_2]$ . This implies that the difference observed between  $P(O_x)^{HO_2+RO_2}$  and  $P(O_x)^{O_x}$  is not due to an offset in the NO measurements.



**Figure 4.15:** Scatter plot of  $\mathbf{P(O_x)^{HO_2+RO_2} - P(O_x)^{O_x}}$  vs.  $\mathbf{k_{NO+peroxy} \times [HO_2+RO_2]}$  for all experiments.

◆ Hypothesis 3: Underestimation of  $\mathbf{l(O_x)}$

An underestimation of the total  $\mathbf{O_x}$  loss rate due to (i) miscalculated or (ii) unaccounted for loss processes in equation (Eq 4. 8) can be suggested.

A miscalculation of one of the terms included in  $\mathbf{l(O_x)}$  could lead to a disagreement between  $\mathbf{P(O_x)^{HO_2+RO_2}}$  and  $\mathbf{P(O_x)^{O_x}}$ . In order to explain the level of discrepancy observed in this study, the miscalculated term has to be one of the largest contributors, i.e. dilution or wall losses, since the miscalculation of minor terms would only have a small impact on  $\mathbf{l(O_x)}$ . Dilution is well constrained from the continuous addition of zero air all along the experiments. The wall loss of  $\mathbf{O_3}$  is considered as constant throughout the experiments. While it may vary with solar irradiance due to potential photo-enhanced processes occurring at the wall surface, it would likely not explain the  $\mathbf{NO}$ -dependence of the disagreement. It is therefore unlikely that a miscalculation of one of the terms included in  $\mathbf{l(O_x)}$  is the cause of the disagreement between  $\mathbf{P(O_x)^{HO_2+RO_2}}$  and  $\mathbf{P(O_x)^{O_x}}$ .

A missing loss process could either be linked to  $\mathbf{O_3}$  or  $\mathbf{NO_2}$ . For instance, reactions of  $\mathbf{RO_2}$  with  $\mathbf{O_3}$  are not considered in the present work. To the best of our knowledge, this type of reactions was not investigated yet and reaction rate coefficients are not known. Assuming that  $\mathbf{RO_2+O_3}$  reaction rate coefficients are similar to that observed for  $\mathbf{HO_2+O_3}$ , including an additional loss of  $\mathbf{O_3}$  from  $\mathbf{RO_2+O_3}$  in  $\mathbf{l(O_x)}$  would increase the total loss rate by less than  $\mathbf{1\ ppb\ h^{-1}}$ , which is 1-2 orders of magnitude too low to explain the discrepancy. In addition,

such a missing loss process would not explain the trend observed between the disagreement and NO. It is therefore very unlikely that the disagreement seen in this work is due the omission of RO<sub>2</sub>+O<sub>3</sub> reactions in the calculation of I(O<sub>x</sub>).

It is important to note that NO<sub>2</sub> wall losses were not included in I(O<sub>x</sub>) since the reported wall-loss rate is small ( $1.1 \cdot 10^{-6} \text{ s}^{-1}$ <sup>160</sup>) compared to the O<sub>3</sub> wall loss rate ( $3.9 \times 10^{-6} \text{ s}^{-1}$ ) and NO<sub>2</sub> concentrations are significantly lower than O<sub>3</sub>. The impact of a significant wall loss of NO<sub>2</sub> would be expected to increase with NO since NO and NO<sub>2</sub> correlate with each other through the O<sub>3</sub>-NO<sub>x</sub> photo-stationary state (Chapter 1, section 1.2.1). In order to check whether a significant loss of NO<sub>2</sub> could be at the origin of the disagreement between the two P(O<sub>x</sub>) quantification methodologies, sensitivity tests were performed by adding this additional loss process in the calculation of I(O<sub>x</sub>). The loss rate was adjusted to try to get a good match between  $\mathbf{P}(\text{O}_x)^{\text{HO}_2+\text{RO}_2}$  and  $\mathbf{P}(\text{O}_x)^{\text{O}_x}$ . These tests were started by considering the same wall loss rate as for O<sub>3</sub>, which had no significant impact on I(O<sub>x</sub>). A significant change in I(O<sub>x</sub>) is observed when the NO<sub>2</sub> wall loss rate is increased by two orders of magnitude. However, a reasonable agreement between  $\mathbf{P}(\text{O}_x)^{\text{HO}_2+\text{RO}_2}$  and  $\mathbf{P}(\text{O}_x)^{\text{O}_x}$  was only found for some time periods of the isoprene, i-pentane+n-hexane, α-pinene and mesitylene experiments, while for other time periods a significant disagreement remains (up to 120 ppb h<sup>-1</sup> for the mesitylene experiment). The high wall loss rate that needs to be implemented in the calculations and the variable agreement observed during individual experiments suggest that the present hypothesis cannot explain the observed difference between  $\mathbf{P}(\text{O}_x)^{\text{HO}_2+\text{RO}_2}$  and  $\mathbf{P}(\text{O}_x)^{\text{O}_x}$ . More investigations should however explore whether a J-dependent NO<sub>2</sub> loss rate could better explain the observed disagreement.

Another possible O<sub>x</sub> loss process that can be suggested is the photolysis of NO<sub>3</sub>. In fact, the reaction between O<sub>3</sub> and NO<sub>2</sub> results in the formation of NO<sub>3</sub> (R 4. 1), whose rapid photolysis leads to the reformation of the reactants (R 4. 2 and R 4. 3). According to IUPAC, there is a competing photolytic pathway that leads to the formation of NO and O<sub>2</sub> (R 4. 4)<sup>161</sup>, which constitutes a loss process for O<sub>x</sub>. IUPAC reports that approximately 10% of NO<sub>3</sub> photolyze into NO+O<sub>2</sub> between 400 and 700 nm (R 4. 4).





The photolysis frequency of  $\text{NO}_3$  being rapid during daytime, this loss process can be quantified using the following equation:

$$l(\text{O}_x \text{ from } \text{NO}_3 + h\nu) = 2 \times k_{\text{O}_3+\text{NO}_2} [\text{O}_3][\text{NO}_2] \times 10\% \quad \text{Eq 4. 15}$$

where  $k_{\text{O}_3+\text{NO}_2} = 3.52 \times 10^{-17} \text{ cm}^3 \text{ molecule}^{-1} \text{ s}^{-1}$  is the rate coefficient for R 4. 1 at 298 K.

Calculations performed for the selected experiments reveal that this loss process is not significant, with  $l(\text{O}_x \text{ from } \text{NO}_3 + h\nu) < 1 \text{ ppb h}^{-1}$ , hence ruling out this possibility. While we cannot rule out an “unknown” loss process involving  $\text{O}_3$  and/or  $\text{NO}_2$  that would scale with  $\text{NO}$ , we did not succeed in identifying other potential candidates.

Although the origin of the disagreement observed between  $\mathbf{P}(\text{O}_x)^{\text{HO}_2+\text{RO}_2}$  and  $\mathbf{P}(\text{O}_x)^{\text{O}_x}$  remains unclear, the probability of an artifact in  $\text{HO}_2+\text{RO}_2$  measurements at high  $\text{NO}$  is a reasonable explanation, which would be consistent with the  $\text{NO}$  trend observed in chapter 3 when comparing IMT-CA and FZJ-FAGE measurements. This aspect should be investigated in priority. However, when  $\mathbf{P}(\text{O}_x)^{\text{HO}_2+\text{RO}_2}$  is calculated from speciated measurements of  $\text{HO}_2$  and  $\text{RO}_2$  (FZJ-FAGE), a  $\text{NO}$ -dependent disagreement is also observed between  $\mathbf{P}(\text{O}_x)^{\text{HO}_2+\text{RO}_2}$  and  $\mathbf{P}(\text{O}_x)^{\text{O}_x}$ , with differences being approximately twice lower. This implies that if an artifact on IMT-CA measurements is discovered, this may not be sufficient to explain the full disagreement observed in this study and other potential reasons may need to be discovered.

## 5. Conclusions

To conclude, besides evaluating the performance of IMT-CA for measuring peroxy radicals in chapter 3, the ROxComp intercomparison campaign was also a valuable exercise to assess whether this instrument could be used to quantify ozone production rates in the atmosphere.

Taking advantage of the selectivity of IMT-CA in the detection of peroxy radicals, i.e. the CA detecting only radicals leading to the formation of ozone, the fraction of  $\text{RO}_2$  leading to organic nitrate/nitrite formation being undetected, the gross production rate of  $\text{O}_x$  species

can be directly inferred from the measured sum of HO<sub>2</sub>+RO<sub>2</sub> if the  $\frac{[\text{HO}_2]}{[\text{HO}_2]+[\text{RO}_2]}$  ratio is assumed to be 0.5 and an average rate coefficient is used for the reaction between peroxy radicals and NO ( $k_{\text{peroxy}+\text{NO}}$ ). The analysis presented in this chapter indicates that the gross ozone production rate inferred from this simplification is within 1 % of values that would be derived from the real peroxy radical partitioning. Indeed, it was found that the  $\frac{[\text{HO}_2]}{[\text{HO}_2]+[\text{RO}_2]}$  ratio, derived from speciated measurements of HO<sub>2</sub> and RO<sub>2</sub> from FZJ-FAGE, falls within the range of 0.4 to 0.6. This implies that using the sum of HO<sub>2</sub>+RO<sub>2</sub> from the CA to calculate the gross  $p(\text{O}_x)$  would be an effective strategy, yielding to an error lower than 1%.

Significant O<sub>x</sub> loss processes were observed within the chamber, where dilution and O<sub>3</sub> wall losses were, on average, the predominant processes. Non-negligible chemical losses were also noted, including OH+NO<sub>2</sub>, O<sub>3</sub>+alkene, O<sub>3</sub>+HO<sub>2</sub>, O<sub>3</sub>+hv and O<sub>3</sub>+OH. Dilution and wall losses accounted for respectively 46 and 18% of the total O<sub>x</sub> loss rates on average, taking into account all experiments discussed in this chapter, and chemical processes for the remaining fraction. On a practical way, the investigation of the ozone budget through the determination of  $\mathbf{P}(\text{O}_x)^{\text{HO}_2+\text{RO}_2}$  as presented in Chapter 1 (section 2.2.3), would only require to account for chemical losses in  $l(\text{O}_x)$  as shown in the following equation. Surface deposition (SD) and advection (A), which by analogy would represent wall losses and dilution during the chamber experiments, are included as independent terms in this equation. The O<sub>x</sub> loss rate due to chemical processes is denoted as  $l'(\text{O}_x)$  in this equation.

$$\mathbf{P}(\text{O}_x)^{\text{HO}_2+\text{RO}_2} = p(\text{O}_x) - l'(\text{O}_x) - \text{SD} + \text{A} \quad \text{Eq 4. 16}$$

The analysis of the selected RO<sub>x</sub>Comp experiments showed that  $l'(\text{O}_x)$  is driven by O<sub>3</sub>+HO<sub>2</sub>, NO<sub>2</sub>+OH, and sometime alkene+O<sub>3</sub>. It was found that  $l'(\text{O}_x)$  is significant compared to  $p(\text{O}_x)$ , which resulted in net  $\mathbf{P}(\text{O}_x)^{\text{HO}_2+\text{RO}_2}$  values being lower than gross  $p(\text{O}_x)$  values by 5-44%. In order to quantify atmospheric  $\mathbf{P}(\text{O}_x)^{\text{HO}_2+\text{RO}_2}$ , it is therefore necessary to have access to OH, HO<sub>2</sub> and HO<sub>2</sub>+RO<sub>2</sub> measurements. Using only HO<sub>2</sub>+RO<sub>2</sub> measurements would provide an upper limit of  $\mathbf{P}(\text{O}_x)^{\text{HO}_2+\text{RO}_2}$ .

For low NO conditions,  $\mathbf{P}(\text{O}_x)^{\text{HO}_2+\text{RO}_2}$  was found to be in good agreement with  $\mathbf{P}(\text{O}_x)^{\text{O}_x}$ . Conversely, for high NO conditions,  $\mathbf{P}(\text{O}_x)^{\text{HO}_2+\text{RO}_2}$  was significantly larger than  $\mathbf{P}(\text{O}_x)^{\text{O}_x}$  when NO was higher than 0.5 ppb. The disagreement increases almost linearly with NO to reach a factor of 8-20 around 9 ppb of NO. Interestingly, a similar disagreement



was reported in the literature when gross  $p(O_x)$  values were calculated from ambient measurements of peroxy radicals and compared to values directly measured using the MOPS technique or calculated from radical concentrations simulated by box models. While this similarity is intriguing, we cannot establish whether the source of the disagreement is the same.

Among the potential reasons invoked to explain the disagreement observed between  $P(O_x)^{HO_2+RO_2}$  and  $P(O_x)^{O_x}$  during ROxComp, the presence of an artifact in  $HO_2+RO_2$  measurements from IMT-CA at high NO may be possible. However, a NO-dependent disagreement is also observed when using speciated measurements of  $HO_2$  and  $RO_2$  from FZJ-FAGE, with differences that are approximately twice lower, indicating that a potential artifact in the IMT-CA measurements may not be sufficient to explain the full disagreement.

Other reasons were also proposed, namely (i) a miscalibration of one of the instruments, (ii) an offset in the NO measurements, and (iii) a miscalculated or (iv) missing loss process in  $l(O_x)$ , the latter including  $NO_2$  wall losses,  $RO_2+O_3$  reactions and  $NO_3$  photolysis. It was shown that these processes cannot explain the disagreement between the two  $P(O_x)$  quantities. Further investigative studies are needed to confirm or identify the origin of the discrepancy.

## References

1. Miliordos E, Xantheas SS. On the Bonding Nature of Ozone (O<sub>3</sub>) and Its Sulfur-Substituted Analogues SO<sub>2</sub>, OS<sub>2</sub>, and S<sub>3</sub>: Correlation between Their Biradical Character and Molecular Properties. *J Am Chem Soc.* 2014;136(7):2808-2817.
2. Coca M, González-Benito G, García-Cubero MT. Chemical Oxidation With Ozone as an Efficient Pretreatment of Lignocellulosic Materials. In: *Biomass Fractionation Technologies for a Lignocellulosic Feedstock Based Biorefinery*. Elsevier; 2016:409-429.
3. US EPA O. NAAQS Table. Published April 10, 2014. Accessed September 16, 2022. <https://www.epa.gov/criteria-air-pollutants/naaqs-table>
4. Ashmore MR. Assessing the future global impacts of ozone on vegetation. *Plant Cell Environ.* 2005;28(8):949-964.
5. Li C, Balluz LS, Vaidyanathan A, Wen XJ, Hao Y, Qualters JR. Long-Term Exposure to Ozone and Life Expectancy in the United States, 2002 to 2008. *Medicine (Baltimore)*. 2016;95(7):8.
6. Organization (WMO) WM, Administration (NASA) National Aeronautics and Space, Administration (NOAA) National Oceanic and Atmospheric, Programme (UNEP) United Nations Environment, Commission E, World Meteorological Organization (WMO). *GORMP, 44. WMO/UNEP Scientific Assessment of Ozone Depletion: 1998*. WMO; 1999.
7. Anenberg SC, Horowitz LW, Tong DQ, West JJ. An Estimate of the Global Burden of Anthropogenic Ozone and Fine Particulate Matter on Premature Human Mortality Using Atmospheric Modeling. *Environ Health Perspect.* 2010;118(9):1189-1195.
8. Anenberg SC, Henze DK, Tinney V, et al. Estimates of the Global Burden of Ambient PM<sub>2.5</sub>, Ozone, and NO<sub>2</sub> on Asthma Incidence and Emergency Room Visits. *Environ Health Perspect.* 2018;126(10):107004.
9. Zhang J (Jim), Wei Y, Fang Z. Ozone Pollution: A Major Health Hazard Worldwide. *Front Immunol.* 2019;10:2518.
10. IPCC AR6-WGI Atlas. Accessed September 13, 2023. <https://interactive-atlas.ipcc.ch/atlas>
11. Lefohn AS, Malley CS, Smith L, et al. Tropospheric ozone assessment report: Global ozone metrics for climate change, human health, and crop/ecosystem research. *Elem Sci Anthr.* 2018;6:27.
12. U.S. EPA. Integrated Science Assessment (ISA) for Ozone and Related Photochemical Oxidants (Final Report, Apr 2020). U.S. Environmental Protection Agency, Washington, DC, EPA/600/R-20/012, 2020.
13. Integrated Science Assessment for Ozone and Related Photochemical Oxidants ISA 2013. Published online 2013. [www.epa.gov/ord](http://www.epa.gov/ord)

14. AR6 Synthesis Report: Climate Change 2023. Published 2023. Accessed April 10, 2023. <https://www.ipcc.ch/report/ar6/syr/>
15. Intergovernmental Panel On Climate Change. *Climate Change 2021 – The Physical Science Basis: Working Group I Contribution to the Sixth Assessment Report of the Intergovernmental Panel on Climate Change*. 1st ed. Cambridge University Press; 2023.
16. Mills G, Harmens H, Wagg S, et al. Ozone impacts on vegetation in a nitrogen enriched and changing climate. *Environ Pollut*. 2016;208:898-908.
17. IPCC. Climate Change 2013: The Physical Science Basis. GlobalChange.gov. Accessed December 22, 2020. <https://www.globalchange.gov/browse/reports/ipcc-climate-change-2013-physical-science-basis>.
18. Sinha B, Singh Sangwan K, Maurya Y, et al. Assessment of crop yield losses in Punjab and Haryana using 2 years of continuous in situ ozone measurements. *Atmospheric Chem Phys*. 2015;15(16):9555-9576.
19. Adams RM, Crocker TD, Thanavibulchai N. An economic assessment of air pollution damages to selected annual crops in Southern California. *J Environ Econ Manag*. 1982;9(1):42-58.
20. Monks PS, Archibald AT, Colette A, et al. Tropospheric ozone and its precursors from the urban to the global scale from air quality to short-lived climate forcer. *Atmospheric Chem Phys*. 2015;15(15):8889-8973.
21. Ozone injury | ICP Vegetation. Accessed October 10, 2023. <https://icpvegetation.ceh.ac.uk/get-involved/ozone-injury>.
22. Finlayson-Pitts BJ, Pitts JN. Overview of the Chemistry of Polluted and Remote Atmospheres. In: *Chemistry of the Upper and Lower Atmosphere*. Elsevier; 2000:1-14.
23. Seinfeld JH, Pandis SN. *Atmospheric Chemistry and Physics: From Air Pollution to Climate Change*. 2nd ed. J. Wiley; 2006.
24. Crutzen PJ, Lawrence MG, Poschl U. On the background photochemistry of tropospheric ozone. *Tellus B*. 1999;51(1):123-146.
25. Monks PS. Gas-phase radical chemistry in the troposphere. *Chem Soc Rev*. 2005;34(5):376.
26. Camredon M, Aumont B. Modélisation chimique de l’ozone et des oxydants gazeux Chemical modelling of ozone and gaseous oxidants. *Pollut Atmos*. 2007;(193):10.
27. Stone D, Whalley LK, Heard DE. Tropospheric OH and HO<sub>2</sub> radicals: field measurements and model comparisons. *Chem Soc Rev*. 2012;41(19):6348.
28. Lightfoot PD, Cox RA, Crowley JN, et al. Organic peroxy radicals: Kinetics, spectroscopy and tropospheric chemistry. *Atmospheric Environ Part Gen Top*. 1992;26(10):1805-1961.

29. Ivatt PD, Evans MJ, Lewis AC. Suppression of surface ozone by an aerosol-inhibited photochemical ozone regime. *Nat Geosci.* 2022;15(7):536-540.
30. Dyson JE, Whalley LK, Slater EJ, et al. Impact of HO<sub>2</sub> aerosol uptake on radical levels and O<sub>3</sub> production during summertime in Beijing. *Atmospheric Chem Phys.* 2023;23(10):5679-5697.
31. Dieter HE. Radical ideas. *Atmos Chem.* 1998;279:2.
32. Zaripov RB, Konovalov IB, Kuznetsova IN, Belikov IB, Zvyagintsev AM. WRF ARW and CHIMERE models for numerical forecasting of surface ozone concentration. *Russ Meteorol Hydrol.* 2011;36(4):249-257.
33. Tsimpidi A, Karydis V, Zavala M, Lei W, Molina L, Pandis S. Evaluation of a Three-Dimensional Chemical Transport Model (PMCAMx) in the Mexico City Metropolitan Area. *AGU Spring Meet Abstr.* 2007;1:05.
34. Byun D, Schere KL. Review of the Governing Equations, Computational Algorithms, and Other Components of the Models-3 Community Multiscale Air Quality (CMAQ) Modeling System. *Appl Mech Rev.* 2006;59(2):51-77.
35. Sillman S. Tropospheric Ozone: The Debate over Control Strategies. *Annu Rev Energy Environ.* 1993;18:26.
36. LaCount MD, Haeuber RA, Macy TR, Murray BA. Reducing power sector emissions under the 1990 Clean Air Act Amendments: A retrospective on 30 years of program development and implementation. *Atmos Environ.* 2021;245:118012.
37. Aksoyoglu S, Keller J, Oderbolz DC, Barmpadimos I, Prévôt ASH, Baltensperger U. Sensitivity of ozone and aerosols to precursor emissions in Europe. *Int J Environ Pollut.* 2012;50(1/2/3/4):451.
38. Baier BC. Direct ozone production rate measurements and their use in assessing ozone source and receptor regions for Houston in 2013. *Atmos Environ.* Published online 2015:9.
39. Rubin MB. THE HISTORY OF OZONE. THE SCHÖNBEIN PERIOD, 1839-1868. *Bull Hist Chem.* 2001;26(1):17.
40. Heard DE, ed. *Analytical Techniques for Atmospheric Measurement.* Blackwell; 2006.
41. Cantrell CA, Stedman DH, Wendel GJ. Measurement of atmospheric peroxy radicals by chemical amplification. *Anal Chem.* 1984;56(8):1496-1502.
42. Ashbourn SFM, Jenkin ME, Clemitshaw KC. Laboratory Studies of the Response of a Peroxy Radical Chemical Amplifier to HO<sub>2</sub> and a Series of Organic Peroxy Radicals. *J Atmos Chem.* 1998;29:34.
43. Wang Z, Yang B, Zhang T. A method for the selective measurement of HO<sub>2</sub> and RO<sub>2</sub> radical concentrations using a Nafion-PERCA system. *J Atmospheric Chem.* 2016;73(4):397-406.

44. Sadanaga Y, Matsumoto J, Sakurai K ichi, et al. Development of a measurement system of peroxy radicals using a chemical amplification/laser-induced fluorescence technique. *Rev Sci Instrum.* 2004;75(4):864-872.
45. George M, Andrés Hernández MD, Nenakhov V, Liu Y, Burrows JP. Airborne measurement of peroxy radicals using chemical amplification coupled with cavity ring-down spectroscopy: the PeRCEAS instrument. *Atmospheric Meas Tech.* 2020;13(5):2577-2600.
46. Chen W, Wang G, Lahib A, et al. *Peroxy Radical Measurements by Photoacoustic Spectroscopy Coupled to Chemical Amplification.* pico; 2021.
47. Chen Y, Yang C, Zhao W, et al. Ultra-sensitive measurement of peroxy radicals by chemical amplification broadband cavity-enhanced spectroscopy. *The Analyst.* 2016;141(20):5870-5878.
48. Duncianu M, Lahib A, Tomas A, Stevens PS, Dusanter S. Characterization of a chemical amplifier for peroxy radical measurements in the atmosphere. *Atmos Environ.* 2020;222:117106.
49. Reichert L. Investigation of the effect of water complexes in the determination of peroxy radical ambient concentrations: Implications for the atmosphere. *J Geophys Res.* 2003;108(D1):4017.
50. Wood EC, Deming BL, Kundu S. Ethane-Based Chemical Amplification Measurement Technique for Atmospheric Peroxy Radicals. *Environ Sci Technol Lett.* 2017;4(1):15-19.
51. Edwards GD, Cantrell CA, Stephens S, et al. Chemical Ionization Mass Spectrometer Instrument for the Measurement of Tropospheric HO<sub>2</sub> and RO<sub>2</sub>. *Anal Chem.* 2003;75(20):5317-5327.
52. Fuchs H, Holland F, Hofzumahaus A. Measurement of tropospheric RO<sub>2</sub> and HO<sub>2</sub> radicals by a laser-induced fluorescence instrument. *Rev Sci Instrum.* 2008;79(8):084104.
53. Hornbrook RS, Crawford JH, Edwards GD, et al. Measurements of tropospheric HO<sub>2</sub>; and RO<sub>2</sub> by oxygen dilution modulation and chemical ionization mass spectrometry. *Atmospheric Meas Tech.* 2011;4(4):735-756.
54. Whalley LK, Edwards PM, Furneaux KL, et al. Quantifying the magnitude of a missing hydroxyl radical source in a tropical rainforest. *Atmospheric Chem Phys.* 2011;11(14):7223-7233.
55. Yin X, Dong L, Wu H, et al. Sub-ppb nitrogen dioxide detection with a large linear dynamic range by use of a differential photoacoustic cell and a 3.5 W blue multimode diode laser. *Sens Actuators B Chem.* 2017;247:329-335.
56. Volpe Horii C, Zahniser MS, Nelson, Jr. DD, McManus JB, Wofsy SC. Nitric acid and nitrogen dioxide flux measurements: a new application of tunable diode laser absorption spectroscopy. In: Fried A, ed.; 1999:152-161.

57. Matsumoto J, Kajii Y. Improved analyzer for nitrogen dioxide by laser-induced fluorescence technique. *Atmos Environ.* 2003;37(34):4847-4851.
58. Kebarian PL, Herndon SC, Freedman A. Detection of Nitrogen Dioxide by Cavity Attenuated Phase Shift Spectroscopy. *Anal Chem.* 2005;77(2):724-728.
59. Yamamoto Y, Sumizawa H, Yamada H, Tonokura K. Real-time measurement of nitrogen dioxide in vehicle exhaust gas by mid-infrared cavity ring-down spectroscopy. *Appl Phys B.* 2011;105(4):923-931.
60. Kasyutich VL, Bale CSE, Canosa-Mas CE, Pfrang C, Vaughan S, Wayne RP. Cavity-enhanced absorption: detection of nitrogen dioxide and iodine monoxide using a violet laser diode. *Appl Phys B.* 2003;76(6):691-697.
61. Harren FJM, Cotti G, Oomens J. Photoacoustic Spectroscopy in Trace Gas Monitoring. :25.
62. Sigsby JE, Black FM, Bellar TA, Klosterman DL. Chemiluminescent method for analysis of nitrogen compounds in mobile source emissions nitric oxide, nitrogen dioxide, and ammonia. *Environ Sci Technol.* 1973;7(1):51-54.
63. Kebarian PL, Wood EC, Herndon SC, Freedman A. A Practical Alternative to Chemiluminescence-Based Detection of Nitrogen Dioxide: Cavity Attenuated Phase Shift Spectroscopy. *Environ Sci Technol.* 2008;42(16):6040-6045.
64. Li Z, Hu R, Xie P, et al. Simultaneous measurement of NO and NO<sub>2</sub> by a dual-channel cavity ring-down spectroscopy technique. *Atmospheric Meas Tech.* 2019;12(6):3223-3236.
65. Thornton JA, Wooldridge PJ, Cohen RC. Atmospheric NO<sub>2</sub>: In Situ Laser-Induced Fluorescence Detection at Parts per Trillion Mixing Ratios. *Anal Chem.* 2000;72(3):528-539. doi:10.1021/ac9908905.
66. Bozóki Z, Pogány A, Szabó G. Photoacoustic Instruments for Practical Applications: Present, Potentials, and Future Challenges. *Appl Spectrosc Rev.* 2011;46(1):1-37.
67. Zheng H, Dong L, Yin X, et al. Ppb-level QEPAS NO<sub>2</sub> sensor by use of electrical modulation cancellation method with a high power blue LED. *Sens Actuators B Chem.* 2015;208:173-179.
68. Nussbaumer CM, Parchatka U, Tadic I, et al. Modification of a conventional photolytic converter for improving aircraft measurements of NO<sub>2</sub> via chemiluminescence. *Atmospheric Meas Tech.* 2021;14(10):6759-6776.
69. Wood EC, Charest JR. Chemical Amplification - Cavity Attenuated Phase Shift Spectroscopy Measurements of Atmospheric Peroxy Radicals. *Anal Chem.* 2014;86(20):10266-10273.
70. Langridge JM, Ball SM, Jones RL. A compact broadband cavity enhanced absorption spectrometer for detection of atmospheric NO<sub>2</sub> using light emitting diodes. *The Analyst.* 2006;131(8):916.

71. Cazorla M, Brune WH. Measurement of Ozone Production Sensor. *Atmospheric Meas Tech.* 2010;3(3):545-555.
72. Sklaveniti S, Locoge N, Stevens PS, Wood E, Kundu S, Dusanter S. Development of an instrument for direct ozone production rate measurements: measurement reliability and current limitations. *Atmospheric Meas Tech.* 2018;11(2):741-761.
73. Sadanaga Y, Kawasaki S, Tanaka Y, Kajii Y, Bandow H. New System for Measuring the Photochemical Ozone Production Rate in the Atmosphere. *Environ Sci Technol.* 2017;51(5):2871-2878.
74. Jeffries HE. An Experimental Method for Measuring the Rate of Synthesis, Destruction, and Transport of Ozone in the Lower Atmosphere. 1973:1.
75. Cazorla M, Brune WH, Ren X, Lefer B. Direct measurement of ozone production rates in Houston in 2009 and comparison with two estimation methods. *Atmos Chem Phys.* 2012:10.
76. Atkinson R, Baulch DL, Cox RA, et al. Evaluated kinetic and photochemical data for atmospheric chemistry: Volume I - gas phase reactions of Ox, HOx, NOx; and SOx; species. *Atmospheric Chem Phys.* 2004;4(6):1461-1738.
77. Nelson BS, Stewart GJ, Drysdale WS, et al. In situ Ozone Production is highly sensitive to Volatile Organic Compounds in the Indian Megacity of Delhi. 2021:36.
78. Kanaya Y, Akimoto H. Direct Measurements of HOx Radicals in the Marine Boundary Layer: Testing the Current Tropospheric Chemistry Mechanism. *Chem Rec.* 2002;2(3):199-211.
79. Stockwell WR, Kirchner F, Kuhn M, Seefeld S. A new mechanism for regional atmospheric chemistry modeling. *J Geophys Res Atmospheres.* 1997;102(D22):25847-25879.
80. Karamchandani P, Zhang Y, Chen S, Balmori–Bronson R. Development of an extended chemical mechanism for global–through–urban applications. *Atmospheric Pollut Res.* 2012;3(1):1-24.
81. Yarwood G, Jung J, Whitten GZ, Heo G, Mellberg J, Estes M. Updates to the carbon bond mechanism for version 6 (CB6). 2010:4.
82. Carter WPL. Development of a condensed SAPRC-07 chemical mechanism. *Atmos Environ.* 2010;44(40):5336-5345.
83. Schmid PJ, Henningson DS. A new mechanism for rapid transition involving a pair of oblique waves. *Phys Fluids Fluid Dyn.* 1992;4(9):1986-1989.
84. Saunders SM, Jenkin ME, Derwent RG, Pilling MJ. *Protocol for the Development of the Master Chemical Mechanism, MCM v3 (Part A): Tropospheric Degradation of Non-Aromatic Volatile Organic Compounds.*; 2002.
85. Ling ZH, Guo H, Lam SHM, Saunders SM, Wang T. Atmospheric photochemical reactivity and ozone production at two sites in Hong Kong: Application of a Master

- Chemical Mechanism-photochemical box model: Atmospheric photochemical reactivity. *J Geophys Res Atmospheres*. 2014;119(17):10567-10582.
86. Elshorbany YF, Kleffmann J, Kurtenbach R, et al. Summertime photochemical ozone formation in Santiago, Chile. *Atmos Environ*. 2009;10.
  87. Ren X. OH and HO<sub>2</sub> Chemistry in the urban atmosphere of New York City. *Atmos Environ*. 2003;37(26):3639-3651.
  88. Sheehy PM, Volkamer R, Molina LT, Molina MJ. Oxidative capacity of the Mexico City atmosphere? Part 2: A RO<sub>x</sub> radical cycling perspective. 2008:55.
  89. Sommariva R, Brown SS, Roberts JM, et al. Ozone production in remote oceanic and industrial areas derived from ship based measurements of peroxy radicals during TexAQS 2006. *Atmospheric Chem Phys*. 2011;11(6):2471-2485.
  90. Ryerson TB. Effect of petrochemical industrial emissions of reactive alkenes and NO<sub>x</sub> on tropospheric ozone formation in Houston, Texas. *J Geophys Res*. 2003;108(D8):4249.
  91. Dusanter S, Vimal D, Stevens PS, Volkamer R, Molina LT. Measurements of OH and HO<sub>2</sub> concentrations during the MCMA-2006 field campaign – Part 1: Deployment of the Indiana University laser-induced fluorescence instrument. *Atmos Chem Phys*. 2009:21.
  92. Shirley TR, Brune WH, Ren X, et al. Atmospheric oxidation in the Mexico City Metropolitan Area (MCMA) during April 2003. *Atmos Chem Phys*. 2006:14.
  93. Whalley LK, Stone D, Dunmore R, et al. Understanding in situ ozone production in the summertime through radical observations and modelling studies during the Clean air for London project (ClearfLo). *Atmospheric Chem Phys*. 2018;18(4):2547-2571.
  94. Tan Z, Fuchs H, Lu K, et al. Radical chemistry at a rural site (Wangdu) in the North China Plain: observation and model calculations of OH, HO<sub>2</sub> and RO<sub>2</sub> radicals. *Atmospheric Chem Phys*. 2017;17(1):663-690.
  95. Wang G, Shen F, Yi H, et al. Laser absorption spectroscopy applied to monitoring of short-lived climate pollutants (SLCPs). *J Mol Spectrosc*. 2018; 348: 142-151.
  96. Miklós A, Hess P, Bozóki Z. Application of acoustic resonators in photoacoustic trace gas analysis and metrology. *Rev Sci Instrum*. 2001;72(4):20.
  97. Beck HA, Niessner R, Haisch C. Development and characterization of a mobile photoacoustic sensor for on-line soot emission monitoring in diesel exhaust gas. *Anal Bioanal Chem*. 2003; 375: 8.
  98. Wang G, Kulinski P, Hubert P, et al. Filter-free light absorption measurement of volcanic ashes and ambient particulate matter using multi-wavelength photoacoustic spectroscopy. *Prog Electromagn Res*. 2019; 166: 59-74.
  99. Koskinen V, Fonsen J, Kauppinen J, Kauppinen I. Extremely sensitive trace gas analysis with modern photoacoustic spectroscopy. *Vib Spectrosc*. 2006;42(2):239-242.



100. Sharma N, Arnold IJ, Moosmüller H, Arnott WP, Mazzoleni C. *Photoacoustic and Nephelometric Spectroscopy of Aerosol Optical Properties with a Supercontinuum Light Source*. *Atmos. Meas. Tech. Discuss.*; 2013:6293-6327.
101. Bernhardt R, Santiago GD, Slezak VB, Peuriot A, González MG. Differential, LED-excited, resonant NO<sub>2</sub> photoacoustic system. *Sens Actuators B Chem.* 2010;150(2):513-516.
102. R. Wiegand J, Mathews LD, D. Smith G. A UV-Vis Photoacoustic Spectrophotometer. *Anal Chem.* 2014;86:6049-6056.
103. Lack DA, Richardson MS, Law D, et al. Aircraft Instrument for Comprehensive Characterization of Aerosol Optical Properties, Part 2: Black and Brown Carbon Absorption and Absorption Enhancement Measured with Photo Acoustic Spectroscopy. *Aerosol Sci Technol.* 2012;46(5):555-568.
104. Petzold A, Niessner R. Photoacoustic soot sensor for in-situ black carbon monitoring. *Appl Phys B Laser Opt.* 1996;63(2):191-197.
105. Song K, Cha HK, Kapitanov VA, et al. Differential Helmholtz resonant photoacoustic cell for spectroscopy and gas analysis with room-temperature diode lasers. *Appl Phys B Lasers Opt.* 2002;75(2-3):215-227.
106. Rouxel J, Coutard JG, Gidon S, et al. Miniaturized differential Helmholtz resonators for photoacoustic trace gas detection. *Sens Actuators B Chem.* 2016;236:1104-1110.
107. E. Kinsler L, R. Frey A, B. Coppers A, V. Sanders J. *Fundamentals of Acoustics L Kinsler*. Wiley/Blackwell.; 1999.
108. Meyers RA, ed. *Encyclopedia of Analytical Chemistry: Applications, Theory and Instrumentation*. 1st ed. Wiley; 2006.
109. Kauppinen J, Wilcken K, Kauppinen I, Koskinen V. High sensitivity in gas analysis with photoacoustic detection. *Microchem J.* 2004:9.
110. Kosterev AA, Bakhirkin YA, Curl RF, Tittel FK. Quartz-enhanced photoacoustic spectroscopy. *OPTICS LETTERS.* 2022;27(21):3.
111. Kuusela T, Kauppinen J. Photoacoustic Gas Analysis Using Interferometric Cantilever Microphone. *Appl Spectrosc Rev.* 2007;42(5):33.
112. Pryputniewicz RJ. Current Trends and Future Directions in MEMS. *Exp Mech.* Published online 2012:15.
113. Haisch C. Photoacoustic spectroscopy for analytical measurements. *Meas Sci Technol.* 2012;23(1):012001.
114. Bohren A, Lerber T von, Sigrist MW. Mid-BR photoacoustic trace gas spectroscopy with an optical parametric oscillator based difference frequency generation laser source. In: *Advanced Solid State Lasers (2000), Paper ME4*. Optica Publishing Group; 2000:ME4.

115. Kirchstetter TW, Novakov T, Hobbs PV. Evidence that the spectral dependence of light absorption by aerosols is affected by organic carbon: spectral light absorption by aerosols. *J Geophys Res Atmospheres*. 2004;109(D21):12.
116. Abichou G, Ngagine SH, Ba TN, et al. A New Photoacoustic Soot Spectrophone for Filter-Free Measurements of Black Carbon at 880 nm. *Molecules*. 2022;27(18):6065.
117. Arnott WP, Moosmüller H, Walker JW. Nitrogen dioxide and kerosene-flame soot calibration of photoacoustic instruments for measurement of light absorption by aerosols. *Rev Sci Instrum*. 2000;71(12):4545.
118. Nakayama T, Suzuki H, Kagamitani S, Ikeda Y, Uchiyama A, Matsumi Y. Characterization of a Three Wavelength Photoacoustic Soot Spectrometer (PASS-3) and a Photoacoustic Extinctionmeter (PAX). *J Meteorol Soc Jpn Ser II*. 2015;93(2):285-308.
119. Vandaele AC, Hermans C, Simon PC, et al. Measurements of the NO<sub>2</sub> absorption cross-section from 42 000 cm<sup>-1</sup> to 10 000 cm<sup>-1</sup> (238–1000 nm) at 220 K and 294 K. *J Quant Spectrosc Radiat Transfer*. 1998;59:171-184.
120. Le Neindre B, Vodar B, eds. *Experimental Thermodynamics Volume II: Experimental Thermodynamics of Non-Reacting Fluids*. Springer US; 1968.
121. Masse volumique de l'air, densité, kg/m<sup>3</sup>, air, temperature, humidite relative, massique. Published 2001. Accessed October 4, 2023. <https://www.thermexcel.com/french/tables/massair.htm>
122. Kosterev AA, Mosely TS, Tittel FK. Impact of humidity on quartz-enhanced photoacoustic spectroscopy based detection of HCN. *Appl Phys B*. 2006;85(2-3):295-300.
123. Ajtai T, Filep Á, Schnaiter M, et al. A novel multi-wavelength photoacoustic spectrometer for the measurement of the UV-vis-NIR spectral absorption coefficient of atmospheric aerosols. *J Aerosol Sci*. 2010;41(11):1020-1029.
124. Lang B, Breitegger P, Brunnhofer G, et al. Molecular relaxation effects on vibrational water vapor photoacoustic spectroscopy in air. *Appl Phys B*. 2020;126(4):64.
125. Miyakawa T, Mordovskoi P, Kanaya Y. Evaluation of black carbon mass concentrations using a miniaturized aethalometer: Intercomparison with a continuous soot monitoring system (COSMOS) and a single-particle soot photometer (SP2). *Aerosol Sci Technol*. 2020;54(7):811-825.
126. Bond TC, Doherty SJ, Fahey DW, et al. Bounding the role of black carbon in the climate system: A scientific assessment: black carbon in the climate system. *J Geophys Res Atmospheres*. 2013;118(11):5380-5552.
127. Bond TC, Bergstrom RW. Light Absorption by Carbonaceous Particles: An Investigative Review. *Aerosol Sci Technol*. 2006;40(1):27-67.

128. Lee J. Performance Test of MicroAeth® AE51 at Concentrations Lower than 2  $\mu\text{g}/\text{m}^3$  in Indoor Laboratory. *Appl Sci*. 2019;9(13):2766.
129. Radney JG, Zangmeister CD. Measurement of Gas and Aerosol Phase Absorption Spectra across the Visible and Near-IR Using Supercontinuum Photoacoustic Spectroscopy. *Anal Chem*. 2015;87(14):7356-7363.
130. Hamasha KM, Arnott WP. Photoacoustic measurements of black carbon light absorption coefficients in Irbid city, Jordan. *Environ Monit Assess*. 2010;166(1-4):485-494.
131. Lack DA, Lovejoy ER, Baynard T, Pettersson A, Ravishankara AR. Aerosol Absorption Measurement using Photoacoustic Spectroscopy: Sensitivity, Calibration, and Uncertainty Developments. *Aerosol Sci Technol*. 2006;40(9):697-708.
132. Schmid O, Artaxo P, Arnott WP, et al. Spectral light absorption by ambient aerosols influenced by biomass burning in the Amazon Basin. I: Comparison and field calibration of absorption measurement techniques. *Atmos Chem Phys*. 2006:20.
133. HITRANonline - Absorption Cross Section Search. Published 2023. Accessed September 30, 2023. <https://hitran.org>
134. Lamsal LN, Martin RV, Van Donkelaar A, et al. Ground-level nitrogen dioxide concentrations inferred from the satellite-borne Ozone Monitoring Instrument. *J Geophys Res*. 2008;113(D16):D16308.
135. SAPHIR. Accessed June 28, 2023. <https://www.fz-juelich.de/en/iek/iek-8/scientific-infrastructure/saphir>
136. SAPHIR | Eurochamp. Accessed June 28, 2023. <https://www.eurochamp.org/simulation-chambers/SAPHIR>
137. Richter CA. *Ozone Production in the Atmosphere Simulation Chamber SAPHIR*. Forschungszentrum, Zentralbibliothek; 2008.
138. Rohrer F, Bohn B, Brauers T. Characterisation of the photolytic HONO-source in the atmosphere simulation chamber SAPHIR. *Atmos Chem Phys*. 2005.
139. Bohn B, Rohrer F, Brauers T, Wahner A. Actinometric measurements of NO<sub>2</sub> photolysis frequencies in the atmosphere simulation chamber SAPHIR. *Atmos Chem Phys*. 2005.
140. Yang C, Zhao W, Fang B, et al. Improved Chemical Amplification Instrument by Using a Nafion Dryer as an Amplification Reactor for Quantifying Atmospheric Peroxy Radicals under Ambient Conditions. *Anal Chem*. 2019;91(1):776-779.
141. Cho C, Fuchs H, Hofzumahaus A, et al. Experimental chemical budgets of OH, HO<sub>2</sub>, and RO<sub>2</sub> radicals in rural air in western Germany during the JULIAC campaign 2019. *Atmospheric Chem Phys*. 2023;23(3):2003-2033.

142. Dusanter S, Vimal D, Stevens PS. Technical note: Measuring tropospheric OH and HO<sub>2</sub> by laser-induced fluorescence at low pressure. A comparison of calibration techniques. *Atmos Chem Phys*. 2008;8:321-340.
143. Cantrell CA, Zimmer A, Tyndall GS. Absorption cross sections for water vapor from 183 to 193 nm. *Geophys Res Lett*. 1997;24(17):2195-2198.
144. Sander SP, Friedl RR, Barker JR. Chemical Kinetics and Photochemical Data for Use in Atmospheric Studies Evaluation Number 16 Supplement to Evaluation 15: Update of Key Reactions. *JPL*. 2010;(09-31).
145. Lew MM, Dusanter S, Stevens PS. Measurement of interferences associated with the detection of the hydroperoxy radical in the atmosphere using laser-induced fluorescence. *Atmospheric Meas Tech*. 2018;11(1):95-109.
146. Hofzumahaus A, Brauers T, Aschmutat U, et al. Reply [to “Comment on ‘The measurement of tropospheric OH radicals by laser-induced fluorescence spectroscopy during the POPCORN field campaign’ by Hofzumahaus *et al.* and ‘Intercomparison of tropospheric OH radical measurements by multiple folded long-path laser absorption and laser induced fluorescence’ by Brauers *et al.* ”]. *Geophys Res Lett*. 1997;24(23):3039-3040.
147. Dillon TJ, Crowley JN. Reactive quenching of electronically excited NO\*<sub>2</sub> and NO\*<sub>3</sub> by H<sub>2</sub>O as potential sources of atmospheric HO<sub>x</sub> radicals. *Atmospheric Chem Phys*. 2018;18(19):14005-14015.
148. MCM Website CH<sub>3</sub>O<sub>2</sub>. Accessed August 31, 2023. <http://chmlin9.leeds.ac.uk/MCMv3.3.1/browse.htm?species=CH3O2>
149. MCM Website CH<sub>4</sub>. Accessed September 21, 2023. <http://chmlin9.leeds.ac.uk/MCMv3.3.1/browse.htm?species=CH4>
150. MCM Website C<sub>5</sub>H<sub>8</sub>. Accessed September 21, 2023. <http://chmlin9.leeds.ac.uk/MCMv3.3.1/browse.htm?species=C5H8>
151. MCM Website. Accessed September 21, 2023. <http://chmlin9.leeds.ac.uk/MCMv3.3.1/roots.htm>
152. Newland MJ, Bryant DJ, Dunmore RE, et al. *Rainforest-like Atmospheric Chemistry in a Polluted Megacity*. Gases/Field Measurements/Troposphere/Chemistry (chemical composition and reactions); 2020.
153. Whalley LK, Stone D, Bandy B, et al. Atmospheric OH reactivity in central London: observations, model predictions and estimates of in situ ozone production. *Atmospheric Chem Phys*. 2016;16(4):2109-2122.
154. Sanchez D, Jeong D, Seco R, et al. Intercomparison of OH and OH reactivity measurements in a high isoprene and low NO environment during the Southern Oxidant and Aerosol Study (SOAS). *Atmos Environ*. 2018;174:227-236.
155. Ren X, Van Duin D, Cazorla M, et al. Atmospheric oxidation chemistry and ozone production: Results from SHARP 2009 in Houston, Texas: ATMOSPHERIC

PHOTOCHEMISTRY IN HOUSTON. *J Geophys Res Atmospheres*. 2013;118(11):5770-5780.

156. Thornton JA. Ozone production rates as a function of NO<sub>x</sub> abundances and HO<sub>x</sub> production rates in the Nashville urban plume. *J Geophys Res*. 2002;107(D12):4146.
157. Martinez M. OH and HO<sub>2</sub> concentrations, sources, and loss rates during the Southern Oxidants Study in Nashville, Tennessee, summer 1999. *J Geophys Res*. 2003;108(D19):4617.
158. Baier B, Brune W, Miller D, et al. *Higher Measured than Modeled Ozone Production at Increased NO<sub>x</sub> Levels in the Colorado Front Range*. Gases/Field Measurements/Troposphere/Chemistry (chemical composition and reactions); 2017.
159. Griffith SM, Hansen RF, Dusanter S, et al. Measurements of hydroxyl and hydroperoxy radicals during CalNex-LA: Model comparisons and radical budgets. *J Geophys Res Atmospheres*. 2016;121(8):4211-4232.
160. Doussin JF, Fuchs H, Kiendler-Scharr A, Seakins P, Wenger J, eds. *A Practical Guide to Atmospheric Simulation Chambers*. Springer International Publishing; 2023.
161. IUPAC Task Group on Atmospheric Chemical Kinetic Data Evaluation. Published online 2001. <http://iupac.pole-ether.fr>.



## General conclusions and perspectives

This PhD project was dedicated to (i) improve and better understand uncertainties associated to a chemical amplifier for atmospheric measurements of peroxy radicals and (2) evaluate a methodology for real time monitoring of ozone production rates. The latter, if implemented by measurement networks, would provide useful information on the ozone budget and its chemical formation regimes, which would help public authorities in the management of pollution peaks.

A photoacoustic spectrometer (PAS) operating at 880 nm was optimized and characterized at the LPCA laboratory (ULCO) for the measurement of atmospheric black carbon. Optimizing the modulation frequency, sampling flow rate and laser power led to a sensitivity of  $0.22 \mu\text{V}/(\mu\text{g m}^{-3})$  and a  $3\text{-}\sigma$  LoD of  $2.5 \mu\text{g m}^{-3}$  at a time resolution of 1 s. Further improvements can be achieved using longer time resolutions, more microphones, a higher laser power, and by refining the strategy used to dry the sample. This PAS offers advantages over filter-based techniques, such as lower uncertainties ( $< 10\%$ ) and fast measurement time (1 s).

A second PAS was designed, assembled and characterized for the measurement of  $\text{NO}_2$ , including 2 measurement channels, with the idea of coupling it to a chemical amplifier for peroxy radical measurements. Various parameters were optimized to achieve the best sensitivity and lowest LoD, including laser power, modulation frequency and sampling flow rate. Calibrations of the prototype demonstrated a sensitivity of about  $0.09 \mu\text{V ppb}^{-1}$  and a  $3\text{-}\sigma$  LoD of 7-9 ppb for the two channels at a time resolution of 1 s. Integrating the measurements over 1 min is expected to improve the LoD to approximately 1 ppb for each channel. It was found that the main drawback is the impact of water-vapor on the measurements, which leads to a large background signal that needs to be subtracted (sensitivity equivalent to 6.5 ppb of  $\text{NO}_2$  per ppth of water-vapor).

Due to the high LoD and the impact of water-vapor on the measurements, the current PAS prototype was considered unsuitable for measuring  $\text{NO}_2$  from the chemical amplifier. Future improvements are necessary, focusing on background and noise reduction by upgrading the current PAS with Nafion dryers, optimized lens systems, low-noise lock-in and pre-amplifiers, and acoustic isolations. Additionally, simplifying the setup could be done using laser modules incorporating the power modulation electronic and new resonators

exhibiting closer resonance frequencies, which would make the PAS system more compact, simpler to use, and more appropriate for field applications.

On the other hand, this prototype constitutes an innovative approach for the measurement of ambient NO<sub>2</sub>. In fact, its capability of detecting simultaneously the background and sample signals offers a more effective mitigation of potential water-vapor effect, which is one of the main issue in PAS measurements.

The Chemical Amplifier (CA), coupled to two commercial NO<sub>2</sub> instruments relying on the cavity attenuated phase shift technology, was deployed during the RO<sub>x</sub> Comparison campaign (RO<sub>x</sub>Comp). This intercomparison exercise for peroxy radical instruments took place at the SAPHIR chamber in Forschungszentrum Jülich (FZJ), Germany. Various experiments were conducted to test the instruments' performances, generating different types of peroxy radicals under different conditions of temperature and irradiation, including O-functionalized and nitrooxy-peroxy radicals. An emphasis was put on testing matrix effects, varying levels of species that are abundant in the atmosphere such as water-vapor, ozone and NO<sub>x</sub>. This campaign was a valuable opportunity to better characterize the performances of the IMT chemical amplifier, with the goal of identifying areas of agreement and discrepancies with other radical instruments. In this manuscript, IMT-CA measurements were compared to the laser-induced fluorescence instrument from FZJ (FZJ-FAGE).

Significant outcomes related to data processing (calibration, zeroing, etc.) were (i) the identification and correction for a miscalibration of IMT-CA and (ii) the testing of a correction procedure made to address a measurement bias linked to ozone. Experiments performed to investigate whether RH could have an impact on IMT-CA measurements showed no impact and confirmed that the chain length is properly parameterized as a function of RH. Regarding the O<sub>3</sub> bias, while most experiments indicate that this bias is properly parameterized and removed, a few experiments question whether it is subtracted correctly. Further testing of IMT-CA is needed to better understand the origin of this bias and whether it is necessary to subtract it.

Overall, IMT-CA demonstrated reasonable performances, with an agreement within 30% with FZJ-FAGE. However, several aspects highlighted below needs further scrutiny.



- Significant differences in the measurement of  $\text{HO}_2+\text{RO}_2$  were observed when IMT-CA was compared to FZJ-FAGE under varying NO conditions (hundreds of ppt to several ppb). It was shown that the agreement exhibits a trend with NO. Compared to FZJ-FAGE, IMT-CA measures lower concentrations at  $\text{NO} < 200\text{-}300$  ppt, similar concentrations between 300ppt and 0.5-1 ppb of NO, and higher concentrations for  $\text{NO} > 0.5\text{-}1$  ppb. This trend, if confirmed when the measurement datasets are finalized, will be further investigated using box modeling.
- IMT-CA proved to be efficient in detecting various types of peroxy radicals (i.e. O-functionalized and nitrooxy-peroxy). However, one experiment involving the oxidation of  $\beta$ -pinene by  $\text{NO}_3$  seems to indicate that high generation oxidation products formed when all  $\beta$ -pinene was consumed (peroxy radicals or closed shell molecules) impact either the IMT-CA or FZJ-FAGE measurements (or both). Future box modeling of this experiment will help investigating this aspect.

The last part of this PhD was dedicated to evaluate the suitability of IMT-CA for the quantification of ozone production rates in the atmosphere. For this purpose, results of selected photooxidation experiments from ROxComp were also used to compare  $\text{O}_x$  ( $\text{O}_3+\text{NO}_2$ ) production rates calculated from  $\text{HO}_2+\text{RO}_2$  radicals measured by IMT-CA and values inferred from the change in  $\text{O}_x$  inside the SAPHIR chamber. This work indicates that, the methodology of using the sum of  $\text{HO}_2+\text{RO}_2$  and an average rate coefficient for the reaction of peroxy radicals with NO instead of speciated measurements of  $\text{HO}_2$  and  $\text{RO}_2$  and individual reaction rate coefficients, is suitable to quantify the gross  $\text{O}_x$  production rate. Yields for the formation of organic nitrates in  $\text{RO}_2+\text{NO}$  reactions do not need to be included in the calculations since IMT-CA only detects  $\text{RO}_2$  radicals leading to the formation of ozone, which is a significant advantage to infer  $\text{O}_x$  production rates.

Regarding the quantification of net  $\text{O}_x$  production rates, it requires subtracting the total  $\text{O}_x$  loss rate resulting from chemical processes ( $\text{O}_3+\text{HO}_2$ ,  $\text{NO}_2+\text{OH}$ ,  $\text{alkene}+\text{O}_3$ ), which in turn requires to have access to ancillary measurements of OH,  $\text{HO}_2$  and alkenes. Using only  $\text{HO}_2+\text{RO}_2$  measurements would only provide an upper of the net  $\text{O}_x$  production rate.

When comparing net  $\text{O}_x$  production rates,  $P(\text{O}_x)$ , derived from (i) IMT-CA measurements and (ii) temporal variations of  $\text{O}_x$  species in SAPHIR, the level of agreement changes with NO. While the two methodologies provide similar values when  $\text{NO} < 0.5\text{-}1$

ppb, net  $O_x$  production rates inferred from peroxy radicals when  $NO > 0.5-1$  ppb are significantly larger than values inferred from temporal changes in  $O_x$  species. The disagreement increases almost linearly with  $NO$  to reach a factor of 8-20 around 9 ppb. It is interesting to note that a similar discrepancy was noted during field campaigns performed in ambient air when gross ozone production rates calculated from ambient measurements of peroxy radicals are compared to values directly measured using the MOPS technique or calculated from radical concentrations simulated by box models. However, we could not establish whether the source of the disagreement is the same.

Several potential reasons were addressed to explain the discrepancy observed between the two  $P(O_x)$  quantification methods. Several of them have been ruled out, including (i) an instrument miscalibration, (ii) an offset in  $NO$  measurements, and (iii) a miscalculated or (iv) missing loss process in  $I(O_x)$ , the latter including  $NO_2$  wall losses,  $RO_2+O_3$  reactions and  $NO_3$  photolysis. The presence of a measurement artifact associated to IMT-CA when  $NO > 0.5-1$  ppb may be possible, which would also explain part of the  $NO$ -trend observed when IMT-CA and FZJ-FAGE measurements are compared in chapter 3. However, a  $NO$ -dependent disagreement is also observed when speciated measurements of  $HO_2$  and  $RO_2$  from FZJ-FAGE are used to calculate  $P(O_x)$  instead of  $HO_2+RO_2$  measurements from IMT-CA, with differences that are approximately twice lower. This indicates that a potential artifact associated to IMT-CA measurements may not be sufficient to explain the full disagreement. Further investigations are needed to identify the precise origin(s) of this discrepancy, such as performing new chamber experiments in which we can systematically vary the  $NO$  level while oxidizing a VOC.

To conclude on this work, despite that 2-channel PAS was not coupled to IMT-CA due to the lack of sensitivity, the main objective was successfully accomplished. Through this work, we gained valuable insights into the measurement of ambient peroxy radicals and the quantification of ozone production rates, highlighting some aspects that need to be further investigated.

The  $P(O_x)$  methodology (measuring the rate of formation of a pollutant rather than its concentration), when optimized, is expected to attract the attention of measurement networks involved in monitoring air quality and climate change. The deployment of this type of instrumentation over a large spatial scale would help improving our knowledge of

ozone formation chemistry in various environments, validating predictive atmospheric models, and therefore improving predictions related to global warming.



## Appendix: Publications and presentations on conferences

### Publication:

Abichou, G.; Ngagine, S.H.; Ba, T.N.; Wang, G.; Flament, P.; Deboudt, K.; Dusanter, S.; Sigrist, M.W.; Tomas, A.; Chen, W. A New Photoacoustic Soot Spectrophone for Filter-Free Measurements of Black Carbon at 880 nm. *Molecules*. 2022, 27, 6065.

### Presentations on conference:

- International conference: Goldschmidt 2023, Lyon, France, 09-14 Jul. 2023  
Poster: Goufrane Abichou, Ahmad Lahib, Marina Jamar, Weidong Chen, Hendrik Fuchs, Anna Novelli, Michelle Färber, Alexandre Tomas, Sébastien Dusanter. Evaluation of a methodology for ozone production rate quantification in ambient air.
- CaPPA scientific day, Lille, France, 10 Mar. 2023  
Oral presentation: Goufrane Abichou, Nesrine Shamas, Ahmad Lahib, Sébastien Dusanter, Alexandre Tomas, Weidong Chen, Coralie Schoemaeker, Christa Fittschen, Laure Pillier, Sébastien Batut, Amaury Lahccen. Measurements of ROx radicals in the atmosphere.
- Workshop part of the ROxComp intercomparison exercise held in the SAPHIR simulation chamber, FZJ, Jülich, Germany: online, 07-08 Feb. 2023  
Goufrane Abichou, Ahmad Lahib, Sébastien Dusanter. Deployment of The IMT Chemical Amplifier during ROxComp 2022.
- GDR EMIE Plenary Days, Dunkerque, France, 14-17 Jun. 2022  
Oral presentation: Goufrane Abichou, Sébastien Dusanter, Alexandre Tomas, Tong N. Ba, Markus W. Sigrist, Weidong Chen. Development of photoacoustic sensor for the measurement of peroxy radicals and ozone production in the atmosphere.
- MTE pole PhD student day, Calais, France, 01 Jul. 2021  
My Thesis in 180 Seconds: Goufrane Abichou, Sébastien Dusanter, Alexandre Tomas, Weidong Chen. Improvement of a Chemical Amplifier for measuring peroxy radicals in the atmosphere – Application to the quantification of ozone production rates.
- International conference: 7th International Conference on Sensors and Electronic Instrumentation Advances (SEIA' 2021), Palma de Mallorca, Spain, 22-24 Sept. 2021  
Oral presentation: Goufrane Abichou, Soulemane H. Ngagine, Tong N. Ba, Gaoxuan Wang, Pascal Flament, Karine Deboudt, Sébastien Dusanter, Alexandre Tomas, Markus W. Sigrist, Weidong Chen. Filter-free measurements of carbonaceous particles using photoacoustic spectroscopy (PAS) operating at 880 nm

## Abstract

### **Development of an innovative instrument for the measurement of peroxy radicals and ozone production in the atmosphere**

Tropospheric ozone ( $O_3$ ) is a major air pollutant with adverse effects on health, climate and vegetation. This pollutant is produced through a complex series of photochemical reactions involving primary precursors such as volatile organic compounds (VOCs) and nitrogen oxides ( $NO_x$ ). In the troposphere, the oxidation of VOCs leads to the formation of peroxy radicals ( $HO_2+RO_2$ ) that convert nitrogen monoxide (NO) into  $NO_2$ , whose subsequent photolysis leads to the formation of  $O_3$ . Current  $O_3$  reduction strategies rely on the use of atmospheric chemistry models in order to predict how  $O_3$  formation, and as a consequence ambient  $O_3$  concentrations, will respond to regulations in VOC and  $NO_x$  emissions. However, there are limitations associated to this methodology due to uncertainties in (i) emission inventories, (ii) atmospheric chemical mechanisms, and (iii) the simulation of air mass transport. It is therefore essential to develop alternative methods for real-time monitoring of  $O_3$  formation, which would help in the design of more efficient regulation strategies.

The aim of this PhD project was to test an innovative methodology for the assessment of ozone production rates,  $P(O_3)$ , from direct ambient observations. This methodology implies measuring simultaneously NO and the sum of  $HO_2+RO_2$  in ambient air to compute  $P(O_3)$  as the reaction rate between peroxy radicals and NO. In this context, a Chemical Amplifier (CA) developed at IMT Nord Europe for measuring  $HO_2+RO_2$  was tested and optimized. The CA measures peroxy radicals through their conversion into  $NO_2$ . A first step in this work was to develop a 2-channel Photoacoustic Absorption Spectrometer (PAS) for  $NO_2$  measurements. Unfortunately, the PAS sensitivity was not good enough to be coupled to the CA and thus, an approach was proposed to use it for ambient  $NO_2$  measurements. In a second phase of this thesis, the CA's reliability (coupled to  $NO_2$  monitors that are more performant than the PAS) was tested during an intercomparison study (ROxCOMP) at the SAPHIR simulation chamber in Forschungszentrum Jülich, Germany. The last part of this work was devoted to evaluate the  $P(O_3)$  quantification methodology using chamber experiments from ROxCOMP.

**Keywords:** Metrology, ozone, atmospheric chemistry, peroxy radicals, climate change

## **Développement d'un instrument innovant dédié à la mesure des radicaux peroxyes et la production d'ozone dans l'atmosphère**

L'ozone troposphérique ( $O_3$ ) est un polluant majeur qui a des effets néfastes sur la santé, le climat et la végétation. Ce polluant est produit lors de réactions photochimiques complexes impliquant des précurseurs primaires tels que les composés organiques volatils (COV) et les oxydes d'azote ( $NO_x$ ). Dans la troposphère, l'oxydation des COV conduit à la formation de radicaux peroxyes ( $HO_2+RO_2$ ) qui convertissent le monoxyde d'azote (NO) en  $NO_2$ , la photolyse de ce dernier étant la source principale de l' $O_3$ . Les stratégies d'abattement de l'ozone reposent sur l'utilisation de modèles de chimie atmosphérique afin de prédire l'impact de réductions des émissions en COV et  $NO_x$  sur la formation d' $O_3$ , et par conséquent ses concentrations ambiantes. Cependant, cette méthodologie présente certaines limites en raison des incertitudes associées (i) aux inventaires d'émissions, (ii) aux mécanismes chimiques et (iii) à la simulation du transport des masses d'air. Il est donc essentiel de développer des méthodes alternatives pour la surveillance en temps réel de la formation d'ozone, ce qui permettrait de proposer des stratégies de régulation plus efficaces. L'objectif principal de ce projet de thèse consistait à tester une méthodologie de quantification de la vitesse de production d'ozone,  $P(O_3)$ , à partir d'observations ambiantes. Cette méthodologie implique la mesure simultanée de NO et de la somme des  $HO_2+RO_2$  dans l'air ambiant. Dans ce contexte, un amplificateur chimique (CA) développé à l'IMT Nord Europe pour la mesure des  $HO_2+RO_2$  a été testé et optimisé. Cet instrument mesure la somme des radicaux peroxyes suite à leur conversion chimique en  $NO_2$  et une première étape de ce travail a été de développer un spectromètre d'absorption photoacoustique (PAS) à 2 voies pour la mesure du  $NO_2$ . Il s'est avéré que la sensibilité du PAS n'était pas suffisante pour être couplé au CA, ainsi cet instrument a plutôt été exploité pour proposer une nouvelle approche pour la mesure du  $NO_2$  ambiant. Dans une deuxième phase de cette thèse, la fiabilité du CA (couplé à des analyseurs de  $NO_2$  plus performants que le PAS) a été testée lors d'une campagne d'intercomparaison (ROxComp) à la chambre de simulation SAPHIR du Forschungszentrum Jülich, Allemagne. La dernière partie de ce travail a été consacrée à l'évaluation de la méthodologie de quantification de  $P(O_3)$  sur la base des expériences en chambre de simulation réalisées lors de ROxCOMP.

**Mots clés :** Métrologie, ozone, chimie atmosphérique, radicaux peroxyes, changement climatique

## Résumé

L'ozone troposphérique est un polluant atmosphérique majeur, tant en termes de santé (irritation des voies respiratoires supérieures) que de climat (effet de serre). Ce polluant n'est pas émis directement dans l'atmosphère, mais est produit photo-chimiquement par le rayonnement solaire en présence de précurseurs chimiques primaires : les composés organiques volatils (COV) et les oxydes d'azote ( $\text{NO}_x = \text{NO} + \text{NO}_2$ ). Compte tenu du caractère secondaire de ce polluant et de la complexité de sa chimie de formation, des modèles de chimie atmosphérique prédictive sont généralement utilisés pour évaluer les stratégies de réduction. Cependant, de multiples sources d'erreurs sont associées aux inventaires d'émissions, à la chimie et au transport des masses d'air, ce qui limite la fiabilité de ces modèles prédictifs. Il est donc essentiel de développer des approches alternatives permettant d'évaluer les stratégies de réduction les plus efficaces.

L'objectif principal de cette thèse de doctorat consistait à évaluer la fiabilité de la quantification des vitesses de production d'ozone sur la base de mesures simultanées de radicaux peroxy ( $\text{HO}_2 + \text{RO}_2$ ) et de monoxyde d'azote (NO) dans l'air ambiant. La vitesse de production d'ozone,  $P(\text{O}_3)$ , est déduite du taux d'oxydation du NO en  $\text{NO}_2$  en raison de sa réaction avec les radicaux peroxy. La métrique  $P(\text{O}_3)$  serait utile pour les autorités publiques dans la gestion des pics de pollution, car des mesures en temps réel de  $P(\text{O}_3)$  aideraient à évaluer le régime de formation de l'ozone à un endroit particulier (limité par les  $\text{NO}_x$  ou saturé en  $\text{NO}_x$ ), à identifier les périodes d'activités photochimiques intenses conduisant à des épisodes de pollution, et à tester les prédictions des modèles atmosphériques.

Le travail effectué au cours de cette thèse consistait à (i) tester et améliorer un Amplificateur Chimique (CA) développé au CERI EE, IMT Nord Europe pour mesurer les radicaux peroxy dans l'air ambiant et (ii) évaluer la fiabilité de la méthodologie pour quantifier les vitesses de production d'ozone à partir de mesures concomitantes de radicaux peroxy et de NO.

- Pour (i), il a été nécessaire de développer un Spectromètre d'Absorption Photo-acoustique (PAS) à deux canaux pour les mesures de  $\text{NO}_2$ , simultanément à la sortie des réacteurs de fond et d'amplification du CA. L'objectif était de remplacer deux analyseurs commerciaux de  $\text{NO}_2$ , précédemment utilisés sur le CA, dans le but de réduire significativement le coût de construction des instruments CA. Il a également été nécessaire de tester la fiabilité du CA pour mesurer les radicaux peroxy en



participant à une étude d'inter-comparaison à la chambre de simulation SAPHIR au Forschungszentrum Jülich, en Allemagne. Le CA a été comparé à d'autres instruments utilisant différentes techniques analytiques.

- Pour (ii), les résultats des expériences en chambre mentionnées ci-dessus ont été utilisés pour enquêter sur la fiabilité de la méthodologie de quantification de  $P(O_3)$  en combinant des mesures simultanées de radicaux peroxy et de NO.

Ce projet de doctorat a été mis en œuvre comme suit :

1. Premiers 18 mois à l'ULCO, LPCA, Dunkerque :

- Optimisations et caractérisation d'un instrument PAS existant dédié aux mesures de la suie (BC), avec pour objectif de se former sur cette technologie.
- Construction et caractérisation du PAS à deux canaux pour le  $NO_2$  au LPCA, et évaluation de sa pertinence pour les mesures de radicaux peroxy en utilisant la technique PERCA au CERI EE.

2. Derniers 18 mois à l'IMT Nord Europe, CERI EE, Douai :

- Participation à la campagne d'inter-comparaison ROxComp réalisée au Forschungszentrum Jülich GmbH (Allemagne) en août 2022, avec pour objectif de comparer l'amplificateur chimique IMT à d'autres instruments capables de mesurer les radicaux peroxy, et donc d'améliorer notre compréhension des incertitudes associées à cette technique.
- Evaluation de la méthodologie de quantification de la vitesse de production d'ozone à l'aide de données d'expériences réalisées dans la chambre de simulation SAPHIR pendant le ROxComp.

## **Chapitre 1 : Ozone troposphérique : impacts, chimie et réglementations**

Ce chapitre est une étude bibliographique fournissant un contexte et des motivations. Il comprend une description de la chimie de formation de l'ozone dans la troposphère, mettant en évidence le rôle des radicaux peroxy et des oxydes d'azote, et abordant ses impacts sur le climat, la végétation et la santé humaine. De plus, différentes approches proposées pour mesurer les radicaux peroxy et les vitesses de production d'ozone sont présentées dans ce chapitre, ainsi qu'un bref aperçu des campagnes de mesures de radicaux peroxy et de  $P(O_3)$  sur le terrain. Ces derniers ont été utiles pour la compréhension de la formation de l'ozone troposphérique dans différentes régions du monde au cours des deux dernières décennies. Les  $P(O_3)$  modélisées et calculées à partir de mesures et de modèles  $RO_x$  étaient en accord

dans l'identification de la chimie de l'ozone dans diverses mégapoles et zones industrielles, qui s'est avérée être une chimie limitée par les  $\text{NO}_x$ .

Malgré l'avantage des modèles pour considérer la contribution des  $\text{RO}_2$  individuels à la quantification de  $\text{P}(\text{O}_3)$ , cette méthode a montré une sous-estimation cohérente par rapport aux méthodes directes et indirectes de mesure de  $\text{P}(\text{O}_3)$ . En revanche, la comparaison entre les  $\text{P}(\text{O}_3)$  mesurées et celles calculées à partir des mesures  $\text{RO}_x$  a révélé une dépendance de leur accord à la concentration de  $\text{NO}$ .

Bien que les techniques présentées pour la mesure de  $\text{P}(\text{O}_3)$  (MOPS & OPR) soient en amélioration continue, des incertitudes significatives dans leurs mesures sont toujours observées, principalement liées à la formation de HONO et aux pertes murales de  $\text{NO}_2$ . Parmi ces trois méthodes, le calcul de  $\text{P}(\text{O}_3)$  basé sur les mesures  $\text{RO}_x$  semble être le plus précis. Par conséquent, cette approche a été adoptée dans le présent travail pour être étudiée pour le suivi des vitesses de production d'ozone lors d'expériences en chambre.

## **Chapitre 2 : Développement et caractérisation des spectromètres photo-acoustiques**

Ce chapitre présente certains travaux de recherche et développement effectués sur la technologie de spectroscopie photoacoustique. Il rapporte le travail effectué pour tester et améliorer un prototype existant de PAS fonctionnant à 880 nm pour la détection et la quantification de la suie (Black Carbon, BC). L'objectif de ce travail était de prendre en charge l'utilisation d'un PAS (formation) et d'optimiser ses performances, afin de concevoir ultérieurement une configuration améliorée de PAS pour les mesures de  $\text{NO}_2$ . Une série de paramètres a été optimisée, par exemple, le débit d'échantillonnage de gaz, la puissance du laser et la fréquence de résonance de la cellule d'échantillonnage PA. Toutes ces optimisations ont conduit à un meilleur rapport signal/bruit (SNR) et donc à de meilleures caractéristiques de performance.

Une fois l'instrument optimisé, la matière particulaire (PM) émise par la fumée d'encens a été utilisée pour étalonner le PAS. Des mesures côte à côte de ces particules ont été effectuées à l'aide d'un instrument de référence (Aéthalomètre AE51), ce dernier fournissant les concentrations de PM échantillonnées par le PAS.

La deuxième partie de ce chapitre est consacrée à la présentation du développement, de la caractérisation et de l'étalonnage du PAS- $\text{NO}_2$  à deux canaux. De manière similaire au

BC-PAS, une série de paramètres a été améliorée afin d'atteindre la sensibilité optimale (optimisation de la réponse) et la meilleure limite de détection (réduction du bruit de mesure). Parmi ces paramètres, la fréquence de modulation du faisceau laser s'est avérée optimale à 6,22 kHz et 6,50 kHz pour les canaux 1 et 2, respectivement, tandis que la puissance laser optimale s'est avérée être de 0,8 et 0,7 W pour les canaux 1 et 2. Le débit d'échantillonnage conduisant au meilleur rapport signal sur bruit s'est révélé être de 0,4 L min<sup>-1</sup> pour les deux canaux.

L'instrument PAS a ensuite été étalonné à l'aide d'un mélange standard de NO<sub>2</sub>. Les expériences de calibration ont indiqué une sensibilité d'environ 0,09 μV ppb<sup>-1</sup> pour chaque canal, et une 3-σ LoD de 6,9 ppb et 8,7 ppb pour les canaux 1 et 2, respectivement, à une résolution temporelle de 1 s. Ces limites de détection peuvent être améliorées à 0,9 et 1,1 ppb, respectivement, en intégrant les mesures sur 1 minute. L'effet de la vapeur d'eau sur les mesures s'est avéré important, avec une sensibilité d'environ 0,65 μV ppth<sup>-1</sup>, équivalent à 6,5 ppb de NO<sub>2</sub> par ppth de H<sub>2</sub>O.

Ce travail a été finalisé par une série de mesures ambiantes et intérieures en parallèle avec un analyseur NO<sub>x</sub> de référence pour valider la configuration développée.

Le travail effectué au cours de cette thèse a principalement porté sur l'assemblage du dispositif et l'évaluation de ses performances. Cependant, aucun test n'a été mené pour évaluer la stabilité de la sensibilité sur une longue période. Il sera donc nécessaire de mener ces tests lors de futures expériences de caractérisation pour déterminer la fréquence à laquelle l'instrument doit être calibré. En raison de la haute LoD et de l'impact important de la vapeur d'eau sur les mesures, il a été conclu que la version actuelle de l'instrument PAS n'est pas adaptée à la mesure du NO<sub>2</sub> à partir de l'amplificateur chimique et que des améliorations supplémentaires sont nécessaires sur l'instrument PAS. Par conséquent, l'instrument PAS n'a pas été couplé à l'amplificateur chimique comme initialement prévu dans cette thèse. Les études décrites dans les chapitres 3 et 4 ont été réalisées en utilisant un amplificateur chimique couplé à deux moniteurs CAPS.

Les améliorations futures de l'instrument PAS se concentreront sur l'amélioration de sa limite de détection en réduisant le niveau de bruit. Cela peut être réalisé par divers moyens, notamment la mise en œuvre d'isolations acoustiques, l'utilisation d'un sécheur Nafion et d'un système de lentilles optimisé, et l'incorporation de verrous et de préamplificateurs à

faible bruit. De plus, l'utilisation de lasers à diode émettant à 448,1 nm contribuerait à améliorer la sensibilité.

Une simplification de la configuration est également incluse dans le plan d'amélioration, principalement en remplaçant le laser assemblé à domicile, qui nécessite plusieurs dispositifs associés tels que des pilotes, des générateurs de forme d'onde et des alimentations électriques, par un module laser permettant à la fois le contrôle de sa puissance et de sa modulation. De nouveaux résonateurs avec des géométries identiques et très précises seront utiles pour fonctionner aux mêmes fréquences de modulation, permettant l'utilisation d'un seul laser pour les deux canaux connectés en série.

### **Chapitre 3 : Comparaison de l'amplificateur chimique IMT à un instrument de fluorescence induite par laser pendant ROxComp**

Ce chapitre rend compte du déploiement de l'amplificateur chimique IMT (CA) lors de la campagne d'inter-comparaison (ROxComp) réalisée au SAPHIR (Simulation de la Photochimie Atmosphérique dans une grande chambre de réaction), Jülich, Allemagne en août 2022. Au cours de cette campagne, plusieurs expériences en chambre ont été menées pour mettre à l'épreuve les instruments radicaux, produisant différents types de radicaux peroxy sous différentes conditions de température, d'humidité, de NO<sub>x</sub> et de rayonnement solaire. Une comparaison détaillée de l'IMT-CA avec un instrument de fluorescence induite par laser (FZJ-FAGE) a été réalisée afin d'étudier ses performances et sa précision dans des conditions chimiques contrastées.

SAPHIR est une chambre de simulation atmosphérique exploitée par le département "Geosphere ICG-2: Troposphere" de l'Institut de Chimie et de Dynamique, situé sur le campus du centre de recherche Forschungszentrum Jülich (FZJ) en Allemagne.

L'objectif de ROxComp était d'évaluer la fiabilité des techniques de mesure RO<sub>x</sub> (OH, HO<sub>2</sub> et RO<sub>2</sub>) développées par différents groupes de recherche internationaux, tels que l'amplification chimique (CA : IMT Nord Europe, Université de Brême, Université Anhui), la fluorescence induite par laser (LIF-FAGE : Université de Lille, Université de Leeds, FZJ) et la spectrométrie de masse par ionisation chimique (CIMS : Deutscher Wetterdienst, Leopold-Franzens Universität Innsbruck).

On a profité de cet exercice d'inter-comparaison pour tester l'amplificateur chimique IMT et pour améliorer notre compréhension des incertitudes associées aux mesures CA, ce

qui était un aspect important pour développer et évaluer l'approche de quantification des vitesses de production d'ozone proposée au chapitre 4.

Parmi les connaissances acquises lors de cette campagne, une mauvaise calibration de l'IMT-CA a été identifiée grâce à des calibrations croisées utilisant des sources radicales d'autres groupes. Ce problème a été ensuite investigué plus en détail dans notre laboratoire et il a été constaté que la concentration d'isoprène ajoutée dans le calibrateur IMT, utilisée pour convertir OH en radicaux RO<sub>2</sub>, était suffisamment élevée pour générer une amplification significative des radicaux peroxy lorsque les réacteurs CA étaient en mode de fond, ce qui a conduit à une sous-estimation de la longueur de la chaîne radicalaire. Ce problème a été corrigé et sera facilement résolu pour les futures calibrations en diminuant la concentration d'isoprène.

Les expériences ROxComp ont permis d'étudier si l'humidité relative (RH) pourrait avoir un impact sur les mesures IMT-CA. Il a été constaté que l'ajout d'humidité lors de différentes expériences n'a pas affecté l'accord entre IMT-CA et FZJ-FAGE. De plus, ces mesures étaient utiles pour s'assurer que la longueur de la chaîne IMT-CA est correctement paramétrée en fonction de l'humidité relative.

Des tests en laboratoire ont montré qu'une correction des mesures IMT-CA est nécessaire pour éliminer un biais de mesure qui évolue avec l'ozone dans des conditions sèches et humides. Une paramétrisation de ce biais a été dérivée en fonction de l'O<sub>3</sub> ambiant et de la vapeur d'eau. En étudiant comment les mesures IMT-CA réagissent aux conditions changeantes d'O<sub>3</sub> et d'humidité pendant ROxComp, il a été constaté que ce biais d'O<sub>3</sub> semble être correctement éliminé pour la plupart des expériences. Cependant, les résultats de quelques expériences suggèrent le contraire. Ce point est déroutant et nécessite des tests supplémentaires de l'IMT-CA pour mieux comprendre l'origine du potentiel biais d'O<sub>3</sub> et s'il est correctement pris en compte.

Les expériences ROxComp ont également permis d'étudier si le NO impacte la comparaison IMT-CA/FZJ-FAGE. Bien que l'accord entre les deux instruments soit dans les 30% la plupart du temps, des expériences menées à des concentrations de NO allant de quelques centaines de ppt à plusieurs ppb ont révélé une divergence systématique. Il a été constaté que l'IMT-CA mesure (1) des concentrations de radicaux peroxy inférieures à FZJ-FAGE lorsque les concentrations de NO sont inférieures à 200-300 ppt, (2) des concentrations plus élevées lorsque les concentrations de NO sont supérieures à 1 ppb, et

(3) des concentrations similaires dans des conditions intermédiaires. Cette tendance au NO n'est pas facile à comprendre et peut être due à l'utilisation de jeux de données préliminaires de mesures de HO<sub>2</sub>+RO<sub>2</sub>.

Le point discuté ci-dessus doit être étudié plus en détail lorsque les ensembles de données sont finalisés. Si la tendance est toujours observée, des enquêtes approfondies sur les changements dans d'autres paramètres dans toutes les expériences qui ont été sélectionnées pour montrer cette tendance devront être menées pour garantir que le NO est à l'origine de la divergence observée. Il serait utile de confirmer ces résultats en menant de nouvelles expériences dans des chambres atmosphériques où on peut faire varier progressivement le NO pendant l'oxydation des COV ciblés. La modélisation en boîte des expériences en chambre rapportées devrait également fournir des informations supplémentaires qui aideront à comprendre cette divergence.

Les expériences ROxComp ont également permis de vérifier si différents types de radicaux peroxy (c'est-à-dire des radicaux peroxy nitrooxy et fonctionnalisés à l'oxygène) sont détectés efficacement par IMT-CA. Les expériences menées avec différents types d'oxydants (OH, O<sub>3</sub>, NO<sub>3</sub>) ont montré que l'IMT-CA est capable de détecter des radicaux carbonylés, hydroxylés et nitrooxy-peroxy avec une bonne efficacité. Cependant, il a été constaté que les espèces générées par l'oxydation de COV secondaires par NO<sub>3</sub> impactent les mesures IMT-CA ou FZJ-FAGE (ou les deux).

En résumé, la participation à ROxComp a été bénéfique pour valider l'IMT-CA dans une chambre de simulation de taille atmosphérique, pour identifier et résoudre des problèmes de calibration, et d'incertitudes de mesures de cet instrument. Les prochaines étapes de cette collaboration comprennent l'application de ces connaissances pour développer des approches pour calculer les vitesses de production d'ozone in situ lors de futures expériences de caractérisation du système IMT-CA. Des mesures directes de radicaux OH et des mesures de COV sont également envisagées pour valider et améliorer les estimations des vitesses de production d'ozone.

#### **Chapitre 4 : Quantification des vitesses de production d'ozone à partir de mesures simultanées de radicaux peroxy et de NO**

Ce chapitre est une étude méthodologique basée sur des données d'expériences réalisées dans la chambre de simulation SAPHIR pendant la campagne ROxComp, différentes

conditions atmosphériques et chimiques. L'objectif était d'évaluer la fiabilité de la méthodologie proposée pour quantifier les vitesses de production d'ozone à partir de mesures concomitantes de HO<sub>2</sub>+RO<sub>2</sub> et de NO dans l'air ambiant.

Dans ce travail, on a adopté l'approche indirecte pour la mesure de P(O<sub>3</sub>), où les radicaux peroxy ont été mesurés à l'aide du CA développé à l'IMT et NO a été quantifié en utilisant un analyseur NO<sub>x</sub> basé sur la chimiluminescence. Les valeurs de P(O<sub>3</sub>) déduites des mesures de radicaux peroxy ont ensuite été comparées aux vitesses de production d'ozone déduites du changement temporel des espèces O<sub>x</sub> (O<sub>3</sub>+NO<sub>2</sub>) à l'intérieur de la chambre.

Dans ce chapitre, les expériences RO<sub>x</sub>Comp, sélectionnées pour évaluer la méthodologie de quantification de P(O<sub>3</sub>), consistaient en la photo-oxydation de COV dans des conditions atmosphériques. Pendant ces expériences, la chambre a été exposée à la lumière du soleil, ce qui a entraîné la formation d'ozone à des taux de production variables et dans différents régimes chimiques.

En tirant parti de la sélectivité de l'IMT-CA dans la détection des radicaux peroxy, c'est-à-dire que le CA ne détecte que les radicaux conduisant à la formation d'ozone, la fraction de RO<sub>2</sub> conduisant à la formation de nitrate/nitrite organique étant non détectée, le taux de production brut des espèces O<sub>x</sub> peut être directement déduit de la somme mesurée de HO<sub>2</sub>+RO<sub>2</sub> si le ratio  $\frac{[HO_2]}{[HO_2]+[RO_2]}$  est supposé être de 0,5 et un coefficient de vitesse moyen est utilisé pour la réaction entre les radicaux peroxy et le NO ( $k_{\text{peroxy}+\text{NO}}$ ). L'analyse présentée dans ce chapitre indique que la vitesse de production brute d'ozone déduite de cette simplification est inférieure de 1 % aux valeurs qui seraient dérivées du partitionnement réel des radicaux peroxy. En effet, il a été constaté que le ratio  $\frac{[HO_2]}{[HO_2]+[RO_2]}$ , dérivé des mesures spécifiées de HO<sub>2</sub> et RO<sub>2</sub> de FZJ-FAGE, se situe dans la plage de 0.4 à 0.6. Cela implique que l'utilisation de la somme de HO<sub>2</sub>+RO<sub>2</sub> du CA pour calculer le p(O<sub>x</sub>) brut serait une stratégie efficace, conduisant à une erreur inférieure à 1 %.

Des processus significatifs de perte d'O<sub>x</sub> ont été observés dans la chambre, où la dilution et les pertes de paroi d'O<sub>3</sub> étaient, en moyenne, les processus prédominants. Des pertes chimiques non négligeables ont également été notées, notamment OH+NO<sub>2</sub>, O<sub>3</sub>+alcène, O<sub>3</sub>+HO<sub>2</sub>, O<sub>3</sub>+hv et O<sub>3</sub>+OH. La dilution et les pertes de paroi représentaient respectivement 46 et 18 % des taux de perte totaux d'O<sub>x</sub> en moyenne, en tenant compte de toutes les expériences discutées dans ce chapitre, et les processus chimiques pour la fraction restante.

D'une manière pratique, l'investigation du budget de l'ozone par la détermination de  $P(O_x)^{HO_2+RO_2}$ , ne nécessiterait que de tenir compte des pertes chimiques dans  $l(O_x)$  comme le montre l'équation suivante :

$$P(O_x)^{HO_2+RO_2} = p(O_x) - l'(O_x) - SD + A$$

Le dépôt de surface (SD) et l'advection (A), qui par analogie représenteraient les pertes de paroi et la dilution pendant les expériences en chambre, sont inclus comme termes indépendants dans cette équation. Le taux de perte d' $O_x$  dû aux processus chimiques est désigné par  $l'(O_x)$  dans cette équation.

L'analyse des expériences ROxComp sélectionnées a montré que  $l'(O_x)$  est entraîné par  $O_3+HO_2$ ,  $NO_2+OH$ , et parfois alcène+ $O_3$ . Il a été constaté que  $l'(O_x)$  est significatif par rapport à  $p(O_x)$ , ce qui a entraîné des valeurs nettes de  $P(O_x)^{HO_2+RO_2}$  inférieures de 5 à 44 % aux valeurs brutes de  $p(O_x)$ . Afin de quantifier  $P(O_x)^{HO_2+RO_2}$  atmosphérique, il est donc nécessaire d'avoir accès aux mesures de OH,  $HO_2$  et  $HO_2+RO_2$ . Utiliser uniquement les mesures de  $HO_2+RO_2$  fournirait une limite supérieure de  $P(O_x)^{HO_2+RO_2}$ .

Pour des conditions de NO faibles, il a été constaté que  $P(O_x)^{HO_2+RO_2}$  est en bon accord avec  $P(O_x)^{O_x}$ . En revanche, pour des conditions de NO élevées,  $P(O_x)^{HO_2+RO_2}$  était significativement plus élevé que  $P(O_x)^{O_x}$  lorsque NO était supérieur à 0,5 ppb. Le désaccord augmente presque linéairement avec NO pour atteindre un facteur de 8 à 20 autour de 9 ppb de NO. Il est intéressant de noter qu'un désaccord similaire a été rapporté dans la littérature lorsque les valeurs brutes de  $p(O_x)$  étaient calculées à partir de mesures ambiantes de radicaux peroxy et comparées aux valeurs mesurées directement à l'aide de la technique MOPS ou calculées à partir de concentrations de radicaux simulées par des modèles en boîte. Bien que cette similarité soit intrigante, nous ne pouvons pas établir si la source du désaccord est la même.

Parmi les raisons potentielles invoquées pour expliquer le désaccord observé entre  $P(O_x)^{HO_2+RO_2}$  et  $P(O_x)^{O_x}$  lors de ROxComp, la présence d'un artefact dans les mesures de  $HO_2+RO_2$  de l'IMT-CA à haute NO est possible. Cependant, un désaccord dépendant de NO est également observé lors de l'utilisation de mesures spécifiées de  $HO_2$  et  $RO_2$  de FZJ-FAGE, avec des différences approximativement deux fois plus faibles, indiquant qu'un artefact potentiel dans les mesures de l'IMT-CA pourrait ne pas être suffisant pour expliquer le désaccord complet.



D'autres raisons ont également été proposées, à savoir (i) une mauvaise calibration d'un des instruments, (ii) un décalage dans les mesures de NO, et (iii) un processus de perte mal calculé ou (iv) manquant dans  $I(O_x)$ , ce dernier incluant les pertes de paroi de NO<sub>2</sub>, les réactions RO<sub>2</sub>+O<sub>3</sub> et la photolyse de NO<sub>3</sub>. Il a été démontré que ces processus ne peuvent pas expliquer le désaccord entre les deux quantités de  $P(O_x)$ . Des études investigatrices supplémentaires sont nécessaires pour confirmer ou identifier l'origine de la divergence.

Pour conclure sur ce travail, bien que le PAS à 2 canaux n'ait pas été couplé à l'IMT-CA en raison du manque de sensibilité, l'objectif principal a été atteint avec succès. À travers ce travail, nous avons acquis des informations précieuses sur la mesure des radicaux peroxy ambiants et la quantification des vitesses de production d'ozone, mettant en évidence certains aspects qui doivent être approfondis.

La méthodologie de  $P(O_x)$  (mesurer le taux de formation d'un polluant plutôt que sa concentration), lorsqu'elle est optimisée, devrait attirer l'attention des réseaux de mesure impliqués dans la surveillance de la qualité de l'air et du changement climatique. Le déploiement de ce type d'instrumentation à grande échelle spatiale aiderait à améliorer notre connaissance de la chimie de la formation de l'ozone dans divers environnements, à valider les modèles atmosphériques prédictifs et donc à améliorer les prédictions liées au réchauffement climatique.